EFFICIENT COUPLING OF SINGLE EPITAXIAL QUANTUM DOTS TO PLASMONIC WAVEGUIDES

Von der Universität Bayreuth
zur Erlangung des Grades eines
Doktors der Naturwissenschaften (Dr. rer. nat.)
genehmigte Abhandlung

von
MICHAEL SEIDEL
geb. in Tirschenreuth

Angefertigt am
Lehrstuhl für Experimentalphysik III
der Universität Bayreuth

UNIVERSITÄT
BAYREUTH

1. Gutachter:	Prof. Dr. Markus Lippitz
2. Gutachter:	Prof. Dr. Jürgen Köhler

Tag der Einreichung:	18. April 2024
Tag des Kolloquiums:	6. September 2024

ABSTRACT

Metallic nanostructures can confine electromagnetic fields far below the optical wavelength, thus circumventing the diffraction limit. Surface plasmon polaritons, the collective oscillations of conduction band electrons coupled to electromagnetic waves, are associated with high amplitudes of the electric field, concentrated in tiny volumes. This local field enhancement can manipulate the light-matter interaction at the nanoscale. In particular, the coupling of plasmonic waveguides to individual quantum emitters offers exciting prospects. For instance, one could envision a nanocircuit in which the presence or absence of a single photon controls the transmission of another photon, i.e., a single-photon transistor. An ideal quantum plasmonic nanocircuit would feature a source of indistinguishable photons that is coupled with near-unity efficiency to a low-loss single-mode waveguide, with an enhanced emission rate due to the Purcell effect. For such an application, excellent single-photon sources are essential. Epitaxially grown semiconductor quantum dots are considered a near-ideal quantum light source due to their brightness, stability, and narrowband excitonic transitions. On the other hand, wet-chemically grown single-crystalline silver nanowires exhibit strong confinement, single-mode operation, and the lowest propagation losses of plasmonic waveguides in the visible and infrared. As promising as the direct combination of near-surface epitaxial quantum dots and silver nanowires seems to be, it faces tremendous challenges that include reduced photon extraction as well as high attenuation of the propagating plasmon, both consequences of the high refractive index environment of the bulky semiconductor host. These and other issues are addressed in this thesis through novel coupling schemes that are numerically modeled, experimentally realized and optically characterized.

The thesis begins with a compact theoretical framework that covers the fundamentals of epitaxial quantum dots, the electromagnetics of propagating surface plasmons, and the modeling of emitters in the vicinity of plasmonic waveguides. Two- and three-dimensional finite element models are used to describe guided plasmonic modes at nanowires, as well as the coupling of quantum emitters into such waveguide modes. Quantities such as the effective mode index, the coupling efficiency, and the Purcell factor are introduced. In contrast to most other works, plasmonic waveguides in inhomogeneous environments, given by semiconducting substrates, are also considered. For the experimental characterization, different optical imaging techniques operating at cryogenic temperatures (20 K), including cathodoluminescence spectroscopy, confocal laser scanning, and photoluminescence imaging, are applied.

The first presented quantum dot–plasmon coupling scheme is termed *intermediate field coupling*. It relies on a planar dielectric layer ($n = 1.4$), acting as a spacer between the semiconductor substrate ($n = 3.4$) containing the GaAs quantum dot and the plasmonic waveguide. By tuning the film thickness, one can accomplish either efficient quantum dot–waveguide coupling or efficient waveguide propagation. Numerical simulations show that the optimal overall performance is not achieved in the near field but in the intermediate field for a film thickness around 130 nm. The experimental conditions for such an intermediate field coupling are provided by simply spin-coating a low-index dielectric and dispersing silver nanowires. When the lateral distance between the nanowire and the quantum dot becomes sufficiently small ($\lessapprox 100\,\mathrm{nm}$), coupling is demonstrated by launching surface plasmons through quantum dot luminescence. High-resolution cathodoluminescence imaging determines the lateral quantum dot–nanowire positions precisely ($< 30\,\mathrm{nm}$), and the experimentally measured coupling efficiency can be explained by a simple interference model that includes reflections of surface plasmons at the nanowire end. Intermediate field coupling can be applied to other types of emitters in high-index environments (e.g. nitrogen-vacancy centers in diamond), does not rely on nanostructuring processes, and is robust against emitter–waveguide displacement, both laterally and in growth-direction. The latter allows the use of deeply buried quantum dots with exceptional quantum optical properties. Hence, intermediate field coupling paves the way to a lifetime-limited, truly nanoscale single-plasmon source.

The second coupling scheme is based on the integration of single epitaxial quantum dots into semiconductor mesa structures that are surrounded by a dielectric layer with a lower refractive index. This approach promises increased coupling efficiency due to a reduced distance to the plasmonic waveguide on top, and increased propagation efficiency due to the dielectric that supports more efficiently propagating waveguide modes. Numerical models for a disk-shaped AlGaAs mesa (several hundred nanometers in diameter) on a silver backplane suggest that the mesa can act as a dielectric nanoresonator that either suppresses or enhances the quantum dot emission, which can be taken advantage of to design single-plasmon sources with efficiencies up to 50 %. Although the optimized target structure is feasible with advanced nanostructuring methods, an experimental realization uses a fabrication-wise simpler design based on GaAs substrates. The nanostructure is processed by deterministic integration of the quantum dots via in situ electron beam lithography, planarization of the etched topography, and dispersion of colloidal silver nanowires. Even though coupling of a mesa–waveguide hybrid structure is observed, both coupling and propagation efficiency are affected by imperfect planarization and consequential nanowire bending. Unlike intermediate field coupling, the *mesa-based coupling* approach is technologically demanding and relies on precise and deterministic fabrication methods. However, the nanoresonator-enhanced coupling scheme offers unprecedented efficient single-plasmon generation and efficient propagation through plasmonic waveguides and, therefore, opens up a path towards a scalable plasmonic quantum circuitry.

ZUSAMMENFASSUNG

Metallische Nanostrukturen besitzen die Fähigkeit, elektromagnetische Felder weit unterhalb der optischen Wellenlänge einzuschränken und damit das Beugungslimit zu umgehen. Oberflächenplasmonen, d.h., an elektromagnetische Wellen gekoppelte kollektive Oszillationen von Leitungsbandelektronen, gehen mit hohen elektrischen Feldamplituden einher, die in winzigen Volumina konzentriert sein können. Diese lokale Feldverstärkung kann dazu genutzt werden, die Licht-Materie-Wechselwirkung auf der Nanoskala manipulieren. Insbesondere die Kopplung von plasmonischen Wellenleitern an einzelne Quantenemitter verspricht grundlegend neue Anwendungsfelder. So ist beispielsweise einen Einzelphotonentransistor denkbar, bei dem die An- oder Abwesenheit eines einzelnen Photons die Transmission eines anderen Photons steuert. Ein idealer quantenplasmonischer Nanoschaltkreis bestünde aus einer Quelle ununterscheidbarer Photonen, die nahezu jedes emittierte Photon in einen verlustarmen, einmodigen Wellenleiter einkoppelt, wobei die Emissionsrate durch den Purcell-Effekt erhöht wird. Für eine solche Anwendung sind exzellente Einzelphotonenquellen unerlässlich. Epitaktisch gewachsene Halbleiter-Quantenpunkte gelten aufgrund ihrer Helligkeit, Stabilität und schmalbandigen exzitonischen Übergängen als nahezu ideale Quantenlichtquellen. Demgegenüber erlauben nasschemisch gezüchtete einkristalline Silbernanodrähte eine starke räumliche Lichteinschränkung auf eine einzige Mode, und weisen die geringsten Ausbreitungsverluste plasmonischer Wellenleiter im sichtbaren und infraroten Spektralbereich auf. So vielversprechend die direkte Kombination von oberflächennahen epitaktischen Quantenpunkten und Silbernanodrähten erscheint, sie ist mit enormen Herausforderungen konfrontiert. Dazu gehören, unter anderem, eine schwache Lichtauskopplung sowie eine hohe Dämpfung der propagierenden Plasmonen, beides bedingt durch den hohen Brechungsindex des die Quantenpunkte umgebenden Halbleiterkristalls. Um derartigen Schwierigkeiten zu begegnen, werden neuartige Kopplungsdesigns numerisch modelliert, experimentell realisiert und optisch charakterisiert.

Zu Beginn werden die theoretischen Grundlagen epitaktischer Quantenpunkte, die elektromagnetische Beschreibung propagierender Oberflächenplasmonen, und die Modellierung von Emittern in der Nähe plasmonischer Wellenleiter in kompakter Form behandelt. Zwei- und dreidimensionale Finite-Elemente-Modelle werden eingesetzt, um plasmonische Wellenleitermoden an Nanodrähten und die Einkopplung von Quantenemittern in solche Moden zu untersuchen. Größen wie effektiver Modenindex, Kopplungseffizienz und Purcell-Faktor werden eingeführt. Insbesondere werden plasmonische Wellenleiter in inhomogener Umgebung, gegeben durch Halbleitersubstrate, berücksichtigt. Für die experimentelle Charakterisierung werden verschiedene optische Abbildungsverfahren bei tiefen Temperaturen (20 K) eingesetzt. Dazu gehören beispielsweise Kathodolumineszenzspektroskopie, konfokales Laserscanning und Photolumineszenzabbildung.

Das erste Quantenpunkt–Plasmon–Kopplungsdesign wird als *intermediate field coupling* bezeichnet. Es basiert auf einer planaren dielektrischen Schicht ($n = 1.4$), die als Abstandshalter zwischen dem Halbleitersubstrat ($n = 3.4$), das den GaAs-Quantenpunkt enthält, und dem plasmonischen Wellenleiter dient. Durch Anpassung der Schichtdicke kann entweder eine effiziente Quantenpunkt–Wellenleiter–Kopplung oder eine effiziente Wellenleiterausbreitung erreicht werden. Numerische Simulationen zeigen, dass die optimale Gesamtperformance nicht im Nahfeld, sondern im Übergangsbereich zum Fernfeld (*intermediate field*) bei einer Schichtdicke von etwa 130 nm erreicht wird. Die experimentellen Bedingungen für *intermediate field coupling* können unkompliziert durch Spincoating einer dielektrischen Schicht mit niedrigem Brechungsindex und dem Aufbringen von Nanodrähten aus kolloidalem Silber geschaffen werden. Für hinreichend kleine laterale Abstände ($\lessapprox$ 100 nm) zwischen Nanodraht und Quantenpunkt kann die Kopplung durch Anregung von Oberflächenplasmonen mittels Quantenpunktlumineszenz gezeigt werden. Hochauflösende Kathodolumineszenzbilder erlauben die Bestimmung der lateralen Quantenpunkt–Nanodraht–Positionen mit hoher Genauigkeit ($<$ 30 nm), sodass die experimentell gemessene Kopplungseffizienz mittels eines einfachen Interferenzmodells, das die Reflektion von Oberflächenplasmonen am Drahtende berücksichtigt, beschrieben werden kann. *Intermediate field coupling* lässt sich auf andere Emittertypen in Umgebungen mit hohem Brechungsindex (z.B. Stickstofffehlstellenzentren in Diamant) übertragen, erfordert keine aufwendigen Nanostrukturierungsverfahren, und ist robust gegenüber einem Versatz zwischen Emitter und Wellenleiter, sowohl lateral als auch in Wachstumsrichtung. Letzteres ermöglicht die Verwendung von tief vergrabenen Quantenpunkten mit herausragenden quantenoptischen Eigenschaften. Dadurch ebnet *intermediate field coupling* den Weg zu einer lebensdauerbegrenzten, nanoskaligen Einzelplasmonenquelle.

Das zweite Kopplungsschema basiert auf der Integration einzelner epitaktischer Quantenpunkte in Halbleitermesastrukturen, die von einer dielektrischen Schicht mit niedrigerem Brechungsindex umgeben sind. Dieser Ansatz verspricht eine erhöhte Kopplungseffizienz aufgrund des geringeren Abstands zum darüber liegenden plasmonischen Wellenleiter sowie eine erhöhte Ausbreitungseffizienz aufgrund des Dielektrikums, das weitreichendere Wellenleitermoden unterstützt. Numerische Modelle für eine scheibenförmige AlGaAs-Mesa (mit einem Durchmesser von einigen hundert Nanometern) auf einem Silbersubstrat zeigen, dass die Mesa als dielektrischer Nanoresonator agieren kann, der die Quantenpunkt-Emission entweder unterdrückt oder verstärkt. Dies ermöglicht das Design von Einzelplasmonen-Quellen mit Effizienzen von bis zu 50 %. Obwohl die optimierte Zielstruktur prinzipiell mit fortgeschrittenen Methoden der Nanostrukturierung herstellt werden kann, wird für die experimentelle Realisierung ein vereinfachtes Design auf Basis von GaAs-Substraten gewählt. Zunächst werden Quantenpunkte mittels in-situ Elektronenstrahllithographie in die Mesa integriert, anschließend wird die geätzte Topographie planarisiert, und schließlich werden kolloidale Silbernanodrähten aufgebracht. Obwohl die Kopplung einer Mesa–Wellenleiter–Hybridstruktur beobachtet werden kann, wird sowohl die Kopplungs-, als auch die Ausbreitungseffizienz durch eine unzureichende Planarisierung sowie einer Biegung der Nanodrähte beeinträchtigt. Im Gegensatz zum *intermediate field coupling* ist die *mesa-basierte Kopplung* technologisch anspruchsvoll und erfordert präzise und deterministische Nanofabrikationsprozesse. Allerdings verspricht die mit dielektrischen Nanoresonatoren verstärkte Emitter–Wellenleiter–Kopplung eine bisher unerreichte Effizienz bei der Erzeugung einzelner Plasmonen, eine effiziente Ausbreitung durch plasmonische Wellenleiter und ebnet damit den Weg zu skalierbaren plasmonischen Quantenschaltkreisen.

PUBLICATIONS

---

articles in scientific journals

1. M. Seidel, Y. Yang, T. Schumacher, Y. Huo, S. da Silva, S. Rodt, A. Rastelli, S. Reitzenstein and M. Lippitz *Intermediate Field Coupling of Single Epitaxial Quantum Dots to Plasmonic Waveguides*, **Nano Letters 23, 10532-10537 (2023)**

contributions on international conferences

1. M. Seidel, Y. Yang, S. da Silva, T. Schumacher, A. Rastelli, S. Reitzenstein and M. Lippitz, *Intermediate-field Coupling of Single Epitaxial Quantum Dots to Plasmonic Nanowires*, **Talk**, DPG spring meeting 2023 - Dresden/Germany
2. M. Seidel, Y. Yang, S. da Silva, T. Schumacher, A. Rastelli, S. Reitzenstein and M. Lippitz, *Coupling Single Epitaxial Quantum Dots to Plasmonic Waveguides*, **Poster**, DPG spring meeting 2022 - Regensburg/Germany

further contributions on workshops and seminars

1. M. Seidel and M. Lippitz *Coupling Single Epitaxial Quantum Dots to Plasmonic Waveguides*, Talk, Seminar, October 2022 - Hirschegg, Kleinwalsertal/Austria
2. M. Seidel and G. Herink *Development of an optical pump/ THz probe spectrometer for probing transient carrier dynamcis*, Talk, Seminar, October 2019 - Hirschegg, Kleinwalsertal/Austria
3. M. Seidel and G. Herink *Development of a compact, sensitive optical-pump/THz-probe spectrometer for probing transient carrier dynamics*, New frontiers in optical technologies: Summer School, Poster, August 2019 - Tampere/Finland

contributions of collaborators

1. J. Alin, M. Seidel, T. Schumacher and M. Lippitz *Greyscale Lithography with Photoresist for Plasmonic Coupling*, Poster, DPG spring meeting 2023 - Dresden/Germany
2. V. Dichtl, M. Seidel, G. Schäfer and M. Lippitz *Ultrafast spectroscopy of single quantum dots utilizing synchronized GHz-Oscillators*, Poster, DPG spring meeting 2022 - Regensburg/Germany
3. J. Lang, M. Seidel, and G. Herink *A ultrafast Optical-pump/THz-probe spectrometer based on sub-diffraction field confinement*, Poster, DPG spring meeting 2022 - Regensburg/Germany

CONTENTS

1

INTRODUCTION

In 1873, Ernst Abbe formulated the resolution criterion for optical microscopes, stating that diffraction of light limits the smallest resolvable distance between two objects to about half the wavelength [1]. During the last decades, technological advances have shown that this physical limit can be bypassed, for example by the development of super-resolution microscopy techniques [2]. The field of *plasmonics* shares this sub-diffraction character, but exploits collective oscillations of electrons in conducting materials. The resulting electromagnetic fields are strongly bound to the interface between a metal and a dielectric, thus circumventing the diffraction limit. In particular, metallic nanostructures can confine electromagnetic fields to tiny volumes [3]. Modern nanofabrication methods such as electron beam lithography create unlimited possibilities for fundamental concepts [4] and application-oriented devices [5]. In addition, the resulting high electric field amplitudes close to plasmonic nanostructures open up new ways to shape light-matter interaction on a fundamental level [6].

Active plasmonic systems, i.e., plasmonic structures that interact with quantum emitters such as molecules, color centers, or quantum dots, received increasing attention in the last 15 years [7]. Strong coupling, the formation of mixed states between light and matter, has been achieved for single colloidal quantum dots in plasmonic nanoresonators [8]. But also the weak coupling regime, where the emission rate of the emitter is enhanced by the Purcell effect, promises rich physics and innovative devices [9]. In particular, plasmonic waveguides offer enhanced light-matter interaction in their proximity, but also allow the transport of single-photon states through propagating surface plasmons [10]. The preservation of the quantum light character by the plasmon [11] is fundamental for the emerging field of *quantum plasmonics*. This area of research was sparked by the proposal of a single-photon transistor, where the presence (or absence) of a single photon controls the transmission of another photon [12]. The nonlinearity that is required for photon interaction could be achieved by coupling to plasmonic elements.

A serious prerequisite on the way towards photonic quantum computing is high-quality *single-photon sources* [13]. The most mature platform is spontaneous parametric down-conversion in nonlinear crystals, where an incident laser beam generates entangled photon pairs [14]. Such single-photon sources, combined with beam splitters, phase shifters, and single-photon detectors, have been used to demonstrate quantum algorithms for rather small numbers of photonic qubits in bulky interferometric setups [15]. However, scalability is indispensable to outperform classical computational schemes in the long run, so on-chip solutions are required. *Epitaxial quantum dots* are single-photon sources that can be integrated into photonic circuits [16] and can naturally generate single photons on-demand. Compared to other quantum emitters, their stability, brightness, and exceptional quantum optical properties – including lifetime-limited ultra-narrowband optical transitions – make them a close-to-ideal source of single photons [17]. In addition, quantum dots can produce entangled photon pairs as well as highly indistinguishable photons [18]. Even though promising experimental results towards *integrated quantum circuits* based on epitaxial quantum dots are obtained, for example two-photon quantum interference on a chip [19], several hurdles need to be overcome. These include an efficient photon extraction scheme, controlled positioning of the quantum dot and the waveguide, low-loss waveguide transmission, as well as the preservation of high-quality quantum dot properties after more or less excessive nanostructuring in its vicinity. Another issue for scalable designs arises from the structural inhomogeneity of remote quantum dots that leads to variations in their emission wavelength. While the dielectric waveguide platform is being actively explored to address the above issues [20], a plasmonic counterpart is pending, even though it promises a strong Purcell enhancement that is difficult to achieve for dielectric coupling schemes, and an even smaller device footprint.

This thesis attempts to fill this gap by bringing together epitaxial quantum dots and plasmonic waveguides. It focuses on the first step towards a quantum plasmonic nanocircuit, namely the quantum dot–waveguide coupling and subsequent propagation through the plasmonic waveguide. The coupling of self-assembled quantum dots to plasmonic waveguides has been demonstrated by *Bracher et al.* [21]; however, the waveguide width was on the order of a few micrometers, so that several quantum dots contributed to the propagating plasmon. The coupling of a single quantum dot to a nanoscale plasmonic waveguide circuit has been shown by *Wu et al.* [22] who used an indirect coupling scheme via a dielectric waveguide mode. In this thesis, direct coupling concepts are designed from fundamental considerations and numerically evaluated through extensive simulations. The proposed coupling schemes are then realized experimentally and the results are explained using comprehensive models. It is shown that epitaxial quantum dots can be coupled robustly to silver nanowires via a far field contribution of a leaky waveguide mode; this intermediate field coupling opens a path towards a Fourier-limited single-plasmon source. Furthermore, a dielectric–plasmonic hybrid structure is proposed that achieves highly efficient quantum dot–waveguide coupling in simulations, and an experimental proof-of-concept study of a similar nanostructure is performed.

The thesis is structured as follows: Chapter 2 gives a comprehensive theoretical background on emitter–waveguide coupling. It includes a description of epitaxial quantum dots, the fundamentals of surface plasmons, and the numerical analysis of the coupling between propagating plasmons and emitters. The experimental methods used to characterize quantum dot–driven plasmonic waveguides are presented in chapter 3. Most prominently, cathodoluminescence and optical spectroscopy at cryogenic temperatures serve that purpose. In chapter 4, the intermediate field coupling of single GaAs quantum dots to silver nanowires is presented. This experimental and numerical study is based on a simple yet effective design involving a dielectric layer between the semiconductor surface and the plasmonic waveguide. Applying optimized sample screening routines, the launching of surface plasmons through quantum dot emission is detected, and the observed coupling efficiency is modeled by an interference effect. The last two chapters deal with quantum dots that are integrated into semiconductor mesa structures and their coupling to plasmonic waveguides. In chapter 5, such a hybrid nanostructure is designed and optimized by numerical simulations. In particular, the delicate design of the semiconductor mesa promises a highly efficient single-plasmon device. Finally, chapter 6 describes the experimental realization of such a nanostructure, which involves the deterministic lithographic integration of GaAs quantum dots as well as a planarization step to accommodate the plasmonic waveguides. Although the approach achieves detectable quantum dot–waveguide coupling, the efficiency of the nanostructure is compromised by experimental constraints. The work concludes with an outlook in chapter 7.

2

THEORY AND SIMULATION OF EMITTER–WAVEGUIDE COUPLING

This chapter provides the theoretical context for the qualitative and quantitative description of the coupling between single quantum emitters and plasmonic waveguides. The description focuses on epitaxial quantum dots and their interaction with propagating surface plasmons, although it is not limited to this class of emitters. In section 2.1, the fundamental principles of semiconductor quantum dots are outlined. The epitaxial growth of self-assembled GaAs quantum dots and their (quantum) optical properties are characterized by photoluminescence measurements. Section 2.2 covers the basic principles of propagating surface plasmons and already addresses the effects of a nearby material with a high refractive index. At first, surface plasmons at plane interfaces are considered; afterwards, waveguide eigenmodes of nanowires on high-index substrates are discussed. The latter affords solving the wave equation within two-dimensional numerical simulations. Finally, the coupling of emitters to plasmonic waveguide modes is described in section 2.3. Different coupling parameters can be obtained from two- and three-dimensional numerical simulations: While an eigenmode analysis allows to quantify the coupling strength to specific waveguide modes, a three-dimensional model excited by a dipole source provides information about the total emission rate of the emitter. Important quantities such as the Purcell enhancement or the waveguide efficiency are introduced in this section and will be used in later chapters of this thesis.

2.1 EPITAXIAL QUANTUM DOTS

Quantum dots are semiconductor nanoparticles made up of thousands of atoms. Due to their small size, their optical and electrical properties vary distinctively from the macroscopic crystal. The reason for this is the confinement of the charge carriers' wave function inside the quantum dot. Depending on the exact geometry and materials involved, discrete energy levels can evolve, similar to the discrete energy levels in atoms. For this reason, quantum dots are often referred to as artificial atoms. There are two main types of quantum dots: colloidal nanocrystals and epitaxially grown quantum dots. Colloidal quantum dots (e.g., CdSe/ZnS core-shell structures) can be synthesized in large numbers from solution and have entered everyday life, for example, as light emitters in displays or as customizable dyes for the imaging of biological processes. In contrast, self-assembled quantum dots can spontaneously nucleate during molecular beam epitaxy, for example, due to strain between two materials with different atomic lattice constants in the case of InGaAs/GaAs quantum dots. The epitaxial growth of such quantum dots requires a high level of technology (e.g., ultra-high vacuum) and is therefore costly. However, the extraordinary optical properties of these quantum dots promise to shape the second quantum revolution through effects such as superposition and entanglement. Single epitaxial quantum dots are not only routinely grown and spectroscopically studied but also provide a solid-state platform that is favorable for on-chip applications, anticipating scalable quantum optical devices.

Although very different in processing and (envisioned) application, both types of quantum dots are based on identical physical principles, most notably the quantum confinement of charge carriers. This fundamental working principle and its realization in semiconductor heterostructures are sketched in section 2.1.1. The growth process and structure of self-assembled GaAs quantum dots, which are used in this thesis, are described in section 2.1.2. Finally, the optical properties of such quantum dots are characterized in section 2.1.3 by means of photoluminescence spectroscopy.

2.1.1 *Introduction to semiconductor quantum dots*

A simple picture that is frequently used to demonstrate quantum confinement is the particle inside an one-dimensional potential well [23], as sketched in Figure 2.1a. Here, the potential is constant $V = 0$ inside the well with length L, while it is infinite outside of the well. The Schrödinger equation

$$-\frac{\hbar}{2m}\Delta\psi(\mathbf{r}) + V(r)\psi(\mathbf{r}) = E\psi(\mathbf{r}) \tag{2.1}$$

for a particle with mass m is then solved by

$$\psi_n(z) = \sqrt{\frac{2}{L}}\sin\left(\frac{\pi n z}{L}\right). \tag{2.2}$$

The first three solutions are drawn in Figure 2.1a. Due to the infinite potential, the wave function of the particle (e.g., electron) is zero outside of the well. The energy eigenvalues of the confined states are

$$E_n = \frac{\hbar^2 k_n^2}{2m}, \tag{2.3}$$

with the discretized wave vector

$$k_n = \frac{\pi}{L}n \quad \text{and} \quad n = 1, 2, 3, \ldots \quad . \tag{2.4}$$

Only discrete states can be populated by the electron. In reality, quantum confinement can be accomplished by a heterostructure composed of two materials with different band gaps, as drawn in Figure 2.1b for GaAs that is sandwiched between AlGaAs. The corresponding band gap of GaAs is $E_{\text{gap,GaAs}} = 1.42\,\text{eV}$ [24] at room temperature, while the band gap of $\text{Al}_x\text{Ga}_{1-x}\text{As}$ increases with higher Aluminium fractions x, reaching $E_{\text{gap,AlAs}} = 2.16\,\text{eV}$ for $x = 1$ [25].

Of course, the above description of free electrons does not hold for periodic potentials given in semiconductor crystals. Therefore, the concept of an effective mass m^* is introduced. This is the mass that an electron seems to have, depending on its position

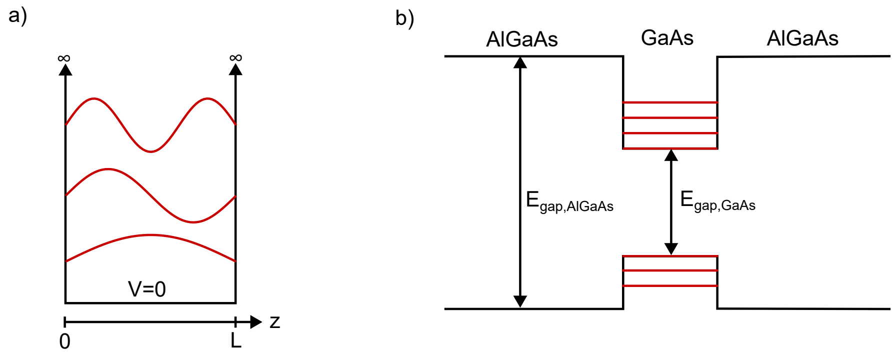

Figure 2.1: **Quantum confinement of the wavefunction inside semiconductor quantum dots.** (a) Particle inside an one-dimensional potential well. Analytical solutions of the Schrödinger equation are drawn for infinitely high potential barriers. (b) Heterojunctions of semiconductor materials with different band gaps confine the carrier wavefunction, for example if GaAs is sandwiched between AlGaAs. Discrete states can evolve, similar to those in atoms.

in reciprocal space. In the center of the Brillouin zone, the dispersion relation of the valence and conduction bands can often be approximated by parabolic functions

$$E(\mathbf{k}) = E_0 + \frac{\hbar^2 \mathbf{k}^2}{2m^*}, \tag{2.5}$$

with a constant band offset E_0. For example, electrons at the Γ-point in the conduction band of GaAs have an effective mass of $m^* = 0.067m_0$, with m_0 being the free electron mass. The effective mass approximation is also applied to valence band holes. In GaAs, three valence bands can be identified: heavy-hole, light-hole, and split-off band [26]. These bands originate from the overlap of atomic p-orbitals in the zinc-blende crystal structure and differ with respect to their angular momentum quantum number. An important feature is the overlap of conduction band minimum and valence band maximum in GaAs at $k = 0$, which results in a direct band gap that can be addressed optically without a momentum exchange with the crystal lattice.

The spatial extension that is required for the quantum confinement can be estimated from the charge carrier's De Broglie wavelength [27]

$$\lambda_B \sim \frac{h}{\sqrt{2m^* k_B T}} \tag{2.6}$$

at a temperature T. Here, k_B and h are the Boltzmann and Planck constants, respectively, and m^* is the effective mass of the charge carrier in the semiconductor crystal. Typical De Broglie wavelengths at low temperatures are in the range of $10 - 100\,\text{nm}$. Obviously, lower temperatures increase the De Broglie wavelength and consequently increase the quantization of the energy levels. In addition to the confinement length, the confinement dimensionality also defines the energetic landscape. It can be shown that the density of states (DOS) for a bulk material increases continuously from the onset of the conduction band. The degree of singularity in the DOS now increases with additional confinement dimensions [28]: For the two-dimensional confinement apparent in quantum wells, the DOS grows plateau-like. One-dimensional confinement results in quantum wires, where the DOS follows a sawtooth shape. Only for quantum dots, where the confinement acts along all three dimensions, discrete states are obtained. These atom-like states can be observed via sharp lines in luminescence spectra (see section 2.1.3).

2.1.2 *Epitaxial growth of self-assembled GaAs quantum dots*

In this section, the epitaxial growth process leading to high-quality GaAs/AlGaAs quantum dots is described briefly. These quantum dots differ inherently from the most common type of epitaxial quantum dots based on InGaAs/GaAs materials. InGaAs quantum dots are grown in Stranski-Krastanow mode, which relies on strain due to the lattice mismatch of the crystal materials. In contrast, GaAs/AlGaAs quantum dots are strain-free, which comes together with a variety of advantages, including a higher level of symmetry [29]. In particular, the droplet etching method has proven to create quantum emitters of extraordinary properties (a compact review is given in [30]). Such quantum dots – grown by S. Covre da Silva and Y. Huo at the Rastelli group at JKU Linz – are used for the experiments presented in this thesis, and therefore the droplet etching method is presented in the following. For a more detailed description, see [31] or various publications from the Rastelli group.

The first report on the self-assembly of nanoholes in GaAs substrates dates back more than 15 years [32]. In this work, the local etching of a GaAs surface has been observed when nanodroplets are annealed under low Arsenic flux at high temperatures (about 500 °C). Since then, droplet epitaxy has been optimized and is already outperforming traditional Stranski-Krastanow-grown dots in certain aspects [31]. A complete sample processing flow for quantum dots, as the ones used in this thesis, is schematically sketched in Figure 2.2. On top of a GaAs substrate, an AlGaAs layer of 100 nm is grown, that will act as the lower confinement barrier (see Figure 2.2a). The subsequent deposition of Al forms nanodroplets on top of the AlGaAs surface (Figure 2.2b). The Al droplets react with the underlying surface in such a way that As diffuses into the droplet, which partially liquifies the AlGaAs material below the droplet. Additional As flux then activates the diffusion of Al and Ga atoms out of the droplet into the surrounding region, finally forming nanoholes with depths of about $5 - 10\,\mathrm{nm}$ in the AlGaAs surface (Figure 2.2c). Typical lateral dimensions are about 50 nm [33]. These nanoholes are filled afterwards by depositing the GaAs wetting layer with a thickness of 2.3 nm, which is allowed to diffuse into the nanoholes. In the last step, the upper AlGaAs confinement barrier is grown; for the near-surface quantum dots used in this thesis, capping layers between $15 - 40\,\mathrm{nm}$ are applied. In order to passivate the surface, 1 nm of GaAs and a monolayer of Si is deposited. The droplet density and size (and therefore the quantum dot density and size) are determined by the substrate temperature, deposition rate, and the amount of deposited Al [30]. The emission wavelength is given by the depth of the nanoholes, the amount of

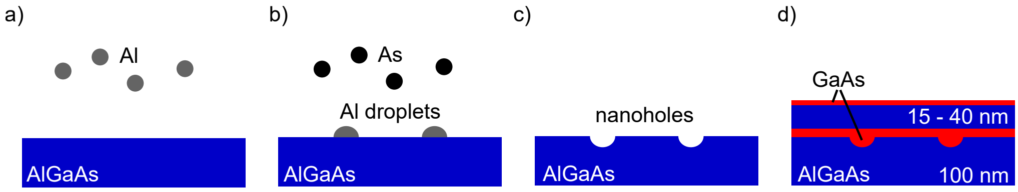

Figure 2.2: **Epitaxial growth of GaAs/AlGaAs quantum dots via the droplet etching method.** The image is adapted from [30]. (a) Aluminium is deposited on top of the lower AlGaAs barrier, resulting in the formation of Aluminium droplets. (b) Under arsenic flux, the AlGaAs crystal is partially liquified below the droplets. (c) Diffusion of Aluminium and Gallium atoms away from the droplet creates nanoholes in the AlGaAs. (d) The nanoholes are filled with GaAs, which diffuses into the holes. The upper AlGaAs barrier is grown on top and passivated by a thin GaAs layer. The GaAs substrate is not shown.

GaAs filling, and the Al content of the barriers [34]. Typical values for the Al fraction are $33\,\% - 40\,\%$. Throughout this thesis, slightly different quantum dot samples are used. See Appendix A.1 for a detailed description of these samples.

2.1.3 *Optical properties of GaAs quantum dots*

Optical excitation of a bulk semiconductor can promote an electron from the valence band to the conduction band if the incident photon energy is comparable to the band gap. Consequently, a hole is created in the valence band. Coulomb interaction between the negatively charged electron and the positively charged hole leads to the formation of an exciton (X), a bound electron-hole pair. The exciton energy [23]

$$E_X = E_e + E_h - \frac{\mu e^4}{32\pi^2\hbar^2\epsilon_r^2\epsilon_0^2} \tag{2.7}$$

is lowered compared to the free carrier gas via the negative binding energy, similar to the hydrogen atom. Furthermore, the Bohr radius

$$a_B = \frac{4\pi\epsilon_r\epsilon_0\hbar^2}{\mu e^2}. \tag{2.8}$$

can be assigned. Here, the reduced mass of the two-body system is given by

$$\frac{1}{\mu} = \frac{1}{m_e^*} + \frac{1}{m_h^*} \tag{2.9}$$

the effective electron mass m_e^* and the effective hole mass m_h^*. Assuming the Γ-valley values for the effective masses of electron $m_e^* = 0.063 m_0$ and the heavy hole $m_e^* = 0.060 m_0$ in bulk GaAs, as well as the static dielectric constant $\epsilon_r = 13.18$, one obtains an excitonic binding energy of $-4.7\,\text{meV}$ and Bohr radius of $a_B = 11.5\,\text{nm}$.

The Bohr radius a_B gives the critical length scale for confined excitons. Depending on the size of the quantum dot, different confinement regimes can be identified: if the size is small compared to the Bohr radius, the confinement energy dominates over the Coulomb interaction. In the weak confinement regime, where the quantum dot is larger than the Bohr radius, Coulomb interactions play a major role. The height of the GaAs quantum dots used in this thesis is comparable to the Bohr radius along the growth direction [33]; however, the lateral confinement is weak since the quantum dots extend about 50 nm in the sample plane. According to [35], measured excitonic lifetimes of $\approx 250\,\mathrm{ps}$ indeed indicate weak confinement for this type of quantum dots since such lifetimes fall below the lower limit that is imposed by strong confinement [36].

The direct band gap of GaAs quantum dots allows an efficient exciton-photon interaction via the radiative transition from the conduction to the valence band. The rate of the groundstate-exciton transition is given by Fermi's golden rule [26]

$$\gamma_{X,0} = \frac{2\pi}{\hbar} \left|\langle\psi_X|\, \hat{\epsilon}\mathbf{p}\, |\psi_0\rangle\right|^2 \delta(E_X - E_0 - \hbar\omega), \tag{2.10}$$

where $\psi_{X,0}$ and $E_{X,0}$ represent the excitonic and ground state wavefunction and energy, respectively. The polarization state of the photon is given by $\hat{\epsilon}$ and the dipole operator is $\mathbf{p}$. The delta function $\delta(E_X - E_0 - \hbar\omega)$ guarantees energy conservation by selecting the photon with energy $\hbar\omega$. Fermi's golden rule states that the dipole transition matrix element needs to be finite for the transition to be allowed. In GaAs quantum dots, an exciton typically consists of a conduction band electron and a heavy hole [27]. Both the electron spin state ($|\uparrow\rangle$ or $|\downarrow\rangle$) and the hole spin state ($|\Uparrow\rangle$ or $|\Downarrow\rangle$) are quantized along the growth direction, with an electron spin projection of $\pm\frac{1}{2}$ and a heavy-hole spin projection of $\pm\frac{3}{2}$. Consequently, the emission of a circularly polarized photon is allowed from bright states with anti-parallel spin configuration ($|\uparrow\Downarrow\rangle$ or $|\downarrow\Uparrow\rangle$), while emission from the dark exciton with parallel spins ($|\uparrow\Uparrow\rangle$ or $|\downarrow\Downarrow\rangle$) is forbidden due to angular momentum conservation. While the two bright excitonic states are degenerated in theory, anisotropic exchange interaction can lead to a mixing of the states: This results in two energy states $|X_H\rangle$ and $|X_V\rangle$ (see energy level scheme in Figure 2.3a) that emit linearly polarized photons along the horizontal (H) and vertical (V) directions during the transition to the ground state $|0\rangle$. Here, the horizontal and vertical directions both lie in the sample plane, perpendicular to the growth axis (z).

Since in practice, quantum dots typically exhibit varying degrees of ellipticity, the degeneracy of the bright excitonic states is lifted by the fine structure splitting E_{FSS}. In order to observe the fine structure splitting experimentally, polarisation-dependent spectra of the excitonic transitions are recorded, as shown in Figure 2.3b. A rotatable $\lambda/2$-waveplate is placed in the detection path of the microscope, followed by a fixed polarizer (a detailed description of the optical setup can be found in Figure 3.6). This configuration allows to spectrally separate the distinct emission of the two excitonic states that vary energetically by the fine structure splitting. A Lorentzian function is fitted to each spectrum to determine the central wavelength, which is displayed as a black cross, respectively. In order to make the small wavelength shift more visible, each spectrum is interpolated afterwards. By analyzing the central wave-

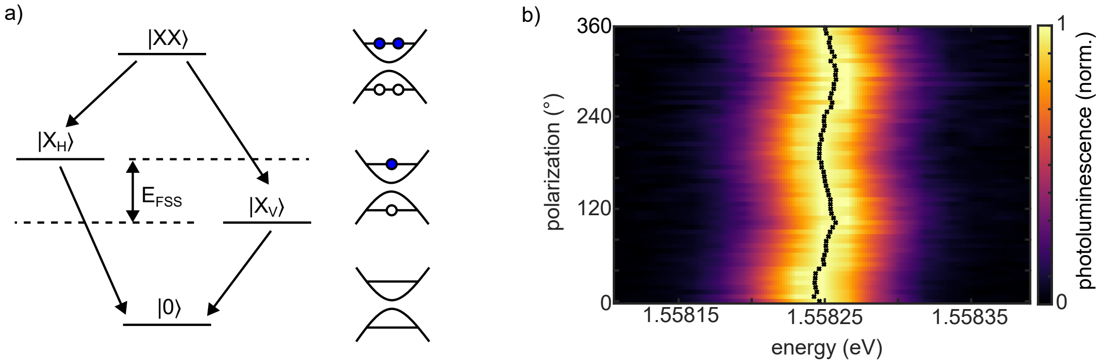

Figure 2.3: **Excitonic states in GaAs quantum dots.** (a) Energy level scheme. Two excitonic states are separated by the fine structure splitting (FSS). Electron (hole) configurations are illustrated by full (empty) circles. (b) Fine structure splitting in near-surface GaAs quantum dots, measured via polarization-dependent photoluminescence at low temperatures, yielding a value of $E_{FSS} = 15\,\mu\text{eV}$. The black crosses correspond to the central wavelength of a Lorentz fit to each spectrum. To increase the visibility, the spectra are interpolated.

lengths of each peak, the fine structure splitting is determined to be $E_{FSS} = 15\,\mu\text{eV}$, indicating a relatively high degree of symmetry of the investigated quantum dot [33].

As already sketched in Figure 2.3a, also higher excitations than the neutral exciton are possible, for example, the biexciton consisting of two electrons and two holes. Such multi-excitonic states are populated under non-resonant excitation through the generation of electron-hole pairs within the barriers or the wetting layer and subsequent diffusion to the quantum dot. The biexciton state $|XX\rangle$ can decay to the ground state $|0\rangle$ by taking one of two possible paths via the almost degenerate $|X_{H,V}\rangle$ states, accompanied by the emission of a linearly polarized photon pair. Since the energy difference of the transition $|XX\rangle \rightarrow |X\rangle$ differs from the $|X\rangle \rightarrow |0\rangle$ transition due to the Coulomb interaction (see Equation 2.7 and also Figure 2.4a), a single-photon source can be obtained by spectrally filtering one of these emission lines. If the fine structure splitting would be small compared to the natural recombination linewidth, both paths of the biexciton–exciton cascade are indistinguishable, and a polarization-entangled two-photon state is emitted [37]. Such considerations make the radiative biexciton–exciton cascade a promising candidate for an on-demand entangled photon source.

While an advantage of non-resonant optical pumping lies in the fact that simple bandpass filtering can separate the quantum dot emission from the laser background, there are several drawbacks of this excitation method [27]: a temporal emission-jitter is introduced due to the carrier capturing and relaxation process; furthermore, defects close to the dot lead to fluctuations in the emission wavelength and, therefore result in line broadening. These effects severely limit the photon indistinguishability. Consequently, resonant excitation schemes have been developed: In a resonance fluorescence experiment, the $|X\rangle$-state is excited directly, which requires careful discrimination between quantum dot emission and laser scattering [38, 39]. Another

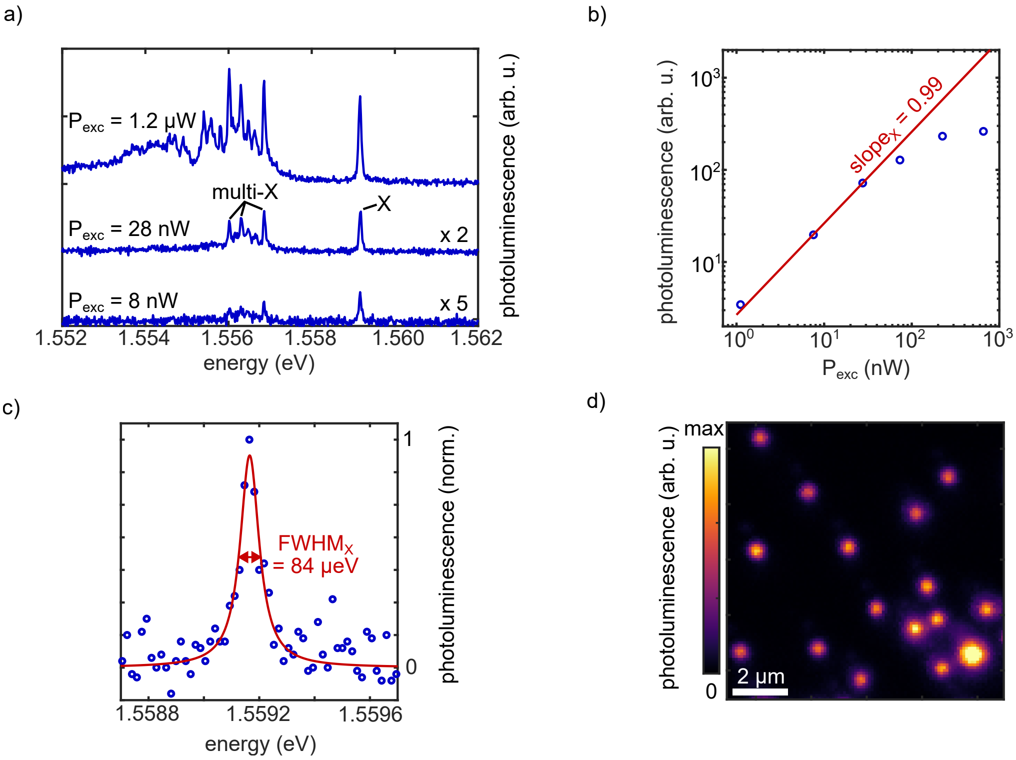

Figure 2.4: **Fundamental properties of GaAs quantum dots, characterized through low-temperature photoluminescence measurements.** (a) Photoluminescence spectra for varying excitation power. In addition to the neutral exciton (X), transitions from higher excitation states are present, including the biexciton and charged exciton states. (b) Saturation curve for the excitonic transition. A power function fit (red line) determines a linear power dependence for small excitation powers. (c) Highlight of the excitonic transition at low excitation. A Lorentz fit (red line) determines the full-width-half-maximum to 84 µeV. (d) Confocal laser scanning microscope image.

scheme involves a two-photon absorption process that excites the $|XX\rangle$-state, which allows to produce highly indistinguishable and entangled photons [18].

Photoluminescence spectra of a single GaAs quantum dot for above-band excitation at $\lambda = 532\,\text{nm}$ are shown in Figure 2.4a. In addition to the neutral exciton (X) at 1.559 eV, there are multi-excitonic transitions at an energy of about 1.556 eV observed. The shift to lower energies is caused by the Coulomb interaction of the charged particles, which reduces the binding energy. The higher excitation states involve – apart from the biexciton (XX) – for example, the positively charged trion (one electron and two holes) as well as the negatively charged trion (two electrons and one hole). For a detailed assignment of multi-excitonic states in GaAs quantum dots, see [40] by the Rastelli group. For increasing laser excitation power P_{exc}, the multi-excitonic transitions dominate the spectrum due to their nonlinear power scaling, while the neutral exciton scales linear with excitation power. This can be seen in Figure 2.4b, where the integrated intensity of the excitonic line is measured for increasing excitation powers. Only for excitation levels below $P_{exc} = 100\,\text{nW}$ a linear power dependence is found, while for higher excitation levels, a saturation is observed. Under weak excitation of $P_{exc} = 8\,\text{nW}$, the excitonic linewidth is determined by a Lorentz fit to FWHM $= 84\,\mu\text{eV}$ in Figure 2.4c. This value slightly exceeds the resolution limit of the spectrometer, which is about $40\,\mu\text{eV}$. The natural linewidth given by the excitonic recombination lifetime of 200 ps is about $3\,\mu\text{eV}$ for GaAs quantum dots [41]. However, the small burial depth of 40 nm is accompanied by coupling to surface states, which leads to substantial line broadening for these dots [42, 43]. A confocal laser scanning microscope image (for details on the experimental setup, see section 3.2) in Figure 2.4d demonstrates a low quantum dot density of $0.15\,\mu\text{m}^{-2}$ on the substrate. The low density poses an important prerequisite for quantum optical experiments since the emission of a single dot can be separated via the far field.

2.2 PROPAGATING SURFACE PLASMON POLARITONS

Plasmons are collective oscillations of the electron density at metal surfaces or small metal particles. The term polariton originates from the natural coupling of these charge oscillations to electromagnetic waves. Surface plasmon polaritons (SPPs) are, therefore, the quasi-particles of such light-matter interaction that is inherently connected to the existence of free electrons, available in the conduction bands of metals. Frequently, surface plasmon polaritons are abbreviated to surface plasmons or plasmons, also in this thesis. SPPs can travel on the surface of extended metal structures, which then is called a plasmonic waveguide. The combination of several features makes surface plasmons unique: First, the plasmon can confine electromagnetic waves below the diffraction limit. For example, the silver nanowires that are used in this work to guide surface plasmons have diameters of 50 nm, which is only 1/16 of the free-space wavelength of the excitation light. One implication of the small feature size is a strong electromagnetic near field that can tailor the light-matter interaction via the Purcell effect [44]. Since the quantum light character of its excitation source is conserved in the plasmon [11, 45, 46], quantum plasmonic applications are getting more and more attention. In particular, self-assembled quantum dots are considered a promising platform for the generation of high-quality single or indistinguishable photons. As intriguing as the combination of plasmonic waveguides and epitaxial quantum dots seems, there is only a small amount of literature concerning this field. This is predominantly caused by the high attenuation of surface plasmons at interfaces involving high-index semiconductors.

This chapter provides theoretical fundamentals of surface plasmon polaritons, which are applied to plasmons at high-index materials. A derivation of SPPs from electromagnetic principles is given in section 2.2.1. Starting from the wave equation, an analytical solution for surface plasmons at plane interfaces is obtained. In particular, the influence of the dielectric's refractive index on the propagation characteristics is investigated. Section 2.2.2 discusses the plasmonic waveguide modes of silver nanowires on high-index substrates. These eigenmodes can be obtained from a finite element simulation, assuming infinitely long waveguides.

2.2.1 *Surface plasmon polaritons (SPP) at plane interfaces*

The easiest system that supports surface plasmon polaritons consists of two adjacent media, where medium 1 is characterized by a real-valued dielectric function $\epsilon_1(\omega)$, and medium 2 has a complex-valued dielectric function $\epsilon_2(\omega)$. In the following, the condition for the existence of surface plasmons at plane interfaces, as well as their dispersion relations, are derived from fundamental laws. The description is mostly based on Hecht and Novotny [47], who consider only low-index dielectric materials like air or glass as the upper medium. Therefore, the treatment in this chapter is expanded to high-index dielectrics, as it is the case for semiconductors.

Plasmons can be described fully classical by solving Maxwell's equations. By combining the curl equations, i.e., Faraday's law and Ampere's law, the wave equation

$$\nabla^2 \boldsymbol{E}(\boldsymbol{r},\omega) - \frac{\omega^2}{c^2}\epsilon(\boldsymbol{r},\omega)\boldsymbol{E}(\boldsymbol{r},\omega) = 0 \tag{2.11}$$

is obtained. The free-space speed of light $c = (\epsilon_0\mu_0)^{-1/2}$ is given by the permittivity ϵ_0 and permeability μ_0 of vacuum. The relative magnetic permeability is $\mu = 1$ for the relevant materials at optical wavelengths and is therefore omitted. The coordinate system is defined such that the interface is at $z = 0$, and $\epsilon(r,\omega) = \epsilon_1(\omega)$ if $z > 0$ and $\epsilon(r,\omega) = \epsilon_2(\omega)$ if $z < 0$. Since the right-hand side is zero, no external excitation is assumed, and therefore, the solution is an eigenmode that is localized at the interface between the media. It can be shown that only p-polarized waves, i.e., waves in the yz-plane, with y being the direction of propagation, are solutions to the wave equation:

$$E_j = \begin{pmatrix} 0 \\ E_{j,y} \\ E_{j,z} \end{pmatrix} e^{ik_y y - i\omega t} e^{ik_{j,z} z}, \qquad j = 1,2. \tag{2.12}$$

By applying the interface conditions, for example, the continuity of the parallel component of the electric field

$$E_{y,1} = E_{y,2}, \tag{2.13}$$

and the perpendicular component of the electric displacement field

$$\epsilon_1 E_{z,1} = \epsilon_2 E_{z,2}, \tag{2.14}$$

one can derive the dispersion relations for the wave vector in the propagation direction

$$k_y^2 = \frac{\epsilon_1\epsilon_2}{\epsilon_1+\epsilon_2}\frac{\omega^2}{c^2} \tag{2.15}$$

and for the wave vector's normal component

$$k_{z,j}^2 = \frac{\epsilon_j^2}{\epsilon_1+\epsilon_2}k^2, \qquad j = 1,2. \tag{2.16}$$

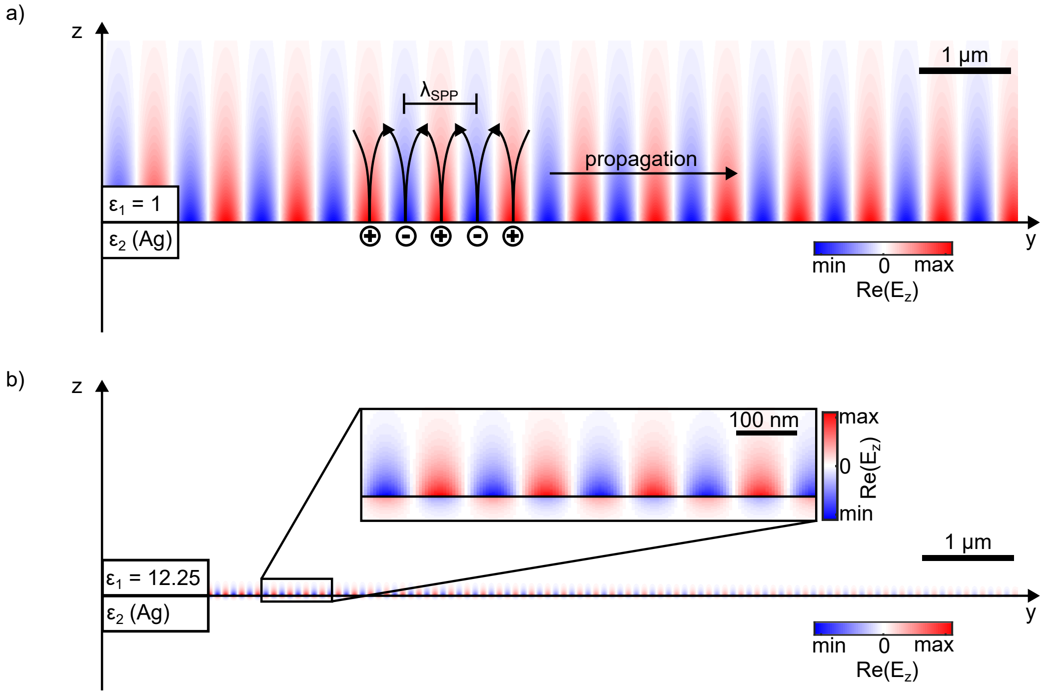

Figure 2.5: **Propagating surface plasmon polaritons (SPPs) at silver/dielectric interfaces for low- and high-indexed dielectrics.** The real part of the out-of-plane electric field component E_z is shown. The surface plasmon wavelength λ_{SPP} and the charge distribution inside the metal are sketched. The free-space wavelength is $\lambda = 795\,\text{nm}$, and the corresponding permittivity of silver is $\epsilon_2 = -30.6 + 0.398i$ [48]. (a) Dielectric permittivity of $\epsilon_1 = 1$, as the case for a silver/air-interface. (b) Dielectric permittivity of $\epsilon_1 = 12.25$, as the case for a silver/AlGaAs interface. An enlarged view of the interface is given in the inset.

For a bound interface mode, two conditions need to be fulfilled: First, a propagating wave requires a real k_y. Second, a bound mode needs to decay perpendicular to the interface, which affords an imaginary k_z in both media. These conditions allow to formulate general rules for the dielectric functions that support such an interface plasmon:

$$\begin{aligned} \text{Re}\Big(\epsilon_1(\omega)\cdot\epsilon_2(\omega)\Big) &< 0, \\ \text{Re}\Big(\epsilon_1(\omega)+\epsilon_2(\omega)\Big) &< 0. \end{aligned} \tag{2.17}$$

The above equations are equal to the statement that the real part of one of the dielectric functions needs to be negative, with an absolute value larger than that of the other dielectric function. In particular, noble metals, like silver or gold, have large negative real parts of the dielectric function, together with a small imaginary part. The latter leads to a damping of the interface wave along the propagation direction, which has been neglected to derive equations 2.17.

Figure 2.5a shows the field distribution of a propagating surface plasmon at the interface between silver and air at a fixed time in terms of the out-of-plane component E_z. The free space wavelength is $\lambda = 795\,\text{nm}$, and the corresponding dielectric function $\epsilon_2 = -30.6 + 0.398\text{i}$ of silver is taken from Johnson and Christy [48]. The oscillating charges at the silver surface are coupled to the light field which penetrates much deeper in the air half-space than in the metal. In propagation direction (y), the electric field phase oscillates with the SPP wavelength

$$\lambda_{SPP} = \frac{\lambda}{\text{Re}(\tilde{n}_{eff})}. \tag{2.18}$$

Here, $\tilde{n}_{eff}$ is the complex-valued effective mode index. For a bound mode, the real part of the mode index exceeds the refractive index of the dielectric $n_{eff} > n_1$, resulting in a plasmon wavelength $\lambda_{SPP} < \lambda$ smaller than the free space wavelength. As already mentioned, the non-zero imaginary part of the metal's dielectric function leads to a damping of the surface plasmon wave along the propagation direction. The exponential decay given by the imaginary part of the effective mode index can be characterized by the $1/e$-propagation length

$$L_p = \frac{1}{2\,\text{Im}(k_y)} = \frac{\lambda}{4\pi\,\text{Im}(\tilde{n}_{eff})} \tag{2.19}$$

for the SPP intensity. Both the SPP wavelength and the propagation length increase with wavelength λ. In this thesis, mainly epitaxial quantum dots are used to excite surface plasmons, with a fixed emission wavelength of about $\lambda_{QD} = 795\,\text{nm}$. Consequently, not the wavelength dependence but rather the influence of the dielectric's refractive index is of interest. The latter tremendously impacts the surface plasmon properties, which immediately becomes clear when replacing air with a dielectric with a dielectric constant of $\epsilon_1 = 12.25$ or $n_1 = 3.5$, common values for semiconductors in the near-infrared. From the electric field distribution shown in Figure 2.5b, three important changes are induced by the high-index dielectric: First, the penetration depth into the high-index dielectric is strongly reduced. At the same time, the out-of-plane component of the electric field is comparably stronger inside the silver, which can be seen in the enlarged inset. Second, the SPP wavelength is much smaller. Third, the attenuation of the SPP is increased, which is already visible on the shown $10\,\mu\text{m}$ scale. In order to get a better understanding of these observations, the surface plasmon properties are characterized in the following.

At first, the dispersion relation for the wave vector in the propagation direction given in Equation 2.15 is evaluated for a plane silver/dielectric interface and shown in Figure 2.6a. For the red curve, a dielectric constant of $\epsilon_1 = 1$ is used, while the blue curve corresponds to $\epsilon_1 = 12.25$. For small photon energies, the dispersion relations approximate their respective light lines given by

$$\omega = c\frac{k_y}{\sqrt{\epsilon_1}}. \tag{2.20}$$

The slope of the high-index light line is therefore reduced by the refractive index of the dielectric $n_1 = \sqrt{\epsilon_1}$. This directly explains the shorter SPP wavelength λ_{SPP} in

Figure 2.5b. Due to the deviation of the high-index dispersion relation from the light line, this effect is even increased at higher energies, resulting in a strong reduction of the surface plasmon wavelength λ_{SPP}. At the quantum dot emission wavelength $\lambda_{QD} = 795\,\mathrm{nm}$, for example, the silver/AlGaAs-plasmon gains an additional momentum of 29 % compared to its (already shifted) light line, while the silver/air-plasmon deviates only weakly from its light line (1.7 %). The maximum value of k_y is obtained for $\mathrm{Re}(\epsilon_2(\omega)) = \epsilon_1$, i.e., when the real part of the metal's dielectric function $\epsilon_2(\omega)$ matches the dielectric constant of the dielectric ϵ_1. For the high-index dielectric, this is the case at lower energies, as can be seen in Figure 2.6a. Above this energy, a bending of the dispersion relation occurs. When the dispersion relation crosses its light line, the interface mode loses its bound character and radiates into the metal half-space. Such modes are usually not desired and, therefore, not discussed further. It has to be noted that the dielectric medium is also dispersive in reality, which has been omitted at this point for the sake of simplicity.

The propagation length L_p of the SPP is a crucial parameter for many applications. It is given as a function of the dielectric constant ϵ_1 in Figure 2.6b for a fixed wavelength of $\lambda = 795\,\mathrm{nm}$ as the blue solid line. There is a drastic decrease in L_p with increasing dielectric constant of the upper medium. While for $\epsilon_1 = 1$, the propagation length is 280 µm, it is only 3.2 µm for $\epsilon_1 = 12.25$, corresponding to a reduction of 87. The reason for this is an increased Ohmic damping inside the metal, induced by the presence of the high-index material. As already discussed above, the surface plasmon wavelength λ_{SPP} decreases significantly with higher ϵ_1, which, in principle, allows to shrink the circuit dimensions accordingly. To account for this, the propagation length is normalized to λ_{SPP} and shown as the reddish curve in Figure 2.6b. In values of λ_{SPP}, the propagation length still decreases from 362 to 18; hence, the plasmon attenuation is only weakly "compensated" by the wavelength shortening.

Also, the penetration depth into the dielectric (dashed lines) depends strongly on its dielectric constant: In the case of low refractive index, the penetration depth into the dielectric is $d_{z,1} = 340\,\mathrm{nm}$, while for high refractive indices, it is only $d_{z,1} = 22\,\mathrm{nm}$. As for the propagation length, the $1/e$-decay constant of the intensity is applied. In terms of λ_{SPP}, the penetration depth is reduced from 44 % to 13 %. Interestingly, the penetration depth into the silver (dotted lines) does not change proportionally: one finds even a slight decrease from $d_{z,2} = 11.3\,\mathrm{nm}$ to $d_{z,2} = 8.6\,\mathrm{nm}$ in absolute values (and an increase from 1.4 % to 5.0 % in terms of λ_{SPP}). Therefore, the explanation that the high-index medium pushes the electric field of the SPP deeper into the metal is not convincing to explain the dramatic propagation losses. Instead, "more" field is pushed into the silver: This can be seen if the discontinuous out-of-plane electric field components of the dielectric side $E_{z,1}$ and the metal side $E_{z,2}$ of the interface are compared with each other as a function of the dielectric constant ϵ_1, as done in Figure 2.6c. Due to the continuity of the electric displacement field $\mathbf{D}$ (see Equation 2.14), one obtains

$$\left|\frac{E_{z,2}}{E_{z,1}}\right| = \frac{1}{|\epsilon_2|}\epsilon_1, \tag{2.21}$$

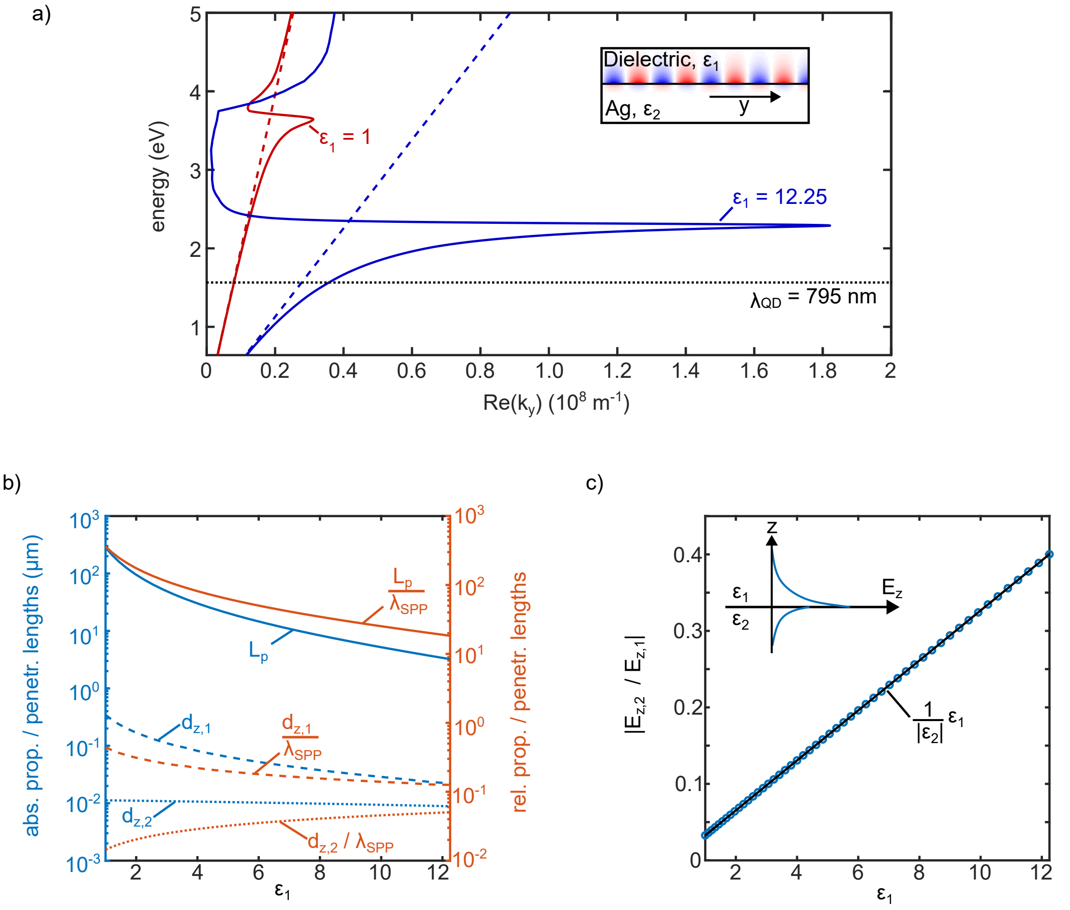

Figure 2.6: **Influence of the dielectric constant ϵ_1 on the properties of a SPP at a silver/dielectric interface.** (a) Dispersion relations for SPPs interfacing a low index dielectric with $\epsilon_1 = 1$ (red line) and a high-index dielectric with $\epsilon_1 = 12.25$ (blue line). The dashed lines correspond to the light line in the respective medium, while the horizontal line indicates the quantum dot emission wavelength $\lambda_{QD} = 795\,\text{nm}$. (b) Propagation length L_p, penetration depth into the dielectric $d_{z,1}$, and penetration depth into the silver $d_{z,2}$. All quantities represent $1/e$-intensity decay constants at λ_{QD}. The blue curves correspond to the absolute values, while the reddish curves are normalized to the plasmon wavelength λ_{SPP} that decreases with higher ϵ_1. (c) Ratio of the out-of-plane field components $|E_{z,1}/E_{z,2}|$ at the interface (blue circles). The increase of the field strength in the metal is directly linked to the dielectric constant's ratio (black line) due to the continuity of $\mathbf{D}$ (Equation 2.14).

a linear increase of the electric field ratio with increasing ϵ_1. The left-hand (right-hand) side of the upper equation is plotted in Figure 2.6c as blue circles (black line). The slope of the linear function is given by the inverse of the absolute of the metal's dielectric function ϵ_2. In other words, the continuity of the perpendicular component of $\mathbf{D}$ is responsible for an increased field strength inside the silver, which in turn causes the Ohmic losses to increase significantly for high-index dielectrics.

It should be noted that only real-valued dielectric functions have been assumed for the dielectric so far. This should be a good assumption for $\mathrm{Al}_x\mathrm{Ga}_{1-x}\mathrm{As}$ compounds with $x > 30\,\%$ that are used to cap the quantum dot layer for the samples used in this thesis (see also Appendix A.1). However, for smaller Al fractions, the band gap decreases, resulting in a non-zero imaginary part: pure GaAs, for example, has a refractive index of $n = 3.69 + 0.0798\mathrm{i}$ [49] at 795 nm. Since only very thin layers of pure GaAs are present in the used quantum dot samples, the influence of the GaAs is neglected in the simulations throughout this thesis, and AlGaAs with $n = 3.44$ [49] is assumed.

2.2.2 *SPP waveguide modes at nanowires in inhomogeneous environments*

In contrast to the surface plasmon at the interface of two half-spaces, there is, in general, no analytical solution for SPPs at nanowires. Even though the quasi-static approximation holds for wires with tiny cross-sections [50], a homogeneous dielectric environment is required. However, if the refractive index of substrate and superstrate differ [51], or more complicated nanowire shapes, e.g., pentagonal cross-sections of colloidal silver nanowires [52] are considered, computational methods are necessary. Therefore, the finite element method is utilized to solve Maxwell's equations numerically using Comsol Multiphysics. This commercial software allows to perform a two-dimensional mode analysis in the cross-sectional plane of the waveguide. Both the wave optics (WO) and the radio frequency (RF) module can be used for such problems. The wave equation 2.11 is solved for a certain frequency ω by time-harmonic fields

$$\mathbf{E}(x,y,z,\omega) = \mathbf{E}(x,z,\omega)e^{-i\tilde{k}_y(\omega)y} = \mathbf{E}(x,z,\omega)e^{-ik_0 n_{eff} y}e^{-y/2L_p}. \tag{2.22}$$

The solution consists of the modal field $\mathbf{E}(x,z,\omega)$ in the transverse plane that evolves in propagation direction according to the complex propagation constant $\tilde{k}_y$. The real part of the propagation constant gives the effective index n_{eff} of the mode, while the imaginary part determines the damping of the wave, characterized by the propagation length L_p. The mode-solving algorithm approximates eigenmodes of the system with their corresponding complex propagation constants.

In this chapter, the eigenmodes of a silver nanowire at the interface of a substrate with a refractive index n_2 and a superstrate with a refractive index n_1 are computed. The geometry is sketched in Figure 2.7a. Note that the size of the nanowire is enhanced relative to the computation box for illustration purposes. The simulation window is enclosed by a perfectly matched layer (PML), an artificial domain that acts as a nearly perfect absorber for electromagnetic fields [53]. For bound waveguide modes, in principle, a perfect electric conductor would also be appropriate. Such a boundary imposes the condition of a vanishing tangential component of the electric field. However, in the inhomogeneous case $n_2 > n_1$, leaky modes can arise under certain conditions. Such modes have an effective mode index that is smaller than the surrounding refractive index; in other words, they are located to the left of the light line in Figure 2.6a and consequently ra-

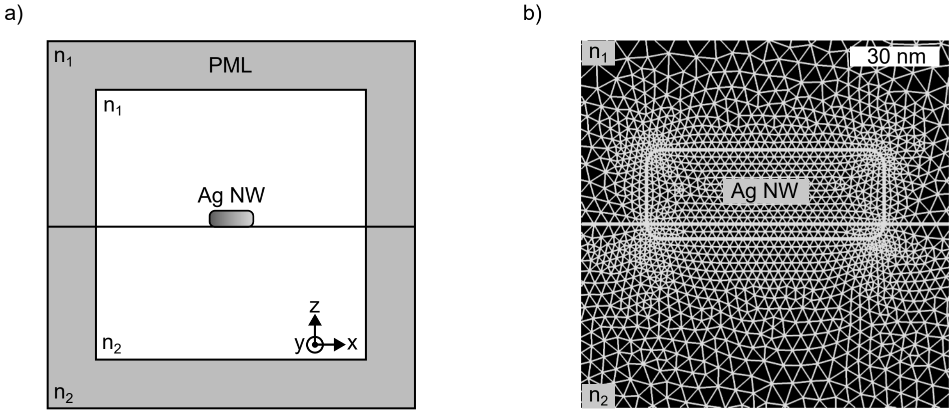

Figure 2.7: **Comsol model for a two-dimensional mode analysis.** (a) Sketch of the geometry: A silver nanowire (Ag NW) is located at the interface of two media with refractive indices n_1 and n_2. Amongst other possible boundary conditions, a perfectly matched layer (PML) can be applied. The size of the nanowire is drawn enlarged relative to the computation box. (b) Mesh around the nanowire. In order to avoid unphysical singularities, corners are rounded, and the nanowire is sunken into the substrate.

diate into the far field. Therefore, a PML is necessary to absorb these radiative modes.

An important aspect of the finite element method is the meshing. It needs to be fine enough to spatially resolve oscillating and evanescent fields. The mesh of the two-dimensional Comsol model is shown for the region around the nanowire in Figure 2.7b. For dielectric media, an element size smaller than $\lambda/10$ is typically required. For media with a large real part of the refractive index, the mesh needs to be refined accordingly. For evanescent plasmonic fields, the penetration depth into the metal is on the order of 10 nm (see section 2.6b) and must be resolved by at least two elements [53], which can make the simulation of plasmonic features computationally intensive. Typical two-dimensional models consist of several thousand elements and are usually solved in less than a minute on the chair's workstation. In order to avoid unphysical singularities, the corners of the nanowire are rounded by a radius of curvature of 5 nm, as can be seen in Figure 2.7b. For the same reason, the nanowire is sunken 5 nm into the substrate.

Guiding plasmonic modes of metal nanowires are theoretically well understood for homogeneous environments $n_1 = n_2$ [50, 54] and low-index substrates with $n_2 \approx 1.5$ [52, 55] for a variety of waveguide configurations. However, less work has been published on nanowires on top of high-index substrates. *Chen et al.* [51] compute the eigenmodes of a two-wire transmission line on top of a high-index substrate. In the following, the highly inhomogeneous case of $n_1 = 1$ and $n_2 = 3.4$ is investigated for a silver nanowire with a height of 30 nm and varying width w. For this system, two main modes can be identified. The corresponding mode profiles are shown in Figure 2.8a and Figure 2.8b for a width of $w = 100$ nm. Both modes can be differentiated via their charge distribution: The fundamental mode is characterized by a charge distribution that is homogeneous in the xz-plane and oscillates periodically along the propagation (y) direction. At a given point in time, the electric field points away (or towards) the waveguide, indicated by the arrows that are defined by the real part of the E_x and E_z components in Figure 2.8a. As a result of the inhomogeneous surroundings, the highest electric field strength is localized at the bottom corners of the waveguide inside the high-index substrate. For the first higher-order mode (Figure 2.8b), in contrast, the charge distribution oscillates not only in waveguide direction but also horizontally along the x-direction. This mode has a cut-off width since only broad waveguides can support such a charge distribution. In principle, there is also a higher-order mode with an orthogonal charge and field distribution; for a circular or square-shaped nanowire in a homogeneous environment, these two modes can be transferred into each other by a 90°–rotation and are, therefore, degenerated [54]. However, for the inhomogeneous case and the small waveguide height of 30 nm chosen here, this higher-order mode is already in the cut-off. For even broader waveguides with $w > 200\,\text{nm}$, more higher-order modes are expected.

As shown in Figure 2.8c, the effective mode index of both modes behaves differently if the waveguide width is decreased. The fundamental mode, which is indicated by the (+) sign, does not experience a cut-off, and its mode index increases. The higher-order mode, indicated by the (+ -) sign, enters the leaky mode regime when the mode index falls below the cut-off value $n_{eff} = 3.4$, which is the case for a waveguide width below $w = 56\,\text{nm}$. In this regime, details of the choice of boundary conditions, e.g., thickness and position of the perfectly matched layers, can influence the mode index that is obtained by the mode solver. Therefore, no values are given in the leaky regime of this particular mode. For large widths w, both modes approximate $n_{eff} \approx 5.4$. Interestingly, the propagation length (Figure 2.8d) of the higher-order mode is enhanced when approaching the cut-off. This is explained by the increasing mode area due to the radiative contribution that "leaks" into the substrate. The fundamental mode, however, suffers stronger propagation losses due to its increasing confinement. The mode dispersion shown in Figure 2.8 qualitatively matches the results of the Lodahl group [51] for a two-wire transmission line on a high-index substrate. For the two-wire geometry, mode hybridization leads to a splitting of the fundamental mode into a symmetric and an antisymmetric mode, which is not the case for a single nanowire that is considered here.

In general, the propagation lengths around 1 µm of such high-index plasmonic modes are relatively short. This poses immense challenges for the design of efficient active plasmonic nanocircuits based on self-assembled quantum dots and is central for later chapters of this thesis. On the other side, leaky plasmonic modes also offer interesting possibilities for light-matter interaction: In chapter 4, the far-field contribution of a leaky mode is exploited in order to couple the emission of self-assembled GaAs quantum dots to silver nanowires that are more than 130 nm away. Furthermore, effective mode indices around 5 are rather unusual; the corresponding decrease of the SPP wavelength offers strong field gradients that have been exploited

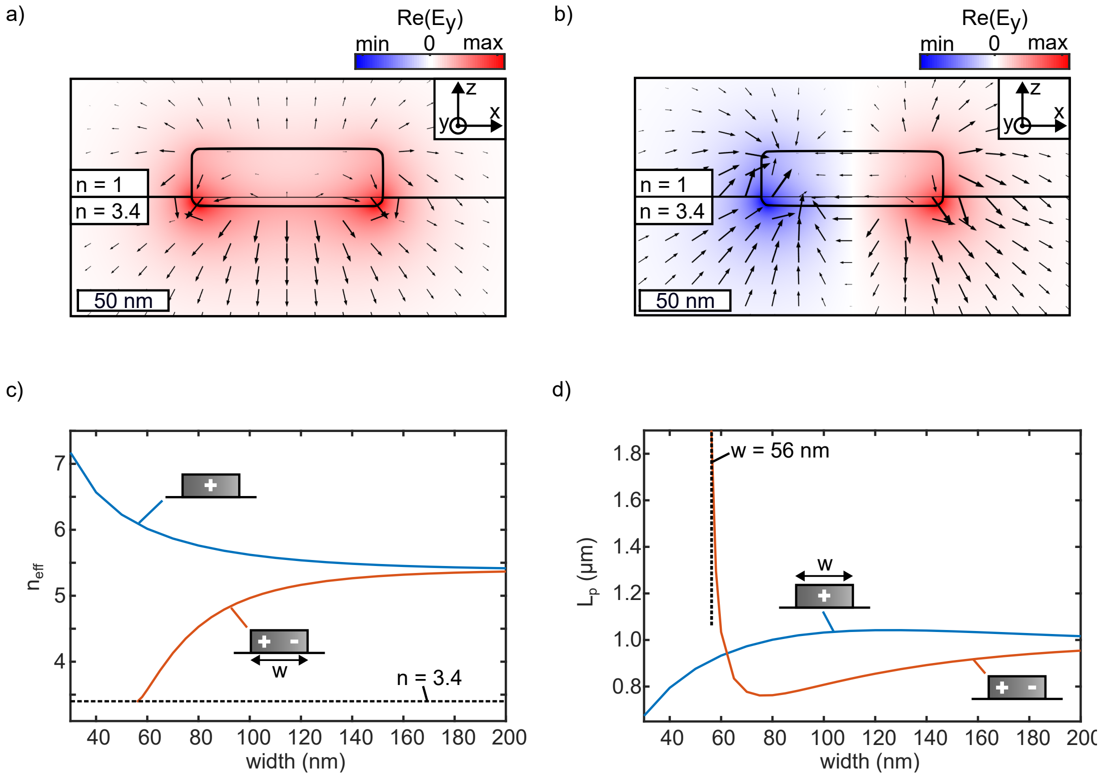

Figure 2.8: **Waveguide modes for a silver nanowire on top of a high-index substrate at $\lambda = 795\,\text{nm}$.** The electric field profile of the fundamental mode (a) and the higher-order mode (b) for a waveguide width of $w = 100\,\text{nm}$. The color corresponds to the electric field component E_y in the waveguide direction, while the arrows are given by the transverse components E_x and E_z. Effective mode index n_{eff} (c) and propagation length L_p (d) of the fundamental (+) and the first higher-order mode (+ -) as a function of the waveguide width w. The dashed lines indicate the cut-off of the higher-order mode for small widths.

to demonstrate the mesoscopic character of epitaxial quantum dots [56]. More sophisticated experiments might allow to address single quantum emitters at an unprecedented spatial scale, mediated by the extremely small SPP wavelength at the semiconductor interface.

2.3 EMITTERS CLOSE TO PLASMONIC WAVEGUIDES

Since the middle of the last century, it has been known that the spontaneous decay rate of a quantum emitter is subject to its nanoscale environment [44]. If a metallic nanostructure is brought close to the emitter, several decay channels are available, as sketched in Figure 2.9. Radiative decay is connected to the emission of a photon into the far field. Non-radiative decay, for example, can happen when the nearby metal heats up resistively through the generation of electron-hole pairs. If a plasmonic waveguide is considered, the emitter can additionally couple to one or more waveguide modes. In this chapter, at first, the decay rate of a quantum emitter into plasmonic waveguide modes is described in section 2.3.1. As an exemplary system, a nanowire in a homogeneous environment is taken, and the computed decay rates are compared with literature. The total decay rate of the emitter can be obtained in three-dimensional finite element simulations. The framework for such computations is given in section 2.3.2 and applied to the nanowire in homogeneous surroundings.

2.3.1 *Decay rate into waveguide modes*

The Lodahl group (*Chen et al.* [50]) developed a framework to compute the modal decay rate of a quantum emitter in proximity to a plasmonic waveguide. It assumes an infinitely extended waveguide in propagation direction and, therefore, the knowledge of the modal electric fields in the cross-sectional plane. The latter can be conveniently calculated using the mode solver of Comsol Multiphysics; therefore, arbitrary waveguide geometries can be investigated. However, certain assumptions are being made in [50]. These include the presence of a single waveguide mode with negligible losses. Furthermore, it is assumed that the transition dipole moment is oriented along a fixed direction. In the following, the validity of these assumptions in the context of epitaxially grown quantum dots coupled to plasmonic waveguides is briefly discussed.

While the dipole moment is clearly fixed for such solid-state emitters, GaAs quantum dots feature two transition dipole moment contributions given by the orthogonal excitons. Since this case is not considered in [50], a slight adaption is necessary, which is described in section 4.2.2. However, in many cases, the electric field lines of the waveguide mode have a preferred direction, and – depending on the location of the emitter – it is sufficient to consider only one direction of the dipole moment. The presence of a single waveguide mode is linked to the nanowire's cross section (see, for example, Figure 2.8); since most experiments are based on colloidal silver nanowires with diameters around 50 nm, higher-order modes should be close to cutoff and therefore are expected to couple weakly to the emitter due to a large mode area. While the assumption of negligible waveguide losses $\mathrm{Im}(n_{eff}) \ll \mathrm{Re}(n_{eff})$ is clearly valid for plasmonic modes in low-index dielectrics, the imaginary-to-real part ratio of the effective mode index can reach up to $5-10\,\%$ for nanowires that are

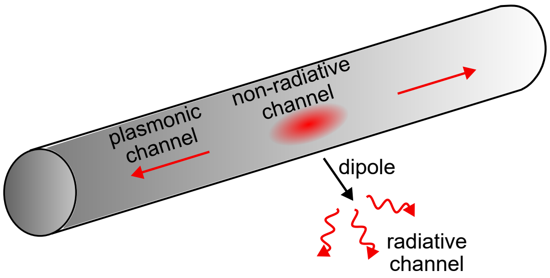

Figure 2.9: **Decay channels for a (dipole) emitter close to a metallic nanostructure.** Radiative, non-radiative, and plasmonic decay are distinguished. If a waveguide structure is considered, the emission can be channeled into guided plasmonic modes. The image is adapted from [50].

directly interfaced with semiconductors. This should be kept in mind when dealing with such lossy waveguide geometries. Since the focus of this work is experimental, the framework of [50] is adopted.

In the following, the derivation of the modal plasmonic decay rate γ_{pl} is summarized. Fermi's golden rule (Equation 2.10) for the spontaneous emission rate of a quantum emitter can be rewritten as [47]

$$\gamma = \frac{2\omega}{3\hbar\epsilon_0}|\mu|^2\rho_\mu(\mathbf{r},\omega), \tag{2.23}$$

with the local density of optical states $\rho_\mu(\mathbf{r},\omega)$ or LDOS, which measures the available number of electromagnetic modes at a position $\mathbf{r}$ into which a photon of a certain frequency ω can be emitted. The quantum emitter is characterized by a transition dipole moment $\boldsymbol{\mu}$ with the unit vector $\hat{\boldsymbol{\mu}}$ of the dipole axis. By applying a dyadic Green's function approach, *Chen et al.* [50] obtain the local density of optical states

$$\rho_{pl}(\mathbf{r},\omega) = \frac{6|\hat{\boldsymbol{\mu}}\cdot\boldsymbol{E}(x,z)|^2}{Nv_g} \tag{2.24}$$

for a plasmonic mode that is projected on the dipole axis $\hat{\boldsymbol{\mu}}$. The group velocity of the propagating waveguide mode is given by

$$v_g = \frac{\int_{A_\infty}(\boldsymbol{E}\times\boldsymbol{H}^*)\cdot\hat{\boldsymbol{y}}\,dA}{\int_{A_\infty}\epsilon_0\epsilon(x,z)|\boldsymbol{E}(x,z)|^2\,dA}, \tag{2.25}$$

and the normalization factor is

$$N = 2\pi\int_{A_\infty}\epsilon(x,z)|\boldsymbol{E}(x,z)|^2\,dA. \tag{2.26}$$

The LDOS is expressed in terms of the modal electric field $\boldsymbol{E}$ and magnetic field $\boldsymbol{H}$ in the xz-plane. The unit vector along the propagation direction is denoted as $\hat{\boldsymbol{y}}$ and the integration is performed over the transverse plane A_∞. Equation 2.24 shows that the LDOS is at its maximum if the dipole moment $\hat{\boldsymbol{\mu}}$ is parallel to the electric field $\boldsymbol{E}$, and zero for the perpendicular case. Furthermore, a small group velocity v_g and a confined mode profile increase the LDOS since the latter increases the value of $\boldsymbol{E}$. In order to obtain a decay rate, the LDOS of Equation 2.24 can be plugged into Equation 2.23. Normalized to the decay rate of an emitter in a homogeneous dielectric medium [47],

$$\gamma_0 = \frac{n\omega^3|\boldsymbol{\mu}|^2}{3\pi\epsilon_0\hbar c^3}, \tag{2.27}$$

with refractive index n, one finally obtains the modal plasmonic decay rate

$$\frac{\gamma_{pl}}{\gamma_0} = \frac{3\pi c\epsilon_0|\hat{\boldsymbol{\mu}}\cdot\boldsymbol{E}(x,z)|^2}{n\,k_0^2\int_{A_\infty}(\boldsymbol{E}\times\boldsymbol{H}^*)\cdot\hat{\boldsymbol{y}}\,dA}, \tag{2.28}$$

where the integrand in the denominator equals twice the time-averaged Poynting vector component in propagation direction (y). The vector fields on the right-hand

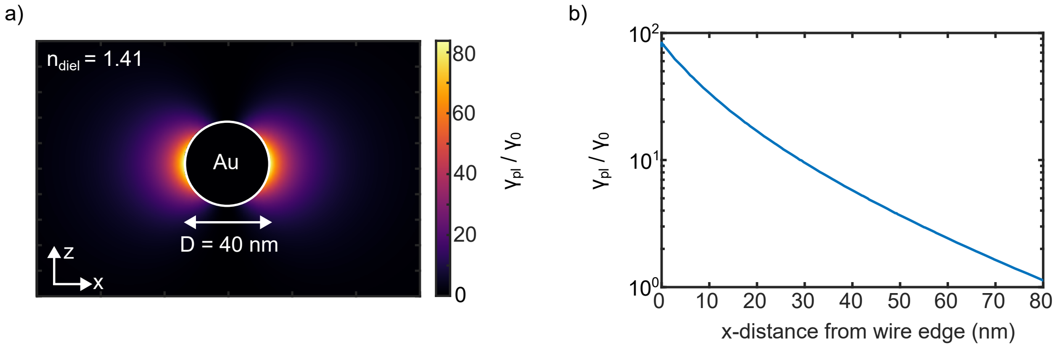

Figure 2.10: **Decay rate into the fundamental waveguide mode of a gold wire surrounded by a dielectric with $n_{diel} = 1.41$.** The (hypothetical) dipole moment is oriented along the x-axis at a wavelength of $\lambda = 1\,\mu\text{m}$, and the wire diameter is $D = 40\,\text{nm}$. The plasmonic coupling rate γ_{pl} is normalized to the emission rate in vacuum γ_0. The geometry parameters match those of *Chen et al.* [50]. (a) Spatial dependency of the normalized decay rate in the cross-sectional plane. (b) Centered slice along the x-axis, starting at the edge of the Au wire.

side of Equation 2.28 can be accessed numerically from Comsol's mode solver. The transverse plane A_∞ is approximated by integration over the computation window. Note that the normalization rate γ_0 is not necessarily the free-space decay rate with $n = 1$, as in most publications. In later chapters of this thesis, the spontaneous emission rate of a dipole in bulk AlGaAs with $n = 3.44$ is assumed as a reference, since the epitaxial GaAs quantum dots can not be (functionally) released from its semiconductor host.

The modal decay rate of a gold nanowire in a homogeneous dielectric environment is given in Figure 2.10a in the (cross-sectional) xz-plane. The electric and magnetic fields that enter Equation 2.28 correspond to the fundamental plasmonic mode of the nanowire. Figure 2.10a spatially resolves the emission rate of an emitter with a dipole moment that is oriented along the x-axis, e.g., $\hat{\boldsymbol{\mu}} = \hat{\boldsymbol{x}}$. Following *Chen et al.* [50], the plasmonic rate γ_{pl} is normalized to the spontaneous emission rate γ_0 of a dipole with the same dipole moment and frequency in vacuum. All parameters of the simulation are chosen identical to [50]: The Au dielectric function $\epsilon_{Au} = -50 + 3.85i$, the refractive index of the surrounding medium $n_{diel} = 1.41$, and the wire diameter $D = 40\,\text{nm}$, as well as the wavelength $\lambda = 1\,\mu\text{m}$. The decay of the emission rate enhancement along the x-axis is given in Figure 2.10b as a function of the distance from the nanowire edge. In z-direction, the line cut is centered with respect to the nanowire. The strongest coupling to the waveguide mode occurs directly at the nanowire edge, with enhancement factors of up to 80. These values reproduce the numbers given by [50] for the specific geometry.

2.3.2 *Purcell factor and nanocircuit efficiency*

In the last chapter, the emission rate into waveguide modes has been quantified via two-dimensional simulations. However, this approach does not consider far field radiation and non-radiative decay channels (refer to Figure 2.9) that are available for an emitter close to a nanostructure. The total decay rate, which includes all contributions, can be extracted from three-dimensional numerical simulations by applying dipole sources. In this chapter, the theoretical background and the computational implementation of such three-dimensional numerical models are described, particularly addressing the case of emitters close to plasmonic waveguides. Finally, this allows to compute the Purcell factor and the waveguide efficiency.

In the following, the most important quantities that can be derived from three-dimensional Comsol models are introduced; the equations are taken from Hecht and Novotny [47] and Comsol's user guide [53]. For the three-dimensional models, the wave equation 2.11 in the frequency domain is modified by a source term on the right hand side

$$\nabla^2 \boldsymbol{E}(\boldsymbol{r},\omega) - k_0^2 \epsilon(\boldsymbol{r},\omega) \boldsymbol{E}(\boldsymbol{r},\omega) = i\omega\mu_0 \boldsymbol{j_s}(\boldsymbol{r},\omega), \tag{2.29}$$

containing the current density $\boldsymbol{j_s}$ that is modeled in Comsol by an electric point dipole. The wave equation with source term is numerically solved in the frequency domain. Often, one is interested in the power throughput

$$P = \int_A \langle \boldsymbol{S} \rangle \cdot \hat{\boldsymbol{n}} \, dA, \tag{2.30}$$

through an arbitrary area A, which can be accessed by integrating the normal component of the time-averaged Poynting vector

$$\langle \boldsymbol{S} \rangle = \langle \boldsymbol{E} \times \boldsymbol{H} \rangle = \frac{1}{2} \mathrm{Re} \left[\boldsymbol{E} \times \boldsymbol{H}^* \right]. \tag{2.31}$$

For example, the total power P_{tot} that is radiated by the dipole is obtained by an integral over the surface of a sphere with a radius of 10 nm that encloses the point dipole. While, in general, the total emitted power P_{tot} depends on the nanoscale environment of the emitter, the average radiated power P_0 of dipole in a homogeneous environment is analytically known

$$P_0 = \frac{|\boldsymbol{\mu}|^2}{4\pi\epsilon_0\epsilon} \frac{n^3\omega^4}{3c^3}, \tag{2.32}$$

and depends on the dipole moment $\boldsymbol{\mu}$, the frequency ω, and the refractive index n of the medium. For a given set of these parameters, the numerically derived dipole power in a homogeneous medium has to match the analytical power P_0. It can be shown that the classical dipole power ratio is identical to the quantum mechanical decay rates so that one can write

$$\frac{\gamma_{tot}}{\gamma_0} = \frac{P_{tot}}{P_0} = F_p. \tag{2.33}$$

The ratio of the decay rates γ_{tot}/γ_0 follows straightforwardly from the classical power ratio P_{tot}/P_0 that is obtained in a three-dimensional computation. Since the change of the inherent decay rate of the emitter is mediated by a Purcell effect, the rate ratio in Equation 2.33 is equivalent to the Purcell factor F_p. This term is also used in later chapters of this thesis.

Often, the emission rate into plasmonic waveguide modes γ_{pl} is connected to the total decay rate γ_{tot} via the β-factor

$$\beta = \frac{\gamma_{pl}}{\gamma_{tot}}. \tag{2.34}$$

The β-factor is a direct measure of the fraction of emitted photons that are channeled into the waveguide. If given together with a propagation length, the β-factor is very helpful in order to evaluate the efficiency of a nanocircuit. However, it has the disadvantage of assuming that the cross-section of the waveguide does not change along the propagation direction and that the waveguide is infinitely long or has no reflections at its end. For example, in chapter 4, it will be shown that reflected plasmons at a nanowire end can modify the coupling efficiency. Such effects are not included in the β-factor. The invariance of the nanocircuit geometry along the propagation direction is violated in chapters 5 and 6, where a semiconductor mesa with finite dimensions encloses the emitter, and the waveguide extends over regions with and without the mesa. Also, in this case, the decay rate γ_{pl} into a waveguide mode is not helpful, and therefore the β-factor has to be replaced. This will be done by distinguishing between incoupling and waveguide efficiency; the definitions of these quantities follow below.

The computational implementation of a three-dimensional Comsol model with a dipole source is sketched in Figure 2.11a. The model is excited by an electric point dipole that is located next to the plasmonic waveguide in a distance Δx. Note that the sketch shows the three-dimensional geometry from the top. The waveguide runs into a perfectly matched layer (PML), an artificial domain that acts as a close-to-perfect absorber. All end facets of the model are terminated by scattering boundary conditions (SBC). Plasmonic waveguide models can contain more than a million (tetrahedral) mesh elements and take a few minutes to run on the chair's workstation if the meshing is optimized. The total power P_{tot} that is emitted by the dipole is computed by Equation 2.30 and will be used for the normalization of the waveguide power throughputs. The energy that is channeled into the waveguide is measured at two positions by integrating the energy flux in the y-direction at a circle that is centered around the waveguide. The first integration circle is located shortly behind the dipole at a distance of $y = 100\,\text{nm}$ (the dipole is located at $y = 0\,\text{nm}$). The obtained incoupling power $\frac{1}{2}P_{in}$ is taken as a measure of the incoupling efficiency

$$\eta_{in} = \frac{P_{in}}{P_{tot}}, \tag{2.35}$$

since an equal amount of power throughput can be measured at $y = -100\,\text{nm}$ due to symmetry. The second integration circle is located at $y = 2\,\mu\text{m}$ and is taken as a measure of the waveguide efficiency

$$\eta_{wg} = \frac{P_{wg}}{P_{tot}} \tag{2.36}$$

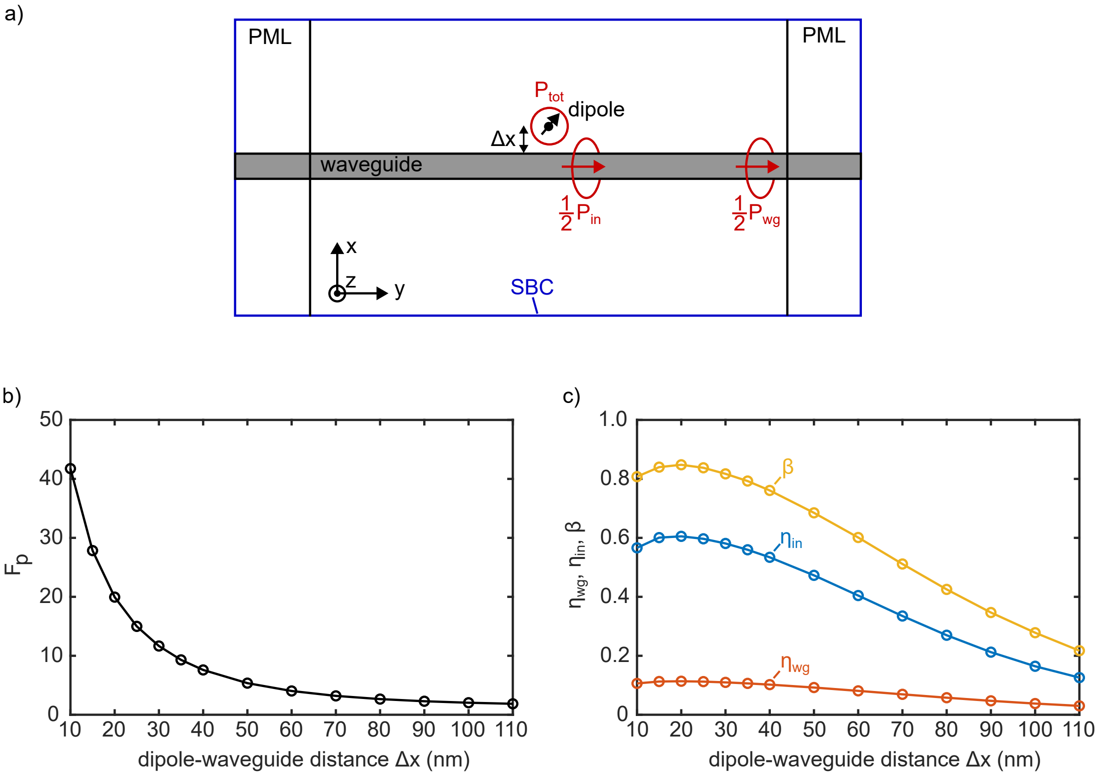

Figure 2.11: **Purcell factor and nanocircuit efficiencies from three-dimensional simulations using a dipole point source.** (a) Sketch of a three-dimensional Comsol model consisting of a dipole source close to a plasmonic waveguide. Perfectly matched layers (PML) and scattering boundary conditions (SBC) are applied. Surface integrals of the energy flux give the respective power throughputs. The refractive indices of the wire and the surroundings, as well as the wire diameter, are identical to Figure 2.10 and *Chen et al.* [50]. (b) Purcell factor F_p as a function of the dipole–waveguide distance. (c) β-factor, incoupling efficiency η_{in}, and waveguide efficiency η_{wg} as a function of the dipole–waveguide distance.

that includes propagation losses. The diameter of the integration circles is chosen three times the wire diameter, which here is $D = 40\,\text{nm}$. This is the diameter that has already been used in Figure 2.10. The refractive indices of the gold wire and the dielectric surrounding are also the same and identical to *Chen et al.* [50]. The Purcell factor (see Equation 2.33) for the emitter is given in Figure 2.11b as a function of the dipole-waveguide distance Δx. As expected, the total decay rate increases with a smaller distance to the waveguide edge, with maximum values exceeding 40. Distances below 10 nm are not computed because the integration sphere around the point dipole has a radius of 10 nm. Since the waveguide in the geometry that is investigated here can be understood as infinitely long, the β-factor is useful and shown as a function of Δx in Figure 2.11c. Here, the maximum value of $\beta = 84\,\%$ is reached at a distance of 20 nm from the nanowire edge. This is caused by the non-radiative decay channel that becomes prominent if the waveguide–dipole distance is small, and is not included in the β-factor. The same values for the β-factor are obtained by *Chen et al.* [50]. The incoupling efficiency η_{in} (Equation 2.35) and the waveguide efficiency η_{wg} (Equation 2.36) are given in Figure 2.11c. Both follow the β-factor qualitatively; The maximum values are $\eta_{in} = 61\,\%$ and $\eta_{wg} = 11\,\%$, respectively. Of course, these quantities suffer from a certain degree of arbitrariness since they depend on the y-location and diameter of the integration circles. As explained above, they become relevant for more complicated geometries as they are investigated in chapters 5 and 6.

It should be noted that other definitions of the waveguide efficiency are possible. Frequently, the energy flux along the waveguide is measured in the whole transverse plane and is multiplied by a normalized mode overlap integral of the electric field distribution with an eigenmode of the waveguide [57]. This is done to get rid of radiation modes (e.g., of a dipole emitter) that are present in the integration plane but do not belong to the waveguide mode. It has been found that the contribution of far field modes is negligible ($\lesssim 1\,\%$) if the integration is performed over a circle centered around the waveguide with a radius that is three times the waveguide radius after a distance of 2 µm. Furthermore, in an experiment, one does usually not distinguish between specific waveguide modes; instead, higher-order modes that may be present contribute to the out-coupled intensity that is measured. Therefore, the above definition of the waveguide efficiency is reasonable.

3

CHARACTERIZATION METHODS FOR QUANTUM DOT–DRIVEN PLASMONIC WAVEGUIDES

In this chapter, the most important experimental methods for the characterization of quantum dot–driven plasmonic waveguides are presented. Mostly, optical microscopy is used to study plasmonic waveguides. In this work, cathodoluminescence spectroscopy is also applied, which serves as a high-resolution imaging technique and is described in section 3.1. Afterwards, the (all-)optical spectroscopy methods involving confocal laser scanning and imaging are presented in section 3.2. Both cathodoluminescence spectroscopy and optical spectroscopy are operated at cryogenic temperatures. Another important tool is whitelight reflection spectroscopy in order to control the thickness of spin-coated dielectric films, which is described in section 3.3.

3.1 LOW-TEMPERATURE CATHODOLUMINESCENCE SPECTROSCOPY

Low-temperature cathodoluminescence (CL) spectroscopy combines high-resolution electron microscopy with access to the optical properties of the sample via cathodoluminescence. In contrast to optical microscopy, a focused electron beam is used as an excitation source, which is raster-scanned over the sample. The resulting high-resolution hyperspectral images will be used to determine the relative positions of coupled quantum dots and nanowires in chapter 4 with high accuracy. The possibility to acquire structural properties via electron microcopy and optical properties by cathodoluminescence in the same measurement device also enables advanced nanostructuring techniques: In situ electron beam lithography allows for the deterministic integration of quantum dot emitters into more or less complex nanostructures. In chapter 6, in situ electron beam lithography will be used to fabricate quantum dot pillars for the efficient coupling to plasmonic waveguides. In section 3.1.1, the experimental setup for cathodoluminescence spectroscopy and its image formation are described. Afterwards, the powerful technique is demonstrated for a quantum dot–nanowire sample in section 3.1.2.

3.1.1 *Experimental setup and image formation*

The cathodoluminescence spectroscopy setup is developed and operated by the Reitzenstein group at TU Berlin and shown in Figure 3.1. Most of the cathodoluminescence measurements shown in this thesis were obtained during a research visit to TU Berlin. The experiments were carried out by PhD student Yuhui Yang, while the data analysis and visualization were done by the author. The setup is based on a high-resolution electron beam lithography system (Raith eLINE) and a custom-designed cathodoluminescence extension (Delmic). Apart from luminescence

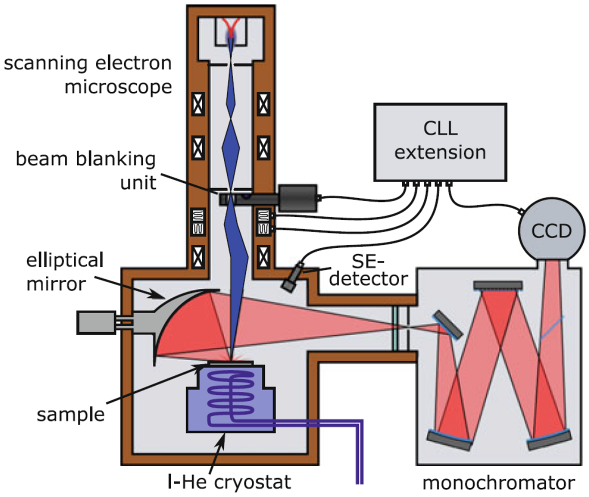

Figure 3.1: **Low-temperature cathodoluminescence spectroscopy setup.** The experiment combines high-resolution electron microscopy with access to optical sample properties via cathodoluminescence. Reprinted from [59] with the permission of Springer Nature.

mapping of the sample, cathodoluminescence lithography (CLL) is also possible. The sample, which is mounted on a liquid helium flow cryostat (Cryovac), is excited by a focused electron beam with an acceleration voltage of 20 kV at a temperature of 20 K. The cathodoluminescence emission of each excitation spot position is collected by an elliptical mirror and mapped onto a silicon CCD via a monochromator, obtaining full spectral information for each pixel. Simultaneously, scattered electrons are detected by a SE-detector, yielding a secondary electron image with the same coordinates. Due to a scanning time of around two minutes for a $10\,\mu m^2$ area with 50 nm step size, the influence of stage drift is negligible. Further details on the cathodoluminescence experiment are given in [58].

An example of a cathodoluminescence data set is shown in Figure 3.2 for a GaAs quantum dot sample with silver nanowires dispersed on top of the sample surface. Equivalent to standard electron microscopy, a secondary electron image (Figure 3.2a) is recorded, displaying a few silver nanowires. The raster-scanned electron beam penetrates the semiconductor and provides charge carriers inside its generation volume [60]. The generated electron-hole pairs diffuse over a certain length [61] through the material and recombine, leading to the emission of luminescence photons. The recombination can happen either within bulk GaAs, within the GaAs wetting layer, or inside a GaAs quantum dot, each leading to a different photon emission energy (see also section 3.1.2). Mostly, the quantum dot emission is of interest, and the selected spectral range is adjusted to match the quantum dot emission wavelength, as done in Figure 3.2b. Here, the cathodoluminescence map shows the emission spots of four GaAs quantum dots. Even though both datasets originate from the same scan and, therefore, share one coordinate system, the discretization of the cathodoluminescence mapping and the electron micrograph can be different. Both datasets can be overlaid with each other, which is done by transparency in Figure 3.2c.

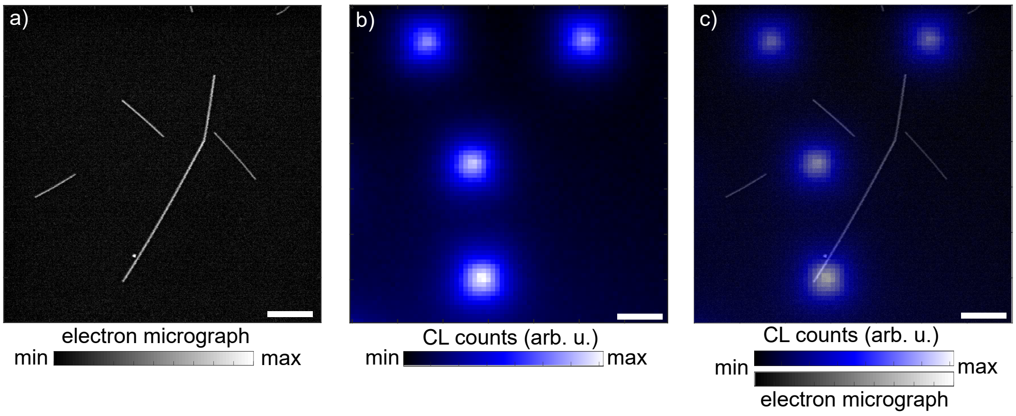

Figure 3.2: **Example of a low-temperature cathodoluminescence data set for a GaAs quantum dot sample with dispersed silver nanowires on top.** (a) Electron micrograph depicting a few silver nanowires. (b) Cathodoluminescence emission map for the same sample region, displaying four quantum dots. (c) Transparency overlay of the electron micrograph and the cathodoluminescence map. All scale bars are 1 µm.

The cathodoluminescence experiment is characterized by the combination of a small excitation area given by the electron beam and a large detection area due to the low-NA elliptical collecting mirror. Consequently, the cathodoluminescence map allows to determine where the excitation occurs but not where the emission originates. In principle, the spatial resolution is not diffraction-limited but is given by the generation volume of the electron beam diameter. The size of the generation volume depends, among others, on the electron energy and the atomic number of the material [60]. However, quite large cathodoluminescence spots are observed in Figure 3.2b; the full width at half maximum is about 1 µm. This can be explained by the presence of carrier diffusion, which leads to a "remote" excitation of the quantum dots. An exponential fit to the flanks of the cathodoluminescence spots suggests a diffusion length of around 500 nm, in good agreement with literature values for GaAs/AlGaAs heterostructures [62]. However, the diffusion length is found to depend critically on the specific quantum dot sample that is investigated (here: O692, see Appendix A.1), as well as on the emission wavelength. The dispersion of the cathodoluminescence signal is discussed in the next chapter.

3.1.2 *Spectral analysis of the quantum dot emission*

More detailed insights into the cathodoluminescence emission processes for GaAs quantum dots can be obtained by emission wavelength filtering. Since a spectrum is measured for each sampling step, the dispersion of the cathodoluminescence signal can be studied with high spatial resolution. Figure 3.3a shows two cathodoluminescence spectra for different positions of the electron beam: for the red curve, the electron beam is directly located above a quantum dot. For the black curve, the electron beam is about 700 nm away, where no quantum dot emission is observed. The measurement spans a wide spectral range from $1.4 - 1.9\,\mathrm{eV}$, which can be divided

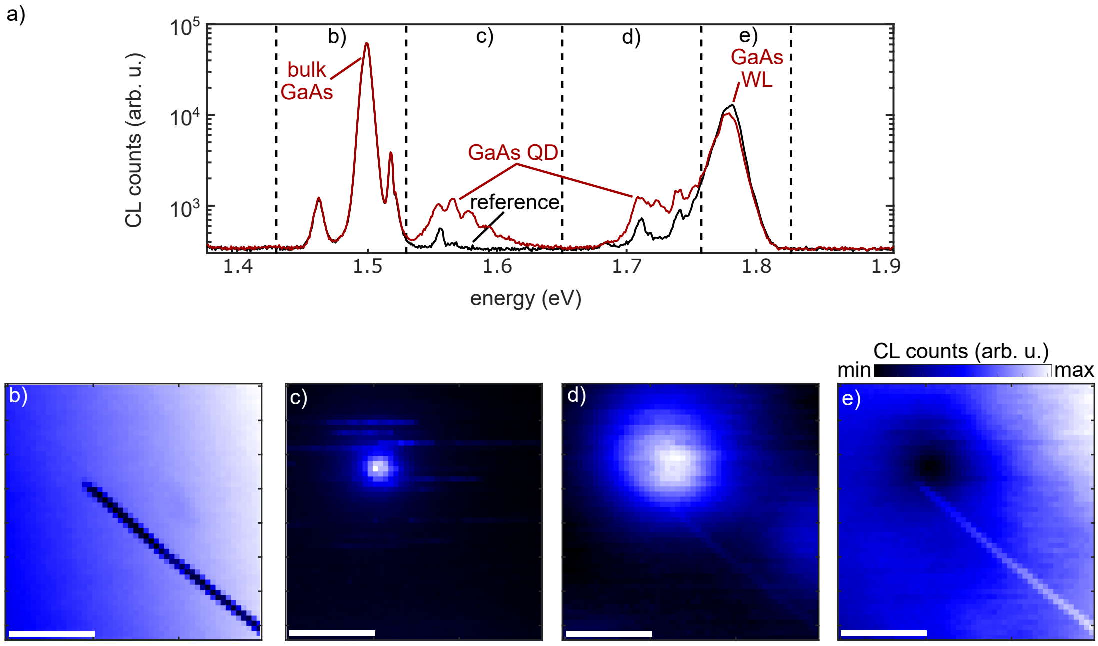

Figure 3.3: **Spectral analysis of the cathodoluminescence of a GaAs quantum dot and its surroundings.** There is a silver nanowire close to the dot. (a) Cathodoluminescence spectra for electron beam excitation directly on the quantum dot (red curve) and excitation about 700 nm away (black reference curve), corresponding to the top left corner in the cathodoluminescence images below. The dashed vertical lines indicate the integration limits for the respective cathodoluminescence image. (b-e) Cathodoluminescence maps for different spectral ranges highlighted in (a), corresponding to bulk GaAs emission, quantum dot emission, and wetting layer (WL) emission. All scale bars are 500 nm.

into four different regimes; for each of these regimes, a cathodoluminescence map can be recorded by integration over the respective wavelength range. The resulting maps are shown in Figure 3.3b-e.

The range from $1.45 - 1.53$ eV, where the quantum dot and reference spectra are identical, is assigned to bulk GaAs with a band gap of 1.52 eV [24] at low temperatures. The corresponding cathodoluminescence map is shown in Figure 3.3b. As one would expect, there is a spatially homogeneous emission from the bulk GaAs that can be excited everywhere in the sample. Interestingly, the silver nanowire seems to hinder the excitation of GaAs luminescence, probably due to electron backscattering. In the quantum dot emission range $1.53 - 1.65$ eV, at least four higher excited states can be observed with significant line broadening. Similar spectra have been detected under intense optical excitation [63] and attributed to the filling of s-, p-, and d-shells [64]. Supposedly, the relatively high beam current of 0.3 nA at 30 µm aperture floods the quantum dot with charge carriers. For a complete spectral analysis of these emission lines, further measurements at lower beam currents would be necessary. The corresponding cathodoluminescence image in Figure 3.3c shows well-localized emission from the quantum dot, with a full width at half maximum of around 300 nm. Note that for this measurement, a different quantum dot sample (Sa665) is used compared to Figure 3.2, displaying a much shorter diffusion length even though the samples are structurally almost identical (see Appendix A.1 for details on the quantum dot samples). For higher energies in the range from $1.65 - 1.76\,\mathrm{eV}$, more lines appear in the spectrum. These transitions are usually not discussed in the literature, but their existence is mentioned in [63]. The corresponding cathodoluminescence image in Figure 3.3d reveals a much broader spot size compared to the "standard" GaAs quantum dot emission at lower energy. Less-confined surface states might be the origin of this emission. The range $1.76 - 1.82\,\mathrm{eV}$ corresponds to the emission of the 2 nm thin GaAs wetting layer (WL) [65], below which the GaAs quantum dots are formed. Interestingly, the corresponding cathodoluminescence map in Figure 3.3e shows a reduction of the wetting layer emission at the quantum dot position, which can be explained by the additional recombination channel that is offered by the quantum dot.

3.2 LOW-TEMPERATURE OPTICAL SPECTROSCOPY

While cathodoluminescence offers high-resolution images, (all-)optical spectroscopy is advantageous in terms of flexibility and time consumption. In addition, an objective with a high numerical aperture (NA) can be utilized to collect the sample's luminescence. The use of high-NA objectives increases not only the detected photon rate but also the detection resolution, which is important to differentiate between remote emission spots, for example, the two ends of a waveguide. In this section, the experimental setup for optical spectroscopy at liquid helium temperatures is presented. The closed-cycle cryostat that is used for sample cooling is described in section 3.2.1. A detailed description of the microscope that combines laser scanning with a spectrometer for imaging and spectroscopy follows in section 3.2.2. In addition, exemplary data sets are given that demonstrate the capabilities of this setup.

3.2.1 *Closed-cycle cryostat*

For the optical spectroscopy setup, a commercial closed-cycle pulse tube cryostat (Cryovac) is used. The cryostat is schematically sketched in Figure 3.4 and has a built-in liquefier that transports liquid helium to the sample holder. The cryogenic-free design offers a relatively inexpensive operation and, in principle, enables unlimited measurement periods. Even though the cryostat is commercial, a significant amount of optimization has been needed in order to ensure stable operation with regard to spectroscopy on the single quantum emitter level. Important work has been done by Gerhard Schäfer, including the reduction of vibrations that is described in his thesis [66]. A remaining issue that has been tackled in the present work is the temperature stability over measurement intervals longer than one day. This will be discussed below. At first, however, the basic design of the cryostat is briefly described.

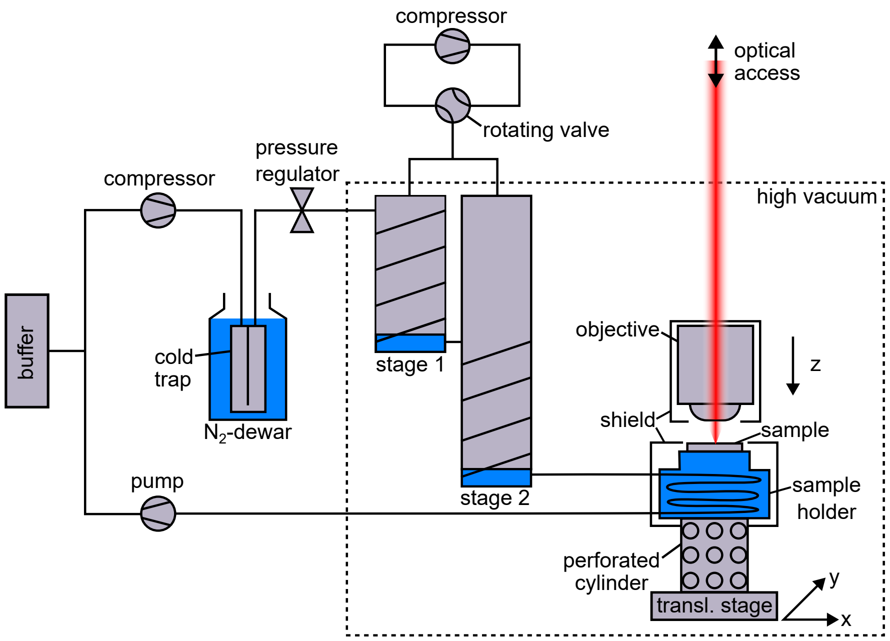

Figure 3.4: **Schematic drawing of the two-stage pulse tube cryostat with an additional helium cycle for sample cooling.** A thin pipe transfers liquid helium from the cold end of stage 2 towards the sample holder. The microscope objective is placed inside the vacuum chamber, which enables small working distances. See the text for a detailed description.

Pulse tube cryocoolers have proven to reach liquid helium temperatures since the 1990s [67]. Their distinctive advantage over other types of cryocoolers lies in the fact that no moving parts are required in the low-temperature part of the device. The resulting low vibration level and the fact that no coolant needs to be replaced even led to the use of a pulse tube cryocooler on the James Webb Space Telescope [68]. The pulse tube used in this work features a two-stage design that has been developed by TransMIT GmbH, and is roughly sketched in Figure 3.4: Both stages are alternately connected to the high- and low-pressure ends of a 6 kW compressor (KDC6000V, Easycool) via a rotating valve. The helium gas pressure is 25 bar at the high-pressure end and 10 bar at the low-pressure end. The rotating valve frequency is 1.348 Hz. The cooling principle is based on repetitive pressure variations that travel along the pulse tube, which results in a step-by-step transfer of the heat from the cold parts to the warm parts. A thermodynamic description of the cooling cycle, as well as the inner design of the pulse tube, can be found in literature (for example [69]) and are not discussed here. Typical temperatures are 55 K at the first stage and 4 K at the second stage of the pulse tube. Through temperature sensors and heating filaments, the temperature at both stages of the pulse tube, as well as the temperature of the sample holder, can be actively controlled via a PID loop.

In a second helium cycle, helium 6.0 (purity $\geqslant 99.9999\,\%$) is liquefied at the cold end of stage 2 of the pulse tube and transferred to the copper sample holder (see Figure 3.4) via a thin capillary. After cooling the sample holder, the helium is re-condensed and pumped to a buffer volume by a scroll pump (XDS35i, Edwards). The helium buffer is at a pressure of about 1 bar and supplies another compressor (PM29007-145, KNF), which pumps helium with around 7 bar through a cold trap. The cold trap includes a carbon filtering unit that is located inside a liquid nitrogen dewar and cleans the helium from impurities in order to avoid condensation at the capillary, which connects the pulse tube with the sample holder. After the cold trap, a pressure regulator is used to control the helium throughput, which determines the cooling rate of the sample. Typically, the pressure before the pulse tube is 3 bar during cool-down and $1-2$ bar during measurement periods. The actual pressure is measured at three points along the helium cycle and can be read out remotely.

In order to insulate the cold fingers of the pulse tube and the sample holder from its environment, these parts are kept in a high vacuum at a pressure below 10^{-5} mbar. Therefore, a pumping station (HiCube 80 Classic, Pfeiffer Vacuum) consisting of a diaphragm and a turbo-molecular pump is used (not shown in the sketch). In order to protect the sample holder from thermal radiation, it is surrounded by a highly reflective cold shield. A special feature of the cryostat is the microscope objective, which is located inside the vacuum chamber. This design allows the use of an objective with a high numerical aperture of $\text{NA} = 0.9$ (see chapter 3.2.2 for details on the optical setup). The collimated laser beam enters the cryostat through a window at the top of the vacuum chamber. In order to focus along the z-direction, the objective is mounted to a vertical translation stage. The sample holder is attached to a perforated stainless steel cylinder that is mounted on top of two translation stages, which move in x- and y-direction. The perforation of the cylinder is designed to reduce the thermal input of the cold sample holder on the moving stages.

The long-term cooling performance of the closed-cycle cryostat is given in Figure 3.5. From top to bottom, the temperature $T_{\text{stage 2}}$ of stage 2 of the pulse tube, the sample temperature T_{sample}, and the objective temperature $T_{\text{objective}}$ are shown over a time period of 10 days. About 6 hours after the start of the cool-down, the pulse tube reaches a temperature of $T_{\text{stage 2}} = 4\,\text{K}$. At this time, the sample temperature is at its minimum of $T_{\text{sample}} = 8\,\text{K}$. Over the next days, the sample temperature gradually increases, and exceeds $T_{\text{sample}} = 21\,\text{K}$ after 5 days, while the pulse tube temperature slowly decreases down to $T_{\text{stage 2}} = 3.2\,\text{K}$, as highlighted in the inset of the upper panel. This is caused by a partial blockage of the capillary between the pulse tube and the sample holder, which reduces the helium flow towards the sample and hence decreases the cooling power. Epitaxial GaAs quantum dots have the advantage that their properties decline rather weakly with rising temperature [65, 70]. In the context of this thesis, sample temperatures up to $T_{\text{sample}} = 20\,\text{K}$ can be conveniently accepted. Interestingly, a heating procedure has been found to temporarily restore sample temperatures well below 20 K in case of a partly pipe blockage. Therefore, stage 2 of the pulse tube is heated to a temperature of up to $T_{\text{stage 2}} = 30\,\text{K}$. In order to avoid overpressure, this is done stepwise in a time interval of $30-60$ min. In the case shown in Figure 3.5, a sample temperature of $T_{\text{sample}} = 11\,\text{K}$ could be restored,

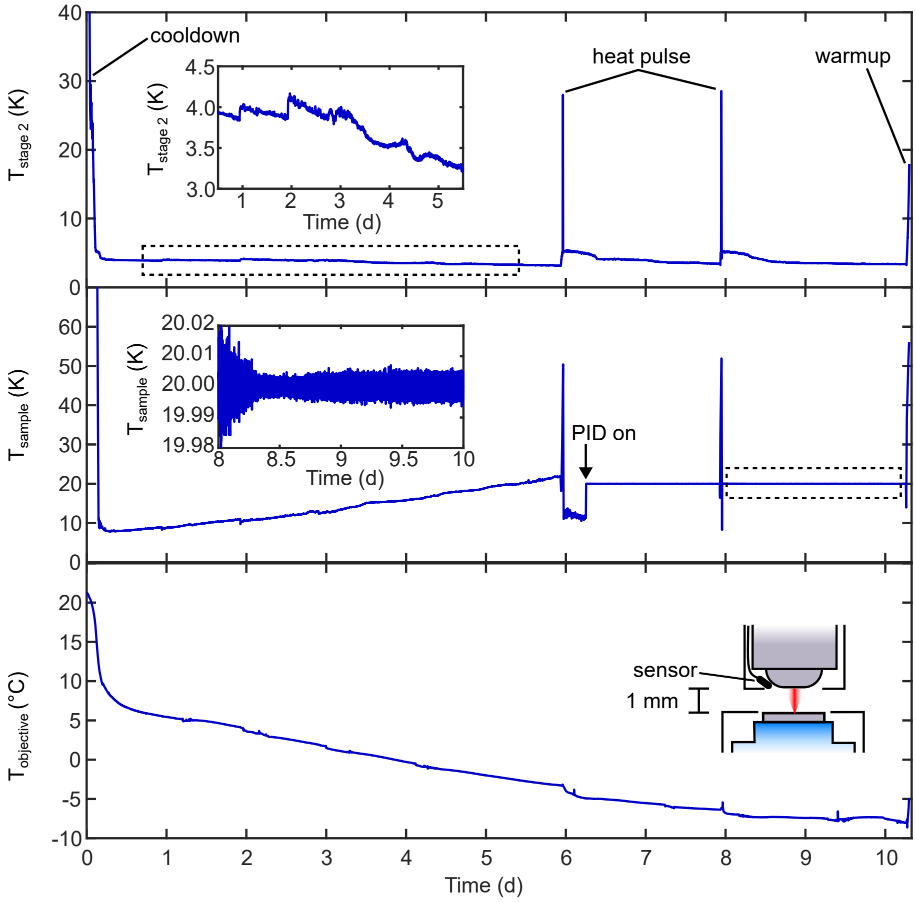

Figure 3.5: **Cryostat performance over a cooling period of 10 days.** From top to bottom: Pulse tube temperature $T_{\text{stage 2}}$, sample temperature T_{sample}, and objective temperature $T_{\text{objective}}$. Selected time intervals (dashed boxes) are shown enlarged in the inset.

most probably caused by the vaporization of impurities in the capillary.* While the uncontrolled operation mode is helpful to understand the processes inside the cryostat, a fixed sample temperature is usually desired. By PID-controlled heating of the sample holder, the sample temperature is kept constant at 20 K from day 6 on, as it can be seen in the middle panel in Figure 3.5. The inset shows that the temperature variation within the loop is on the order of 10 mK. By monitoring the heating power that is required to hold this temperature, it can be estimated when the next heating pulse for the pulse tube is necessary. Here, this is the case at day 8. Since the heating procedure takes less than an hour, stable working conditions are routinely obtained for extended time intervals. Finally, on day 10, the pulse tube compressor is switched off, and the system warms up to reach room temperature.

---

* However, the described heating procedure should not be performed in the case of a total blockage due to high pressure built-up. In this case, the cryostat should be allowed to warm up slowly to room temperature, and an exchange of helium is needed.

As can be seen in the lower panel of Figure 3.5, there is a noteworthy cooling of the objective's tip caused by the objective's small working distance of 1 mm. During cool-down, the objective temperature $T_{\text{objective}}$ decreases from room temperature to $5-10\,^{\circ}\mathrm{C}$, slightly lagging behind the sample temperature. In the following days, the objective temperature decreases further and reaches $-8\,^{\circ}\mathrm{C}$ on day 10. Also, the spikes of the heat pulses on days 6 and 8 can be found in the objective temperature. Interestingly, the cooling of the objective does not seem to affect its optical properties regarding the conducted experiments. The passive aluminium shield might help slow down the cooling process to an acceptable rate; long-term measurements without the shield would be necessary to confirm this. Similar to the objective, the stainless steel cylinder that connects the sample holder with the translation stages experiences a cool-down. The thermal contraction of the cylinder is on the order of several ten micrometers and prevents stable working conditions for several hours after cool-down since constant refocusing would be required. However, at the end of day 1, the contraction rate is small enough to enable stable working conditions.

3.2.2 *Optical setup*

The experimental setup for optical spectroscopy is schematically shown in Figure 3.6. Two different laser sources are available: A continuous wave (CW) diode laser (LDM635, Roithner) at $\lambda = 635\,\mathrm{nm}$ and a modelocked Titanium-Sapphire laser (Gigajet Twin, Laser Quantum) are guided towards the sample by a 90/10-beamsplitter (BS025, Thorlabs). The Titanium-Sapphire laser is spectrally filtered at $\lambda = 795\,\mathrm{nm}$ to a width of a few nanometers beforehand. A half-wave plate (500-900 nm achr., B. Halle) controls the orientation of the linearly polarized lasers by a motorized rotation stage (PRM1/MZ8, Thorlabs). A fast scanning mirror (FSM-300, Newport) builds a $4f$-configuration with a lens pair (focal length $f = 150\,\mathrm{mm}$) and the back focal plane of the objective (MPlanFLN100xBDP, NA= 0.9, Olympus), which is z-positioned by a stepper motor (LS-65, PI Micos). The $4f$-setup effectively transforms a tilt of the scanning mirror into focus displacements in the sample plane, allowing sample mapping up to an area of 80 µm x 80 µm. The sample is cooled down to a temperature below 20 K by a closed-cycle cryostat (see chapter 3.2.1) and can be xy-positioned by two stepper motors (MTS-70, PI Micos). In addition to the laser sources, a whitelight source (MCWHL2, Thorlabs) can be utilized to illuminate the sample by the use of a flip beamsplitter.

In the detection path, three flip bandpass filters (ET775/50 Chroma, BrightLine HC 786/22, and 800/12 Semrock) can separate sample luminescence from the laser excitation. In addition, an analyzer (LPVIS100, Thorlabs) can be flipped into the beam path. Different detection schemes can be selected: For confocal laser scanning, an avalanche photodiode (APD, MPD-PD-050-CTE) in combination with a lens ($f = 75\,\mathrm{mm}$ or $f = 125\,\mathrm{mm}$) is utilized. For spectroscopy, a monochromator (Acton SP2750, Princeton Instruments) with a triple grating turret (600 g/mm, 1200 g/mm, 1800 g/mm) in combination with a low-noise CCD camera (Pixis 100, Princeton Instruments) is applied. The imaging lens ($f = 300\,\mathrm{mm}$), which focuses on the

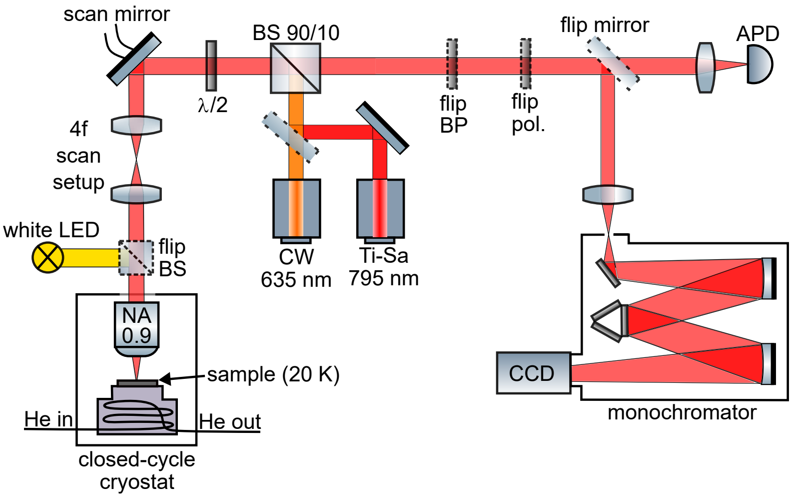

Figure 3.6: **Sketch of the low-temperature optical spectroscopy setup.** The setup combines confocal laser scanning with imaging via a spectrometer. See the text for a detailed description.

entrance slit of the monochromator, can be replaced by a lens with a shorter focal length ($f = 50\,\text{mm}$) for high-resolution spectroscopy. A spatial filter (not shown in the sketch), consisting of two lenses ($f = 150\,\text{mm}$ and $f = 200\,\text{mm}$) and a metal mask, allows to image selected regions in the sample plane.

3.2.3 *Confocal laser scanning*

Confocal laser scanning is a powerful alternative to conventional widefield microscopy. Instead of illuminating the whole sample, a laser is focused and raster-scanned over the sample. Therefore, small areas on the sample can be selectively excited. The signal of interest, for example, scattered laser light or photoluminescence, is imaged through a pinhole and detected by a photodiode. The optical resolution is given by the product of excitation and detection focus, and can – in principle – get beyond the Abbe diffraction limit [47]. However, this presumes a single-mode excitation and a sufficiently small detection pinhole for the chosen magnification. In the setup as applied here, neither of these prerequisites is given; instead, the APD acts as a pinhole due to its small detection area with a diameter of 50 µm, limiting the detection focus to some extent.

An example of an image obtained by confocal laser scanning is given in Figure 3.7, showing the photoluminescence emission spot of a single GaAs quantum dot. Gaussian functions are fitted to the cross-sections through the emission center along the x- and y-direction. The original two-dimensional scan is shown in the inset. The photoluminescence emission is close to diffraction-limited with a full width at half maximum of $\text{FWHM}_x = 560 \pm 40\,\text{nm}$ and $\text{FWHM}_y = 460 \pm 20\,\text{nm}$. The deviation between the x- and y-direction can be explained by the slightly asymmetric mode profile of the laser diode used for excitation. To further increase the resolution, the

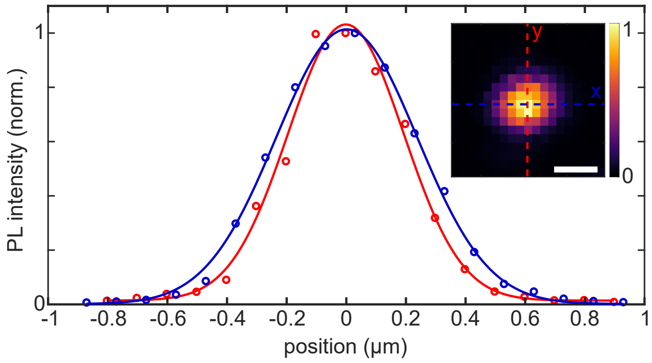

Figure 3.7: **Photoluminescence emission of a single GaAs quantum dot, acquired by confocal laser scanning.** Gaussian functions are fitted to the centered cross-sections along the x-direction (blue) and y-direction (red), yielding $\mathrm{FWHM}_x = 560 \pm 40\,\mathrm{nm}$ and $\mathrm{FWHM}_y = 460 \pm 20\,\mathrm{nm}$. The original data is shown in the inset. The scale bar is 500 nm.

excitation focus would need to be optimized by spatial filtering and a higher filling factor of the objective's back aperture [47]. Similar to the charge carriers generated in cathodoluminescence (see section 3.1), also optically excited carriers undergo diffusion for non-resonant pumping as applied here [27]. Depending on the exact diffusion length of the specific sample and the microscope configuration, the diffusive excitation site broadening can be significant and needs to be considered when evaluating the observed photoluminescence emission spots. A construction of the total point spread function, including carrier diffusion, can be found in section 6.2.2, where it is used to model the spatial width of the photoluminescence emission of integrated quantum dots.

Examples of confocally scanned reflection images are shown in Figure 3.8. The sample consists of colloidal silver nanowires on top of GaAs. Here, the sample reflection of the excitation laser is suppressed by a crossed polarizer in the detection path. The silver nanowires with diameters of around 50 nm efficiently polarize the scattered light, depending on their orientation on the substrate. This can be seen if the laser polarization is tuned via the half-waveplate, while the detection analyzer is adjusted for optimal suppression. The confocal scans shown in Figures 3.8a-e correspond to five different angles of the half-waveplate between $0° - 45°$ and clearly show the polarization contrast. For the optimal angle, the contrast ratio of the nanowires compared to the background can exceed 50, which would be hard to achieve with brightfield microscopy. The nanowire orientation can be averaged out by summing up the reflection images for different polarizations. This is done in Figure 3.8f, where the averaged image is overlaid with an SEM image of the same sample region. The confocal reflection scanning will be applied in chapter 4 in order to identify quantum dot–nanowire systems that have been pre-selected in cathodoluminescence.

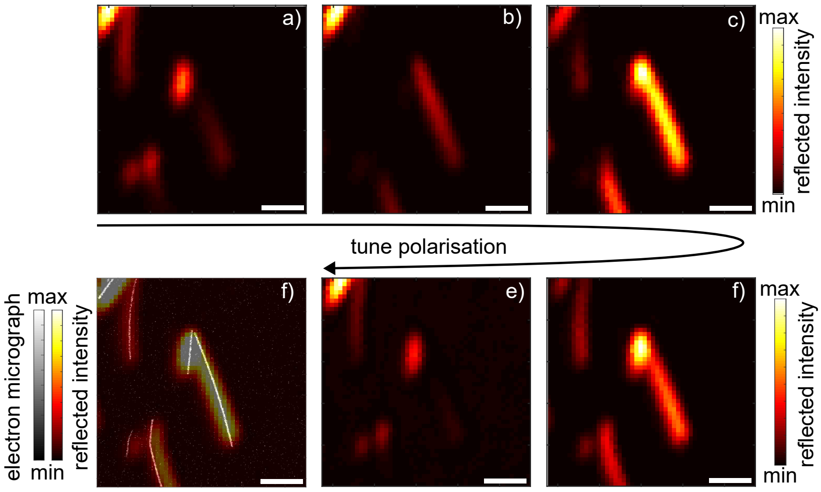

Figure 3.8: **Polarization contrast in confocal laser scanning demonstrated for a silver nanowire.** (a-e) Reflection mapping for different positions ($0° - 45°$) of the half-waveplate to tune the excitation polarization. (f) Polarization averaged reflection image overlaid with an SEM image of the same sample region. All scale bars are 1 µm.

3.2.4 *Imaging and spectroscopy*

Instead of laser scanning and parallel photon counting, the sample surface can be imaged directly onto the CCD camera via the monochromator. For sample excitation, either a focused laser beam or broad whitelight illumination can be used. An example of whitelight illumination is given in Figure 3.9 for a GaAs quantum dot sample with a low density of silver nanowires on top. If the 0th diffraction order is imaged on the CCD chip, a real-space image of the sample plane is obtained, as can be seen in Figure 3.9a. By the use of a NIR bandpass filter (Semrock 800/12) in the detection path, only the dim reddish flank of the reflected whitelight is transmitted, whereas the photoluminescence of the quantum dots is transmitted completely. This results in a comparable brightness of the quantum dots and the substrate, which allows the silver nanowires to be identified by small intensity variations in the reflected light caused by scattering. The contrast ratio between quantum dots and substrate can be further optimized by tilting the bandpass filter slightly in order to tune its transmission range. The mixing of photoluminescence and scattered light can be better understood when the x-axis is replaced by a wavelength-axis, as done in Figure 3.9b. Here, the same sample region as in Figure 3.9a is imaged onto the CCD camera, but the 1st diffraction order of the grating is used to obtain spectral information. The decaying flank of the whitelight source can be seen, which is transmitted within the bandpass range ($770 - 800$ nm), indicated by the harsh drop of the intensity. On top of this broad background, the photoluminescence emission of each quantum dot is visible at the respective y-position, corresponding to the real-space image in Figure 3.9a. The quantum dot sample O690 used here was fabricated roughly ten years before the measurement; the degradation of the

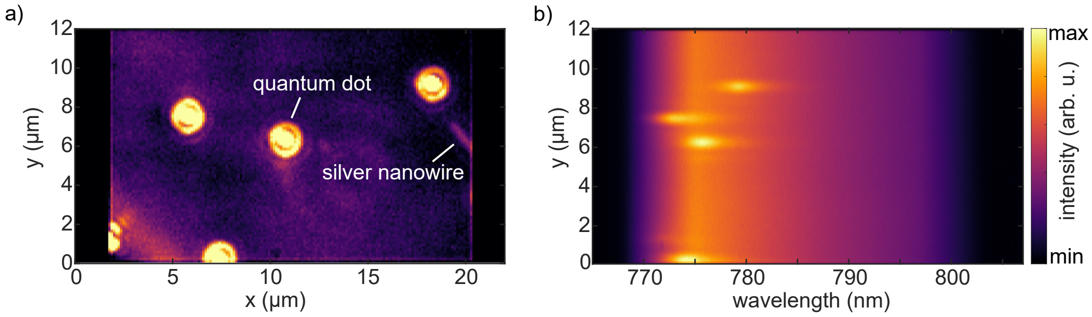

Figure 3.9: **Real-space (a) and wavelength-space (b) camera images of GaAs quantum dots with silver nanowires on top, under whitelight illumination**. Both images display the same sample region. A bandpass before the monochromator filters at the quantum dot emission wavelength so that photoluminescence mixes with whitelight reflection. (a) Real-space image, obtained by imaging the 0th order of the diffraction grating on the CCD camera. (b) Wavelength-space image, obtained by imaging the 1st diffraction order of the grating on the CCD camera.

sample is evident from the spectral broadening, which prevents the assignment of individual transitions.

3.3 WHITELIGHT REFLECTION SPECTROSCOPY FOR FILM THICKNESS CONTROL

Since plasmonic modes at high-index surroundings suffer drastic propagation losses (as discussed in chapter 2.2.1), dielectrics with a low real part of the refractive index are required to fabricate efficient plasmonic nanocircuits. In chapter 4, single GaAs quantum dots are coupled to silver nanowires via the intermediate field. A planar dielectric layer is utilized to ensure the optimal distance, where coupling strength and waveguide losses are balanced (see Figure 4.3). The same trade-off is present in chapter 6, where single GaAs quantum dots are integrated into nanopillars by site-selective etching. In this approach, the dielectric coating primarily serves to planarize the etched topography, facilitating the coupling to silver nanowires. Both approaches have in common that the thickness of the film should be controlled well, with values on the order of 100 nm. To serve this purpose, spin-on-glass IC1-200 (Futurrex) is used. The material has a refractive index of 1.41, and its film thickness can be controlled by the rotation speed of the spin-coating process. In order to reproducibly calibrate spinning speed ω with film thickness t_{IC1}, the film thickness needs to be measured. Here, at first, GaAs quantum dot samples are spin-coated with IC1-200 applying different rotation frequencies before whitelight reflection spectra are recorded to extract the respective film thickness accurately.

The measurement principle is schematically sketched in Figure 3.10a. A whitelight source is incident on the multilayered sample structure. Apart from the air/IC1- and IC1/GaAs-interface, several other interfaces are present inside the epitaxially grown GaAs/AlGaAs heterostructure (O691 quantum dots, see Appendix A.1). The various reflected contributions can interfere with each other, dependent on the respective layer thickness and refractive index. The reflection spectra of a bare GaAs quantum

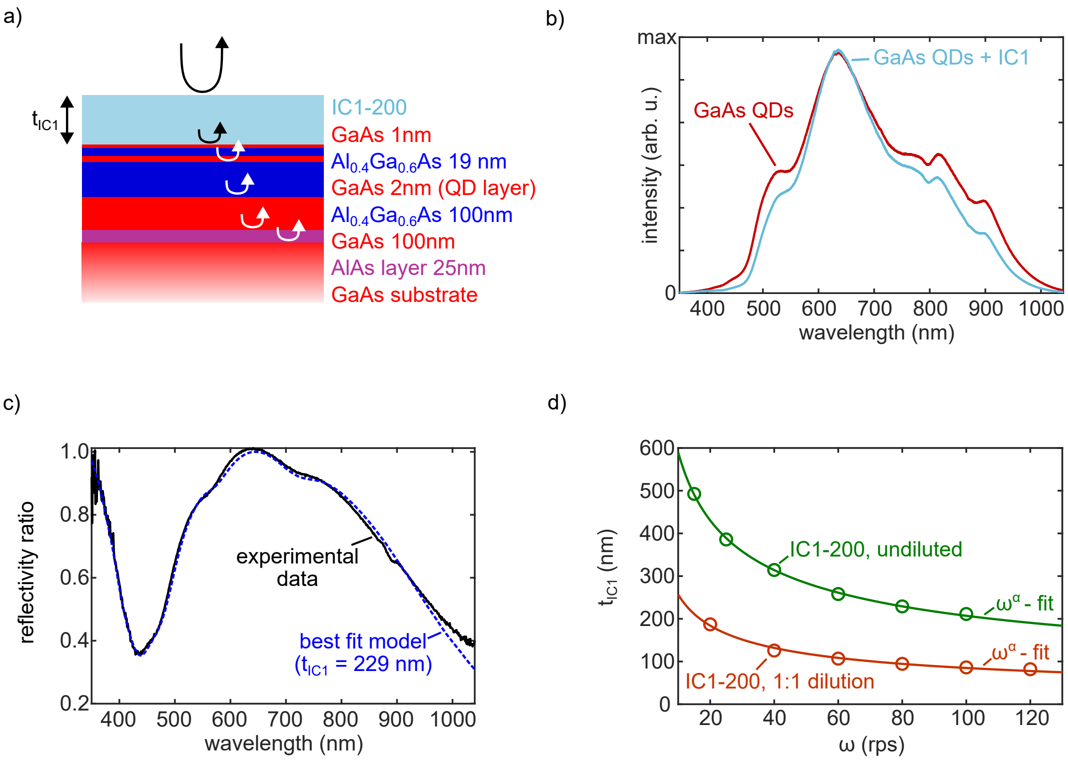

Figure 3.10: **Whitelight reflection spectroscopy for the controlled fabrication of IC1-200 films on top of GaAs quantum dot samples.** (a) Sample structure and measurement principle. (b) Whitelight reflection spectra of a bare GaAs QD sample (red curve) and the same GaAs QD sample after spin-coating IC1-200 (blue curve). (c) Black curve: Reflectivity ratio of both spectra shown in (b). Dashed curve: Transfer matrix model for the reflectivity ratio, with the film thickness t_{IC1} as the only free parameter. (d) Extracted film thickness t_{IC1} as a function of rotation speed ω for undiluted IC1-200 (green circles) and diluted IC1-200 (red circles). The spinning curves are fitted by ω^α, yielding $\alpha = -0.45$ (undiluted) and $\alpha = -0.48$ (diluted).

dot sample and the same sample after coating with IC1-200 are compared in Figure 3.10b. For these measurements, a fiber-based whitelight reflection spectrometer (Ocean Optics VIS-NIR-USB4000) from the KeyLab Device Engineering of Universität Bayreuth is used. In order to obtain the film thickness t_{IC1}, both reflection spectra are divided by each other and a transfer matrix model [71] mimicking the sample structure is fitted to the experimental reflectivity ratio, as shown in Figure 3.10c. Therefore, the function

$$\frac{R_{GaAs+IC1,meas}}{R_{GaAs,meas}} - \frac{R_{GaAs+IC1,model}(t_{IC1})}{R_{GaAs,model}} \tag{3.1}$$

is minimized by least squares, with the measured reflectivity ratio on the left side and the reflectivity ratio given by the transfer matrix method on the right side. The only free parameter is the IC1 film thickness t_{IC1}, while the other layer thicknesses are fixed according to the sample structure in Figure 3.10a. The dielectric functions of the GaAs, AlGaAs, and AlAs components are taken from [49, 72, 73]. For the example given here, the fit yields a film thickness of $t_{IC1} = 229\,\text{nm}$; comparing the resulting reflectivity ratio with the measurement leads to a very good agreement.

In order to cover a wider range of film thicknesses, IC1-200 is diluted with a 1:1 mixture in its solvent n-butanol. For both undiluted and diluted IC1-200, spinning curves are obtained by varying the rotation frequency ω and measuring the respective film thickness t_{IC1}. The results are shown as circles in Figure 3.10d for both dilutions, spanning a range between 80 nm and 500 nm. According to the literature, the film thickness depends with $t \propto \omega^{-\frac{1}{2}}$ on the rotation speed [74]. Fitting a function proportional to ω^{α} to the experimental data leads to $\alpha = -0.45$ for the undiluted IC1 and $\alpha = -0.48$ for the 1:1 dilution, in good agreement with the theory. Slight deviations might be caused by different sizes of the wafer pieces. More details on the spin-coating characteristics of IC1-200 can be found in the bachelor thesis of Julian Alin [75], who studied the film homogeneity and reproducibility on glass coverslips.

4

INTERMEDIATE FIELD COUPLING OF SINGLE EPITAXIAL QUANTUM DOTS TO SILVER NANOWIRES

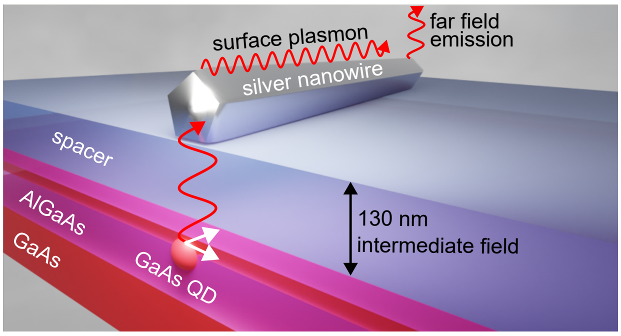

> Parts of this chapter (including the above image) are published in *Intermediate field coupling of single epitaxial quantum dots to plasmonic waveguides* by M. Seidel, Y. Yang, T. Schumacher, Y. Huo, S. Covre da Silva, S. Rodt, A. Rastelli, S. Reitzenstein, and M. Lippitz, Nano Letters 2023, 23, 10532-10537.

Plasmonic nanocircuits that connect single quantum emitters are a promising platform for future quantum optical applications [7]. Two key advantages of plasmonics include the capability to confine electromagnetic fields below the diffraction limit [3] and the resulting enhancement of the light-matter interaction [76]. The optimal nanocircuit consists of a high-quality single-photon source, which is efficiently coupled to a plasmonic waveguide with small propagation losses. On the other side, self-assembled quantum dots are considered one of the best sources of single photons due to their stability, brightness, and narrowband emission [17, 77]. Particularly, the class of strain-free GaAs quantum dots offers outstanding properties [31]. Among plasmonic waveguides, colloidal silver nanowires exhibit the highest propagation lengths over a broad spectral range, reaching from visible to infrared wavelengths [57, 78]. However, the straightforward combination of epitaxial quantum dots and silver nanowires does not achieve the goal since the high refractive index of the semiconductor introduces tremendous radiative and Ohmic losses, as discussed in section 2.2.

In this chapter, the problem is tackled by a novel approach, where the coupling between emitter and waveguide is mediated via the intermediate field instead of the near field. It will be shown computationally that the optimal circuit performance is achieved in the intermediate field. The required coupling distance is experimentally reached via a lower-index dielectric spacer layer sandwiched between the semiconductor and the waveguide. The coupling is demonstrated by launching surface plasmons through quantum dot photoluminescence, and the coupling efficiency is extracted from optical far field imaging. High-resolution cathodoluminescence images allow to determine the lateral coupling distance with high accuracy, which is used to describe the coupling efficiency via a simple interference model.

The chapter is structured in the following way: A brief motivation in section 4.1 recapitulates optical near and far fields for the example of a radiating dipole source. In section 4.2, the intermediate field coupling scheme is introduced and characterized through numerical simulations. In particular, the coupling efficiency and propagation length are computed as a function of the spacer thickness. Afterwards, the sample preparation is discussed in section 4.3. The random placement of quantum dots and nanowires affords pre-selection of possibly coupled nanostructures; the applied imaging techniques are described in section 4.4. Intermediate field coupling is then demonstrated in section 4.5. The procedure to extract the coupling efficiency of a quantum dot–waveguide system is described in section 4.6. Finally, in section 4.7, variations of the coupling efficiency are explained by the interference of plasmons, which are partially reflected at the nanowire end.

4.1 MOTIVATION: OPTICAL NEAR AND FAR FIELDS

The field of plasmonics focuses on optical near fields and light-matter interaction in the near field of variously shaped metallic nanostructures [79–81]. In particular, the coupling of single quantum emitters to plasmonic waveguides has been facilitated via the near field, as reviewed by the Bozhevolnyi group [82]. Many coupling geometries involve emitters placed within small gaps [83, 84], grooves [85], or wedges [86], so that emitter–waveguide distances are small. The work presented in chapter 4 breaks with the assumption that only near fields can mediate emitter–plasmon coupling. Before turning to the actual intermediate field coupling scheme, a short recapitulation of optical near and far fields is given for the example of a radiating electric dipole in free space.

The electric dipole fields can be derived in a physical picture from two oscillating charges with opposite signs $\pm q$ that are distanced by an infinitesimal length piece $d\boldsymbol{s}$, resulting in a dipole moment $\boldsymbol{\mu} = q\,d\boldsymbol{s}$. A more abstract derivation is given by Hecht and Novotny [47], who apply Green's function formalism. In spherical coordinates $\boldsymbol{r} = (r, \theta, \phi)$, the amplitudes of the electric fields are

$$E_r = \frac{|\boldsymbol{\mu}| \cos\theta}{4\pi\epsilon_0\epsilon} \frac{e^{ikr}}{r} k^2 \left[\frac{2}{k^2r^2} - \frac{2i}{kr} \right], \tag{4.1}$$

$$E_\theta = \frac{|\boldsymbol{\mu}| \sin\theta}{4\pi\epsilon_0\epsilon} \frac{e^{ikr}}{r} k^2 \left[\frac{1}{k^2r^2} - \frac{i}{kr} - 1 \right], \tag{4.2}$$

with a vanishing component $E_\phi = 0$. Here, k is the wavevector, and r is the radial distance from the center of the coordinate system. The radial component E_r (also longitudinal field) features two contributions that decay proportional to r^{-3} and r^{-2},

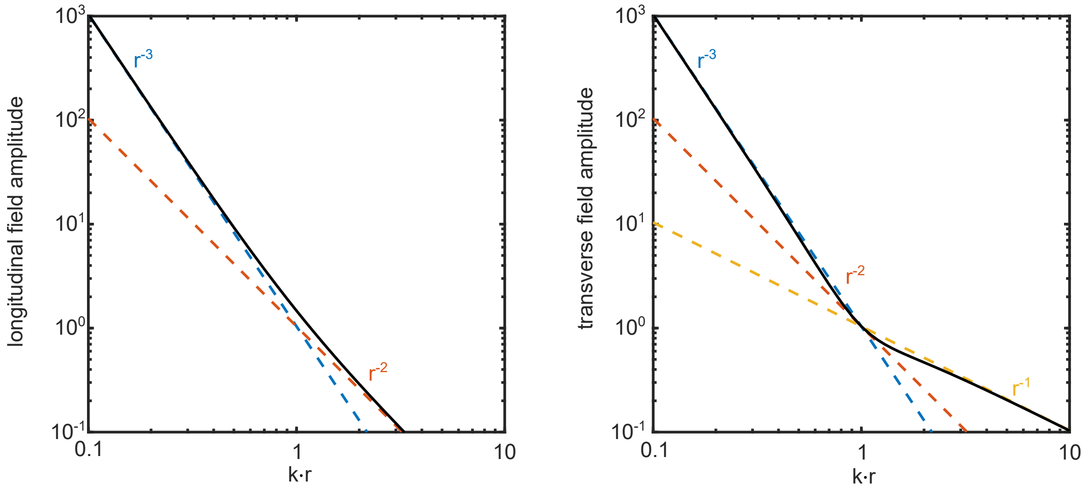

Figure 4.1: **Decay of the electric fields of a dipole in a homogeneous medium.** The solid line represents the field amplitude, while the dashed lines are given by the differently decaying contributions. The absolute value is plotted for a wavelength of $\lambda = 790\,\text{nm}$. (a) Longitudinal field amplitude after Equation 4.1. (b) Transverse field amplitude after Equation 4.2. The equations are taken from Hecht and Novotny [47].

while the transverse field E_θ has three contributions that decay proportionally to r^{-3}, r^{-2}, and r^{-1}. The absolute values of these differently decaying contributions, as well as the total amplitude, are plotted in Figure 4.1a for the longitudinal field and in Figure 4.1b for the transverse field for a wavelength of $\lambda = 790\,\text{nm}$. Three regimes can be identified: In the near field of the dipole ($kr \ll 1$), the short-ranged r^{-3}-term dominates, while in the far field ($kr \gg 1$), the long-ranged r^{-1}-term dominates. The missing of the r^{-1}-term in the longitudinal component means that in the far field, a transverse electromagnetic wave is obtained. At the transition between near and far field, the intermediate field regime is reached at $kr \approx 1$. Here, the differently decaying contributions are comparably large. This is the regime where the coupling of epitaxial quantum dots and silver nanowires will be achieved.

4.2 NUMERICAL ANALYSIS OF THE INTERMEDIATE FIELD COUPLING

In this section, the intermediate field coupling geometry will be introduced. In order to gain both a qualitative and a quantitative understanding of this approach, finite element simulations are performed with Comsol Multiphysics. At first, the study is limited to two dimensions, assuming an infinitely extended waveguide along the propagation direction (section 4.2.1). From the mode analysis, the effective mode index and the propagation length are obtained. Furthermore, the spatial variation of the coupling efficiency for an emitter at a certain position in the waveguide plane is obtained from the mode profiles (section 4.2.2). Therefore, adaptions of the framework described in section 2.3.1 are being made to account for the orthogonal excitonic transitions that exist in self-assembled quantum dots. The two-dimensional mode profiles will be extended analytically along the propagation direction in section 4.7.

4.2.1 *Waveguide mode analysis*

The intermediate field sample geometry is sketched in Figure 4.2a. The GaAs substrate supports the AlGaAs barriers, which contain the GaAs quantum dot layer. A dielectric film acts as a spacer for the plasmonic waveguide, given by a silver nanowire. An infinitely extended waveguide is assumed in the propagation direction. The mode analysis of Comsol is applied to calculate the mode's field profile and the complex effective mode index (compare section 2.2.2). To understand the effect of the spacer layer, its thickness t is varied. The wavelength is fixed at $\lambda = 790\,\text{nm}$, which is the emission wavelength of the GaAs quantum dots. The silver nanowire is modeled by a pentagonal shape, as expected for wet-chemically grown monocrystalline silver [52]. In order to avoid extreme field hot spots, a corner rounding of $10\,\text{nm}$ is assumed. The nanowire size is $d = 50\,\text{nm}$, corresponding to the mean size of the nanowires that are used in the experiment and observed in scanning electron micrographs. The refractive indices for silver ($n_{Ag} = 0.035 + 5.49i$) and AlGaAs ($n_{AlGaAs} = 3.44$) are taken from the literature [48, 49]. For the sake of simplicity, the thin GaAs layer ($\approx 2\,\text{nm}$) and the GaAs substrate are taken as AlGaAs. The dielectric spacer (spin-on-glass IC1-200) is modeled with $n_{spacer} = 1.41$ according to the datasheet of the manufacturer Futurrex, which is in agreement with ellipsometry data [87].

Figure 4.2b shows the dependence of the effective mode index $\tilde{n}_{eff}$ on the spacer thickness t. The real part of the mode index decreases for thicker spacers and approaches $n_{eff} = 1.67$. In this limit, the influence of the high-index semiconductor is negligible, and the spacer essentially behaves like a glass substrate. For the same reason, the propagation length increases drastically for thicker spacer layers. For $t = 300\,\text{nm}$, the propagation length is $L_p = 8.5\,\mu\text{m}$, whereas for $t = 10\,\text{nm}$, the propagation length is only $L_p = 0.31\,\mu\text{m}$.* The strong damping is partly explained by Ohmic losses: the high refractive index of the AlGaAs pushes the electric fields into the metal, where the energy is dissipated in heat, as discussed in section 2.2.1. However, another loss channel can be identified if one looks at the mode's intensity profile in Figure 4.2c for a spacer thickness of $t = 10\,\text{nm}$: The mode radiates into the semiconductor substrate. Such leaky modes on high-index substrates have been theoretically studied by the Lodahl group for a similar geometry [51]. Note that the intensity in the AlGaAs part is multiplied by 100 to increase visibility. The leaky character of the waveguide mode can already be expected from the real part of the effective mode index, which is smaller than the refractive index of AlGaAs ($n_{AlGaAs} = 3.44$). If the thickness of the spacer layer is increased, as in Figure 4.2d, where the thickness is $t = 200\,\text{nm}$, the far field contribution vanishes, and the mode is completely bound to the nanowire.

---

* It should be noted that the exact values for the mode index and the propagation length depend on details of the chosen geometry, for example the size and shape of the nanowire. Furthermore, the exact position of the nanowire with respect to the spacer surface has an influence. Here, the nanowire is lifted $3\,\text{nm}$ above the spacer surface for numerical reasons.

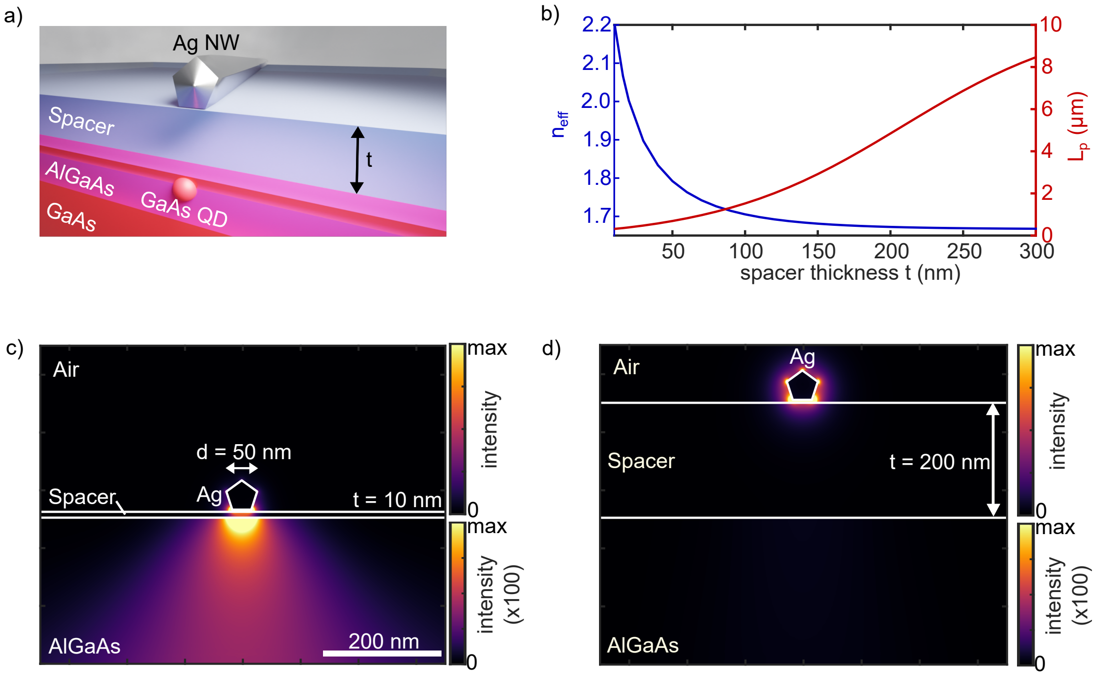

Figure 4.2: **Waveguide mode analysis for the intermediate field coupling scheme as a function of the dielectric spacer thickness.** (a) Sketch of the geometry: A GaAs quantum dot inside AlGaAs barriers is separated from the silver nanowire by the capping layer and a dielectric spacer. (b) Real part of the effective mode index (blue line) and propagation length (red line) as a function of the spacer thickness t. (c, d) Mode profiles for a spacer thickness $t = 10\,\text{nm}$ (c) and $t = 200\,\text{nm}$ (d). The intensity in the semiconductor half-space is multiplied by a factor of 100 to increase the visibility of the radiative contribution.

4.2.2 *Coupling efficiency of an epitaxial quantum dot*

In the last section, the intermediate field coupling scheme has been characterized by mode profiles and their propagation lengths. It has been shown that the dielectric spacer can increase the propagation efficiency drastically. However, a functional nanocircuit not only requires good propagation but also a high coupling efficiency of the quantum emitter to the nanocircuit. Therefore, the spatial variation of the coupling efficiency for an emitter in the cross-sectional plane (xz) of the infinitely extended (y) waveguide is computed. While a framework to compute the normalized decay rate into a plasmonic waveguide mode has already been described in section 2.3.1, a slight adaption is necessary in order to apply the model to epitaxial GaAs quantum dots. This is due to the two orthogonal excitonic transitions that are present in such emitters but are not considered in Equation 2.28 for the normalized decay rate of an emitter with a single dipole moment that is oriented along $\hat{\boldsymbol{\mu}}$. Since the GaAs quantum dots are excited non-resonantly with a photon energy above the

GaAs band gap in the experiment, both excitonic contributions are assumed to add up incoherently. Therefore, we define the coupling efficiency

$$\eta_{in}(x,z) := \frac{\gamma_{pl}}{\gamma_{AlGaAs}} = \frac{3\pi c\epsilon_0}{n_{AlGaAs}\, k_0^2 \int_A S_y\, dA} \left(|\hat{\boldsymbol{\mu}}_1 \cdot \boldsymbol{E}(x,z)|^2 + |\hat{\boldsymbol{\mu}}_2 \cdot \boldsymbol{E}(x,z)|^2 \right) \quad (4.3)$$

as the decay rate into a plasmonic mode normalized to the emission of a dipole in homogeneous AlGaAs. The excitonic dipole moment orientations are given by $\hat{\boldsymbol{\mu}}_1$ and $\hat{\boldsymbol{\mu}}_2$. Furthermore, there is the modal electric field $\boldsymbol{E}$ in the transverse xz-plane, the refractive index $n_{AlGaAs} = 3.44$, and the time-averaged Poynting vector component $S_y = \frac{1}{2}\, Re(\boldsymbol{E} \times \boldsymbol{H}^*) \cdot \hat{\boldsymbol{y}}$ in waveguide direction y, which is integrated over the transverse plane A. Both excitonic dipole transition moments are assumed to have the same absolute value ($|\boldsymbol{\mu}_1| = |\boldsymbol{\mu}_2|$), and contribute to the emission into the waveguide mode depending on their projection on the modal fields. Note the coupling efficiency can exceed unity, even though such high values are not expected for the intermediate field coupling regime.*

It is handy to define normalized electric fields of the waveguide mode

$$\boldsymbol{E}_{norm} = \frac{\boldsymbol{E}}{\sqrt{p}}. \quad (4.4)$$

with the normalization constant

$$p = \frac{3\pi c\epsilon_0}{n_{AlGaAs} k_0^2 \int_A S_y\, dA}, \quad (4.5)$$

that is always positive if the power flows in the y direction. The use of normalized electric fields will turn out particularly useful in section 4.7, where the two-dimensional (xz) modal fields will be propagated along the waveguide axis (y). Consequently, Equation 4.3 simplifies to

$$\eta_{in} = |\hat{\boldsymbol{\mu}}_1 \cdot \boldsymbol{E}_{norm}|^2 + |\hat{\boldsymbol{\mu}}_2 \cdot \boldsymbol{E}_{norm}|^2. \quad (4.6)$$

After evaluation of the dot product and considering that the dipole moment of the GaAs quantum dots is in-plane ($\mu_z = 0$), one obtains

$$\eta_{in} = |\mu_{1,x} E_x + \mu_{1,y} E_y|^2 + |\mu_{2,x} E_x + \mu_{2,y} E_y|^2, \quad (4.7)$$

still using normalized fields $\boldsymbol{E}_{norm}$, but omitting the subscript for easier readability. Exploiting the orthogonality of the excitonic states leads to

$$\eta_{in} = |\mu \sin\theta E_x + \mu \cos\theta E_y|^2 + |\mu \cos\theta E_x + \mu \sin\theta E_y|^2, \quad (4.8)$$

with the angle θ between dipole moment contribution $\boldsymbol{\mu}_1$ and wire axis. The absolute value of the dipole moment μ is equal to one due to the use of unit vectors above.

---

[*] Another definition of the coupling efficiency η_{in} has been given in Equation 2.35, which is computed from three-dimensional simulations. Since all simulations in chapter 4 are two-dimensional, only the definition given in Equation 4.3 is used.

Considering that the electric field is complex-valued, one can apply $|a+b|^2 = |a|^2 + |b|^2 + 2\,Re(ab^*)$ to finally obtain

$$\eta_{in} = |E_x|^2 + |E_y|^2 + 4\sin\theta\cos\theta\, Re(E_x E_y^*). \tag{4.9}$$

The coupling efficiency is dimensionless since the normalization is already included in the electric fields. It is proportional to the absolute square of the in-plane electric field components and a cross term that describes the influence of the dipole moment orientation. In principle, the excitonic orientation can be determined experimentally via the fine structure splitting (compare section 2.1.3). In general, however, the exact orientation of the dipole moment contributions is unknown. Throughout this chapter, an angle of $\theta = 0°$ is assumed, meaning that one exciton is oriented parallel to the nanowire along the y-axis, while the other exciton is perpendicular and therefore pointing in the x-direction. The uncertainty of the unknown dipole moment orientation will be discussed later (see Figure 4.12). Finally, one obtains the coupling efficiency

$$\eta_{in}(x,z) = |E_x(x,z)|^2 + |E_y(x,z)|^2, \tag{4.10}$$

which is used in Figure 4.3a for the intermediate field geometry, applying a spacer thickness of $t = 130\,\text{nm}$. Even though the epitaxial quantum can not leave its AlGaAs host material, the coupling efficiency is given in the whole xz-plane.

The highest coupling efficiency η_{in} of a hypothetical quantum dot is obtained directly at the nanowire, where the emission rate is more than 10 times the bulk emission rate in AlGaAs. Inside the semiconductor, the coupling efficiency is much smaller and does not vary much. Assuming a quantum dot burial depth $z_b = 30\,\text{nm}$ below the semiconductor/spacer interface, the coupling efficiency drops only by a factor of 2 for a lateral displacement of 125 nm along the x-axis. This weak lateral dependence stems from the loosely bound character of the waveguide mode and is beneficial in terms of quantum dot alignment. For most plasmonic applications, an alignment accuracy on the order of 10 nm is needed [80], about a factor of 10 less than here. In the z direction, the coupling efficiency only suffers a decrease of 30 % when going from $z_b = 30\,\text{nm}$ to $z_b = 200\,\text{nm}$. The weak depth dependence suggests that the quantum dot can be placed deeper in the AlGaAs. This is particularly intriguing when one considers that the optical properties of the quantum dots improve rapidly for deeper burial depths [42].

The effect of the spacer thickness on the coupling efficiency η_{in} is shown as the blue curve in the upper panel of Figure 4.3b: With increasing thickness of the spacer layer, the waveguide mode's amplitude at the quantum dot position is decreased, and therefore the coupling efficiency is reduced. Here, the coupling efficiency is evaluated for an emitter that is centered with respect to the nanowire and located at a depth of $z_b = 30\,\text{nm}$. In order to demonstrate the competing factors of coupling efficiency and propagation losses, the propagation length, which is already shown in Figure 4.2b, is added as the red curve. This suggests that there is an optimal spacer thickness where propagation and coupling efficiency trade off.

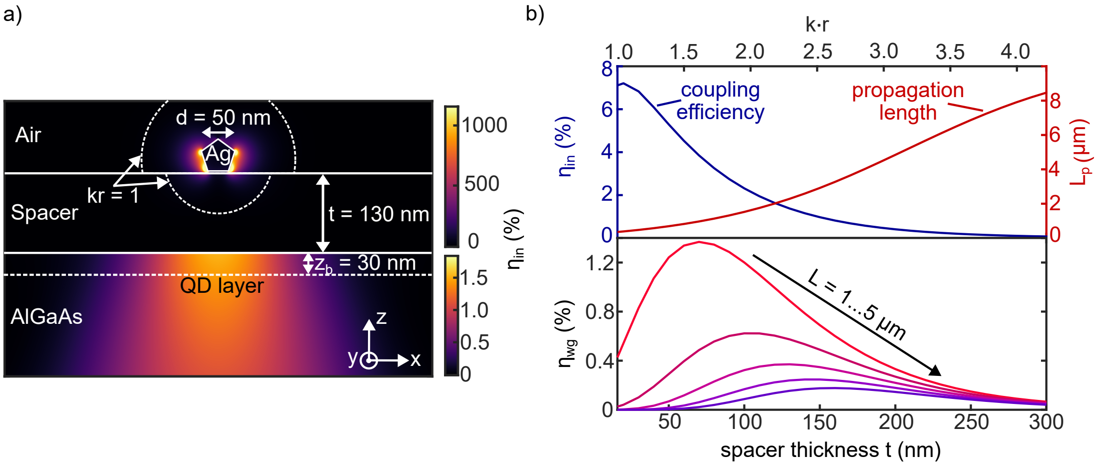

Figure 4.3: **Coupling and waveguide efficiency for the intermediate field coupling scheme.** (a) Map of the coupling efficiency η_{in} into the waveguide mode for a quantum dot with dipole moment in the xy-plane of the sample. The spacer thickness is $t = 130\,\text{nm}$, and the quantum dot burial depth of $z_b = 30\,\text{nm}$ below the semiconductor surface is indicated as the dashed line. The dashed circle enclosing $kr = 1$ illustrates the transition between the near field and the far field. Note that different color scales are assigned to the lower and upper half spaces. (b) Upper panel: Coupling efficiency η_{in} (blue line) and propagation length L_p (red line), as a function of the spacer thickness t. The coupling efficiency is evaluated for an emitter centrally located under the nanowire at $z_b = 30\,\text{nm}$. Lower panel: Waveguide efficiency η_{wg} as a function of spacer thickness t, for five different waveguide lengths L. The additional kr-axis indicates that optimal performance is accomplished in the intermediate field for $kr \gtrsim 1$.

In order to include propagation losses into our consideration, the waveguide efficiency is defined as $\eta_{wg} = \eta_{in}\,\eta_p$, with the propagation efficiency $\eta_p = e^{-L/L_p}$ for a waveguide of length L. Obviously, the optimal spacer thickness also depends on the waveguide length L, as shown for five different lengths between 1 µm and 5 µm in the lower panel of Figure 4.3b. It can be seen that the highest waveguide efficiency η_{wg} is achieved for short waveguides and rather thin spacers. However, for an experimentally meaningful nanocircuit, the waveguide length should at least exceed the spatial resolution of the microscope, i.e., $L \gtrsim 1\,\mu\text{m}$. For such waveguide lengths, the optimum waveguide efficiency is achieved in the intermediate field regime at $kr = 1.6 - 2.6$ or $t = 70 - 160\,\text{nm}$. Here, the spacer thickness t is rewritten in terms of $kr = k_0(n_{AlGaAs}z_b + n_{spacer}t)$ with the vacuum wavevector k_0, accounting for the refractive indices of the respective media. The transition from near to far field is illustrated as the dashed circle enclosing $kr = 1$ in Figure 4.3a, underlining the fact that the quantum dot–waveguide coupling takes place outside the near field.

In summary, it was demonstrated that coupling efficiency and propagation efficiency are competing factors for the proposed coupling geometry. As a consequence, there is an optimal spacer thickness, which happens to be in the intermediate field regime. The exact optimum of the emitter–waveguide distance depends also on the waveguide length. For waveguides with a few micrometers in length, a good overall performance is expected for a film thickness of $t \approx 130\,\text{nm}$, promising a coupling efficiency of $\eta_{in} = 1.38\,\%$ for a centered quantum dot and a propagation length of $L_p = 2.3\,\mu\text{m}$. In the following section, the preparation of a sample that targets such a nanostructure is described.

4.3 SAMPLE PREPARATION

The samples used to demonstrate the intermediate field coupling are based on near-surface self-assembled GaAs quantum dots in AlGaAs barriers that are grown by molecular beam epitaxy on a GaAs substrate. Compare section 2.1.2 for details on the droplet etching process and section 2.1.3 for the optical properties of such quantum dots. In total, three slightly different samples were used that have burial depths of $z_b = 15\,\text{nm}$, $30\,\text{nm}$, and $40\,\text{nm}$. For details on the structure of these sample types (O690, O692, Sa665), see Appendix A.1. According to Figure 4.3a, the slightly different burial depths do not affect the waveguide coupling efficiency notably. Since the molecular beam epitaxy process is highly precise, the actual burial depths of the dots should differ less than $1\,\text{nm}$ from the nominal values, according to the Rastelli group.

For the dielectric spacer, the polysiloxane-based spin-on glass IC1-200 from Futurrex is applied. The spin-coating behavior of IC1-200 has been studied in section 3.3, including spinning curves for the film thickness as a function of rotation speed. To reach a film thickness well below $200\,\text{nm}$, IC1-200 is diluted in isobutanol with a 1:1 mixture. Afterwards, IC1-200 is spin-coated on top of the semiconductor wafer piece at $77\,\text{rps}$ and baked out on a hotplate at $200\,^\circ\text{C}$, resulting in a nominal film thickness of $t = 130\,\text{nm}$. The actual film thickness is determined to $t = 131\,\text{nm}$, $162\,\text{nm}$, $136\,\text{nm}$ for the respective samples by AFM measurements of a scratch edge. The thickness variation between the samples can be explained by different sizes of the wafer pieces. The variation within one sample is estimated to be $\pm 10\,\text{nm}$.

In the last step, chemically-grown monocrystalline silver nanowires (PL-AgW100) from PlasmaChem are diluted in isopropanol and dispersed on top of the outbaked IC1-200 film. Nominally, the silver nanowires should be $100\,\text{nm}$ wide. However, scanning electron micrographs (for example, in Figure 4.7) show that the actual width is around $50 \pm 10\,\text{nm}$. After dispersion of the nanowires, the sample is gently rinsed in ethanol in order to remove the PVP (Polyvinylpyrrolidone) surfactant and dried under nitrogen flux. It has been shown that the thickness of the PVP layer can be effectively reduced to a few nanometers after a single washing cycle [88], as applied here. In addition, the O690 and O692 samples are coated with $5\,\text{nm}$ (nominal) of Al_2O_3 by atomic layer deposition (ALD) in order to fixate the nanowires to the substrate and reduce silver degradation. It has been observed that this step is not necessary if the sample is kept away from strong mechanical vibrations as well as stored and transported under vacuum conditions.

4.4 PRE-SELECTION OF QUANTUM DOT–NANOWIRE SYSTEMS

As a consequence of the probabilistic sample preparation, quantum dots and nanowires are randomly distributed over the substrate, sampling all relative orientations and coupling distances. Therefore, pre-selection of potentially coupled quantum dot–nanowire pairs is required. At first, the coupling probability for the sample configuration is estimated in section 4.4.1, measured in terms of the sample area that needs to be screened. The applied sample screening techniques are presented in the following section 4.4.2. The nanosystems identified as "promising", meaning that the nanowire is laterally close to the dot, are tested for waveguide transmission by laser coupling in section 4.4.3 before intermediate field coupling of quantum dots to silver nanowires is then demonstrated in section 4.5.

4.4.1 *Estimation of the coupling probability*

The coupling probability for a random sample configuration, as sketched in Figure 4.4a can be estimated easily by assuming spatially homogenous distributions of quantum dots and nanowires. At first, one can define a nanowire area percentage

$$p_{nw} = \rho_{nw}\overline{L}\Delta x \tag{4.11}$$

with the nanowire density ρ_{nw}, the average nanowire length $\overline{L}$, and the coupling distance Δx, which is the lateral distance between the dot and the wire that is required to ensure sufficient coupling. By multiplying the nanowire area percentage p_{nw} with the quantum dot density ρ_{qd}, one obtains the density

$$\rho_{nw,qd} = p_{nw}\rho_{qd} \tag{4.12}$$

of quantum dots located within the coupling distance of the nanowires. In terms of the experiment, the average sample area

$$\overline{A}_{qd,nw} = \frac{1}{\rho_{nw,qd}} = \frac{1}{\rho_{nw}\overline{L}\Delta x \rho_{qd}} \tag{4.13}$$

containing one coupled quantum dot–nanowire pair is more practical. Figure 4.4b shows the average sample area $\overline{A}_{qd,nw}$ as a function of the lateral coupling distance Δx. Here, a nanowire density $\rho_{nw} = 0.0027\,\mu\text{m}^{-2}$, a quantum dot density $\rho_{qd} = 0.13\,\mu\text{m}^{-2}$, and an average nanowire length $\overline{L} = 3\,\mu\text{m}$ is assumed. These values are obtained by averaging photoluminescence and SEM images over a sufficiently large sample region. The nanowire density only takes sufficient long ($L > 1\,\mu\text{m}$) nanowires into account, as coupling to shorter wires is experimentally hard to detect with far field optics.

From the equations above, it follows that the required sample area is inversely proportional to the coupling distance, leading to divergent scanning areas for small coupling distances. According to the simulation in Figure 4.3a, the intermediate field coupling scheme features an extraordinarily weak dependence on lateral displacement between quantum dot and nanowire, with the coupling efficiency only

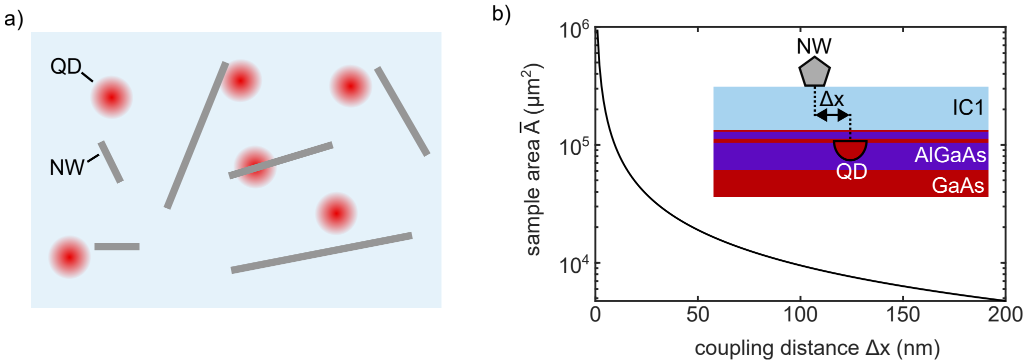

Figure 4.4: **Estimation of the coupling probability for a random assembly of quantum dots (QD) and nanowires (NW).** (a) Illustration of the random quantum dot–nanowire assembly, viewed from the top. (b) Estimation of the average sample area required to find a coupled quantum dot–nanowire pair as a function of the coupling distance Δx.

dropping by a factor of 2 for $\Delta x = 125\,\mathrm{nm}$. For this value, an average sample area $\overline{A} = 7600\,\mu\mathrm{m}^2$ would be required. In contrast, typical near field coupling distances in plasmonics are $\Delta x = 10\,\mathrm{nm}$, which consequently translates into a required sample area enlarged by a factor of 12.5, or $\overline{A} = 95\,000\,\mu\mathrm{m}^2$. Naturally, the absolute numbers are only a rough estimation, especially when considering that not every nanowire supports an efficiently propagating surface plasmon, for example, due to a small nanowire diameter, defects, or kinks [89]. Therefore, the probability of finding a coupled nanosystem might be somewhat smaller. Even though there is a significant advantage in coupling probability for the intermediate field coupling scheme, precise and fast sample screening is indispensable.

4.4.2 *Sample screening methods*

In the course of this work, three different identification techniques for quantum dot–nanowire systems at cryogenic temperatures were established: Cathodoluminescence with secondary electron contrast (see Figure 4.5a), laser scanning photoluminescence with reflection contrast (see Figure 4.5b) and whitelight illumination imaging (Figure 4.5c). The applied experimental setups are described in detail in chapter 3. In the following, these sample screening methods are demonstrated for a quantum dot–nanowire sample and compared in terms of contrast, resolution, and time consumption.

Cathodoluminescence imaging (compare section 3.1) combines the detection of quantum dot emission via cathodoluminescence with highly precise imaging of the silver nanowires via electron microscopy. The measurement principle sketched in Figure 4.5a involves a scanning electron beam that excites luminescence in the quantum dots while the nanowire scatters secondary electrons toward the detector. As already discussed in section 3.1.1, the resolution is – in principle – given by the size of the electron beam, but charge carrier diffusion leads to a significant spatial

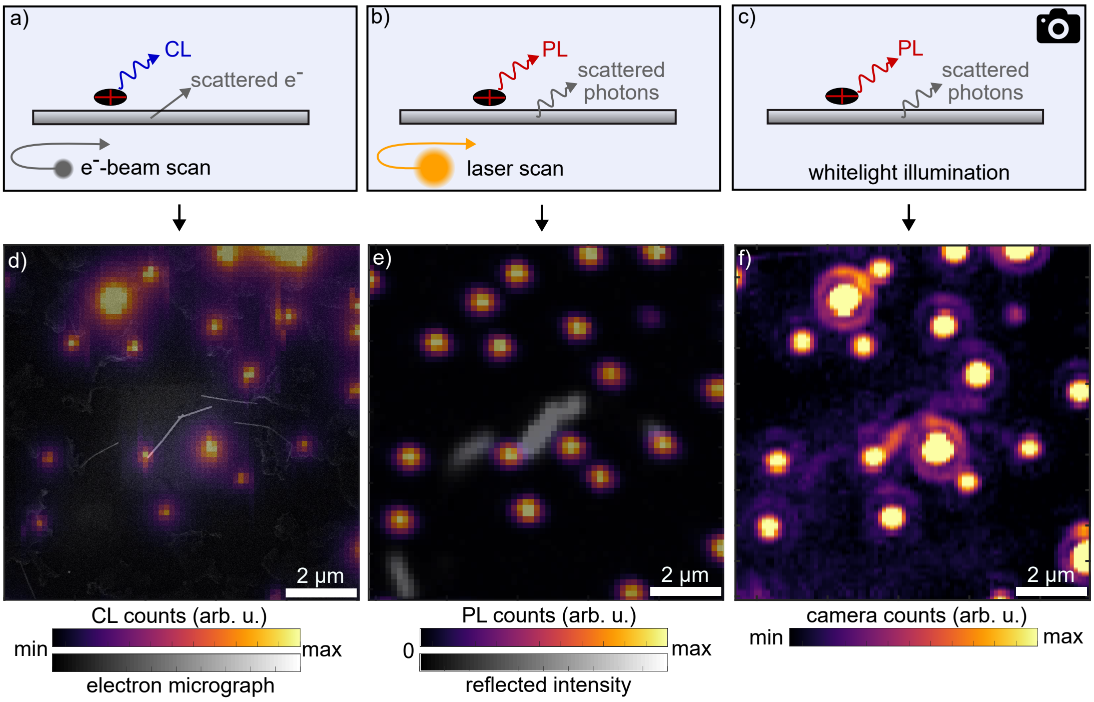

Figure 4.5: **Complementary methods for the pre-selection and identification of quantum dot–nanowire systems** Upper row (a, b, c): Sketches of the respective sample screening measurement process. Lower row (d, e, f): Corresponding data sets. (a) Scanning the electron beam to excite cathodoluminescence, which is detected together with scattered electrons. (b) Scanning the laser focus to excite photoluminescence, which is mapped in a first scan. In a second laser scan, a reflection image is recorded. (c) Whitelight illumination imaging with a CCD camera. (d) Cathodoluminescence image with overlaid electron micrograph. (e) Photoluminescence image overlaid with a reflection image. (f) Camera image under whitelight illumination. Photoluminescence and reflected/scattered photons are mixed. The all-optical images (e, f) are scaled and rotated with respect to the cathodoluminescence image (d).

broadening of the cathodoluminescence emission. Nevertheless, a highly precise localization of nanowires and quantum dots is obtained, especially when considering that both data sets are measured simultaneously in a single electron beam scan. A 100 μm^2 overview scan is given in Figure 4.5d, where the cathodoluminescence image is overlaid with the electron micrograph. It is apparent that the cathodoluminescence emission spots of the quantum dots vary substantially in brightness on a scale of several micrometers. The reason for this lies in the poor detection optics in the cathodoluminescence setup compared to a microscope objective. Besides, it is observed that the contrast of the silver nanowires with respect to the surroundings can vary between different samples and within one sample region. While the nanowire in the middle is resolved very well, the nanowires in the surroundings seem to be covered inhomogeneously. This is very likely caused by contaminations in the vacuum chamber, which freeze out at the cold sample surface. It is observed that the covering layer can be removed to some extent by scanning the electron beam over the sample region of interest, probably due to heat input, consistent with the fact that the contaminations are not present at room temperature. Furthermore, it is found that the nanowire contrast seems to be reduced if the sample is coated with 5 nm of Al_2O_3.

Another technique for the pre-selection of quantum dot–nanowire systems is **confocal laser scanning** (compare section 3.2.3). Here, two subsequent laser scans with an excitation wavelength of $\lambda = 635\,\mathrm{nm}$ are performed. At first, a reflection map is recorded, applying a polarization contrast. Then, a photoluminescence map is measured, as schematically sketched in Figure 4.5b. Both data sets overlaid with each other, are shown in Figure 4.5e. The confocal laser maps are scaled and rotated with respect to the cathodoluminescence coordinate system (Figure 4.5d), which is expected to be more accurate, using the quantum dot emission centers as fixed points. Some of the nanowires in the reflection map feature excellent contrast, while others are not visible at all. This is due to the orientational dependence of the polarization contrast utilized to suppress the direct laser reflection. The orientational dependence can be discarded by averaging over different laser polarizations, as described in section 3.2.3. However, this comes at the cost of longer measurement times and resulting stage drifts. In general, stage drifts between the consecutive photoluminescence and reflection scans can not be excluded, especially for large overview scans, as needed for pre-selection. Together with the diffraction-limited resolution, this makes confocal laser scanning, as applied here, less suitable for pre-selection than cathodoluminescence. Nevertheless, the method is very well suited to identify nanosystems that have been pre-selected in cathodoluminescence and was also used for pre-selection itself due to its in-house availability.

The third applied pre-selection method is **whitelight illumination imaging** (compare section 3.2.4). Here, the sample is illuminated by a broadband whitelight source and imaged onto a CCD camera, as sketched in Figure 4.5c. The signal consists of reflected whitelight and quantum dot photoluminescence with roughly balanced intensity contributions, achieved by bandpass filtering at the photoluminescence wavelength of the quantum dots. Just like the confocal scans, the camera image in Figure 4.5f is scaled and rotated with respect to the cathodoluminescence image that acts as a reference. This method does not allow for a separation of quantum dot emission from the photons that are scattered by the nanowires, which complicates the localization of dots and wires in certain cases. Furthermore, the nanowire contrast depends on its orientation, similar to the confocal laser scan. On the other hand, there are no alignment issues due to the simultaneous imaging of dots and wires. Clearly, the advantage of this method is speed: For the chosen microscope magnification, as in Figure 4.5f, an area of 12 µm x 17.5 µm can be imaged onto the CCD for an integration time of only 5 s. In contrast, a cathodoluminescence scan of the same size takes 1050 s for a step size of 120 nm, corresponding to one pixel on the CCD camera. In other words, the whitelight imaging technique is a factor of 210 faster than cathodoluminescence imaging. Compared to confocal laser scanning with the same step size, whitelight imaging is still a factor of 140 faster if one considers that two consecutive scans need to be recorded.

During the course of this work, all three imaging methods were used to pre-select quantum dot–nanowire pairs, with different proportions. The number of nanosystems which have been identified as promising and were tested for functionality is 15 for cathodoluminescence and at least 42 for confocal laser scanning. For the imaging method, the number of investigated nanosystems was not monitored but should exceed the numbers of the other methods due to the fast screening times. Note that complete data sets, including cathodoluminescence/SEM, confocal photoluminescence/reflection and waveguide propagation images are recorded only for a subset of these nanosystems.

4.4.3 *Waveguide transmission*

It is instructive to test the waveguide transmission with a focused laser before turning to the quantum dot coupling itself. If the propagation length is too small, no SPP emission at the nanowire end would be observable, even though a quantum dot is coupled to the nanowire. For the waveguide transmission experiment, a modelocked Titanium-Sapphire laser at a wavelength of $\lambda = 795\,\mathrm{nm}$ is focused on one of the wire ends, which is shown for an exemplary nanowire in Figure 4.6a. If the polarization of the laser is parallel to the nanowire axis, out-coupling of SPPs at the other wire end is observed. For perpendicular polarization, no surface plasmons propagate along the nanowire. Both the direct laser reflection at one wire end and the out-coupled SPP emission at the other wire end is imaged onto the CCD camera. The waveguide transmission, defined as the SPP emission intensity divided by the laser reflection intensity, is measured for several silver nanowires, with the wire lengths taken from SEM images.

An exponential fit to the transmission data in Figure 4.6b yields a $1/e$-propagation length of $L_p \approx 1.0\,\mu\mathrm{m}$, which is less than half of the value expected from simulations

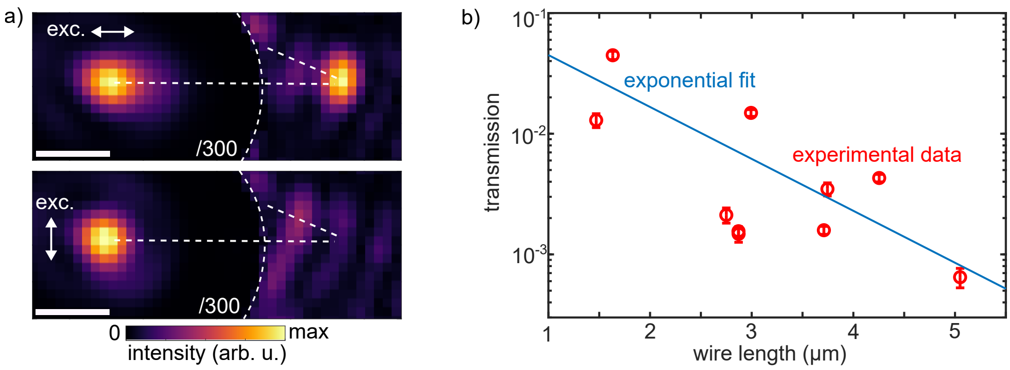

Figure 4.6: **Waveguide transmission for excitation with a focused Titanium-Sapphire laser.** (a) Camera image of an exemplary silver nanowire for parallel and perpendicular polarization of the excitation laser with respect to the nanowire axis. The scale bar is 1 µm. (b) Measured waveguide transmission (red circles) for several nanowires and exponential fit (blue line), suggesting a propagation length of $L_p \approx 1.0\,\mu\mathrm{m}$.

(compare Figure 4.3b). The deviation can be explained by material imperfections and possibly remaining PVP surfactant at the nanowire surface, which has been neglected in the simulation. It should be noted that the fit uncertainty of the propagation length is large due to a significant spread of the data points. This might be caused by small variations of the exact shape of the laser focus, which influence the laser coupling efficiency. Furthermore, the lateral position of the laser with respect to the nanowire end might vary slightly between the different wires. In contrast to laser coupling, the quantum dot coupling in the next section 4.5 is less sensitive to the exact focusing conditions since the laser only generates electron-hole pairs in the environment of the quantum dot.

4.5 DEMONSTRATION OF INTERMEDIATE FIELD COUPLING

In this section, intermediate field coupling is demonstrated by launching propagating SPPs in a silver nanowire via the photoluminescence of a single epitaxial quantum dot. Figure 4.7 depicts two quantum dot–nanowire systems, which are investigated using the complementary detection methods described in the previous section. For system no. 1, the cathodoluminescence image in Figure 4.7a reveals a lateral quantum dot position $(x_{qd}, y_{qd}) = (77 \pm 12\,\mathrm{nm}, 685 \pm 26\,\mathrm{nm})$, obtained by fitting a two-dimensional Gaussian profile to the cathodoluminescence emission spot. A constant offset takes the large background of the GaAs bandgap and the wetting layer emission into account. The coordinate system is defined such that the x-axis is perpendicular, and the y-axis is parallel to the wire, starting from the wire end which is closer to the quantum dot. The uncertainty in x_{qd} (y_{qd}) is composed of the fit uncertainty and the uncertainty of the nanowire center (end) determination. For comparison, a room-temperature SEM image is added as an inset since the low temperatures in the cathodoluminescence setup can reduce the signal contrast due to contaminations, as discussed in section 4.4.2. For system no. 2 in Figure 4.7d, the SEM contrast is even worse for the same reason. Nevertheless, the relative quantum dot position can be accurately determined to $(x_{qd}, y_{qd}) = (8 \pm 11\,\mathrm{nm}, 593 \pm 25\,\mathrm{nm})$ with respect to the close wire end. Later, these positions will be entered into a model that describes the experimentally observed coupling efficiency.

In principle, the quantum dot launches SPPs in the nanowire via cathodoluminescence. However, in the electron beam scanning experiment, it is not possible to distinguish between direct quantum dot emission and remote SPP emission at the nanowire end due to lacking spatial resolution in the detection path. Therefore, the all-optical microscope setup (compare section 3.2.2) is used for the demonstration of intermediate field coupling. In order to identify the nanosystem in the optical microscope, the sample is mapped by confocal laser scans in reflection and photoluminescence, as shown in Figure 4.7b for system no. 1 and in Figure 4.7e for system no. 2. The nanowire outline that is known from the SEM image is drawn as the dashed line in the optical image, respectively. Since this measurement serves only to identify the nanowires, slight sample drifts during the laser scans can be neglected.

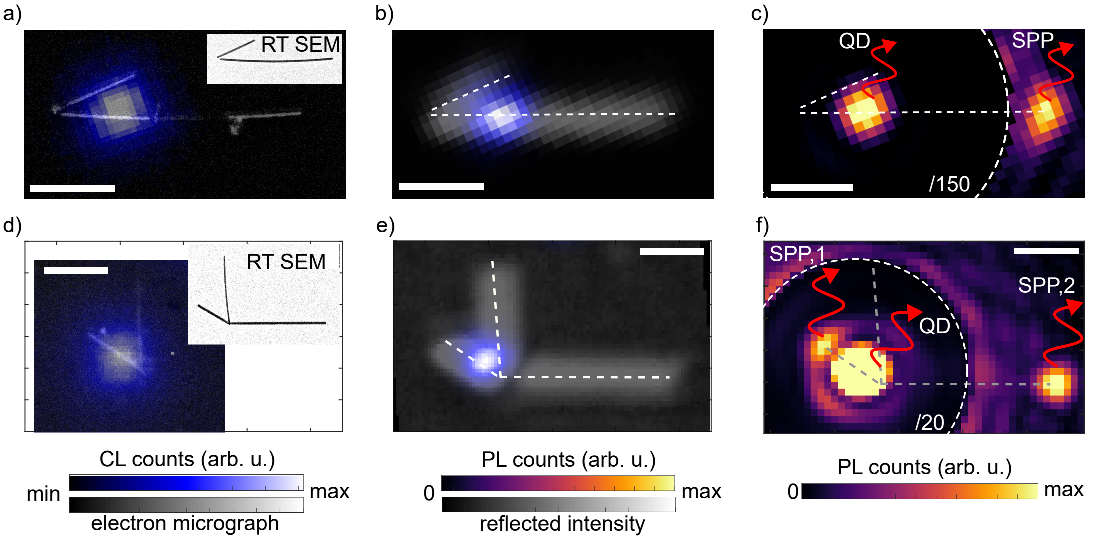

Figure 4.7: **Two quantum dot–nanowire systems that exhibit intermediate field coupling investigated by complementary methods.** (a-c) Coupled nanosystem no. 1. (d-f) Coupled nanosystem no. 2. (a, d) Cathodoluminescence images with overlaid electron micrograph acquired by raster-scanning the electron beam. The inset shows a room-temperature SEM image of the same nanowire, respectively. (b, e) Photoluminescence images with overlaid reflection images of the nanostructure acquired by confocal laser scanning. (c, f) Camera images that show the launching of a SPP for stationary excitation of the quantum dot. To increase the visibility of the SPP emission, the area around the quantum dot is software-attenuated by a factor of 150 and 20, respectively. All scale bars are 1 µm.

Finally, intermediate field coupling is demonstrated in Figure 4.7c and Figure 4.7f by launching and detecting SPPs: Here, the excitation laser is stationary focused on the quantum dot, while the luminescence of the surrounding sample area is imaged onto the CCD camera. Clear emission from the SPP, launched by the coupled quantum dot and scattered at the nanowire end, can be observed. To increase the visibility of the SPP emission, the area around the quantum dot is software-attenuated by a factor of 150 for system no. 1 and 20 for system no. 2. It can be ruled out from the cathodo- and photoluminescence images that the origin of the emission is another quantum dot, which is located at the far nanowire end by chance. Furthermore, the launching of SPPs directly by the excitation laser can be excluded since the laser is blocked by a bandpass with an attenuation of 10^{-7} at the excitation wavelength $\lambda = 635\,\text{nm}$. For further confirmation, photoluminescence spectra for the direct quantum emission and the out-coupled photons of the SPP are found to be identical (see Appendix A.2). Emission from the close wire end is expected but competes with the airy-patterned background of the direct quantum emission as can be seen for nanosystem no. 2. This will be discussed in greater detail in section 4.6.2. There is another short wire that does not show any emission, probably due to the sharp angle it forms with the coupled wire.

Complete data sets were acquired for a total of nine quantum dot–nanowire systems. Such a data set includes cathodoluminescence/SEM, confocal photoluminescence/re-

	nanosystem no.								
	1	2	3	4	5	6	7	8	9
NW diameter (nm)	48	53	53	62	42	60	63	50	45
NW length (µm)	2.87	3.75	4.25	1.63	2.87	2.61	5.05	3.71	3.27
QD burial depth (nm)	15	30	40	40	40	30	30	30	30
IC1 thickness (nm)	131	162	136	136	136	162	162	162	162
x_{qd} (nm)	77	8	48	115	62	162	118	4	143
y_{qd} (nm)	685	593	1290	6	698	807	228	390	505
I_{spp}/I_{qd} $(\cdot 10^{-3})$	5.4	4.2	1.6	17.7	2.1	5.0	0.22	0.26	0.85
$\eta_{in,exp}$ (%)	0.66	1.68	0.49	1.21	0.24	0.41	0.63	0.13	0.22
$\eta_{in,exp,shift}$ (%)	0.85	1.68	0.54	2.18	0.29	1.34	1.19	0.13	0.55

Table 4.1: **Summary of the experimental quantities for nine quantum dot–nanowire systems.** Nanowire (NW) dimensions and relative quantum dot (QD) positions x_{qd} and y_{qd} are obtained from cathodoluminescence/SEM data. The emission ratio I_{spp}/I_{qd} is extracted from the waveguide propagation images. The determination of the experimental coupling efficiency $\eta_{in,exp}$ and the corrected coupling efficiency $\eta_{in,exp,shift}$ is described in section 4.6.1 and section 4.7, respectively. Quantum dot burial depth (nominal value) and IC1 film thickness (measured by AFM) are given for the sake of completeness.

flection scans, waveguide propagation images, and photoluminescence spectra. For three of these nanosystems, complete data sets are given in Appendix A.2. An overview of the experimental quantities extracted from these measurements is given in Table 4.1. The nanowire dimensions and relative quantum positions are obtained from cathodoluminescence data. The quantum dot burial depth is the nominal value from the sample growth protocols, while the IC1 thickness is given from AFM measurements. From the waveguide propagation images, the out-coupled SPP intensity I_{spp} and the direct quantum emission intensity I_{qd} are determined via two-dimensional Gaussian fits at the respective emission spots. For most of the systems, the background of the direct quantum emission is not negligible compared to the SPP emission. This is addressed by allowing the Gaussian to have a constant offset and ellipticity. The intensity ratio I_{spp}/I_{qd} is then obtained by integrating the two-dimensional Gaussian profiles of the SPP and the quantum dot emission spots. According to Table 4.1, the emission ratio I_{spp}/I_{qd} differs significantly (up to a factor of 80) between the nanosystems. In the next section, the actual coupling efficiency $\eta_{in,exp}$ for these nanosystems will be extracted from the measurements and the large variation between the nanosystems will be explained by an interference effect near a waveguide end.

It should be noted that a subset of the investigated nanosystems does not exhibit clear emission at either of the wire ends. Nevertheless, these nanosystems are included in the interference model that will be presented in section 4.7. Their data sets are processed identically to the "functional" nanosystems, and a Gaussian is fitted at the nanowire end where the out-coupling is expected. The resulting emission ratio I_{spp}/I_{qd} is declared as an upper limit for the unknown true signal, which is accounted for by an uncertainty bar reaching zero coupling efficiency in Figure 4.11c. As can be seen in the same figure, the x_{qd}-corrected coupling efficiency $\eta_{in,exp,shift}$ of these data points is in agreement with the model. In other words, the vanishing emission is explained by a low coupling efficiency at the respective quantum dot position, either due to a large lateral offset from the wire axis or due to a destructive interference of the SPPs.

4.6 EXPERIMENTAL COUPLING EFFICIENCY

In this section, the experimental coupling efficiency $\eta_{in,exp}$ is derived from the waveguide propagation images (Figure 4.7c, f). Therefore, a few assumptions need to be made on the nanosystem, which are described in section 4.6.1. Afterwards, a brief discussion on the signal-to-background ratio and how it is influenced by the coupling efficiency and the quantum dot–wire end distance follows in section 4.6.2.

4.6.1 *Extraction of the coupling efficiency*

It is instructive to start by breaking down the intensity ratio I_{spp}/I_{qd} of direct quantum dot emission I_{qd} and remote SPP emission I_{spp}. Throughout the discussion, it is assumed that only a small fraction of the total quantum dot emission I_0 is coupled into the plasmonic mode so that I_0 is unaffected by the nanowire. This is justified by the simulated coupling efficiency $\eta_{in,\mathrm{inf}} = 1.38\,\%$ for a quantum dot centered below an infinitely extended wire for a spacer thickness $t = 130\,\mathrm{nm}$ (see Figure 4.3). Considering that the detected photon rate at the wire end is given by the product of the incoupling efficiency η_{in}, propagation efficiency η_p, and out-coupling efficiency, as sketched in Figure 4.8, one can write

$$\frac{I_{spp}}{I_{qd}} = \frac{I_0 \eta_{in} \eta_p (1 - |r|^2) \eta_{spp,ff}}{I_0 \eta_{qd,ff}}, \tag{4.14}$$

with the field reflection amplitude r of the wire end, accounting for reflected plasmons that effectively reduce the number of out-coupled photons. Furthermore, different far field collection efficiencies of the surface plasmon $\eta_{spp,ff}$, and the quantum dot $\eta_{qd,ff}$ need to be taken into consideration. This allows to calculate back to the actual coupling efficiency

$$\eta_{in,exp} = \frac{I_{spp}/I_{qd}}{e^{-L/L_p}(1 - |r|^2)\frac{\eta_{spp,ff}}{\eta_{qd,ff}}}. \tag{4.15}$$

Here, L is the distance between the quantum dot and the far wire end, and L_p the propagation length of the plasmon. To finally obtain the coupling efficiency, three-dimensional numerical simulations (Comsol Multiphysics) are performed for the complex reflectivity $\tilde{r}$ of the nanowire termination and the far field collection efficiency ratio $\eta_{spp,ff}/\eta_{qd,ff}$.

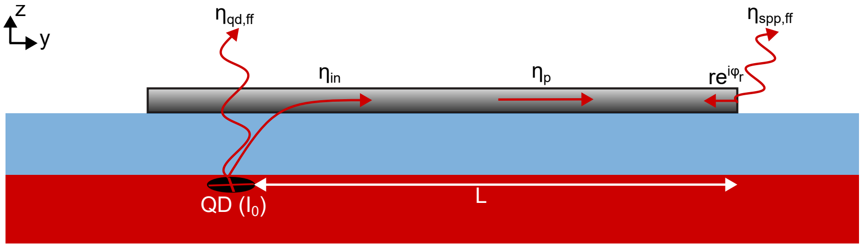

Figure 4.8: **Sketch of the coupling geometry, illustrating the relevant contributions to determine the experimental coupling efficiency η_{in}.**

The **complex reflection coefficient** $\tilde{r} = re^{i\phi_r}$ with the field reflection amplitude r and the reflection phase ϕ_r is retrieved from a model which is basically an extension of the two-dimensional model in Figure 4.3a along the waveguide direction; however, the nanowire terminates before the end of the computation window is reached. The three-dimensional model is excited by the waveguide's eigenmode in the xz-plane by applying the port function in Comsol. A cross-section through the port excitation model is shown in Figure 4.9a. The intensity distribution features fringes that arise from the reflection of surface plasmons at the wire termination. In order to determine the reflection coefficient, the simulated electric field is evaluated along a centered line cut (with respect to the nanowire axis) at $z_b = 30\,\text{nm}$. Now, the analytical intensity distribution for the semi-infinite wire (including reflection at the nanowire end)

$$|E(y)|^2 = \left| E_0 \left[e^{i\tilde{\beta}y} + e^{i\tilde{\beta}(y_0 - y)} \tilde{r} e^{i\tilde{\beta}y_0} \right] \right|^2 \tag{4.16}$$

is fitted to the simulated intensity distribution, as shown in Figure 4.9b. Here, E_0 denotes the initial amplitude of the mode, y is the coordinate along the propagation direction, $y_0 = 3\,\mu\text{m}$ is the position of the wire termination, and $\tilde{\beta} = k_0 \tilde{n}_{eff}$ is the complex propagation constant with the effective mode index $n_{eff} = 1.68 + 0.023i$ from the two-dimensional mode analysis. Finally, the analytical fit obtains a reflection amplitude $r = 0.647$ and a reflection phase $\phi_r = -1.89$.

The complex reflection coefficient of silver nanowires has been calculated [11, 90] and measured [91] by other groups. There is agreement that the reflection amplitude increases for smaller nanowire diameters due to an increasing wave vector mismatch with the far field [10]. However, the exact reflectivity values of silver nanowires with a diameter of around 50 nm span a rather large range $r = 0.6 - 0.98$, which is consistent with the simulation above. Regarding the reflection phase, the literature values $\phi_r = 45^\circ - 90^\circ$ differ substantially from our simulation. The difference might be due to different dielectric environments, namely the GaAs substrate, which has an influence on the reflection amplitude and phase, as well as details of the end facet, which are not known in the experiment [90].

The **far field collection efficiency** for the direct quantum dot emission, $\eta_{qd,ff}$, and the out-coupled SPP, $\eta_{spp,ff}$, differ substantially for the intermediate field sample geometry since the quantum mostly radiates into the high-index GaAs substrate due

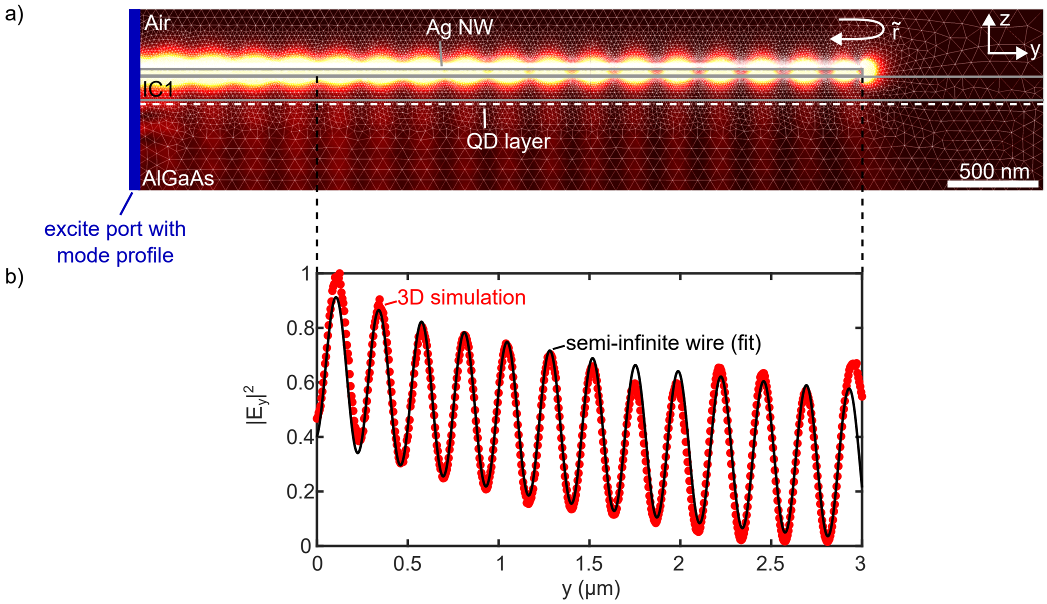

Figure 4.9: **Extraction of the complex reflection coefficient $\tilde{r}$ for the intermediate field coupling scheme.** (a) Three-dimensional model that is excited with the mode profile from Figure 4.3a via a port. Reflection at the waveguide termination leads to an interference pattern in the intensity. (b) Red dots: Simulated intensity from the port model in (a), evaluated at a centered line cut at $z_b = 30\,\text{nm}$. Black line: Fit using the analytical model for the semi-infinite wire, with the complex reflection coefficient as a free parameter.

to total internal reflection [92]. To estimate this, another three-dimensional simulation is performed: Both the quantum dot and the out-coupled SPP are approximated as dipole emitters, located 30 nm below and 155 nm above the semiconductor surface, respectively. The spacer layer thickness and the refractive indices are identical to the mode analysis in Figure 4.3a. By applying the RETOP package [93], the power fraction that is radiated into the upper half-space is computed for the respective dipole positions. Normalized to the total emitted power, one finds $\eta_{qd,ff} = 0.026$ for the quantum dot and $\eta_{spp,ff} = 0.434$ for the plasmon, or $\frac{\eta_{spp,ff}}{\eta_{qd,ff}} \approx 17$. This factor of 17 strongly increases the relative brightness of the SPP emission against the direct quantum dot emission and, therefore, helps to detect the weak out-coupling emission of the SPP.

With the reflection coefficient and the collection efficiencies determined from these simulations, one can finally compute the experimental coupling efficiency $\eta_{in,exp}$ for each nanosystem according to Equation 4.15. The propagation length for the propagation loss correction will be determined in section 4.7 by the interference model to $L_p = 0.86\,\mu\text{m}$. Using this value, the coupling efficiency $\eta_{in,exp}$ for each nanosystem is given in Table 4.1.

4.6.2 *Signal-to-background ratio*

As already mentioned before, remote SPP emission has to compete with direct quantum dot emission, which is the dominant background source for this type of measurement. This raises the question of how the signal-to-background ratio is affected by the wire length since a longer distance to the quantum dot reduces the background, but, at the same time, decreases the SPP intensity due to propagation losses. In this context, it is particularly interesting that for most of the nanosystems, SPP out-coupling is observed only from the far wire end, even though the emission at the near wire end – typically in a distance below 1 µm – should be resolvable in the microscope image. The competition between SPP emission and the background of the quantum dot emission can be easily understood by a cross-section through an exemplary uncoupled quantum dot emission spot, given by the red circles in Figure 4.10, which is fitted by an Airy function (black line). The quantum dot intensity distribution is compared to an exponential function (blue lines) that represents the expected SPP emission intensity (following Equation 4.15)

$$I_{spp}(y) = I_{qd}(0)\,\eta_{in,exp}(1-|r|^2)\frac{\eta_{spp,ff}}{\eta_{qd,ff}}e^{-y/L_p} \tag{4.17}$$

as a function of the distance y from the quantum dot. The quantum dot intensity $I_{qd}(0) = 1$ is normalized, while the other parameters $r = 0.65$, $L_p = 0.86\,\mu\text{m}$ and $\frac{\eta_{spp,ff}}{\eta_{qd,ff}} = 17$ are taken from section 4.6.1. For the coupling efficiency $\eta_{in,exp}$, the two nanosystems with the highest and the lowest efficiency, according to Table 4.1, are taken, respectively. For small distances to the quantum dot, the airy-patterned background dominates, even for the most efficiently coupled nanosystem, which is in agreement with the experimental observations. For the least efficiently coupled nanosystem, in contrast, the expected SPP emission intensity is smaller or comparable to the quantum dot background. Consequently, different coupling efficiencies shift

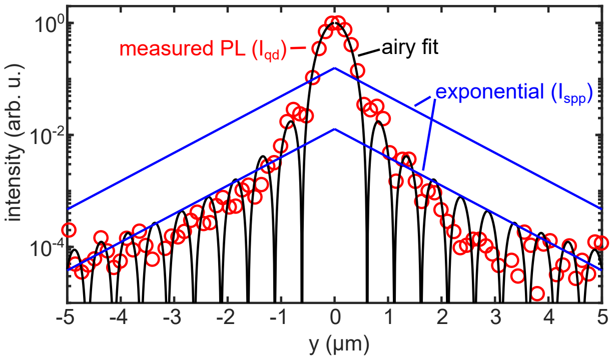

Figure 4.10: **SPP emission-to-quantum dot background as a function of the distance to the quantum dot.** Cross-section through an uncoupled quantum dot emission spot, imaged onto the CCD camera (red circles). An Airy function (black line) is fitted to the measured photoluminescence intensity and compared to two exponentials (blue lines), representing the expected SPP emission intensity I_{spp} after Equation 4.17 as a function of the distance from the emitter at $y = 0$, for the nanosystems with the highest and lowest coupling efficiency, respectively.

the exponential function against the background. This consideration is confirmed if one takes a look at the nanosystem with the highest coupling efficiency, which is system no. 2 in Table 4.1. The corresponding waveguide propagation image in Figure 4.7f features SPP emission also from the short wire end (SPP, 1), overlapping with the quantum dot's Airy pattern. At the far wire end (SPP, 2), the signal-to-background ratio is much higher. In contrast, the weaker coupled system no. 1 (Figure 4.7c) does not show any emission from the short wire end, as expected.

4.7 INTERFERENCE MODEL

In this section, a half-analytic interference model is developed to explain the variations in the observed coupling efficiencies. The interference of propagating surface plasmons is driven by reflections at the wire end: the small diameter of the silver nanowires leads to a significant reflectivity [10, 11], as discussed in section 4.6.1, even though the exact value of the reflection coefficient might vary between the nanosystems. Together with an expected propagation length L_p comparable to or longer than the typical distance y_{qd} from the quantum dot to the near wire end, a substantial modulation of the local coupling efficiency is expected due to an interference

$$|E|^2 = |E_{\mathrm{dir}} + E_{\mathrm{refl}}|^2 \tag{4.18}$$

of the direct surface plasmon E_{dir} and the reflected surface plasmon E_{refl}. This configuration is sketched in Figure 4.11a. In certain cases, both fields can interfere destructively, and no net coupling would be observed, even though the emitter is close to the nanowire.

In most nanosystems, the quantum dot is much closer ($y_{qd} \lesssim 1\,\mu\mathrm{m}$, compare Table 4.1) to one wire end than to the other. Consequently, the SPP amplitude has already decayed significantly at the far wire end, so that reflections from that wire end can be neglected. In other words, a semi-infinite wire is assumed in order to model the position-dependent coupling efficiency in the sample plane (xy). Therefore, reciprocity is assumed, meaning that the amplitude of the waveguide mode is proportional to the coupling strength of a hypothetical emitter to this mode at a certain location. In the next step, the mode profile in the xz-plane (shown in Figure 4.3a) is evaluated at the burial depth $z_b = 30\,\mathrm{nm}$, yielding $\boldsymbol{E}^{mode}(x)$. This mode profile is now developed along the y-direction by interfering the direct wave and the reflected wave, both propagating with an effective mode index $\tilde{n}_{\mathrm{eff}}$. In total, one obtains the coupling efficiency in the xy-plane

$$\eta_{\mathrm{in,sim}}(x,y) = \sum_j \left| E_j^{mode}(x)\left(1 + \tilde{r}\, e^{2\,i\,k_0\,\tilde{n}_{\mathrm{eff}}\,y}\right)\right|^2 \tag{4.19}$$

by an incoherent summation over the dipole moment contributions in $j = x, y$, assuming parallel and perpendicular excitonic orientations with respect to the wire axis. The resulting coupling efficiency map is shown in Figure 4.11b and features the expected oscillations due to interference. With increasing distance from the near wire end, the modulation of the coupling efficiency decreases since the amplitudes

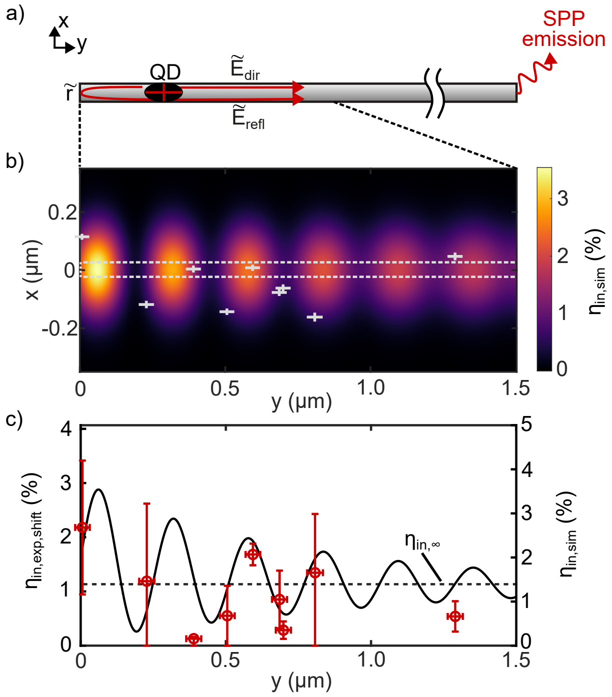

Figure 4.11: **Interference of surface plasmons, caused by reflections at the wire end, explains the variations of the coupling efficiency for nine quantum dot–nanowire systems.** (a) Sketch depicting the interference of direct and reflected SPPs, arising from a non-zero reflectivity at the nanowire end. (b) Simulated map of the coupling efficiency in the sample plane at the burial depth $z_b = 30\,\text{nm}$. The lateral quantum dot positions, obtained from cathodoluminescence images, are displayed by gray crosses; the position uncertainty is given by the size of the crosses. The dashed horizontal lines represent the nanowire width. (c) Simulated coupling efficiency (black line, line cut through the model in (b) along the nanowire axis), and experimental coupling efficiency (red circles), corrected for the offset x_{qd} with respect to the nanowire axis according to Equation 4.20. The dashed line indicates the coupling efficiency $\eta_{in,\infty} = 1.38\,\%$ for a quantum dot that is centered below an infinitely extended wire (see Figure 4.3).

of E_{dir} and E_{refl} diverge. Although measured at different waveguide systems, all nine investigated structures are projected in this map by overlaying the near nanowire ends. The quantum dot positions, as measured by cathodoluminescence imaging, are indicated by the gray crosses, the size of which indicates the position accuracy. This already suggests strong fluctuations in their coupling efficiency.

To compare the interference model with the experimental data of the coupling efficiency, it is more convenient to use a one-dimensional data set. As the mode profile along the x-axis is known, the experimental coupling efficiency (Equation 4.15) is corrected by shifting the measured quantum dot positions to below the waveguide at $x = 0\,\text{nm}$ via

$$\eta_{\text{in,exp,shift}} = \eta_{\text{in,exp}} \frac{\sum_j |E_j^{mode}(0)|^2}{\sum_j |E_j^{mode}(x_{qd})|^2}, \tag{4.20}$$

for the offset x_{qd} of the respective quantum dot through the mode profile $E^{mode}(x)$. This corresponds to the coupling efficiency that would be observed if the quantum dot had been perfectly centered below the waveguide. Finally, the interference model at $x = 0\,\mathrm{nm}$ is fitted to these values in Figure 4.11c by varying the effective mode index, the propagation length, and an overall scaling parameter. The reflection amplitude $r = 0.65$ and phase $\phi_r = -\pi/2$ as well as the air-sided far-field collection efficiency ratio $\eta_{spp,ff}/\eta_{qd,ff} = 17$ are fixed. The best fit is obtained with a mode index of $n_{\mathrm{eff}} = 1.53$, a propagation length $L_p = 0.86\,\mathrm{\mu m}$, and a scaling factor of 1.23, included in the axes in Figure 4.11c. These are the values already used to plot Figure 4.11b.

There is good agreement between the interference model and the corrected coupling efficiency, even though not all individual variations of the nanosystems are being accounted for. Differences in geometry parameters, for example, wire diameter, burial depth, or IC1 thickness, can shift the data points somewhat. In particular, imperfections such as slightly bent wires or small kinks can result in additional losses due to reflections or far field scattering. However, additional scattering events are not observed in the far field propagation images, so that wire imperfections are neglected. The error bars of the coupling efficiency $\eta_{\mathrm{in,exp,shift}}$ consist of the uncertainty of I_{spp}/I_{qd}, stemming from the two-dimensional Gaussian fits, and the uncertainty of the x_{qd}-correction, originating from the uncertainty in the lateral quantum dot position, which is included via propagation of uncertainty. The uncertainty in the propagation loss correction due to the uncertainty in the wire length is about a factor 100 smaller and therefore neglected.

Another relevant source of uncertainty is the unknown dipole moment orientation, which is significant for quantum dots far away from the nanowire axis. The influence of the dipole moment orientations on the coupling efficiency was already quantified in section 4.2.2 by Equation 4.9. Using the model parameters from above, the spatial dependence of the change in coupling efficiency is shown in Figure 4.12 for $\theta = 45°$, the angle at which the cross-term in Equation 4.9 has its maximum. It can be seen that the orientation of the dipole moment is negligible near the nanowire axis at $x = 0$. Right below the nanowire, the electric field points in the propagation direction, and the E_x-component is zero so that the cross-term vanishes. In contrast, for quantum dots far away from the nanowire axis, the coupling efficiency can be modified significantly, up to $\pm 30\,\%$ at the "worst-case" angle $\theta = 45°$. Since the sign of the electric field is unknown, the absolute value of this hypothetical "worst-case" modification is taken as an additional uncertainty for the coupling efficiency of each quantum dot in Figure 4.11c. This is the reason why the error bars in Figure 4.11c are large for quantum dots far away from the wire axis.

Even though the model is inflicted by experimental uncertainties, the fit parameters consistently lie in a reasonable range. The mode index $n_{\mathrm{eff}} = 1.53$ is slightly smaller than the expected value $n_{\mathrm{eff,sim}} = 1.68$ from the mode analysis (see Figure 4.2b). Here, one has to consider that the exact value of the mode index also depends on the details

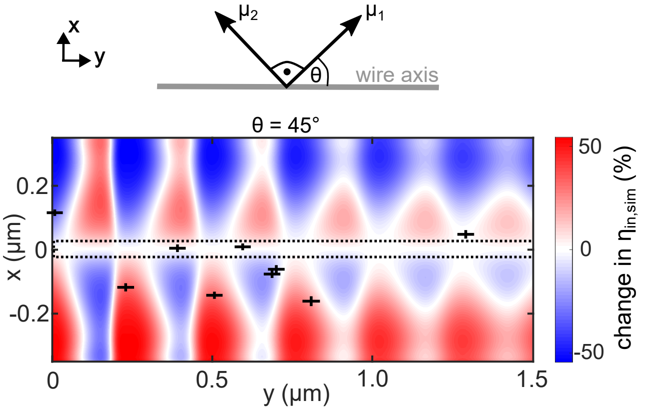

Figure 4.12: **Spatially resolved change in coupling efficiency as a function of the dipole moment orientation.** A hypothetical angle of $\theta = 45°$ between the dipole axes ($\boldsymbol{\mu_1}$ and $\boldsymbol{\mu_2}$) and the nanowire axis is assumed. At this angle, the change in coupling efficiency is at its maximum, according to Equation 4.9. The black crosses indicate the projected quantum dot positions, and the dashed lines correspond to the nanowire width.

of the chosen geometry in the simulation. The propagation length $L_p = 0.86\,\mu\text{m}$ from the interference model is about three times smaller than the propagation length $L_{p,sim} = 2.3\,\mu\text{m}$ from the mode analysis but consistent with the measured propagation length $L_{p,exp} \approx 1\,\mu\text{m}$ (see section 4.4.3), supporting the hypothesis of material imperfections increasing the SPP attenuation. The overall scaling parameter of 1.23 close to 1 indicates that all major contributions are included in the model. It should be mentioned that the scope of the experiment is not to measure the effective mode index or the reflection coefficient of silver nanowires. Therefore, one would need more data points, which could be accomplished by controlled positioning of the nanowires relative to the quantum dots, as the random sample arrangement as applied here requires time-consuming pre-selection. The goal of this experiment is rather to demonstrate and validate the intermediate field coupling scheme by applying a simple, comprehensive model, even though it does not account for the slightly different sample geometries. Therefore, one would need to model the exact sample structures in extensive three-dimensional numerical simulations.

The interference model in Figure 4.11c implies a significant enhancement of the waveguide coupling rate towards the near wire end if compared to the infinitely extended waveguide's coupling rate $\eta_{in,\infty} = 1.38\,\%$. In principle, the coupling rate can be increased up to a factor of 4 for a reflection coefficient $r = 1$, which would result in a coupling efficiency of 5.5 %. This is still small compared to systems based on different emitters, for which coupling efficiencies exceeding 80 % are reported [83], and also less efficient than the indirect mode conversion scheme by *Wu et al.* [22] for similar quantum dots, where the coupling efficiency is 25 %. The total efficiency of the device could be further enhanced by optimizing the photon out-coupling rate, for example, by constructive interference of substrate reflections with direct SPP emission [22]. Another option is perfect impedance matching, which suppresses plasmon reflections completely [94]. This could be accomplished by focused ion beam milling at the far waveguide end, yielding an out-coupling efficiency close to unity.

4.8 SUMMARY

In summary, the coupling of single epitaxial GaAs quantum dots to silver nanowires via the intermediate field has been demonstrated by launching surface plasmons through quantum dot photoluminescence. This was achieved by carefully trading off incoupling and propagation efficiency, utilizing a planar dielectric spacer with a thickness of around 130 nm. The low refractive index of the dielectric overcomes the dramatic propagation losses that would otherwise occur for plasmons interfaced with high-index semiconductors. Fast and precise sample screening methods, including confocal laser scanning and mixed-contrast imaging, have been applied in order to localize potentially coupled nanostructures, and a total of nine quantum dot–nanowire systems are studied by complementary imaging methods. Simultaneous imaging of quantum dots and silver nanowires via low-temperature cathodoluminescence allowed to determine the relative positions of dots and wires with an accuracy of less than 30 nm. Using this information, the observed photoluminescence coupling efficiencies, which are on the order of 1 %, can be explained by a simple half-analytical model. The model is based on numerically computed mode profiles and treats the nanosystem as a semi-infinite wire to include reflections of propagating surface plasmons at the near wire end. Subsequent interference of direct and reflected plasmons spatially modulates the coupling efficiency. By taking the known quantum dot positions into account, the interference model explains the observed variations in the coupling efficiency. Furthermore, reasonable fit outcomes are provided, which additionally suggest a coupling rate enhancement of up to four close to the wire end.

The presented numerical and experimental findings extend the field of plasmonics, which is centered around optical near fields, by exploiting the intermediate field component of the quantum dot emission. Naturally, the coupling efficiency is small compared to other works using different emitters. But for true quantum operation, Fourier-limited single-photons are needed, which are feasible with epitaxial quantum dots coupled via the intermediate field. The intermediate field coupling scheme features distinct advantages over other coupling schemes: the waveguide–emitter alignment requirement is on the order of 100 nm instead of 10 nm for most plasmonic applications. This is a direct consequence of the far field contribution that facilitates the coupling. Furthermore, no nanostructuring processes in the dielectric vicinity of the quantum dot are required for intermediate field coupling, which often degrade its (quantum) optical properties. Finally, the weak depth dependence (see Figure 4.3a) of the coupling efficiency will allow the use of more deeply buried dots, which feature the narrowest line widths. Put this together, a Fourier-limited single plasmon source, which has not been reported so far, is in reach via intermediate field coupling. One application, for example, could be an electrically pumped source of single plasmons by embedding the quantum dots into a diode structure [95].

5

EFFICIENT SINGLE-PLASMON GENERATION BY INTEGRATED QUANTUM DOTS: SIMULATIONS

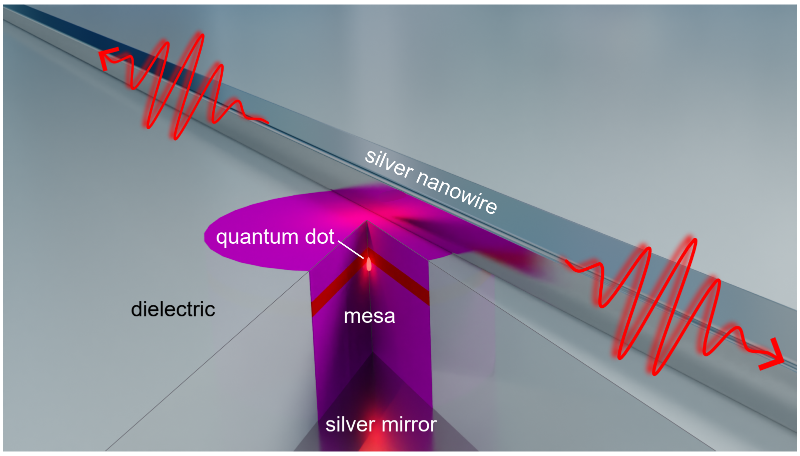

A quantum plasmonic nanocircuit connects multiple single photon sources and detectors with each other through linear optical elements, implemented on the nanoscale via plasmonic waveguides [45]. Epitaxially grown quantum dots serve as excellent sources of single photons for the past two decades [17, 35, 96, 97]. However, their coupling to plasmonic waveguides is relatively unexplored due to the intrinsic losses of surface plasmons at interfaces involving high-index semiconductor materials. Towards the far-reaching goal of an operating quantum plasmonic circuit, several hurdles need to be overcome. A central challenge is the efficient coupling of the quantum emitter to the waveguide, so that in the ideal case every generated photon is channeled into the nanocircuit. Another crucial aspect, which has already been mentioned, is minimizing the attenuation inside the waveguide. Thirdly, the overall emission rate should be enhanced to perform more operations in a certain time interval. The goal of this chapter is the design of a nanostructure that fulfills the above prerequisites. Based on fundamental considerations and finite element simulations, it is shown that a highly efficient nanocircuit can be constructed from the interaction of dielectric and plasmonic modes. Although this chapter is primarily theoretical, care is taken to ensure the proposed nanosystem can be realized with modern nanofabrication techniques and that the explored parameter space remains feasible.

In this chapter, the performance of a plasmonic nanocircuit utilizing the integration of single GaAs quantum dots into mesa structures is numerically analyzed.

A straightforward motivation for the mesa-based coupling scheme is given in section 5.1. From a two-dimensional waveguide mode analysis, the influence of the substrate material is discussed in section 5.2.1. The application of a three-dimensional finite element model in section 5.2.2 finds the mesa geometry to be crucial for the efficiency of the waveguide coupling. The influence of the mesa geometry on the dipole emission rate in the absence of a waveguide is analyzed in greater detail in section 5.3. Finally, these findings are exploited in order to design a highly efficient nanocircuit in section 5.4.

5.1 MOTIVATION OF THE MESA-BASED COUPLING APPROACH

The most common method for achieving efficient coupling of emitters to plasmonic waveguides is to bring them into close proximity. This approach has been successfully demonstrated with various emitters, such as colloidal nanocrystals [98, 99], nitrogen-vacancy centers in diamond [83], and molecules [84]. However, when dealing with epitaxial GaAs quantum dots that are grown into a semiconductor crystal, this presents immediate restrictions. Such quantum dots extend laterally by several tens of nanometers [33], making direct coupling to waveguides from the side very challenging. Although the quantum dots extend vertically only by a few nanometers, a capping layer is essential to ensure quantum confinement. Near-surface quantum dots grown with capping layers as thin as 15 nm overcome this problem, even though their optical properties are somewhat compromised [42, 100].

Thus, it seems straightforward to place a waveguide directly on top of the semiconductor surface, which contains near-surface quantum dots, as illustrated in Figure 5.1a. However, surface plasmons at metal-semiconductor interfaces experience dramatic radiative and Ohmic losses, as discussed in section 2.2.1. If nanowires are used, the propagation losses are even worse due to the confined electric fields (see again section 2.2.2). In this case, propagation lengths of less than a micrometer are expected from simulations, clearly insufficient for a nanocircuit. By applying a dielectric with a smaller real part of the refractive index, the propagation length can be enhanced significantly. This intermediate field coupling has been demonstrated in chapter 4 both experimentally and computationally, and is sketched in Figure 5.1b. By optimizing the film thickness, a balance of propagation and coupling efficiency is found, and coupling is observed even though the distance between the waveguide and the dot is large. However, the coupling efficiency on the order of 1 % is still low. Consequently, other coupling schemes are necessary. The probably most straightforward approach, which is the main idea of this chapter, is sketched in Figure 5.1c: An individual quantum dot is integrated into a mesa structure by etching the surrounding semiconductor material. Afterwards, the missing material is filled up to obtain a planar surface again. Finally, the waveguide is placed on top of the mesa structure. The final structure promises two main advantages over the configurations in Figure 5.1a and Figure 5.1b: On the one hand, there is a small distance between the quantum dot and the waveguide, a necessity for high coupling efficiency. On the other hand,

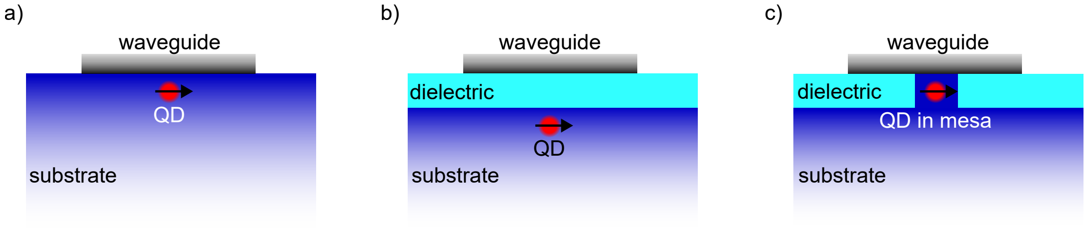

Figure 5.1: **Sketch of three basic geometries for the coupling of an epitaxial quantum dot and a plasmonic waveguide.** (a) Direct coupling. (b) Coupling through a dielectric spacer layer (*intermediate field coupling*). (c) Coupling through a mesa structure, which is planarized by a dielectric (*mesa-based coupling*).

propagation losses are minimized due to the dielectric spacer which surrounds the mesa.

Of course, other coupling schemes are possible. For example, one could spatially modify the dielectric layer in Figure 5.1b in such a way that it vanishes at the position of the quantum dot. This was accomplished via greyscale photolithography in the master thesis of Julian Alin [101] and promises to increase the coupling efficiency while maintaining good propagation. However, numerical simulations performed by master student Tim Pfadenhauer [102] show that the gain in coupling efficiency is moderate, while the resulting bend of the nanowire adds another loss channel. The only published work that accomplishes the coupling of single epitaxially grown quantum dots to nanoscale plasmonic waveguides uses a different approach. *Wu et al.* [22] incorporated the quantum dot in an AlGaAs bar acting as a dielectric waveguide, which is tapered at its end in order to convert the dielectric mode into a plasmonic mode of a two-wire transmission line. Even though the coupling efficiency of about 25 % is impressive, the mode conversion poses inherent losses, and the dielectric coupling does not feature any Purcell enhancement. Since the mesa configuration (Figure 5.1c) is considered the most promising approach, numerical simulations for such a geometry are performed in the next section.

5.2 PLASMONIC WAVEGUIDES ON TOP OF SEMICONDUCTOR MESA STRUCTURES

In this section, the finite element method is used to simulate plasmonic modes for mesa–waveguide hybrid structures. At first, a two-dimensional mode analysis is used to gain a basic understanding of plasmonic modes in infinitely extended mesa–waveguide structures. Afterwards, three-dimensional simulations are performed in order to evaluate the influence of finite length mesa. Particular attention is given to the choice of substrate, which is a central degree of freedom for the design of plasmonic nanocircuits. For example, *Wu et al.* [22] accomplished to detach a thin AlGaAs membrane containing GaAs quantum dots from its GaAs substrate and subsequently transferred it to a new substrate (in this case, a silicon wafer with silicon oxide capping). The lower refractive index of the underlying silicon oxide not only benefits the propagation of surface plasmons along the two-wire transmission line but also facilitates constructive interference of the SPP emission with substrate reflections.

5.2.1 *Waveguide modes in infinitely extended structures*

In order to obtain a general understanding of the mesa–waveguide structure, the two-dimensional mode solver of Comsol Multiphysics is used. By doing so, infinitely extended waveguides along the propagation direction (y) are assumed, and the modal fields in the xz-plane are computed. The investigated geometry consists of a silver nanowire with a diameter of 50 nm on top of an AlGaAs bar with a height of 80 nm and a width of 300 nm. The dimensions of the AlGaAs bar are taken from [22]. The mode profiles depend heavily on the choice of substrate. Therefore, three different materials are selected: The high-index dielectric AlGaAs ($n_{AlGaAs} = 3.44$), a glass-like low-index dielectric ($n_{glass} = 1.4$), and silver ($n_{Ag} = 0.035 + 5.49i$). The wavelength $\lambda = 790\,\text{nm}$ is the emission wavelength of the GaAs quantum dots. It is assumed that the transition dipole moments of the hypothetical emitter point along the x- and y-axes, i.e., parallel and perpendicular to the waveguide. The decay rate is normalized to the emission of a dipole in homogeneous AlGaAs and spatially resolved in the mode profiles in Figures 5.2a-c.

If the substrate is AlGaAs and, therefore, the same material as the mesa, a leaky mode is obtained (see Figure 5.2a). This is apparent from the low real part of the effective mode index $n_{eff} = 1.72$ and the small propagation length of $L_p = 0.68\,\mu\text{m}$. The radiation is in the direction of the substrate and can be clearly seen in the mode profile. Another loss channel is given by Ohmic damping since the high refractive index of the semiconductor tends to push the bound fields into the lossy silver, as discussed in section 2.2.1. A different mode evolves if the high-index semiconductor substrate is replaced by a low-index glass substrate, as can be seen in Figure 5.2b. Now, the mode is fully bound to the waveguide structure. Obviously, this is a hybrid mode of both plasmonic and dielectric nature. The latter is apparent from the strong field contribution inside the AlGaAs bar, which is given by the fundamental dielectric TE mode. The effective mode index $n_{eff} = 2.21$ and the high propagation length of $L_p = 84\,\mu\text{m}$ reflect the low confinement and the low attenuation, a distinctive feature of dielectric waveguide modes. If the substrate is silver, another interesting mode is available, which is shown in Figure 5.2c. In this configuration, not only the nanowire supports a surface plasmon, but also the interface between the AlGaAs mesa and the silver backplane. This results in a truly plasmonic "sandwich" mode, which is completely bound to the waveguide structure, as can be seen from a high effective mode index of $n_{eff} = 3.64$ and a propagation length of $L_p = 2.1\,\mu\text{m}$. The latter is much smaller than the propagation length of the half-dielectric mode in Figure 5.2b but larger than the propagation length of the leaky mode in Figure 5.2a.

Figure 5.2d compares the normalized decay rates of the discussed waveguide modes along a vertical line (z-axis) through $x = 0\,\text{nm}$. The corresponding materials are added in the top panel of the graph in order to illustrate the respective waveguide

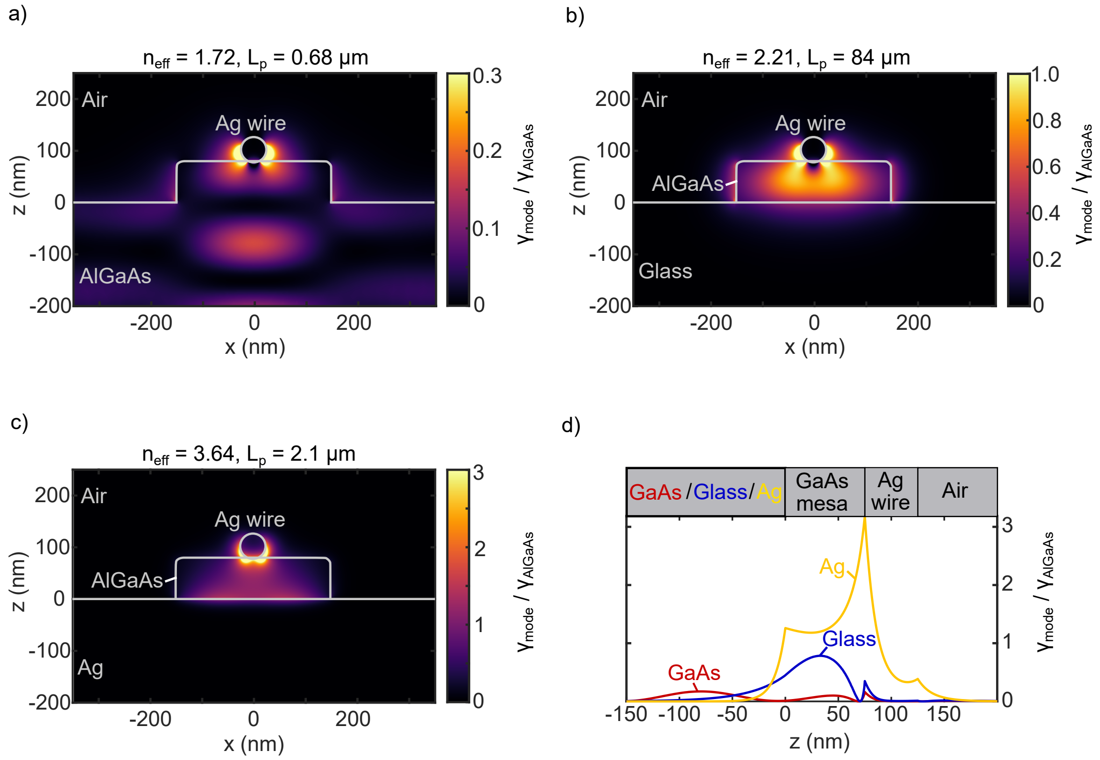

Figure 5.2: **Comparison of waveguide modes in three infinitely extended nanowire–mesa structures with varying substrates.** A silver nanowire with a diameter of 50 nm is on top of an AlGaAs bar with a height of 80 nm and a width of 300 nm. The modal decay rates are normalized to the emission in homogeneous AlGaAs for an emitter with dipole orientations along the x- and y-direction. (a) Leaky mode, which partly radiates into the AlGaAs substrate ($n_{AlGaAs} = 3.44$). (b) Hybrid plasmonic-dielectric mode, which is obtained for a glass substrate ($n_{Glass} = 1.4$). (c) Plasmonic sandwich mode with confined fields between the Ag wire and Ag substrate ($n_{Ag} = 0.035 + 5.49i$). (d) Normalized decay rates along the vertical z-axis at $x = 0$ nm, comparing the waveguide modes shown in (a-c).

structure. These values give the incoupling efficiency for a hypothetical emitter with in-plane (xy) dipole moments, located centrally with respect to the waveguide. The decay rates are given for all positions along the line cut, even though a quantum dot can only be placed inside the AlGaAs host and not in the other materials. The smallest coupling efficiency is obtained for the leaky mode with the AlGaAs substrate. For example, at $z = 45$ nm, corresponding to a burial depth of 35 nm, the decay rate $\gamma_{mode}/\gamma_{AlGaAs} = 0.10$ is small compared to a normalized decay rate of 1 for a dipole emitter in bulk AlGaAs. However, it is interesting that the coupling can be better if the emitter is buried more deeply in the AlGaAs; for example, at $z = -80$ nm, a modal decay rate of $\gamma_{mode}/\gamma_{AlGaAs} = 0.17$ is achieved. The reason for this is the presence of a far field contribution of the leaky waveguide mode. Nonetheless, the coupling efficiency of this mode is low compared to the other two modes: The dielectric–plasmonic hybrid mode features decay rates of up to $\gamma_{mode}/\gamma_{AlGaAs} = 0.78$ at $z = 32$ nm, mainly given by the dielectric coupling which dominates inside the AlGaAs. The plasmonic "sandwich" mode features its highest electric fields at the metal/dielectric interfaces, which decay with increasing distance from the boundary, as expected for a truly plasmonic mode. Therefore, there is a minimum of the decay rate inside the AlGaAs mesa; however, the normalized decay rate of $\gamma_{mode}/\gamma_{AlGaAs} = 1.25$ at $z = 40\,\text{nm}$ is still higher than the decay rates of the other two modes. This underlines the capability of plasmonics, not only to confine electric fields but also to guide these fields along a waveguide. Furthermore, there might be an additional Purcell enhancement, which increases the total emission rate of the emitter and can not be determined from a two-dimensional mode analysis.

From the above considerations, it follows that the choice of substrate is accompanied by a different suitability for an efficient single plasmon source. An AlGaAs substrate results in a leaky and, therefore, lossy mode with low coupling efficiency. A glass substrate supports a dielectric–plasmonic hybrid mode with small propagation losses and moderate coupling efficiency; however, the mode area is large, so that the advantage compared to a fully dielectric mode with practically no propagation losses is questionable. Due to the hybrid nature of this mode, a tapered AlGaAs waveguide could be used for a dielectric–plasmonic mode conversion, similar to *Wu et al.* [22], where the plasmonic two-wire transmission line is placed to the sides of the AlGaAs bar. More calculations would be necessary to compare the coupling, propagation, and mode conversion efficiencies of these two coupling schemes. Clearly, the most promising waveguide structure is obtained for a silver backplane. The resulting "sandwich" mode features the highest coupling efficiency and is well-confined between the plasmonic waveguide and the metal substrate. However, the propagation length of $L_p = 2.1\,\mu\text{m}$ is rather short; it is clear that the AlGaAs bar needs to be finite in length in order to reduce the propagation losses. Consequently, such a geometry with a finite AlGaAs mesa based on a silver backplane is investigated in the next section, utilizing three-dimensional finite element simulations. Additionally, this allows to compute the influence of the nanoscale environment on the overall emission rate via the Purcell factor.

5.2.2 *Mesa–waveguide hybrids with finite lengths*

For the three-dimensional simulations, the geometry of the mode analysis shown in Figure 5.2c is extended along the waveguide direction (y). While the silver nanowire runs into a perfectly matched layer and is, therefore, quasi-infinite in length, the AlGaAs bar is cut off at a certain length L_{AlGaAs}. The AlGaAs block is 80 nm in height and surrounded by a dielectric with $n = 1.4$ that matches the height of the AlGaAs block. The upper half-space is assumed to be air, while the substrate is silver. All the other parameters, including the AlGaAs width, the nanowire diameter, and the refractive indices, are chosen identically to section 5.2.1. Due to the symmetry of the geometry, it is sufficient to compute only a quarter of the full model (see Figure 5.3b, c). The symmetry planes are assigned perfect magnetic (electric) conductors for the plane that is parallel (perpendicular) to the orientation of the dipole moment.* A y-dipole is placed in the center of the AlGaAs block at a height of 50 nm above the silver/AlGaAs interface. A sphere with a radius of 10 nm that surrounds the emitter is used to obtain the Purcell factor F_p after normalization via the analytically known power of a dipole with the same dipole moment but located in bulk AlGaAs (see again section 2.3.2). The Purcell factor is shown in Figure 5.3a for different lengths L_{AlGaAs} of the AlGaAs block. It can be seen that there is strong Purcell enhancement for certain block lengths, with values up to $F_p = 10.7$ at $L_{AlGaAs} = 500\,\text{nm}$. For other block lengths, there is no Purcell enhancement; instead, there is slight suppression. This can be explained by standing waves inside the AlGaAs block: The periodicity in L_{AlGaAs} is in good agreement with multiples of the surface plasmon wavelength $\lambda_{SPP}/2 = \lambda/(2n_{eff})$, with the free-space wavelength $\lambda = 790\,\text{nm}$ and the real part of the effective mode index $n_{eff} = 3.64$ from the "sandwich" mode in Figure 5.2c. The multiples of $\lambda_{SPP}/2$ are indicated as dashed lines in Figure 5.3a and shifted by 65 nm, corresponding to a phase shift of 17°. This could be caused by an impedance mismatch of the waveguide mode at the AlGaAs/dielectric interface, since the silver nanowire supports a mode with a much longer effective wavelength if embedded in low-index dielectrics. Even though most of the maxima in the Purcell factor can be described with this single-mode interference, there are a few exceptions where F_p is small. This can be explained by the presence of at least one other mode, which is excited by the dipole and interferes with the "sandwich" mode.

Since the Purcell factor includes all present decay channels, it is not clear from the upper panel in Figure 5.3a where the emitted photons go. Of course, only photons that are converted into propagating surface plasmons along the silver nanowire are of interest. Therefore, the waveguide efficiency $\eta_{wg} = P_{wg}/P_{tot}$ is used, which measures the power throughput P_{wg} in the waveguide at a distance of 2 µm from the dipole (more detailed description in section 2.3.2). It is normalized to the total emitted dipole power P_{tot} for the corresponding length L_{AlGaAs} of the AlGaAs block and thus determines how many of the total photons emitted by the dipole are channeled into the waveguide. The waveguide efficiency – including both directions – is shown as the blue circles in the lower panel of Figure 5.3a. It is quite obvious that the waveguide efficiency is mostly inverse to the Purcell enhancement in the upper panel. For example, at $L_{AlGaAs} = 500\,\text{nm}$, where the total decay rate is maximum, there is a minimum in η_{wg}. Note that this does not necessarily mean that the absolute number of photons in the waveguide is small compared to other block lengths L_{AlGaAs}. It means that the device efficiency is low because of other decay channels. For the geometry here, the silver backplane poses a substantial alternative decay channel due to the excitation of surface plasmons at the AlGaAs/silver interface. This can be quantified by computing the total dissipated power

$$P_{diss} = \int_V \boldsymbol{j} \cdot \boldsymbol{E} \, dV \tag{5.1}$$

---

[*] Attention has to be paid if the point dipole is located at the symmetry plane or the section of two symmetry planes: In these cases, the absolute value of the dipole moment μ needs to be multiplied by $\frac{1}{\sqrt{2}}$ for a half model or $\frac{1}{2}$ for a quarter model in order to match the results of a full model.

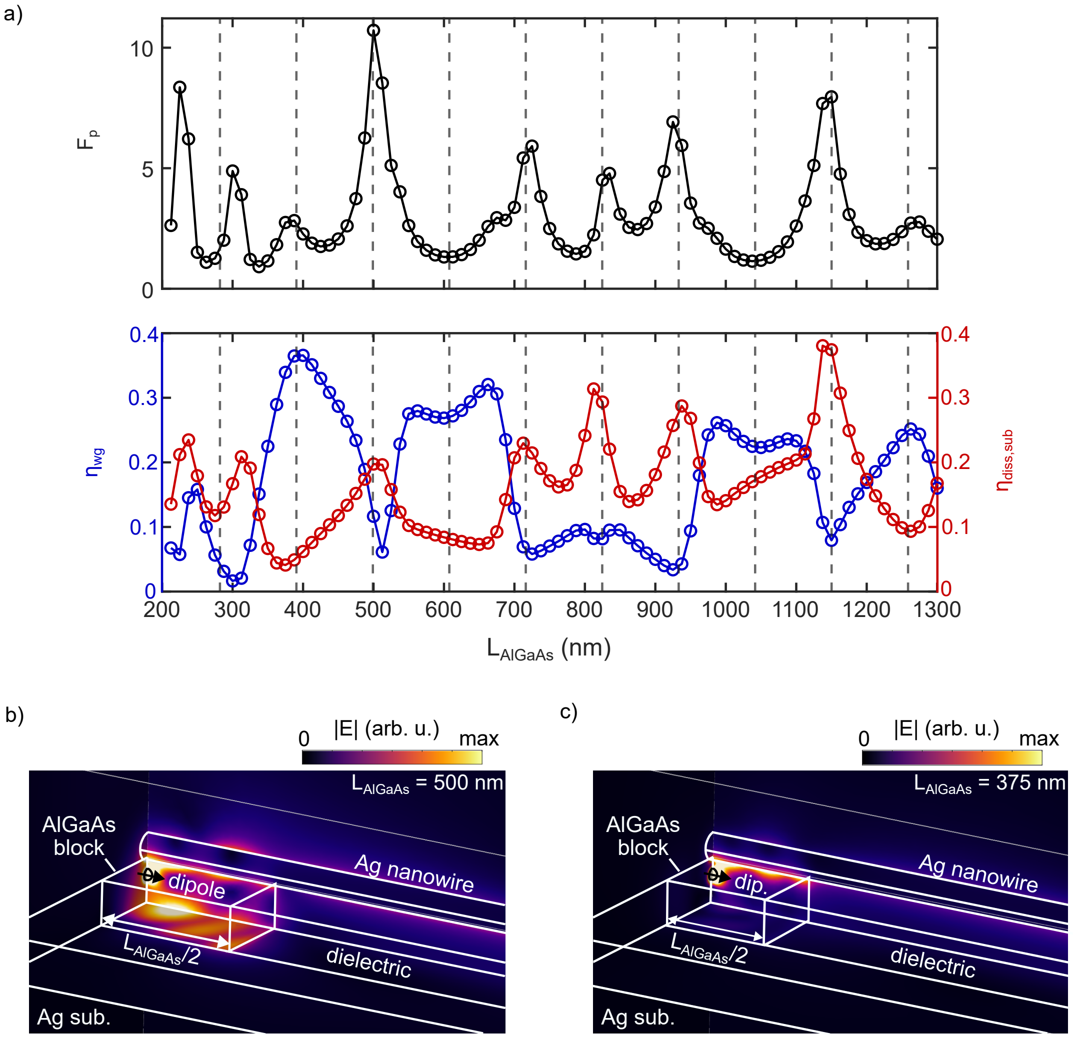

Figure 5.3: **Three-dimensional finite element simulations of a silver nanowire on top of an AlGaAs block with varying length $\mathbf{L_{AlGaAs}}$.** A dipole is located at the center of the AlGaAs block, with its orientation along the waveguide axis. The block is planarized with a dielectric with $n = 1.4$. The substrate is silver. (a) Purcell factor F_p (upper panel), waveguide efficiency η_{wg} (lower panel, blue circles) and substrate dissipation efficiency $\eta_{diss,sub}$ (lower panel, red circles) for varying lengths L_{AlGaAs}. The dashed lines correspond to multiples of $\lambda_{SPP}/2$, given by the effective mode index from the mode shown in Figure 5.2c. (b, c) Absolute of the electric field for a block length of $L_{AlGaAs} = 500\,\text{nm}$ (b) and $L_{AlGaAs} = 375\,\text{nm}$ (c), respectively. Due to the symmetry of the geometry, it is enough to compute a quarter of the full model.

with the current density $\boldsymbol{j}$, which is integrated over the silver substrate with volume V. After normalization via the total emitted power P_{tot} of the dipole, one can define the dimensionless substrate dissipation efficiency

$$\eta_{diss,sub} = \frac{P_{diss}}{P_{tot}} \tag{5.2}$$

that is shown as red circles in the lower panel of Figure 5.3a. In contrast to the waveguide efficiency, the substrate dissipation follows the total Purcell enhancement and, therefore, suggests that interference of the substrate surface plasmon mainly drives the Purcell effect. This is confirmed when comparing the field distribution in terms of the absolute electric field $|E(x, y, z)|$ for $L_{mesa} = 500\,\text{nm}$ (see Figure 5.3b) and $L_{mesa} = 375\,\text{nm}$ (Figure 5.3c): At $L_{mesa} = 500\,\text{nm}$, the dipole excites both the plasmon at the silver nanowire and the surface plasmon at the AlGaAs/silver interface, with respective efficiencies of $\eta_{wg} = 11.7\,\%$ and $\eta_{diss,sub} = 19.7\,\%$. In contrast, at $L_{mesa} = 375\,\text{nm}$, there is almost no substrate surface plasmon visible, as expected from only $\eta_{diss,sub} = 4.1\,\%$ in Figure 5.3a. This is accompanied by a high waveguide efficiency of $\eta_{wg} = 33.9\,\%$. Of course, there are other decay channels present, for example, far field radiation into the upper half-space, which are not explicitly discussed here.

Figure 5.3 states that the dimensions of the AlGaAs block immensely impact the dipole emission characteristics and the nanocircuit performance. Depending on the block length, either the overall decay rate or the coupling to the waveguide is enhanced. This provides a powerful tool for engineering the emission properties in a specific manner. If the waveguide efficiency alone is optimized, one can generate single plasmons on demand, for example, via pulsed excitation of the quantum dot. On the other hand, the total number of photons coupled into the waveguide can also be optimized. In this case, the product of Purcell factor and waveguide efficiency is the quantity of interest. No matter which design objective is followed, it is clear that the nanoscale environment given by the AlGaAs mesa is crucial for the overall performance of the nanocircuit. Therefore, in the next section, a simplified geometry without a plasmonic waveguide will be studied. This allows to extract the influence of the mesa geometry on the dipole emission rate and also reduces the model size, which relaxes the computational requirements.

5.3 NANORESONATORS FOR EPITAXIAL QUANTUM DOTS

In this section, the influence of the semiconductor mesa geometry on the emission properties of an incorporated dipole emitter is characterized. Therefore, the plasmonic waveguide is left away, and the rectangular cross-section is replaced by a circular one. This reduces the whole system to two parameters, namely the radius r and the height h of the cylindrical AlGaAs mesa. Furthermore, a disk-shaped mesa is easier to fabricate via lithography than a block with a rectangular cross-section. In fact, the experimental realization of a mesa-based plasmonic nanocircuit in chapter 6 uses AlGaAs disks. The investigated geometry is sketched schematically in Figure 5.4a. The cylindrical AlGaAs mesa is located on top of a silver substrate. A dielectric with a refractive index of $n = 1.4$ surrounds the mesa since, later, a nanowire needs to be supported. The distance of the dipole emitter to the top surface of the AlGaAs mesa is fixed at $z_b = 40\,\text{nm}$. The upper half-space is air. The mesa radius and height are varied in a range from $r = 50 - 500\,\text{nm}$ and $h = 60 - 300\,\text{nm}$ in steps of 10 nm, respectively. Analogously to Figure 5.3a, the Purcell factor F_p is computed,

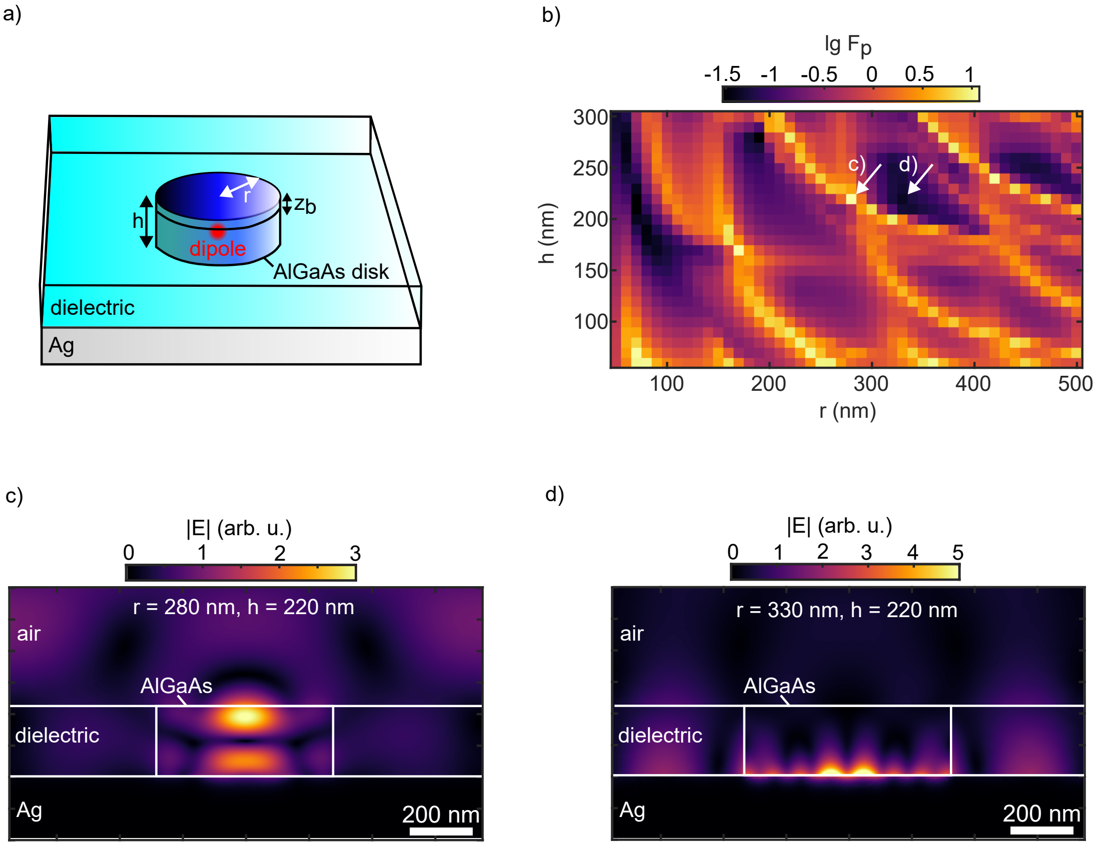

Figure 5.4: **An AlGaAs disk on a silver substrate features extreme emission suppression or emission enhancement, depending on the disk radius and height.** (a) Sketch of the geometry. On top of the silver substrate, there is an AlGaAs disk with radius r and height h. A dipole emitter is located centrally in the disk with its height fixed at a burial depth $z_b = 40\,\text{nm}$ below the mesa top surface. The AlGaAs cylinder is surrounded by a low-index dielectric and air. (b) Purcell factor F_p as a function of disk radius r and disk height h. A local maximum ($F_p = 11.9$) and a local minimum ($F_p = 0.043$) are indicated by arrows. Note the logarithmic scale. (c, d) Cross-section through a three-dimensional mode analysis for two selected parameter sets, where the Purcell factor is at its maximum (c) and minimum (d), respectively. Note that no dipole emitter is needed for mode analysis.

normalized to the emission of a dipole in a homogenous AlGaAs environment. The result is shown in Figure 5.4b, with the Purcell factor in a logarithmic scale. There is a tremendous variation, reaching from strong emission suppression ($F_p = 0.029$) to strong emission enhancement ($F_p = 11.9$), depending on the radius and height of the cylinder. This implies a change in dipole emission of more than a factor of 400, caused by the interplay of plasmonic and dielectric modes into which the dipole can emit. The branches of high Purcell enhancement in Figure 5.4b already suggest the presence of an underlying mode structure. To illustrate this, a three-dimensional mode analysis is performed for selected parameter sets where the Purcell factor is extremal. Cross-sections through the cylindrical mesa are shown for $r = 280\,\text{nm}$, $h = 220\,\text{nm}$ in Figure 5.4c, and for $r = 330\,\text{nm}$, $h = 220\,\text{nm}$ in Figure 5.4d. These parameters belong to the local maximum and local minimum of the Purcell factor, which are highlighted with arrows in Figure 5.4b, respectively.

The eigenmode in Figure 5.4c is mostly dielectric and features a maximum of the electric field at the (hypothetical) position of the dipole 40 nm below the mesa surface. The high Purcell enhancement of 11.9 is caused by a dielectric resonance. These resonances are very sharp, as can be seen from the mode structure in Figure 5.4b, which is only weakly resolved for the chosen discretization of 10 nm in the mesa radius and height. Theoretically, the Purcell enhancement is therefore underestimated; however, in an experimental realization, fabrication tolerances and material imperfections need to be considered. Since the AlGaAs mesa does not absorb photons at the emission wavelength, one expects a huge increase in the far field emission if the dielectric resonance condition is fulfilled. In contrast, the eigenmode in Figure 5.4d is mostly plasmonic and features a node in the electric field at the position of the dipole. Due to the lack of decay channels, the total emission of the dipole is suppressed drastically by a factor of about 23 compared to the reference dipole in bulk AlGaAs, corresponding to a Purcell factor of $F_p = 0.043$. This is not the smallest Purcell factor in Figure 5.4b; higher suppression, however, can only be achieved for radii smaller than 100 nm. Such mesa sizes are comparable to the lateral quantum dot extension [33] and, therefore, extremely challenging to fabricate.

A nanosystem that exhibits extreme suppression, as shown in Figure 5.4d, could be intriguing for a quantum plasmonic circuit: If the nanowire could be treated as a small perturbation of the system, then emission into the waveguide is the only relevant decay mechanism offered to the dipole and would therefore dominate. Of course, this assumption is speculative at this point since the system needs to be seen as a whole. In the next section, a silver nanowire is placed on top, and its coupling to the emitter is evaluated. If the nanowire is indeed only a small perturbation, the regions with strong suppression in Figure 5.4b should feature a high coupling and waveguide efficiency.

5.4 NANORESONATOR-ENHANCED WAVEGUIDE COUPLING

In order to investigate the influence of the AlGaAs nanoresonator on the waveguide coupling, a silver nanowire is added to the – otherwise unchanged – geometry of Figure 5.4a. A sketch of the new geometry is drawn in Figure 5.5a. The nanowire has a radius of 25 nm and is placed centrally on top of the mesa. The latter contains the dipole emitter, which is oriented along the waveguide axis. Now, the Purcell factor F_p is computed as a function of mesa radius r and height h using the same parameter space as in the previous section. The resulting Purcell factor map is shown in Figure 5.5b. Interestingly, it clearly resembles the map in Figure 5.4b without the nanowire. The same branches of strong Purcell enhancement can be found, which have already been attributed to resonant dielectric modes in the AlGaAs disk. However, in quantitative terms, a shift to larger Purcell factors is observable if compared to the model without the nanowire. This is easily explained by the

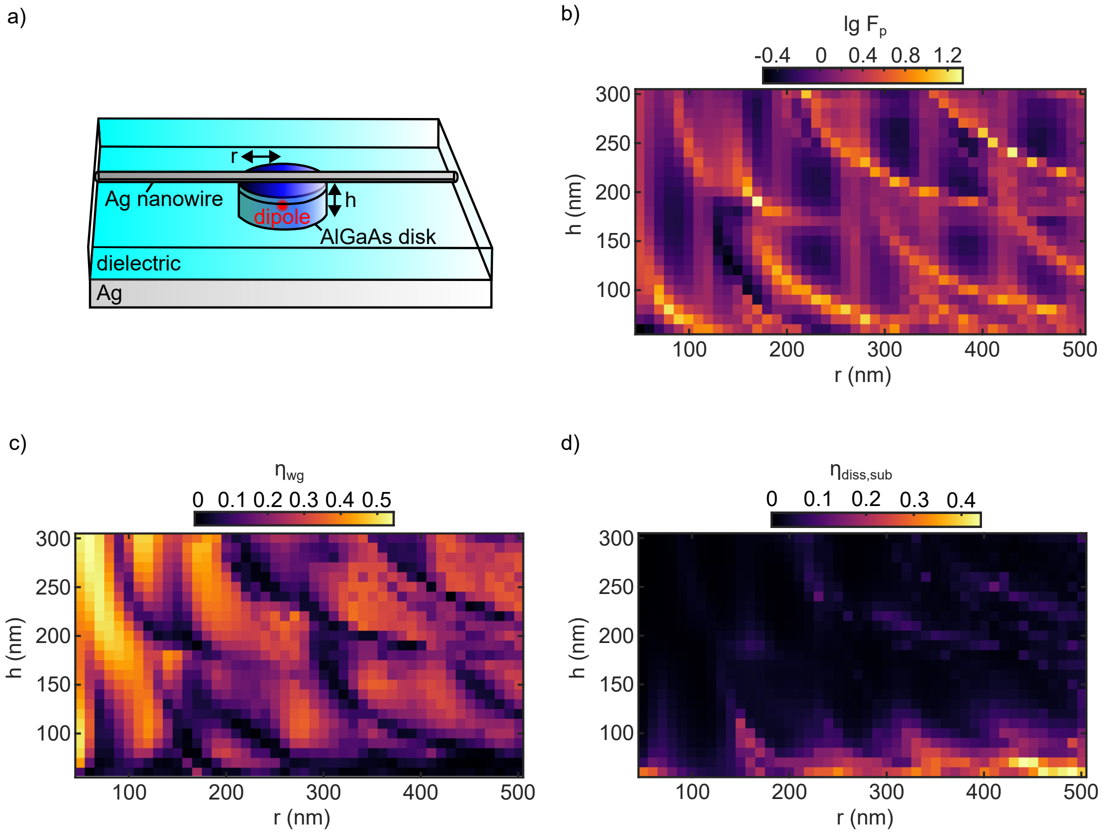

Figure 5.5: **The AlGaAs disk serves as a nanoresonator, which severely impacts the coupling efficiency to the silver nanowire.** (a) Sketch of the geometry, consisting of a silver nanowire with a radius of 25 nm on top of an AlGaAs disk with radius r and height h. All the other materials and parameters are identical to the model in Figure 5.4. (b) Purcell factor F_p as a function of disk radius r and disk height h. Note the logarithmic scale. (c) Waveguide coupling efficiency η_{wg}, normalized to the total emission rate of the respective geometry given by the Purcell factor in (b). The waveguide efficiency is evaluated in a distance of 2 µm from the dipole and includes propagation in both directions. (d) Substrate dissipation efficiency $\eta_{diss,sub}$, normalized to the corresponding total emission rate.

additional decay channel, which is opened through the nanowire. For example, the smallest Purcell factor is now $F_p = 0.29$, about an order of magnitude larger than the smallest Purcell factor without the nanowire. The highest Purcell enhancement is also increased to $F_p = 22.0$; however, this maximum value is subject to a large uncertainty since the narrow dielectric modes are not entirely resolved for the chosen parameter discretization.

The similarity of the Purcell factor maps with and without the nanowire already suggests that the nanowire can indeed be treated as a small perturbation of the whole system. This is further confirmed by the waveguide efficiency map in Figure 5.5c, which adds up the surface plasmon contributions from both directions of the waveguide after a propagation of 2 µm. The waveguide efficiency is basically the inverse of the Purcell factor map: The dielectric resonances appear as dips in η_{wg} since the dipole emits predominantly into these modes, resulting in waveguide efficiencies on the order of $\eta_{wg} \approx 10^{-3}$. In the case of absent dielectric modes, however, coupling to the nanowire is significant: Particularly, laterally small but high nanopillars seem to achieve the best performance. For example, at $r = 60\,\mathrm{nm}$ and $h = 300\,\mathrm{nm}$, the waveguide efficiency reaches $\eta_{wg} = 54.5\,\%$. Of course, a mesa with such a small radius is hard to fabricate without degrading the quantum dot. Definitely realistic are radii above 150 nm, which have been proven to integrate intact quantum dots in chapter 6. For example at $r = 180\,\mathrm{nm}$ and $h = 290\,\mathrm{nm}$, a waveguide efficiency of $\eta_{wg} = 45.5\,\%$ can still be achieved. Another interesting effect comes into play for thin disks with $h < 100\,\mathrm{nm}$, which increases for laterally larger disks: In such geometries, the dipole, which is always 40 nm below the mesa top surface, comes close to the silver backplane and launches surface plasmons at the AlGaAs/Ag interface. This is accompanied by a decrease in the waveguide efficiency and can be quantified by the substrate dissipation efficiency $\eta_{diss,sub}$ shown in Figure 5.5d. The substrate dissipation is normalized to the total emitted power, analogously to the waveguide efficiency, and reaches up to $\eta_{diss,sub} = 44.1\,\%$ for flat disk shapes. For heights larger than 100 nm, the launching of substrate surface plasmons is negligible.

In Figure 5.5c, the waveguide efficiency is shown as a function of the disk radius and height. However, more parameters are involved, including, for example, the radius of the plasmonic waveguide, the dipole position inside the mesa, or the dipole moment orientation. Furthermore, the cylindrical shape of the mesa might not be optimal; also, a block or a bar, which is tapered along the preferential direction given by the nanowire, might be promising. Moreover, the nanowire could be reinforced at the location of the dipole in order to create a cavity by an antenna structure. All this together means that for a global optimization, a multi-dimensional parameter space needs to be searched through. However, already the two-dimensional optimization in Figure 5.5c takes several days on a workstation (including two Intel Xeon 6240 processors with 18 cores each), even though only a quarter of the full model is actually computed through the use of symmetry planes. The reason for the long computation time is the fine meshing, which is necessary to resolve plasmonic features.

Consequently, standard parameter sweeps are no longer a practical solution when it comes to multi-dimensional parameter spaces. This was tackled in the master thesis of Tim Pfadenhauer [102], who applied a Bayesian optimization algorithm in order to iteratively generate the most promising parameter set for the next Comsol simulation, respectively. For a four-dimensional parameter set including mesa radius and height as well as the width and height of a rectangular nanowire, only 500 simulations were necessary to find an optimum of $\eta_{wg} = 53.1\,\%$, using the waveguide efficiency as defined above, at a fabrication-wise feasible combination of parameters. In comparison, Figure 5.5c consists of 1150 calculations with a maximum of only 45.5 % for realistic parameters. One needs to keep in mind that the found optimum could be narrow and, therefore, poses high requirements on nanofabrication. More generally, it can be difficult to gain a physical understanding of the system if one purely relies on such algorithms. However, if the focus is entirely on structural device efficiency optimization, algorithms like Bayesian optimization are the method of choice.

5.5 SUMMARY

In this chapter, numerical simulations have been used to optimize the coupling and waveguiding efficiencies of a nanocircuit based on a quantum dot that is integrated into a semiconductor mesa structure. Such a configuration promises good coupling to the plasmonic waveguide and low attenuation of the propagating surface plasmon due to the lower refractive index of the dielectric filling material. An analysis of fundamental waveguide modes supported by different substrate materials reveals that a silver backplane features the highest modal decay rate. Thus, such nanostructures are examined in detail in the rest of the chapter. At first, the influence of the mesa geometry on the dipole emission rate is characterized. It is found that in the absence of the plasmonic waveguide, the Purcell factor can vary in a range from $F_p = 11.9$ to $F_p = 0.043$, depending on the radius and height of the AlGaAs disk containing the dipole. This is caused by coupling to dielectric resonances in the case of emission enhancement or the unavailability of such modes at the dipole position in the case of emission suppression. Finally, it has been shown that the waveguide efficiency can reach up to $\eta_{wg} = 45.5\,\%$ when a silver nanowire is placed on top of a mesa that would have suppressed the emitter in the absence of a waveguide. In particular, nanopillars with radii smaller than 250 nm achieve the best waveguide efficiency. The proposed nanocircuit design is feasible with advanced nanostructuring methods (e.g., in situ electron beam lithography), but it also affords a substrate transfer of the GaAs quantum dots and careful planarization of the nanopillars.

6

AN EXPERIMENTAL REALISATION OF A MESA-COUPLED QUANTUM DOT–WAVEGUIDE HYBRID

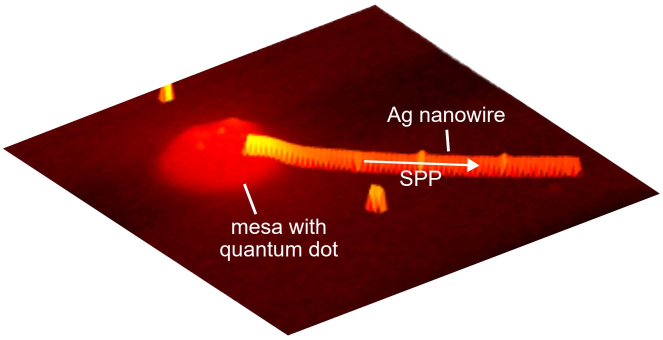

This chapter describes the experimental realization of a simple plasmonic nanocircuit, consisting of a single GaAs quantum dot inside a mesa structure, that is coupled to a silver nanowire. It is therefore closely related to chapter 5, where the performance of such a simple nanocircuit is numerically analyzed. The mesa-based coupling scheme promises highly efficient emitter–waveguide interaction and reduced propagation losses when compared to the intermediate field coupling in chapter 4. While the latter does not afford nanostructuring at all, the mesa approach can only be realized by advanced nanostructuring techniques. In this chapter, a complete sample processing cycle is described, starting from the integration of epitaxial quantum dots into mesa structures to the demonstration of launched surface plasmons via the emission of a single integrated quantum dot. It will be shown that compromises made for the sake of a simplified sample processing, as well as subtle deviations of the fabricated nanostructure from the idealized one, affect the performance of the nanocircuit. Therefore, the work in this chapter must be considered as a first experimental step towards an efficient and scalable quantum plasmonic nanocircuit, and the processing cycle must be further optimized.

The chapter is structured as follows: First, numerical simulations are conducted in section 6.1 in order to assess the potential of a GaAs-based mesa–waveguide nanostructure, a configuration that has been studied only roughly in chapter 5. In particular, the coupling efficiencies are compared to the intermediate field coupling. The integration of quantum dots into mesa structures is described in section 6.2. This is done deterministically by in situ electron beam lithography in cooperation with the Reitzenstein group at TU Berlin. Both photoluminescence and cathodoluminescence are used to characterize the integrated quantum dots. In section 6.3, the free-standing mesa structures are planarized by spin-coating IC1-200, which has already been used as a dielectric spacer layer in chapter 4. Atomic force microscopy is applied to evaluate the resulting topography and degree of planarization. The actual quantum dot–waveguide coupling is then shown in section 6.4. Finally, possible routes towards an optimized nanostructure that is highly efficient and fully scalable in fabrication, are outlined in section 6.5.

6.1 NUMERICAL SIMULATIONS FOR MESAS ON SEMICONDUCTOR SUBSTRATES

The numerical simulations in chapter 5 have shown that the coupling of a plasmonic waveguide to an integrated quantum dot can be extremely efficient for an idealized nanostructure. In particular, nanostructures with metallic backplanes achieved the most promising results, with coupling efficiencies exceeding 50 %. However, regarding an experimental realization, the latter requires a release of the quantum dot membrane from its semiconductor substrate, which complicates the fabrication process and would necessitate the etching of a sacrificial AlAs layer with hydrofluoric acid [22]. Therefore, the experimentally realized mesa–waveguide hybrid will be based on a GaAs substrate, the natural host material for the epitaxial growth of self-assembled GaAs quantum dots. This simplifies the sample fabrication process but may reduce the nanocircuit performance. Since most of the simulations in chapter 5 are based on silver backplanes, the potential of a nanocircuit based on a GaAs substrate needs to be investigated. A two-dimensional mode analysis performed in chapter 5.2.1 has already shown that such configurations can suffer from radiation losses into the substrate. However, the effect of leaky modes should be limited due to the finite size of the mesa, and instead, dielectric resonances of the mesa are expected, although their influence may be smaller due to the identical mesa and substrate materials. Another aspect that has not been considered until now is the influence of a dielectric gap between the nanowire and the mesa. Finally, the diameter of the mesa, which is assumed to be disk-shaped, is of interest. Of course, there are other parameters, for example, the shape and height of the mesa, the quantum dot position, the dipole moment orientation, or the nanowire dimensions, which are kept constant for the sake of simplicity.

The simulations are performed with the finite element solver Comsol Multiphysics, in a full three-dimensional computation. The investigated geometry is schematically sketched in a side view in Figure 6.1a. The cylindrical mesa with a height of 80 nm and a diameter D is surrounded by a flat dielectric spacer layer. The dipole emitter is placed centrally within the mesa, 30 nm below the mesa top surface. The dipole moment is oriented along the waveguide axis, which is expected to be the dominant coupling direction since it coincides with the fundamental plasmonic waveguide mode. The spacer thickness t is measured from the top surface of the mesa and therefore represents the dielectric gap size. The silver nanowire is assumed to be circular in its cross-section with a diameter of 50 nm and is located centrally above the mesa. The refractive indices of AlGaAs ($n_{AlGaAs} = 3.44$) and silver ($n_{Ag} = 0.035 + 5.49i$) are taken from literature [48, 49], while the refractive index of the dielectric spacer

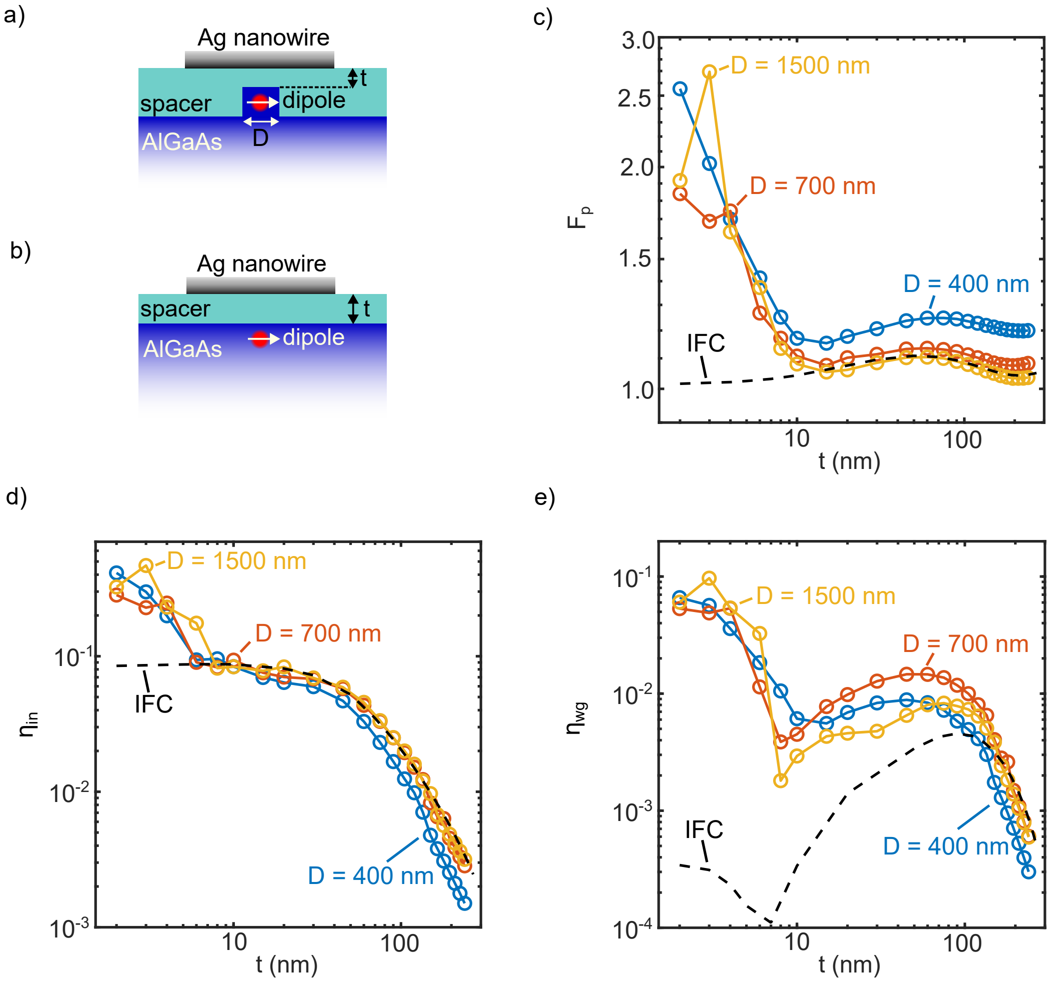

Figure 6.1: **Numerical analysis of a nanocircuit consisting of an emitter inside a cylindrical AlGaAs mesa on top of an AlGaAs substrate, with a centered silver nanowire on top.** The surrounding dielectric spacer thickness t and the mesa diameter D are varied. The nanocircuit performance is compared to the planar intermediate field coupling (IFC) described in chapter 4. Sketch of the planarized mesa geometry (a) and the intermediate field geometry (b) when looked at from the side. In both cases, the dipole is oriented along the waveguide direction and located 30 nm below the mesa top surface (a) or the plane AlGaAs surface (b), respectively. Purcell factor $F_p(c)$, incoupling efficiency η_{in} (d), and waveguide efficiency η_{wg} (e) versus spacer thickness t and mesa diameter D. The corresponding performance of the intermediate field coupling (IFC) is given for comparison.

($n_{spacer} = 1.41$) is taken from the manufacturer of IC1-200, Futurrex. All simulations are performed at a wavelength of $\lambda = 790\,\text{nm}$. The thickness of the spacer layer above the mesa is varied between $t = 2 - 250\,\text{nm}$ and three different mesa diameters $D = 400, 700, 1500\,\text{nm}$ are used. In order to characterize the nanocircuit, the overall Purcell factor F_p, the incoupling efficiency η_{in}, and the waveguide efficiency η_{wg} are computed. The extraction of these quantities from the three-dimensional simulations is described in section 2.3.2. Note that the incoupling and waveguide efficiencies are normalized to the total radiated power of the dipole for the specific geometry. By choosing this kind of normalization, the obtained efficiencies are independent of the Purcell enhancement. If one would normalize for example on the emission rate of the dipole in bulk medium, a higher coupling efficiency could be caused simply by a higher total emission rate, which not necessarily is coupled to the waveguide. In order to evaluate the performance of the mesa-based approach, the intermediate field coupling (IFC) geometry from chapter 4 – again sketched in Figure 6.1b – is used as a reference. This is the baseline model with which the technologically more challenging mesa design has to compete. For reasons of uniformity, the intermediate field geometry is modeled in three dimensions and evaluated analogously to the description above. Interestingly, the obtained coupling and waveguide efficiencies match very well with the results of the two-dimensional mode analysis in Figure 4.3b.

When comparing the nanocircuit performance of the GaAs-based mesa (connected circles) with the IFC geometry (dashed line) in Figures 6.1c-e, it is apparent that both schemes are identical for large dielectric gaps, while the mesa approach is superior only for small gap sizes t. For example, there is a significant Purcell enhancement of up to $F_p = 2.7$ for gap sizes $t < 15\,\text{nm}$ (see Figure 6.1c). However, for thicker dielectric fillers, the Purcell enhancement is comparable to the intermediate field coupling, where the total emission rate is expected to increase by less than 10 %. An exception is the mesa diameter $D = 400\,\text{nm}$, where even large gap sizes result in a Purcell enhancement of about 25 %, which is rather caused by a dielectric resonance than a plasmonic decay channel. This assumption is confirmed by Figure 6.1d, where the coupling efficiency η_{in} to the plasmonic waveguide is smaller for $D = 400\,\text{nm}$ at large gaps, compared to the other mesa diameter. Similar to the Purcell factor, the coupling efficiency is only enhanced for gap sizes $t < 8\,\text{nm}$. While the intermediate field coupling saturates at about $\eta_{in} = 8.5\,\%$ even for very small spacers, coupling efficiencies up to $\eta_{in} = 47\,\%$ are reached for the mesa model. Note that in the symmetric simulation design, propagation in both directions is already assumed. The distinctive advantage of the mesa model over the intermediate field coupling is visible when looking at the waveguide efficiency η_{wg} shown in Figure 6.1e. For spacers $t < 100\,\text{nm}$, the mesa model is superior, with the efficiency difference increasing towards thinner fillers. For example, at $t = 30\,\text{nm}$, the mesa model outperforms the intermediate field coupling by a factor between two and six, depending on the mesa diameter. For very thin dielectric gaps, waveguide efficiencies of up to $\eta_{wg} = 9.7\,\%$ are achieved due to the propagation advantage of the mesa geometry. This has to be set in relation to the optimum efficiency for the intermediate field coupling of $\eta_{wg} = 0.46\,\%$ at $t = 90\,\text{nm}$ and therefore represents an enhancement of 21.

In summary, it has been shown that the mesa geometry can be clearly superior over the intermediate field coupling. This is manifested in an increased coupling and propagation efficiency as well as a significant Purcell enhancement. However, the advantage comes into play only for small dielectric gaps between the mesa and the nanowire. Therefore, it assumes a flat spacer layer, closely matching the top surface of the mesa. If this is not the case, only a moderate enhancement of the waveguide performance is expected, while the incoupling efficiency and the overall emission rate are equal to the intermediate field approach.

6.2 DETERMINISTIC INTEGRATION OF GAAS QUANTUM DOTS

In this chapter, the deterministic integration of GaAs quantum dots into mesa structures is performed. This is done via in situ electron beam lithography, a nanostructuring method that is presented in section 6.2.1. Afterwards, the integrated quantum dots are characterized via photoluminescence in section 6.2.2 and cathodoluminescence in section 6.2.3.

6.2.1 *In situ electron beam lithography*

In situ electron beam lithography (in situ EBL) is an advanced nanostructuring technique which has been implemented for the fabrication of high-quality single-photon sources by the Reitzenstein group at TU Berlin [103]. It allows for the deterministic integration of embedded semiconductor quantum emitters into simple mesa structures [104] and more sophisticated devices like on-chip beamsplitters based on dielectric waveguide structures [105]. The approach is based on cathodoluminescence (CL) spectroscopy and is not limited to a certain semiconductor platform, but mostly used for InGaAs/GaAs materials. In the following, a rough description of the in situ EBL process is given, which is based on the references [58, 103].

The process flow of the in situ electron beam lithography is sketched in Figure 6.2. The experimental setup includes a low-temperature scanning electron microscope with a cathodoluminescence detection unit and has already been described in section 3.1.1. At first, the quantum dot sample is coated with an e-beam resist, e.g., PMMA or CSAR62. Afterwards, the sample is cooled down to a temperature of 20 K and mapped via cathodoluminescence spectroscopy, as illustrated in Figure 6.2a. The area exposed to the 10 kV electron beam is around 15 µm x 20 µm large. The electron dose is a critical parameter, as it defines the tone character of the resist. At intermediate doses of a few $\mathrm{mC\,cm^{-2}}$ as used for cathodoluminescence mapping, the resist is positive-toned and becomes soluble by cracking the PMMA chains. Now, the positions of the quantum dots can be determined by fitting two-dimensional Gaussians to the cathodoluminescence emission spots with an accuracy of $10 - 20\,\mathrm{nm}$. In addition, the emission wavelength of the selected quantum dots is obtained by a spectrometer, which in principle can be used for spectral matching of several emitters. In the next step, mesa structures are written at the selected positions (Figure 6.2b), which is accomplished by entering the negative-tone regime of the resist for electron doses exceeding $20\,\mathrm{mC\,cm^{-2}}$. At such doses, cross-linking of the PMMA chains starts, so that the patterned resist becomes insoluble again. This process can be performed for several sites inside a cathodoluminescence-mapped area. The sample is now warmed up to room temperature and developed (Figure 6.2c), with the overexposed resist remaining as an etch mask. In the last step shown in Figure 6.2d, the resist mask is transferred into the semiconductor by dry plasma etching (ICP-RIE).

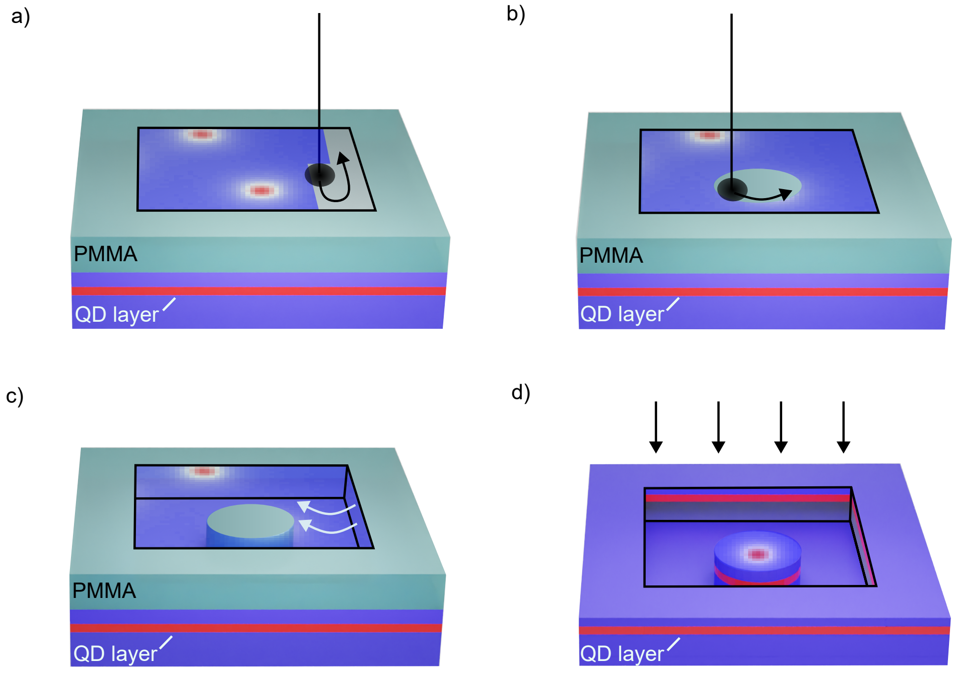

Figure 6.2: **Process flow of the in situ electron beam lithography (in situ EBL).** (a) Cathodoluminescence mapping. The e-beam resist in the mapped area becomes soluble for the developer. (b) Writing of the mesa structure by overexposing the resist inside a circular pattern. The patterned resist becomes insoluble. (c) Development removes the singly exposed resist surrounding the mesa structure. (d) The resist mask is transferred to the semiconductor by dry etching. The image is adapted from [105].

Here, self-assembled GaAs/AlGaAs quantum dots from the Rastelli group with a burial depth of $z_b = 30\,\text{nm}$ are used (sample type O692, see Appendix A.1). The in situ electron beam lithography was performed by PhD student Yuhui Yang. In total, 220 circular mesas with a diameter range spanning $D = 300 - 1500\,\text{nm}$ and an etching depth of about 80 nm are fabricated. The probability for the successful integration of a quantum dot has been studied by Yuhui Yang via cathodoluminescence spectroscopy. As one expects intuitively, it is found that the integration probability increases for larger mesa structures. For diameters $D > 500\,\text{nm}$, all mesas contain a quantum dot. For smaller mesa structures, the probability decreases to about 35% for $D = 300\,\text{nm}$. However, it is not clear from the cathodoluminescence measurements whether in these cases the quantum dot integration failed due to an alignment problem (e.g., caused by drift) or whether the cathodoluminescence emission of the integrated quantum dot is weak and hidden in the background of the wetting layer or band gap luminescence. These and more questions concerning the optical properties of the integrated quantum dots are studied in the next section. Photoluminescence measurements are performed, which is more suitable than cathodoluminescence because of the better collection optics that allow lower excitation levels.

6.2.2 *Photoluminescence characterization*

The etched nanopillars fabricated by in situ electron beam lithography naturally feature an increased surface area around the incorporated quantum dot. Therefore, the optical properties of these integrated quantum dots are likely to be altered or degraded, for example through coupling to surface states [106] or oxidation [100]. In the worst case, the quantum dot with its lateral extension of several tens of nanometers may be destroyed. In order to test the suitability of these integrated GaAs quantum dots for possible quantum optical experiments, a photoluminescence study is performed. Before turning to a quantitative analysis of the photoluminescence data, an instructive qualitative discussion focusing on the mesa structures with the smallest ($D = 300\,\mathrm{nm}$) and largest diameters ($D = 1500\,\mathrm{nm}$) is given.

In the upper row in Figure 6.3, an etched field containing seven cylindrical mesa structures with diameters of $D = 1500\,\mathrm{nm}$ is investigated. The electron micrograph in Figure 6.3a features a clear contrast between the etched field, the mesa structures and the unprocessed substrate, respectively. Here, mostly backscattered electrons are detected via the in-lens detector, which is sensitive to material composition as heavier elements backscatter more efficiently. The contrast between the etched and the unprocessed substrate might originate from the different semiconductor compositions which are seen by the electron beam, since a significant amount of the AlGaAs barriers are removed for an etching depth of 80 nm, leaving the heavier GaAs. The enlarged section in the inset shows that close-to-perfect circular structures can be fabricated. However, for the smallest mesa with diameters $D = 300\,\mathrm{nm}$ shown in Figure 6.3d, the geometric dimension deviates from the intended circular shape, resulting in a rather bumpy shape. In both Figures 6.3a and 6.3d, there is some debris visible, often close to the mesa. This is residual resist that can remain after the etching process and will be removed later (see section 6.3).

For the photoluminescence study, a confocal laser scanning microscope is used, similar to the setup already shown in Figure 3.6. Here, a narrow-band CW laser at $\lambda = 770\,\mathrm{nm}$ (Lion, Sacher Lasertechnik) is applied for reflection mapping and a CW diode laser at $\lambda = 532\,\mathrm{nm}$ (CPS532, Thorlabs) for photoluminescence excitation. The corresponding images for $D = 1500\,\mathrm{nm}$ are given in Figures 6.3b, c, and for $D = 300\,\mathrm{nm}$ in Figures 6.3e, f. The larger mesa structures can be resolved optically in the reflection image, while the smaller mesas can not. Nevertheless, the outlines of the etching fields together with the circular electron beam alignment spots next to the fields can be clearly resolved. These outlines allow to map the electron micrographs to the photoluminescence images and assign the respective mesa diameters. The photoluminescence images demonstrate the successful quantum dot integration. For $D = 1500\,\mathrm{nm}$, all seven mesas contain a quantum dot, proven by the photoluminescence emission spots overlapping with the mesa positions. In addition, the photoluminescence emission spots of the integrated quantum dots seem to be identical to the unprocessed dots outside the etching field. As expected, there is no quantum dot emission from within the etched field except for the mesa

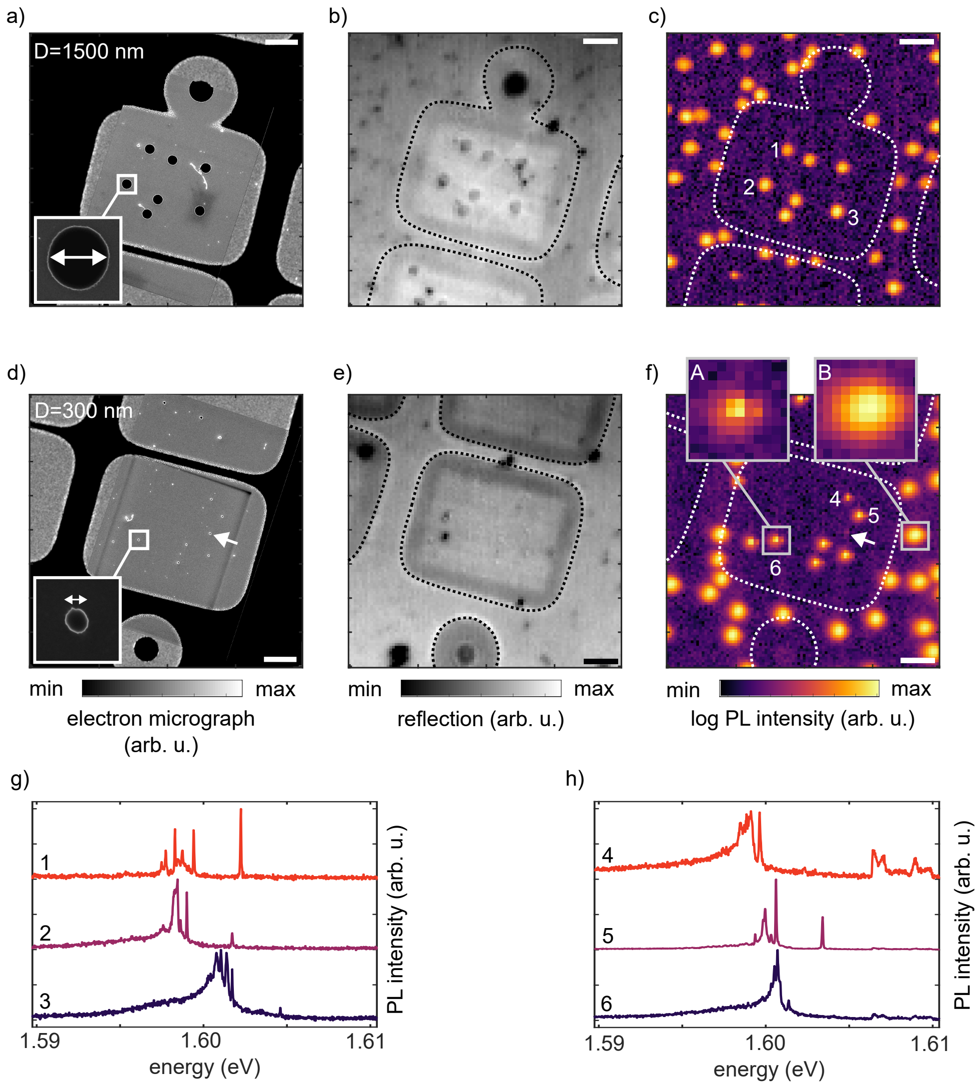

Figure 6.3: **GaAs quantum dots, integrated into cylindrical mesas with two different diameters via in situ electron beam lithography**. Upper row: Mesa diameter $D = 1500\,\mathrm{nm}$. Lower row: $D = 300\,\mathrm{nm}$. (a, d) Electron micrograph of the etched fields containing the mesa. The image consists of a high-resolution micrograph in the center and a lower-resolution micrograph for the outer part. Inset: Magnified detail, highlighting the mesa diameter D. The white arrow in (d) marks a mesa that does not contain a functioning dot, as can be seen in (f). (b, e) Reflection image, obtained by confocal laser scanning at a wavelength of $\lambda = 770\,\mathrm{nm}$. (c, f) Photoluminescence image, obtained by confocal scanning with an excitation laser at $\lambda = 532\,\mathrm{nm}$. Insets in (f): enlarged detail, comparing photoluminescence emission spots of an integrated dot (A) and an unprocessed dot (B). Note the logarithmic intensity scale. All scale bars are $5\,\mu\mathrm{m}$. (g, h) Photoluminescence spectra for three exemplary integrated dots, respectively. The numbers connect the spectra to the corresponding dots in (c) and (f).

dots, since the quantum dot layer at a depth of 30 nm has been removed. Regarding the smaller mesas with diameters $D = 300\,\mathrm{nm}$, a close look reveals that seven out of eight quantum dots have been successfully integrated. One mesa which is marked with an arrow in Figure 6.3d displays no or very weak emission, as can be seen in the logarithmic photoluminescence intensity scale in Figure 6.3f. Interestingly, for all of the mesas with diameters $D = 300\,\mathrm{nm}$, the spatial width of the photoluminescence emission spots is reduced significantly. This is highlighted by the two insets showing an integrated quantum dot (A) and an unprocessed quantum dot (B) and will be studied more thoroughly in this section. For a few integrated quantum dots also photoluminescence spectra are recorded and displayed in Figures 6.3g, h for the respective mesa diameters. For these cases, no significant change is discernible. For both $D = 1500\,\mathrm{nm}$ and $D = 300\,\mathrm{nm}$, there are quantum dots with narrowband excitonic lines, even though partly broadened transitions from higher excited states are prominent.

In total, 56 quantum dots distributed over eight fields and integrated in mesas with nominal diameters $D = 300, 400, 1000$, and $1500\,\mathrm{nm}$ have been analyzed. Each photoluminescence emission spot, including the unprocessed quantum dots as a reference, is fitted by a two-dimensional Gaussian to extract the amplitude, the full width at half maximum (FWHM), and the integral, with the latter as a measure for the total emitted photon number. Amplitude and integral of the mesa quantum dot emission spots are normalized to the average values given by the unprocessed quantum dots, of which about $20 - 30$ per field are recorded. Obviously, this assumes that inherent intensity variations between the unprocessed dots average out. For 23 integrated dots, also the photoluminescence spectrum is measured and a Lorentzian is fitted to the neutral exciton line to determine its linewidth. For a substantial fraction of these spectra, the excitonic line is either weak or broadened dramatically. Nevertheless, a Lorentzian is fitted to these lines, with the start point of the fit keeping fixed at the wavelength where the excitonic transition would be expected. Of course, this is associated with a large uncertainty in the linewidth determination; however, the exact linewidth is not relevant here, but rather the impact of the nearby removal of the barrier layers on the excitonic transition.

The results of the photoluminescence study are shown in Figure 6.4 in dependence on the mesa diameter D, which is extracted for each mesa individually by SEM images. Figure 6.4a displays the aforementioned decrease in the spatially resolved FWHM of the photoluminescence emission spots. Here, the black circles correspond to mesa quantum dots with the specified diameter D, while the red circles are averaged FWHMs of the unprocessed quantum dots next to the etching field. The error bar indicates one standard deviation of the reference quantum dots. For the largest mesa with $D = 1500\,\mathrm{nm}$, the FWHM $\approx 950\,\mathrm{nm}$ is identical to the FWHM of the unprocessed quantum dots. This rather large value is surprising on first sight, but results from the combination of a broadened excitation point spread function (PSF) due to charge carrier diffusion and a large detection PSF: The APD with a sensor diameter of $50\,\mu\mathrm{m}$ and an overall microscope magnification of 42 leads to a rather large collection area of $1.2\,\mu\mathrm{m}$ in the sample plane. On the other hand, cathodoluminescence yields a spatial FWHM $\approx 1000\,\mathrm{nm}$ for unprocessed quantum

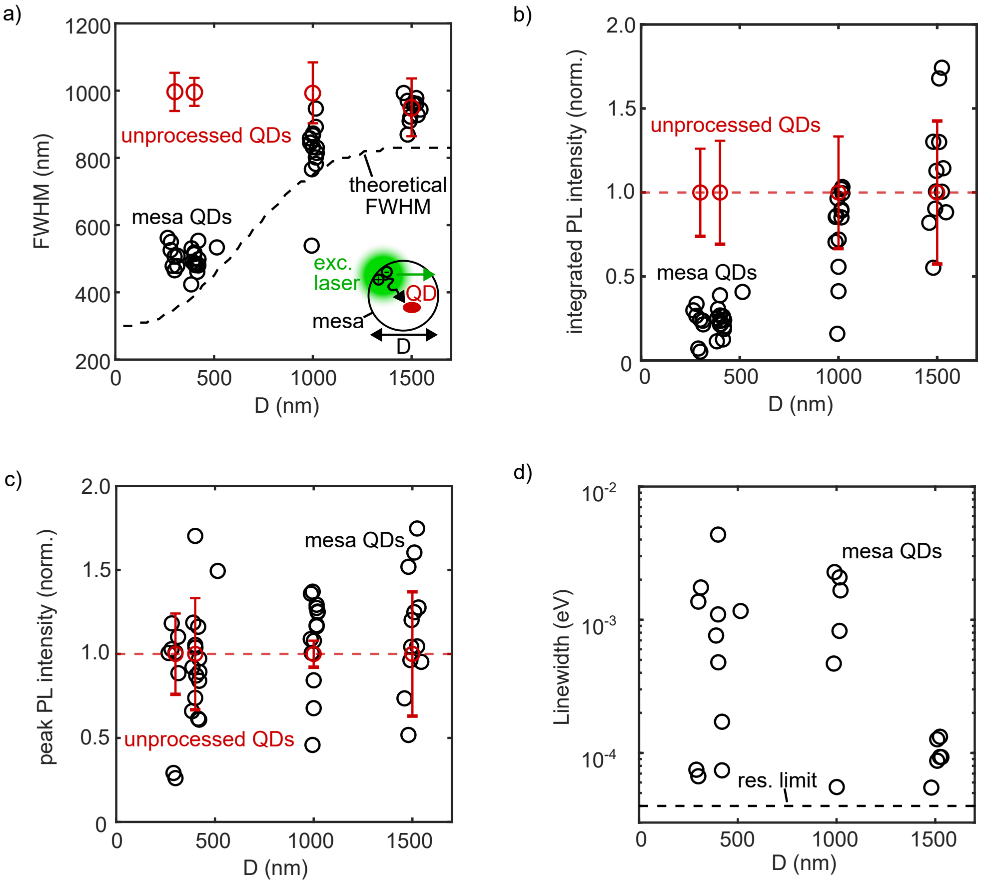

Figure 6.4: **Photoluminescence study of integrated quantum dots encapsulated in cylinders with diameters D.** (a) Spatially resolved full width at half maximum (FWHM) of the photoluminescence emission spots, obtained from confocal laser scans. Black circles: FWHM of processed mesa dots. Red circles: average FWHM of unprocessed dots next to the etching field as a reference. The error bars correspond to one standard deviation of the reference dots. The dashed line represents the theoretical FWHM, following the construction of the total point spread function in Figure 6.5. The inset depicts a sketch of the applied excitation diffusion model. Integrated (b) and peak (c) photoluminescence intensity obtained from confocal laser scans. The intensity values of the processed mesa dots (black circles) are normalized to the average values of the unprocessed reference dots (red circles) for each field with the same mesa diameter D. (d) Spectral linewidth of the excitonic transition for a subset of the studied mesa dots. The dashed line corresponds to the resolution limit of the spectrometer, which is 40 µeV.

dots in the same sample (O692), a width that can only be explained by diffusion processes (compare section 3.1.1). Consequently, the spot size reduction for smaller mesa can be easily explained by the missing barrier and wetting layers around the mesa, effectively restricting the diffusive carrier injection. If this is true, one would expect a decrease of the confocal FWHM with the mesa diameter D, with the floor being the laser excitation PSF. Theoretically, this would be FWHM $= \frac{0.61\lambda}{NA}$, yielding a FWHM of approximately 300 nm for NA $= 0.9$ and $\lambda = 532$ nm. For a direct comparison, the theoretical FWHM values are computed in dependence on the mesa diameter D and shown as the dashed line in Figure 6.4a. For this calculation, the total point spread function of the microscope is constructed according to Figure 6.5. At first, the excitation point spread function

$$\mathrm{PSF}_{exc} = \mathrm{PSF}_{laser} \circledast \mathrm{PSF}_{diff} \tag{6.1}$$

is given by the convolution of the diffraction-limited laser's point spread function PSF_{laser} and the diffusion point spread function PSF_{diff}. The latter one is given by a Gaussian with FWHM $= 1\,\mu\mathrm{m}$ according to the cathodoluminescence data (see section 3.1.1) and a cut-off of at respective the mesa radius, as can be seen in Figure 6.5a. The detection point spread function

$$\mathrm{PSF}_{det} = \mathrm{PSF}_{em} \circledast \mathrm{PSF}_{sensor} \tag{6.2}$$

straightforwardly follows from the convolution of the diffraction-limited emission point spread function PSF_{em} and the APD sensor area imaged onto the sample plane, declared as PSF_{sensor} (see Figure 6.5b). Finally, the total point spread function

$$\mathrm{PSF}_{tot} = \mathrm{PSF}_{exc} \cdot \mathrm{PSF}_{det} \tag{6.3}$$

of the system is given by multiplication of excitation and detection PSF, as depicted in Figure 6.5c. The comparison between theoretical and experimental FWHM in Figure 6.4a shows good agreement, although the measured values are slightly larger. This might be due to an imperfect alignment of the microscope setup. For small mesa diameter D, the deviation can be explained by the fact that the excitation laser

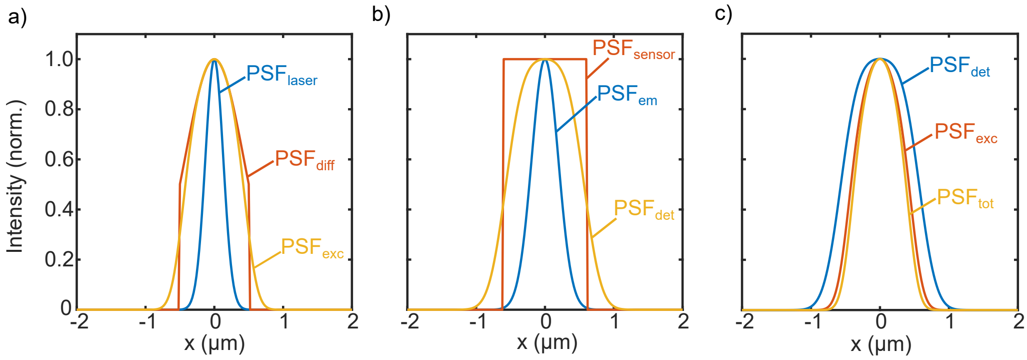

Figure 6.5: **Construction of the total point spread function (PSF) for the confocal microscope setup undergoing excitation broadening due to charge carrier diffusion.** (a) The Gaussian excitation laser focus PSF_{laser} is convoluted with a diffusion point spread function PSF_{diff} to obtain the excitation point spread function PSF_{exc}. The diffusive PSF is taken as a Gaussian with FWHM $= 1\,\mu\mathrm{m}$ according to cathodoluminescence data and cut off of at the mesa radius (here $0.5\,\mu\mathrm{m}$). (b) The diffraction limited emission point spread function PSF_{em} is convoluted with the APD sensor area PSF_{sensor} imaged onto the sample plane to obtain the detection point spread function PSF_{det}. (c) The total point spread function PSF_{tot} is given by the multiplication of excitation PSF_{exc} and detection PSF_{det} point spread function, derived in (a) and (b), respectively.

diode was not spatially filtered and the filling factor of the objective's back aperture was not optimized. This might explain why there is no significant difference between $D = 400\,\text{nm}$ and $D = 500\,\text{nm}$ observable in terms of the FWHM.

Apart from the spatial FWHM, also the total emitted photon number is obtained for each mesa by integrating the fitted two-dimensional Gaussian functions of each photoluminescence emission spot (see Figure 6.4b). Again, the black circles correspond to the integrated quantum dots, whereas the red circles are obtained by averaging over the reference dots, with the error bars given by one standard deviation. Here, the unprocessed quantum dots' intensities are used to normalize the mesa dots' intensity for each field and therefore are fixed to an intensity equal to 1. It is apparent that the integrated photoluminescence intensity is reduced for smaller D, but one has to consider that also the spatial FWHM is reduced, as discussed above. Therefore, the brightness reduction is simply explained by the restricted diffusive excitation for the smaller mesa, leaving only direct excitation.

Now the question arises if an integrated quantum dot still emits the same amount of photons once it is excited, compared to an unprocessed dot. This should be answered by looking at the photoluminescence peak intensity, given by the amplitude of the Gaussian fit and displayed in Figure 6.4c. Here, no clear impact of the mesa diameter is observed, and the mesa quantum dots' peak intensities are identical compared to their unprocessed counterparts. Interestingly, the mesa dots vary about 50 % around the reference value in the integrated quantum dots' peak intensities; however, also the unprocessed quantum dots span a rather large range in peak intensity, given by the standard deviation as error bars. In addition, it has to be considered that the APD detection spectrally integrates not only the excitonic but also multi-excitonic transitions, leading to a more complex emission characteristic and potentially inflicting variations between the quantum dots.

For possible quantum optical operation, not so much the total emitted photon number, but their spectral distribution is of importance. Therefore, the linewidth of the excitonic transition was measured for a subset of the integrated mesa quantum dots (see Figure 6.4d). As already mentioned before, a large span of linewidths is apparent, reaching from several tens of µeV to a few meV (compare Figure 6.3g, h). The very broad lines are probably explained by the sample (O692) degradation, which has been fabricated several years before the measurements and are also observed for unprocessed quantum dots. Unfortunately, there were no reference spectra taken from unprocessed dots of this specific sample. Nevertheless, when comparing spectra of dots integrated into mesa with varying diameters, narrow linewidths below 100 µeV are observed for all investigated mesa diameters. For $D = 1500\,\text{nm}$, very broad emission lines seem to be absent, but more data points would be needed for confirmation. The narrowest observed linewidth is 55 µeV, which is similar to values observed for unprocessed near-surface GaAs quantum dots [43], but still slightly larger than the resolution limit of the applied combination of monochromator (Acton SP2750 with 1800 g/mm grating) and camera (Pixis 100), which is 40 μeV.

6.2.3 *Cathodoluminescence characterization*

Similar to the photoluminescence, also the cathodoluminescence footprint of the integrated quantum dots changes. In the section above, the photoluminescence emission spot size was found to decrease with smaller mesa diameter, which has been attributed to the inhibited diffusion of charge carriers. Even though in cathodoluminescence the mechanism of injecting charge carriers is different, a similar pattern is observable. One example of a quantum dot integrated into a mesa with a diameter of $D = 685\,\text{nm}$ is shown in Figure 6.6a-c. The electron micrograph (Figure 6.6a) and the corresponding cathodoluminescence map (Figure 6.6b) clearly show a reduced intensity for electron beam positions outside the mesa, with the slightly imperfect

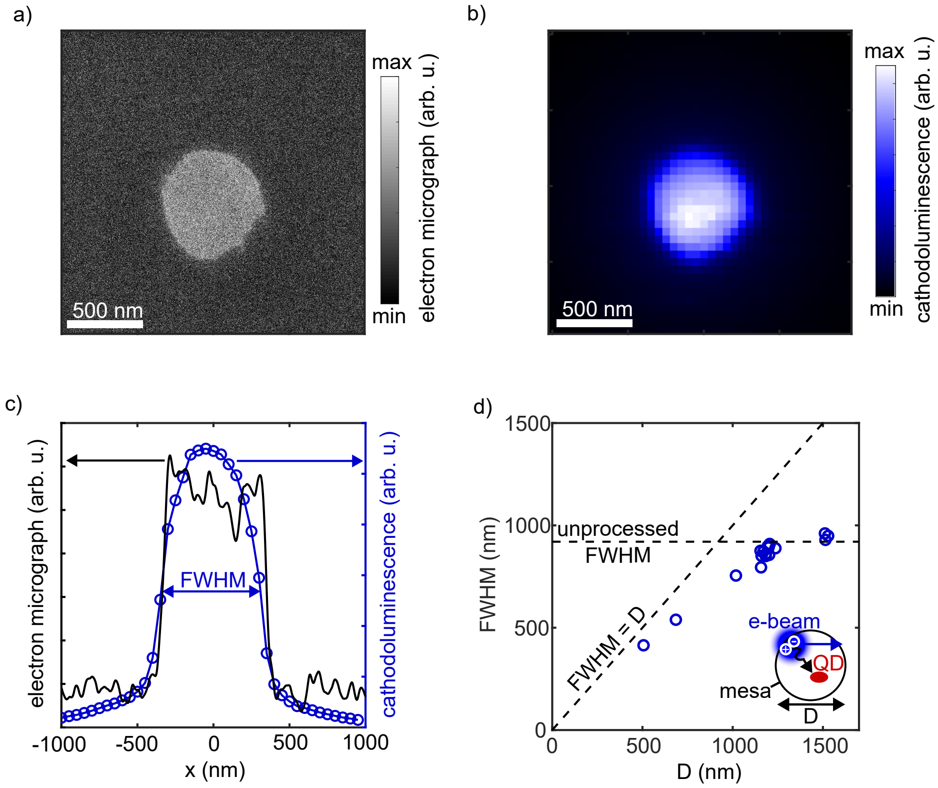

Figure 6.6: **Cathodoluminescence measurements of integrated quantum dots are consistent with the photoluminescence data.** (a) Electron micrograph of a mesa with a diameter of $D = 685\,\text{nm}$. (b) Corresponding cathodoluminescence image. (c) Slices through the electron micrograph (black line, the data is smoothed for better visibility) and the cathodoluminescence map (blue dots, the line is a guide to the eye). (d) FWHM for several mesas with varying diameter D. The horizontal dashed line corresponds to the FWHM of unprocessed dots on the same sample, while the other dashed line represents a FWHM which is given by the mesa diameter.

shape of the mesa imprinted on the cathodoluminescence intensity pattern. In Figure 6.6c, a horizontal slice through both images is shown. It can be clearly seen that the cathodoluminescence intensity does not follow a Gaussian curve anymore due to the excitation cut-off at the mesa edges. Again, this proves the high-resolution imaging capability of the low-temperature cathodoluminescence technique and is consistent with the diffusion cut-off model developed in the previous section. If looking at mesas with varying diameters, the FWHM of the respective cathodoluminescence spot decreases. This can be seen in Figure 6.6d, where the blue circles correspond to individual mesas. The horizontal dashed line corresponds to the average FWHM $= (920 \pm 100)$ nm of unprocessed quantum dots on the same sample (O692). This value is approached by the mesas with large diameter, in full agreement with the photoluminescence spot sizes in Figure 6.4a. For smaller mesa diameter D, the observed cathodoluminescence spot size simply follows FWHM $\propto D$, which is indicated by the other dashed line in Figure 6.6d for a proportionality factor of 1. In contrast to photoluminescence, where the observed spot size for small mesas is diffraction-limited by the excitation spot, this is not the case for cathodoluminescence. Instead, the generation volume of charge carriers by the electron beam determines the spatial resolution [60, 61], which should be much smaller than the optical diffraction limit. To further validate this, more cathodoluminescence measurements of mesas with diameters smaller than 500 nm would be needed.

6.2.4 *Summary*

In summary, it has been demonstrated that epitaxial GaAs quantum dots can be successfully integrated into sub-micrometer sized mesa structures via in situ electron beam lithography. A detailed photo- and cathodoluminescence analysis of the integrated quantum dots shows that the removal of the nearby barrier layers leaves the quantum dots intact, even for lateral quantum dot–surface distances smaller than 150 nm. A decrease in the observed photon number for small mesa structures is directly linked to the mesa diameter and can be traced back to inhibited diffusive excitation due to the absent wetting layer. A cathodoluminescence study confirms this simple model. In addition, the excitonic lineshape seems to be preserved in the etching process, since linewidths below 100 µeV are observed even for mesas with diameters as small as 300 nm. These results are the first step towards a functional single-plasmon source based on a deterministic fabrication process. Next, a plasmonic waveguide will be coupled to the integrated quantum dot pillar.

6.3 PLANARIZATION OF NANOPILLARS BY SPIN-COATING

Before the plasmonic waveguide can be interfaced with the integrated GaAs quantum dots, a planarization step is necessary for several reasons: Firstly, the topography needs to be leveled to avoid kinks or interruptions of the waveguide. Secondly, a planarizing material with a lower refractive index reduces the propagation losses of the surface plasmon. Thirdly, oxidation of the free-standing AlGaAs sidewalls of the etched mesas can be suppressed by encapsulation [100]. Planarization is an important processing step in semiconductor device fabrication. In order to lithographically pattern multiple layers on top of each other, the underlying topography needs to be leveled out. In semiconductor industry, this is done by chemical-mechanical polishing or etch-back processes. However, these planarization processes afford high technological prerequisites. For a proof-of-concept structure, which is the scope of this thesis, these expenses are not reasonable, and simpler solutions are required. In the following, a few general remarks on planarization are given; however, the details of the planarization depend on the respective feature sizes and materials, the used planarization materials as well as the target design objective.

Planarization can be divided into different regimes, which are sketched in Figure 6.7. These regimes vary in their degree of planarization (DOP), which is defined as [107]

$$DOP = 1 - \frac{t_{after}}{t_{before}}, \tag{6.4}$$

with the step height t_{before} before and the step height t_{after} after the planarization. For a low DOP, the planarizing layer closely follows steps in the underlying topography, as shown in Figure 6.7a. If the planarizing layer loosely follows the original step profile, a medium DOP is achieved (Figure 6.7b). This can be the case when the width of the underlying feature is small compared to the intrinsic planarization scale of the material. For some planarization materials like benzocyclobutene, also micro-trenching is observed [100]: instead of overflowing the obstacle, a gap is formed at the feature's sidewalls. For a DOP equal to one, the underlying topography has been leveled out completely and a planar layer is achieved (Figure 6.7c).

It needs to be stated that for the targeted proof-of-concept structure, a full planarization as shown in Figure 6.7c is not necessary or even unwanted, depending on the thickness of the planar layer. Most important for the application here is little to no

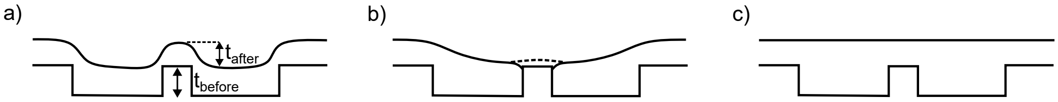

Figure 6.7: **Different planarization regimes.** (a) Low degree of planarization: the planarizing material closely follows the underlying topography. (b) Medium degree of planarization: the planarizing matieral loosely follows the underlying topography. (c) High degree of planarization: The underlying topography is leveled out completely.

overflow at the etched mesa structure, a sufficiently thick film outside of the mesa to ensure enough distance from the loss-inflicting semiconductor substrate, and little steepness to avoid additional losses in the waveguide. Since typical plasmonic waveguide lengths are on the order of a few micrometers and therefore much smaller than the etching field sizes given by the in situ electron beam lithography, a medium degree of planarization as sketched in Figure 6.7b is sufficient. Considering that typical noble metals used in plasmonics can bend over obstacles [108], micro-trenching at the mesa sidewalls should not pose a problem but might be even favored, assuming that overflowing is avoided in that case.

In this work, intermediate coating IC1-200 was chosen as planarization material, which has been already used to fabricate plane layers for the intermediate field coupling approach in chapter 4. According to the manufacturer Futurrex, IC1-200 is applied as a smoothing spin-on dielectric for the planarization of topography in multilevel integrated circuits. Furthermore, a low refractive index of $n = 1.41$ is reported. After outbaking, IC1-200 turns out to be stable at liquid helium temperatures and insoluble in most chemicals. The latter is particularly important because in the further course, the planarization film should be compatible with the fabrication of plasmonic waveguides, for example via electron beam lithography.

In order to test the planarization behavior of IC1-200, cylindrical mesas are fabricated on a standard GaAs wafer via electron beam lithography. The processing parameters, for example, etching depth, are identical compared to the ones used for the in situ electron beam lithography described in section 6.2.1, with the difference that no quantum dots are contained on this test sample. Instead, the GaAs cylinders are written in a 4x4 pattern with 10 µm distance to the next row or column, respectively. After the etching process, the sample is investigated via atomic force microscopy (AFM).

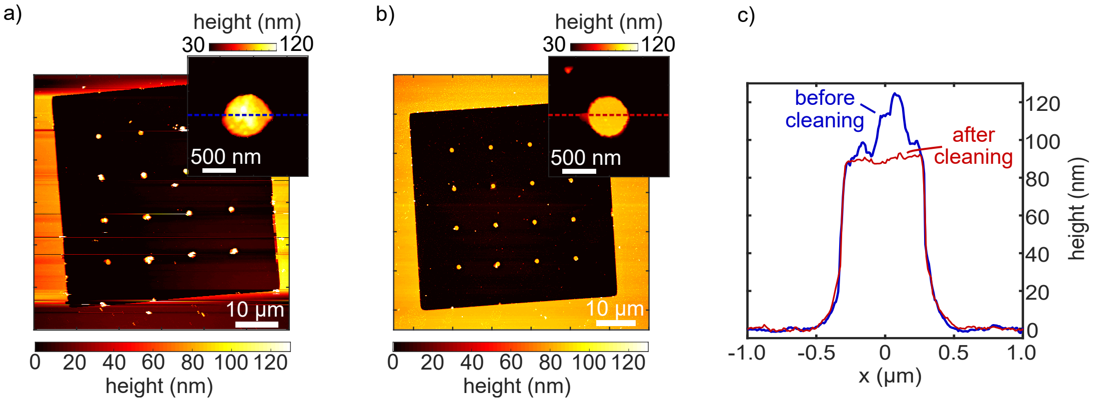

Figure 6.8: **Atomic force microscope images of a GaAs wafer containing a field of nanopillars that are structured via electron beam lithography and etching.** Sample surface before (a) and after (b) a cleaning procedure to remove any residual resist remaining from the fabrication process. The inset depicts an enlarged view of the same mesa. (c) Height profile of the same mesa before and after the cleaning procedure.

One field containing 16 nanopillars is shown in Figure 6.8a. From the AFM image, it is obvious that there is resist from the lithography process remaining on top of most mesas, which produces scanning artifacts. The inset shows a mesa in an enlarged view, where the resist residues are clearly visible. This is problematic since it is particularly important that the plasmonic waveguide is brought close to the mesa top surface. Furthermore, a large obstacle can hinder planarization in its indirect vicinity. Therefore, a cleaning procedure including three rounds of acetone ultrasonic baths and subsequent O_2-plasma ashing (Zepto Q Spezial, Diener) is carried out. The result can be seen in Figure 6.8b: Now, the height of the mesas match the height of the unprocessed region, as expected. Only very few mesas still have resist residues on top. The highlighted mesa shown in the inset features a very smooth surface. Figure 6.8c compares height profiles of the same mesa before and after the cleaning procedure. For this specific mesa, up to 30 nm of resist have been removed from the top of the mesa, an amount definitely relevant for efficient coupling. Since the mesa height matches the height of the unetched surface, one can assume the remaining resist is removed completely.

With a clean and well-defined topography at hand, the planarization properties of IC1-200 can be tested. Therefore, the etched GaAs wafer is coated with IC1-200 three times and AFM images are recorded after each spin-coating step. The corresponding height profiles along a line cut connecting four cylindrical mesas with diameters of 1000 nm each are given in Figure 6.9a. The red curve at the bottom shows the height profile before spin-coating. In the first round of spin-coating, a nominal thickness of $\Delta t_1 = 90\,\text{nm}$ is used, identical to the etching depth. The film thickness is taken from the spin-coating curves which have been measured for planar films on GaAs samples and are given in section 3.3. Since the AFM measures only relative topography, the actual film thickness would need to be determined from a control experiment. Here, it is assumed that the film thickness of $5 - 10\,\mu\text{m}$ next to the etch edge is the same as it was measured on an unstructured plane substrate. This assumption is justified since the height profiles seem to flatten out at the end of the measured region but might introduce some inaccuracy. To estimate this inaccuracy, the actual film thickness far away from the etched field was measured via whitelight reflection spectroscopy (see section 3.3) after the third spin-coating step and determined to be $335 \pm 5\,\text{nm}$, which is about 9 % smaller than the film thickness expected from the nominal values.

As expected, the first spin-coating step completely fills up the etched valley (pink curve). The mesas are overflown to about 40 nm, which is less than the planar film thickness; the planarization behavior, therefore, could be described by "smoothing steps". The second (purple curve) and third (blue curve) spin-coating steps nominally add $\Delta t_2 = 78\,\text{nm}$ and $\Delta t_3 = 115\,\text{nm}$ to the first layer and continue to smooth the underlying geometry. The degree of planarization (as defined in Equation 6.4) increases from $\text{DOP} = 0.52$ in the first step to $\text{DOP} = 0.69$ in the second step to $\text{DOP} = 0.81$ in the final step. It should be noted that the aspect ratio of the axes in Figure 6.9a strongly exaggerates the height differences in comparison to the

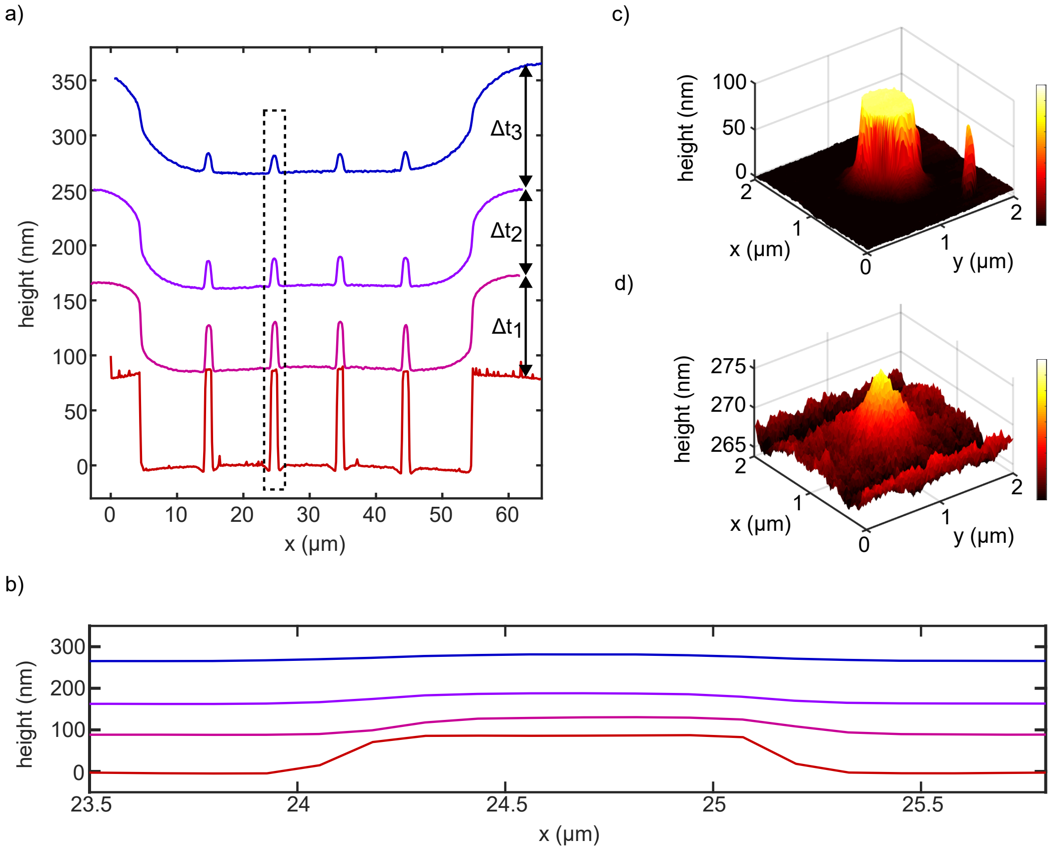

Figure 6.9: **Topography changes after multiple rounds of spin-coating IC1-200 on top of the GaAs nanopillar sample from Figure 6.8, measured with an atomic force microscope.** (a) Height profile of the etching field along a line cut including four cylindrical mesas with diameters of 1000 nm. From bottom to top, the curves correspond to the height profile before spin-coating as well as the height profiles after consecutive spin-coating with a nominal film thickness of $\Delta t_1 = 90\,\text{nm}$, $\Delta t_2 = 78\,\text{nm}$, and $\Delta t_3 = 115\,\text{nm}$, respectively. (b) Detail of the pillar that is highlighted by the dashed box in (a), plotted with equal axis ratio of height and x-coordinate. (c, d) Topography of a pillar with a diameter of 500 nm before spin-coating (c), and a pillar with an identical diameter after three rounds of spin-coating IC1-200 (d).

x-coordinate. Figure 6.9b shows the topography of one pillar for an equal axis ratio for height and x-coordinate. In this representation, the planarizing effect becomes more clear. Figure 6.9c and Figure 6.9d compare the measured height profile of two individual mesas with 500 nm in diameter before and after the spin-coating procedure. Before the planarization, the steep sidewalls and the plateau at the top surface of the mesa are clearly visible. After the planarization, the topography is flattened substantially, so that the residual height difference is only slightly larger than the surface roughness of the IC1, typically a few nanometers. Obviously, this comes at the cost of bringing up more and more material. If a DOP of 80 % would be targeted, more than 250 nm of IC1-200 would be necessary.

Even though high degrees of planarization can be achieved with IC1-200, the spin-coating process always leaves material on top of the mesa. Already in the first spin-coating step, the mesas are overflown to about 40 nm, increasing the distance between the buried quantum dot and the nanowire on top. The resulting dielectric gap restricts the efficiency of the nanocircuit, which has been shown in the simulations at the beginning of this chapter (see again Figure 6.1). If less material is brought up, the overflow would be reduced and the coupling enhanced; however, larger propagation losses "behind" the mesa will arise due to the reduced distance between the nanowire and the semiconductor substrate. From this consideration, it is clear that more advanced planarization methods are necessary to facilitate efficient coupling and a plasmonic Purcell effect while maintaining low-loss propagation at the same time. Some first steps towards alternative planarization routes have been taken in this work, which are collected in section 6.5.2 at the end of this chapter. Nevertheless, according to Figure 6.1e, the overall waveguide efficiency of the mesa geometry is still expected to be a factor of two to six higher than for the intermediate field geometry, for dielectric gaps of the expected size. Furthermore, the dielectric overflow might be reduced for smaller mesa, which has not been investigated here. Therefore, a sample containing integrated GaAs quantum dot is planarized by spin-coating IC1-200 and silver nanowires are interfaced in the next section.

6.4 COUPLING BETWEEN INTEGRATED QUANTUM DOTS AND SILVER NANOWIRES

In this section, the integrated GaAs quantum dots which have been characterized in section 6.2 are interfaced with silver nanowires to demonstrate photoluminescence coupling to plasmonic waveguide modes. At first, the etched quantum dot sample is cleaned from resist residues via ultrasonic baths. Following the description in section 6.3, IC1-200 is spin-coated with a target thickness of 90 nm. This corresponds to the first step of the planarization cycle given in Figure 6.9. After outbaking the sample at 200 °C, colloidal silver nanowires (PL-AgW100, PlasmaChem) are dispersed on top of the planarized sample. Both the nanowires and their dispersion is identical to the description in section 4.3. An overview electron micrograph of the resulting sample is shown in Figure 6.10, clearly resolving both the mesa structures and the nanowires.

It is known from the previous sections that – except for the very small mesas – all mesa structures contain a (functional) quantum dot due to the deterministic lithography. However, the position of the nanowires can not be controlled in the dispersion process, resulting in a random assembly in the second step of the sample preparation. As can be derived from SEM images similar to Figure 6.10, only eight of 220 fabricated mesas (corresponding to 3.6 %) are interfaced with a silver nanowire, neglecting very short or heavily kinked nanowires. One example of a "promising" candidate can already be seen in the center of Figure 6.10.

In order to demonstrate coupling between an integrated quantum dot and a silver nanowire, an optical microscope is used, as shown in Figure 3.6. The setup allows to

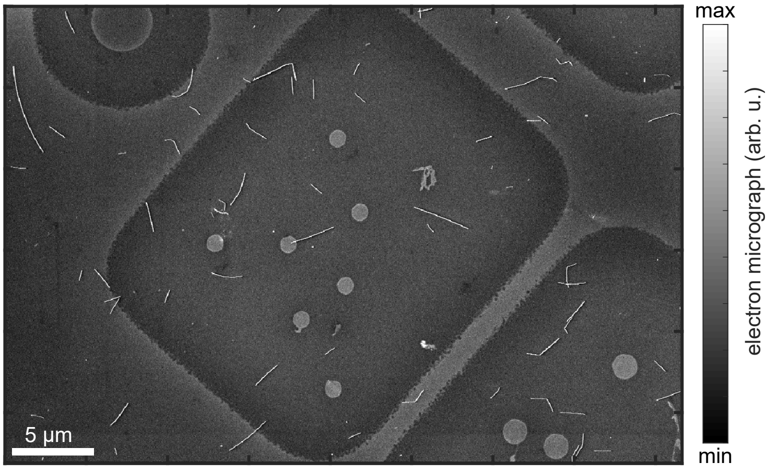

Figure 6.10: **Electron micrograph of the sample containing integrated GaAs quantum dots and silver nanowires.** The cylindrical mesas are fabricated by in situ electron beam lithography and planarized by spin-coating the dielectric IC1-200. Wet-chemically grown silver nanowires are dispersed on top.

image nanowires and quantum dots simultaneously by mixing reflected whitelight and photoluminescence, a convenient method that is described in greater detail in section 3.2.4. In Figure 6.11a, a mesa with a diameter of 650 nm and a silver nanowire on top is imaged onto the CCD camera, applying this mixed contrast technique. For further confirmation, also a conventional darkfield microscope (Olympus GX51, equipped with a Thorlabs DCC1645C CMOS camera) image of the same nanostructure is shown in Figure 6.11b. Since darkfield mode detects scattered photons, only the edges of the mesa are bright while the center appears darker. Due to the limited optical resolution, the effect becomes more clear for mesas with larger diameters. Nevertheless, both the mesa and the nanowire are clearly visible and consistent with the whitelight illumination image. Finally, coupling is demonstrated in Figure 6.11c. Here, an excitation laser at a wavelength of $\lambda = 635\,\text{nm}$ is focused on the integrated quantum dot, and photoluminescence of the surrounding sample region is imaged onto the CCD camera. Apart from the direct quantum dot emission, another emission spot is detected at the nanowire end, about 50 times weaker in intensity. Surface plasmons are launched by the quantum dot, propagate along the nanowire, and scatter into the microscope objective. Spatial filtering at the entrance slit of the monochromator allows to separate the weak SPP emission from the direct quantum dot emission. The comparison of the corresponding photoluminescence reveals identical spectra, which are shown in Figure 6.11d. For better visibility, both spectra are normalized to their maximum intensity. The quantum dot spectrum is rather broad and lacks an excitonic line. As discussed in section 6.2.2, this is not necessarily a consequence of the sample processing, but rather caused by the age of the quantum dot sample.

Unfortunately, the mesa–nanowire hybrid shown in Figure 6.11 is the only nanosystem where coupling could be observed from a clear SPP emission. Nevertheless, one

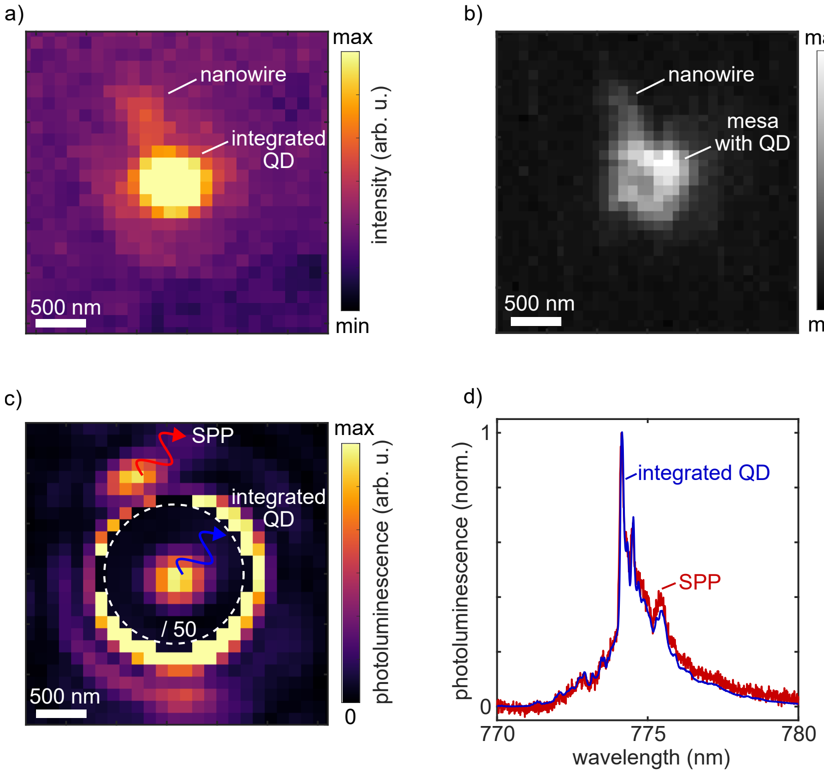

Figure 6.11: **An integrated GaAs quantum dot is coupled to a silver nanowire, which is demonstrated by launching surface plasmons.** (a) Microscope image of the coupled mesa–nanowire hybrid under whitelight illumination. Both photoluminescence and reflection are detected by the CCD camera. (b) Darkfield microscope image of the same nanostructure. (c) Surface plasmons are launched by the integrated quantum dot's photoluminescence, while the excitation laser is stationary focused on the mesa structure. The region around the mesa is software attenuated by a factor of 50. (d) Integrated quantum dot and scattered surface plasmon show identical (normalized) spectra.

could try to infer a coupling efficiency and compare it with the intermediate field coupling scheme discussed in chapter 4. Even though highly simplified, we apply Equation 4.15, where propagation losses, wire end reflectivity, and far field collection rates are used to obtain the experimental coupling efficiency from the SPP and quantum dot emission ratio as given in Figure 6.11c. Basically, the mesa–waveguide structure is treated like a nanosystem for the planar intermediate field geometry. We correct propagation losses along a length $L = 1.08\,\mu\text{m}$, which is the distance between both emission spots, and assume a propagation length of $L_{prop} = 0.86\,\mu\text{m}$, the same value as determined for the intermediate field geometry. Furthermore, we take the wire termination reflection coefficient $r = 0.65$ and the far field collection efficiency ratio $\eta_{spp,ff}/\eta_{qd,ff} = 17$ from the same consideration. This leads to a hypothetical coupling efficiency $\eta_{in,exp} = 0.45\,\%$ in the same order of magnitude as observed for the intermediate field coupling (see Figure 4.11c). Of course, this value is afflicted with high uncertainty: the propagation losses might be underestimated since the nanowire is closer to the GaAs, especially at the beginning of the wire; also a bending of the nanowire could cause additional losses. Other than in Figure 4.11c, we do not correct for a lateral displacement of the quantum dot, since the exact position is unknown for this specific case. The far field radiation pattern might be changed due to the mesa, even though the far field photoluminescence images did not exhibit substantial changes if the excitation laser is focused directly on the quantum dot. Taken together, it seems that the mesa–nanowire structure does not outperform the intermediate field coupling in terms of coupling efficiency. However, more functional nanosystems would be necessary to confirm this.

To better understand the coupling between the integrated quantum dot and the silver nanowire, more precise imaging techniques would be needed. In chapter 4, cathodoluminescence was established as a powerful imaging method, since it allows the precise localization of nanowires and quantum dots and therefore an exact determination of the coupling distance. For the mesa-supported coupling, the quantum dot–nanowire positions need to be measured relative to the mesa, which obviously changes the dielectric environment and therefore the coupling. Unfortunately, no high-resolution cathodoluminescence images could be recorded for the coupled system in Figure 6.11 due to sample damage during transport. However, for two other nanosystems, where no coupling is observed, cathodoluminescence images could be recorded and are shown in Figures 6.12a, c. In addition, AFM images of the same nanosystems are given in Figures 6.12b, d, respectively. Both data sets taken together give a very precise idea of the nanostructure, and, in principle, one could try to mimic the exact geometries in three-dimensional finite element simulations. However, it is not clear what could be learned from such an extensive study of individual nanosystems, which vary in several geometric parameters. Moreover, the dipole moment orientation introduces another degree of freedom.

Nevertheless, one could speculate why no coupling to surface plasmons is detectable for these systems. For the nanosystem in the upper part of Figure 6.12, it is apparent from the cathodoluminescence image that the quantum dot is located "behind" the nanowire, at a distance of about 220 nm to the nanowire end. Consequently, the incoupling efficiency is expected to be small. In contrast, for the nanosystem shown in the lower part of Figure 6.12, the nanowire is located centered on top of the quantum dot, which itself is centered within the mesa. In this case, however, the large mesa diameter of 1500 nm could cause high propagation losses. This is supported by the simulations in Figure 6.1e, where the waveguide efficiency for a mesa diameter of 1500 nm is the smallest at moderate dielectric gap sizes. Eventually, destructive interference of direct surface plasmons and plasmons which are reflected at the near nanowire termination may occur.

From the AFM images of both nanosystems (Figures 6.12b, d), a bending of the nanowire over the edge of the mesa is clearly visible. For better visualization, the scaling of the height axis is different from the lateral axes. A bending radius of roughly 10 µm can be determined. Similar bending behavior has been observed for silver nanowires placed over shallow holes, fabricated via greyscale lithography by

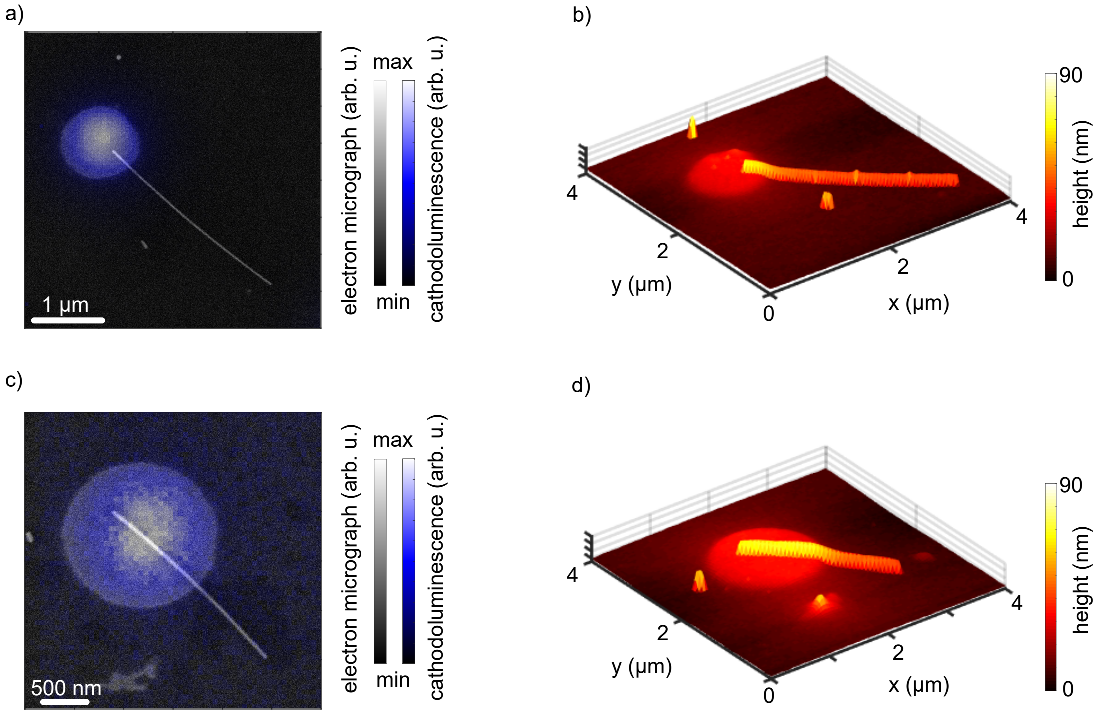

Figure 6.12: **Cathodoluminescence and atomic for microscope images of two mesa–nanowire systems.** No coupling is observed for these specific systems. (a, c) Cathodoluminescence images, overlaid with simultaneously recorded electron micrographs. (b, d) AFM images reveal the bending of the silver nanowire over the planarized mesa.

master student Julian Alin [101]. Guided plasmonic modes in bent silver nanowires with different diameters have been analyzed in literature [109, 110]. In [109], the pure bending loss in curved silver nanowires was determined experimentally to 6 dB at a bending radius of 10 µm. This is equivalent to a transmittance of 25 % after one bend; however, for the situation here, two bends are probably the more accurate description, even though the exact topography might be somewhat more complicated. According to this estimation, the bending losses are substantial for the present sample geometry. However, it needs to be noted that in [109], silver nanowires with much larger diameters, namely 750 nm, have been used. This might affect the conversion to free space radiation, which is the reason for the SPP attenuation at the bending site.

In summary, it has been experimentally demonstrated that GaAs quantum dots integrated into cylindrical mesas can couple to silver nanowires by launching surface plasmons. Due to the probabilistic nanowire dispersion, only a few mesa–nanowire pairs with close lateral distances could be manufactured; for the majority of them, no coupling to surface plasmons is observed. The surface plasmon emission intensity for the coupled mesa–nanowire system seems comparable to the intermediate field coupling. This is probably caused by imperfect planarization, which reduces the coupling efficiency and leads to additional propagation losses due to a bending of the nanowire.

6.5 ROUTES TOWARDS HIGHLY EFFICIENT COUPLING AND SCALABLE DESIGNS

For the ultimate goal of an efficient single-plasmon source, two major aspects need to be optimized. Firstly, the planarization of the mesa is weak. More sophisticated planarization methods need to be applied, to level the filling material with the top surface of the mesa. This would enhance the coupling efficiency and avoid bending losses. In order to further reduce propagation losses, the etching depth could be increased. The second major aspect is the lack of deterministic waveguide alignment due to the random nanowire assembly. For a perfectly planarized mesa structure, the alignment robustness of the intermediate field approach is no longer present and lateral coupling distances at the order of 10 nm are necessary. In this case, a random nanowire assembly is not a reasonable option, particularly when only a limited number of integrated quantum dots are fabricated. First steps towards an optimized mesa–waveguide nanostructure have been taken in this work, although the fabrication of such a device is yet to show. In the next section, paths towards advanced planarization and deterministic waveguide alignment are described.

6.5.1 *Approaching determinstic mesa–waveguide alignment*

The next step towards an integrated quantum plasmonic circuit could be the on-chip Hong-Ou-Mandel interference from separate quantum dots, which has been realized using dielectric waveguides [19]. It is clear that for such applications, a fully deterministic circuitry fabrication is necessary [111], especially when considering that spectrally identical ultra-narrowband quantum emitters need to interfere with each other. Since the in situ electron beam lithography (EBL) already controls the quantum dot integration deterministically, the focus here is on the positioning of the plasmonic waveguide. With aligned EBL, this could be accomplished with high accuracy and in a scalable fashion. For example, *Pfeiffer et al.* [80] directly located near-surface GaAs quantum dots via a specific feature in the electron micrograph, achieving a 10 nm alignment accuracy; the AlGaAs mesas could serve a similar purpose.

Since evaporated metal structures on glass coverslips usually offer high contrast in SEM images, a test sample based on such structures is designed (see Figure 6.13). In a first EBL step, large markers with a size of $\sim$ 50 µm are written into the e-beam resist, which are not shown in Figure 6.13. Later, these serve to relocate the position of the target structures on the substrate, for example with respect to the substrate corner. Furthermore, smaller markers of the "touching rectangle"-type are written, here at the corners and in the middle of each writing field. Furthermore, target structures in the form of rectangles with dimensions of 300 nm x 800 nm are written. After development, gold evaporation, and subsequent lift-off, the sample is coated with resist again. Now, the target structures are relocated using the markers without exposing the area around the target structures. In the next critical step, a write field alignment needs to be conducted. Therefore, the position of at least three "touching rectangles" needs to be read out in order to adjust the SEM coordinate

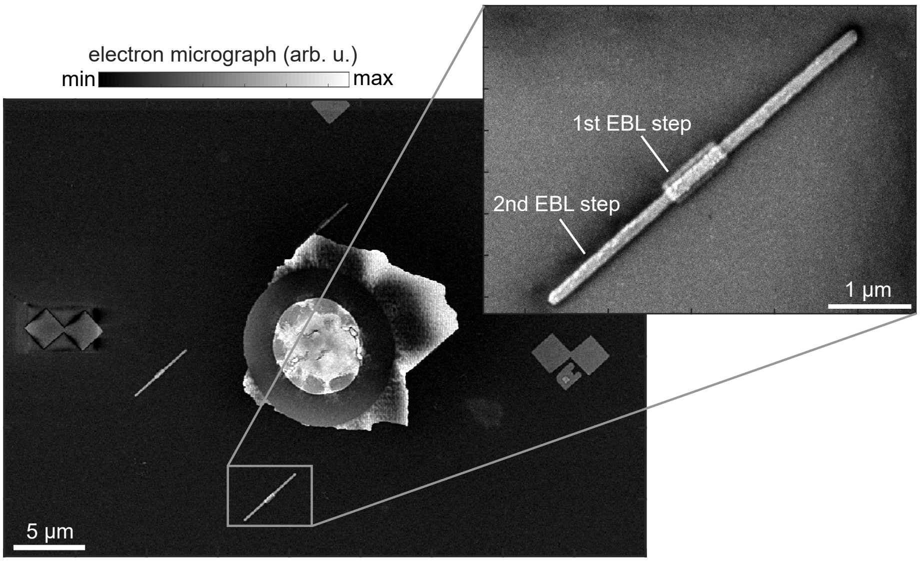

Figure 6.13: **Aligned electron beam lithography performed on a glass substrate with evaporated metal structures.** Markers and target structures are written in a first step of EBL. In a second step, a waveguide is written in alignment with the target structure. The inset shows a magnified version of the 1st and 2nd EBL steps.

system for scaling, shift, and rotation. This process can result in overexposure at the marker in the middle of the write field, as can be seen in Figure 6.13. Using the corrected coordinate system, the aligned structure is written, in this case, a waveguide with a width of 180 nm and a length of 2.4 µm. After development, silver evaporation, and lift-off, the final structure as shown in Figure 6.13 is obtained. For the magnified structure in the inset, the relative displacement can be determined to 136 nm, while other structures show even larger displacements. In order to draw conclusions about the relatively high inaccuracy, a plasmonic grating structure extending over the complete write field is written in both the first and second EBL step. It is found that the alignment accuracy varies systematically over the write field, indicating an incorrect write field alignment. However, the shown sample is only a first step towards a controllable positioning, and further tests need to be performed.

In the future, the described aligned EBL process could be adapted to GaAs-based samples by including marker structures during the in situ EBL and subsequent etching. The positions of the integrated quantum dots could then be measured relative to the markers through cathodoluminescence, yielding high spatial resolution (see for example Figure 4.11). By reading out these markers, the plasmonic waveguides can then be aligned with respect to the quantum dots. This should enable a similar high positioning accuracy as *Pfeiffer et al.* [80]. Consequently, the combination of marker-based in situ EBL for the quantum dot integration and marker-aligned EBL for the plasmonic waveguide structuring allows a completely deterministic process flow with highest alignment accuracy.

6.5.2 *Possible schemes for an optimized planarization*

Numerical simulations (for example in Figure 6.1) show that highly efficient coupling and a plasmonic Purcell enhancement are only possible when the plasmonic waveguide comes very close to the AlGaAs mesa. Furthermore, it has been shown that the planarization of IC1-200 by spin-coating inevitably leaves material on top of the mesa, which limits the device efficiency distinctively. Therefore, more advanced planarization techniques are necessary; three possible solutions are presented in the following, for which the first steps have been taken in the course of this thesis.

The first planarization idea includes the spin-coating of an etch-sensitive material on top of the integrated mesa structures, as sketched in Figure 6.14a. If the film thickness is large compared to the mesa height, a high degree of planarization can be achieved according to Figure 6.9. Depending on the actual material and film thickness, the underlying topography should be flattened to a large extent. In the second step, the material is etched down until the planarization layer levels with the top surface of the mesa. Obviously, the challenge is to avoid over-etching and exposing the mesa structures. At the Reitzenstein group, this process was tested using the photopolymer benzocyclobutene (BCB). By repeated dry etching and subsequent measurement of the BCB film thickness by a profilometer, the etching rate was determined. Angled SEM images suggest a successful planarization of a few nanostructures; however, the resulting BCB layer is not uniform in height, which heavily reduces the planarization yield. This could be caused by an inhomogeneous BCB film already after the spin-coating process. Therefore, further optimization of this process is necessary. Instead of BCB, also PMMA can be used. First tests with the e-beam resist AR-P 662.04 on a GaAs-based sample suggest a uniform decrease of the film thickness after a few minutes in low-pressure O_2-plasma, which is already visible with the eye due to a color change caused by thin-film interference. This should be a relatively straightforward approach to obtain better planarization results.

A different planarization idea, suggested by master student Julian Alin [101], could be the use of a greyscale photoresist, as shown in Figure 6.14b. These kinds of photoresists allow to control the amount of material that is removed during development through the dose of light exposure. Since the mesa can be optically resolved (see Figure 6.3b), a laser with a wavelength around $\lambda = 400\,\text{nm}$ can be focused onto the mesa. By carefully adjusting the light dose within the Gaussian focus, predominantly the overflown material is exposed. In subsequent development, this material is removed, leaving a flat surface.

Both planarization routes are based on e-beam- or photoresists, which are typically not used in a permanent device since they might dissolve in further processing. This needs to be considered for the design of the plasmonic waveguides which follows after the planarization. Even though some resist films are stable after an outbake, others might dissolve in common solvents that are routinely used during subsequent lithography or for the dispersion of nanowires. A simple workaround, as done by

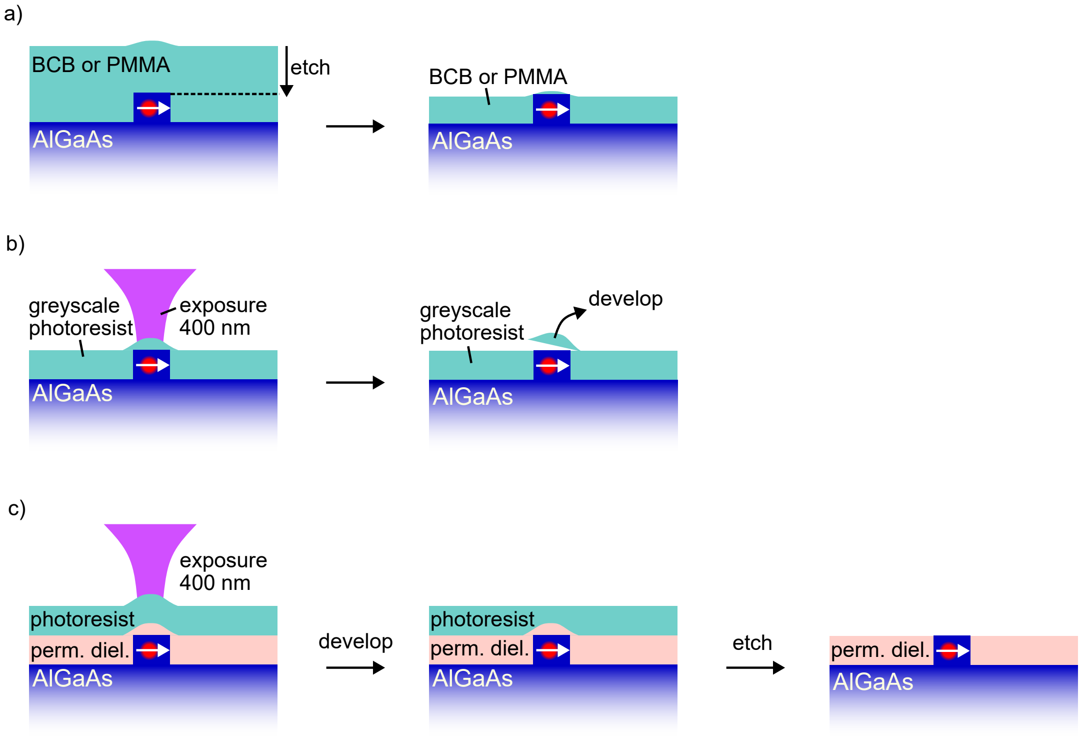

Figure 6.14: **Suggestions for an optimized planarization process.** (a) Planarization by etching down a film of BCB or PMMA, which is thick in comparison to the mesa height. (b) Selective planarization with a greyscale photoresist. Only the material on top of the mesa is removed during development. (c) By combining the exposure and development of a greyscale photoresist with a subsequent etching step, a permanent device could be designed.

Julian Alin, is to apply nanowires that are dissolved in water instead of isopropanol. However, other solutions are needed if EBL fabricated waveguides are considered. In order to achieve this, the planarization methods in Figure 6.14a and 6.14b could be combined, as sketched in Figure 6.14c: At first, a permanent but etch-sensitive dielectric is spin-coated. Afterwards, a greyscale photoresist is applied on top. The overflown material on top of the mesa is exposed to blue light and developed. This creates a flat surface, which finally is etched down to the top surface of the mesa, leaving only the permanent dielectric. Of course, this approach is technologically more challenging and affords a delicate choice of materials. However, it could enable the scalable design of efficient quantum plasmonic nanocircuits via lithography.

6.6 SUMMARY

In this chapter, a simple plasmonic nanocircuit based on GaAs quantum dots embedded in nanopillars has been realized. For the sake of easier nanofabrication, the quantum dots are kept on the GaAs substrate used for epitaxial growth. Numerical simulations show that the resulting waveguide efficiency of up to 10 % is worse than for a silver backplane, but better than intermediate field coupling, as long as the dielectric gap between the mesa and the waveguide is small. The successful integration of near-surface grown GaAs quantum dots into cylindrical mesa structures via in situ electron beam lithography is demonstrated and the properties of the processed quantum dots are characterized through photo- and cathodoluminescence. For both techniques, a decrease in the spatial width of the luminescence spots is observed for smaller pillar diameters, which can be consistently explained by a diminished diffusive excitation as a consequence of the etching process. However, the emission properties of the integrated quantum dots do not seem to differ from their unprocessed counterparts for mesa diameters down to 300 nm. The planarization of the etched nanopillars with the dielectric spin-on-glass IC1-200 results in the formation of hills on top of the mesa structures, leading to a dielectric gap of about 40 nm between the mesa surface and the dispersed silver nanowires.

Nevertheless, a functional nanocircuit is observed where quantum dot photoluminescence launches surface plasmons in the nanowires, although the waveguide efficiency is comparable to intermediate field coupling. A curved nanowire as a result of hill forming might introduce additional propagation losses. Three major challenges are identified for future optimization of the nanocircuit: First, a low-index dielectric or metallic backplane is necessary to boost the coupling and propagation efficiency. Second, the planarization process needs to be optimized. This could be achieved through an additional etching step or selective planarization of bumps, for example by the application of a greyscale photoresist. Finally, the probabilistic assembly of silver nanowires needs to be replaced by targeted positioning to increase the yield of potentially coupled structures. This could be achieved by an aligned electron beam lithography step following the deterministic nanopillar etching.

7

CONCLUSION AND OUTLOOK

This thesis is dedicated to the study of light-matter interaction at the single quantum emitter level. In particular, epitaxially grown GaAs quantum dots and their coupling to propagating surface plasmon are investigated both experimentally and numerically. Such a coupled quantum dot–plasmon system is envisioned for an on-chip single-photon source that could lead to nanoscale photonic quantum information processing devices [7, 10, 12]. It combines the extraordinary quantum optical properties of self-assembled quantum dots [18, 77] and the sub-diffraction confinement and guiding of light through plasmonic waveguides [3, 57]. While other quantum emitters have been repeatedly and efficiently coupled to propagating surface plasmons [82], there are few experiments using self-assembled quantum dots [21, 22] despite their superior properties as single-photon sources. The thesis addresses several key issues towards the far-reaching goal of a quantum plasmonic nanocircuit based on epitaxial quantum dots as sources of single photons. Most prominent, the already omnipresent and inherent losses of sub-wavelength plasmons [112] increase even more when interfaced with high-index semiconductors such as GaAs. The quantum dot host material, namely the AlGaAs barrier required for quantum confinement, also affects photon extraction and subsequent coupling to plasmonic waveguide modes. Other challenges include the deterministic fabrication and controlled positioning of quantum dot–waveguide structures, as well as the preservation of (quantum) optical properties through nanostructuring processes.

Chapter 4 introduces an innovative yet simple coupling concept where a dielectric spacer layer of lower refractive index balances propagation and coupling efficiency. Numerical simulations show that the highest overall efficiency for such a geometry is achieved for spacer thicknesses around 130 nm, meaning that the coupling is mediated by the intermediate field of the assumed dipole emission. A probabilistic sample design involving randomly dispersed colloidal silver nanowires requires suitable sample screening routines to identify coupled quantum dot–nanowire systems at cryogenic temperatures. While all-optical microscopy allows rapid sample imaging, cathodoluminescence scanning provides a highly precise localization of quantum dots and nanowires with a lateral accuracy of $< 30\,\text{nm}$. Intermediate field coupling is demonstrated through launching surface plasmons by single GaAs quantum dots and detecting them by nanowire end scattering. Interference of direct plasmons and plasmons reflected at a nearby nanowire end spatially modulates the experimentally observed coupling efficiency, which is about 1 %. By combining the knowledge of the exact relative quantum dot positions and the numerically obtained mode profiles, the semi-analytical interference model comprehensively explains the observed coupling efficiencies for a total of nine nanosystems; the obtained fit parameters, including the complex effective mode index and the complex reflection coefficient of the nanowire end, yield reasonable values when compared with literature.

Chapter 5 approaches the coupling of single epitaxial quantum dots to plasmonic waveguides in a more general way. A dielectric–plasmonic nanostructure featuring a quantum dot that is partly released from its semiconductor host is numerically studied. Such a mesa structure promises high coupling efficiency and efficient propagation, especially when the GaAs substrate is replaced by a silver backplane. It is found that the semiconductor mesa acts as a dielectric nanoresonator for the quantum dot emission, and that the Purcell enhancement and the waveguide coupling strongly depend on the geometric dimensions of the mesa. More specifically, the emission of a dipole inside a disk-shaped AlGaAs mesa can be strongly enhanced ($F_p > 11$) or suppressed ($F_p < 0.05$) for certain (manufacturable) radii and heights. While the case of emission enhancement might be interesting for ultrafast single-plasmon sources, the case of emission suppression could lead to a highly efficient single-plasmon device: If a silver nanowire is offered to the dipole that would have been suppressed by the dielectric nanoresonator, a waveguide efficiency of 45 % is expected for a radius of $r = 180\,\mathrm{nm}$ and a height of $h = 290\,\mathrm{nm}$ of the AlGaAs mesa on a silver mirror. This means that almost every second photon emitted by the quantum dot can be detected after 2 µm of plasmon propagation on the silver nanowire.

Chapter 6 focuses on the experimental realization of a coupled mesa–waveguide nanostructure. In contrast to chapter 5, where mostly structures with a silver backplane are numerically investigated, the experimentally studied structures are based on GaAs substrates. This simplifies the fabrication process, since no substrate transfer is required, but also affects the overall waveguide efficiency due to increased radiation and propagation losses, which is expected to be 10 % at best for GaAs substrates. Nevertheless, this would still outperform intermediate field coupling, where the waveguide efficiency does not exceed 0.5 % for 2 µm long nanowires. Single GaAs quantum dots are deterministically integrated into disk-shaped mesa by in situ electron beam lithography. This process localizes quantum dots through cathodoluminescence and allows to pattern arbitrary structures by dry etching. A detailed photo- and cathodoluminescence spectroscopic study finds no significant degradation of the integrated GaAs quantum dots. An observed broadening of the luminescence spots is explained by the spatial restriction of charge carrier diffusion due to the missing semiconductor material in the surroundings of the mesa. In the next fabrication step, a dielectric layer is spin-coated to planarize the topography after etching. Although a high degree of planarization can be achieved, the underlying topography is partially transferred to the dielectric. Consequently, after the dispersion of silver nanowires, a dielectric gap is formed between the top surface of the mesa and the nanowire. Such a low-index gap of about 40 nm is found to be detrimental to the coupling efficiency in simulations. Coupling of integrated GaAs quantum dots to silver nanowires by surface plasmons is observed for a single nanostructure. The detected plasmon emission is comparable to that measured in chapter 4. In addition to the detrimental effects described above, a bent nanowire, as observed in atomic force microscope images, could introduce additional propagation losses. However, more coupled nanosystems would be necessary to quantitatively compare both approaches.

In summary, two different coupling concepts for epitaxial quantum dots and plasmonic waveguides are realized. *Intermediate field coupling* can be achieved without any nanostructuring processes, so that the quantum dots are preserved in their semiconductor host material. The robust leaky mode coupling scheme allows the use of deeply buried quantum dots, or quantum dots embedded in functionalized structures, which have demonstrated exceptionally narrow linewidths close to the Fourier limit [95, 113, 114]. Hence, intermediate field coupling is a candidate for a previously unreported solid-state source of indistinguishable plasmons [45]. The generation of polarization-entangled plasmons via the biexciton-exciton cascade could be another feasible goal [18]. An obvious drawback is the comparatively low coupling efficiency and the radiative losses during propagation. Both aspects are addressed by *mesa-based coupling*, which can be designed either for enhanced overall decay rates or for highly efficient single-plasmon generation. Unprecedented efficiencies of more than 50 % for the coupling of epitaxial quantum dots to plasmonic waveguides are obtained in simulations. Of course, the experimental realization described in this thesis suffers from serious limitations; to achieve a nanostructure closer to the idealized one, a substrate transfer to silver or gold, as well as an optimized planarization process, will be required. Instead of a metallic backplane, a distributed Bragg-reflector could increase the coupling efficiency but might still be associated with significant propagation losses. Increasing the distance between the nanowire and the semiconductor substrate could reduce these propagation losses; such a design would feature a relatively tall nanopillar to accommodate the quantum dot. Instead of a disk-shaped mesa, other geometries that respect the preferential direction given by the waveguide could provide more efficient plasmon generation.

If one shifts the goal from singular proof-of-concept structures to more applicable designs, the inevitable losses of nanoscale plasmonic waveguides in the visible and near-infrared are often considered a show-stopper [112]. One could increase the propagation length to some extent by using wider waveguides at the propagation parts and narrow waveguides at the coupling site. However, the device footprint could become comparable to the dielectric platform, where transmission losses are much lower. Embracing this fact, a scalable design could include dielectric waveguides for long-range propagation and mode conversion to a plasmonic waveguide that couples to the quantum emitter, as originally proposed by *Chang et al.* [12]. Efficient dielectric-to-plasmonic mode conversion schemes are available [22, 115]. Broadband coupling to dielectric waveguides could be combined with plasmonic cavities or antennas to manipulate the radiative decay rate [80, 116, 117] or to boost waveguide directionality [118].

A different, all-plasmonic design could accept the small propagation lengths by exploiting the sub-diffraction character of plasmonics, which allows feature sizes far below the Abbe criterion. Although convenient for experiments with far field optics, two remote emitters or other on-chip elements do not necessarily need to be separated by micrometers. In addition, the high refractive index of the semiconductor results in plasmon wavelengths that are much smaller than the free-space wavelength and consequently in an operation far from the light line of the plasmon dispersion. Strong plasmonic field gradients at metal-semiconductor interfaces have already been used to demonstrate the mesoscopic character of epitaxial quantum dots [56]. The associated high spatial resolution might allow separate addressing of two adjacent quantum emitters. Self-assembled quantum dot molecules [119] could be an example to demonstrate a controlled manipulation of coupled quantum emitters on a length scale below 100 nm. This could pave the way towards an ultra-compact, deep plasmonic quantum nanocircuit based on one of the best available sources of quantum light.

A
APPENDIX

A.1 QUANTUM DOT SAMPLE STRUCTURE

Figure A.1 shows the exact sample structure of the epitaxially grown quantum dots. Two slightly different types are used. The newer sample Sa665 (Figure A.1a) features a burial depth of 40 nm. The older samples O690, O691, and O692 (Figure A.1b) have burial depths of 15 nm, 20 nm, and 30 nm, respectively. In addition, these samples include an AlAs layer that can be used as a sacrificial layer for a release of the quantum dot membrane from the GaAs substrate [22]. The sample Sa665 has been grown in 2021 by S. Covre da Silva, while O69-type samples have been grown by Y. Huo around 2013, both in the group of A. Rastelli.

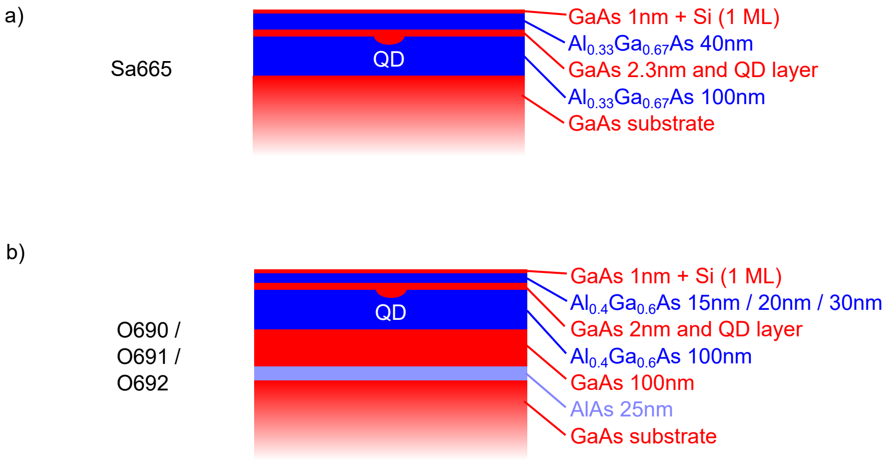

Figure A.1: **Sketch of the quantum dot sample structures used in this thesis.** The newer sample Sa665 (a) varies slightly with respect to the burial depth and an additional AlAs layer from the older samples O690, O691, and O692 (b).

A.2 ADDITIONAL NANOSYSTEMS FOR INTERMEDIATE FIELD COUPLING

Figure A.2 shows three additional data sets for quantum dot–nanowire systems (no. 3, 4, and 5 from Table 4.1) that are coupled via the intermediate field. Two coupled nanosystems have already been shown in Figure 4.7. Cathodoluminescence images with simultaneously measured electron micrographs are given in Figure A.2a. Photoluminescence images with overlaid reflection images, obtained by confocal laser scanning, are given in Figure A.2b. The nanowire outline from the SEM image in (a) is drawn as a dashed line, after a coordinate system correction that takes the cathodoluminescence image as reference. The waveguide propagation images that demonstrate intermediate field coupling are shown in Figure A.2c. Here, the quantum dot (red circle) is excited stationary by a focused laser, and the surrounding sample area, including the nanowire end (blue circle), is imaged onto a CCD camera.

For further confirmation, photoluminescence spectra of direct quantum dot emission (red line) and surface plasmon out-coupling (blue line) are compared in Figure A.2d. These spectra are measured by spatial filtering of the corresponding sample regions before the entrance slit of the monochromator. For better comparison, the spectra are normalized. The weaker intensity of the plasmonic emission is apparent from the noisier data. As expected, there is good agreement between direct quantum dot emission and surface plasmon emission. The excitonic emission line (X) features a linewidth of $60 - 80\,\mu\mathrm{eV}$, similar to the unprocessed quantum dots in Figure 2.4c. The line broadening is expected for near-surface grown quantum dots and caused by interaction of the exciton with surface states [43].

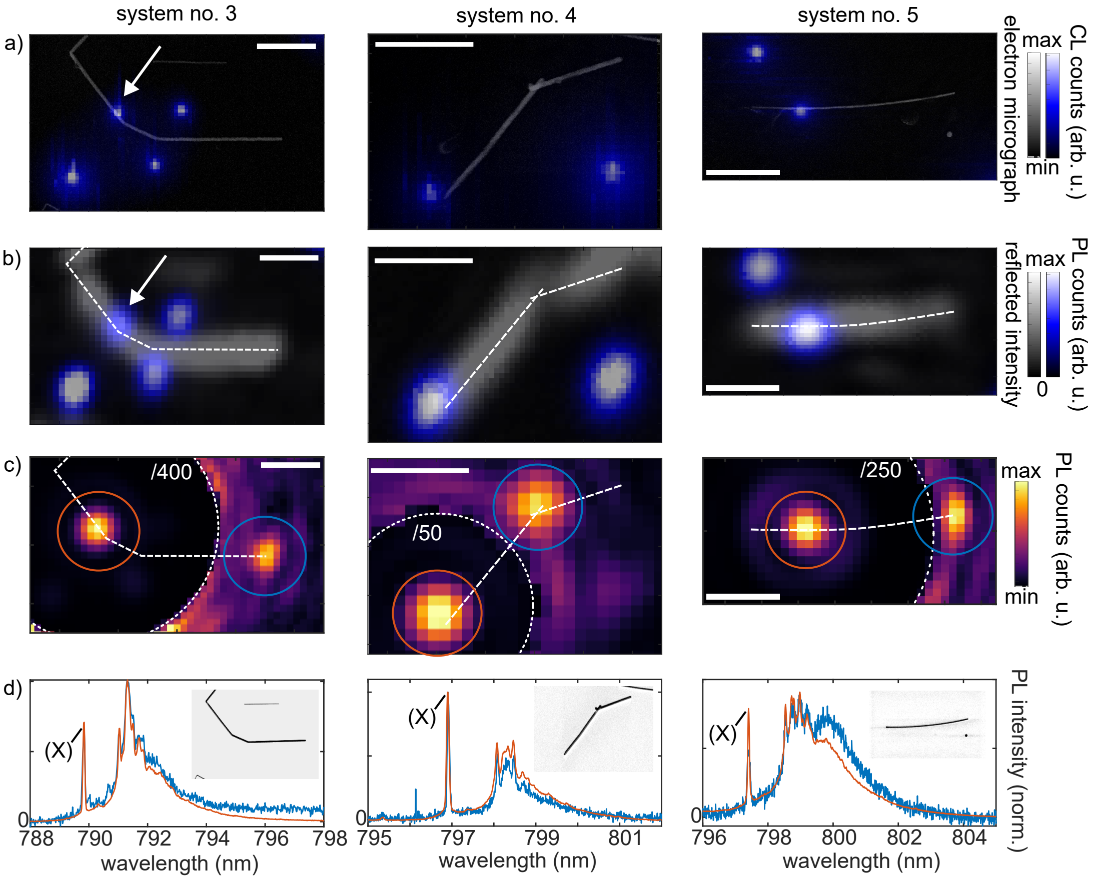

Figure A.2: **Additional data for three quantum dot–nanowire systems that are coupled via the intermediate field.** (a) Cathodoluminescence image overlaid with a simultaneously measured electron micrograph. (b) Photoluminescence image overlaid with a reflection image, measured by confocal laser scanning. The nanowire outline from the SEM image in (a) is drawn as a dashed line. (c) Waveguide propagation images, demonstrating the launching of surface plasmons by quantum dot luminescence. The red circle indicates the excited quantum dot, and the blue circle highlights the scattered plasmon at the nanowire end. For better visibility of the plasmon emission, the region around the quantum dot is software-attenuated. (d) (Normalized) photoluminescence spectra of the quantum dot emission (blue line) and the out-coupled surface plasmon (red line). The (X) indicates the excitonic transition line. Inset: room temperature SEM image of the respective nanowire. All scale bars are 1 µm.

BIBLIOGRAPHY

[1] E. Abbe. "Beiträge zur Theorie des Mikroskops und der mikroskopischen Wahrnehmung." In: *Archiv für mikroskopische Anatomie* 9 (1873), pp. 413–468. DOI: `https://doi.org/10.1007/BF02956173`.

[2] S. W. Hell and J. Wichmann. "Breaking the diffraction resolution limit by stimulated emission: stimulated-emission-depletion fluorescence microscopy." In: *Optics Letters* 19 (1994), pp. 780–782. DOI: `10.1364/OL.19.000780`.

[3] D. K. Gramotnev and Bozhevolnyi S. I. "Plasmonics beyond the diffraction limit." In: *Nature Photonics* 4 (2010), pp. 83–91. DOI: `https://doi.org/10.1038/nphoton.2009.282`.

[4] L. Novotny and N. Van Hulst. "Antennas for light." In: *Nature Photonics* 5 (2011), pp. 83–90. DOI: `10.1038/nphoton.2010.237`.

[5] N. Liu, M. Mesch, T. Weiss, M. Hentschel, and H. Giessen. "Infrared perfect absorber and its application as plasmonic sensor." In: *Nano Letters* 10.7 (2010), pp. 2342–2348. DOI: `10.1021/nl9041033`.

[6] P. Vasa and C. Lienau. "Strong light–matter interaction in quantum emitter/metal hybrid nanostructures." In: *ACS Photonics* 5.1 (2018), pp. 2–23. DOI: `10.1021/acsphotonics.7b00650`.

[7] M. S. Tame, K. R. McEnery, Ş. K. Özdemir, J. Lee, S. A. Maier, and M. S. Kim. "Quantum plasmonics." In: *Nature Physics* 9 (2013), pp. 329–340. DOI: `10.1038/nphys2615`.

[8] H. Groß, J. M. Hamm, T. Tufarelli, O. Hess, and B. Hecht. "Near-field strong coupling of single quantum dots." In: *Science Advances* 4.3 (2018), eaar4906. DOI: `10.1126/sciadv.aar4906`.

[9] O. Bitton, S. N. Gupta, and G. Haran. "Quantum dot plasmonics: from weak to strong coupling." In: *Nanophotonics* 8.4 (2019), pp. 559–575. DOI: `10.1515/nanoph-2018-0218`.

[10] A. V. Akimov, A. Mukherjee, C. L. Yu, D. E. Chang, A. S. Zibrov, P. R. Hemmer, H. Park, and M. D. Lukin. "Generation of single optical plasmons in metallic nanowires coupled to quantum dots." In: *Nature* 450 (2007), pp. 402–406. DOI: `10.1038/nature06230`.

[11] R. Kolesov, B. Grotz, G. Balasubramanian, R. J. Stöhr, A. L. Nicolet, P. R. Hemmer, F. Jelezko, and J. Wrachtrup. "Wave-particle duality of single surface plasmon polaritons." In: *Nature Physics* 5 (2009), pp. 470–474. DOI: `10.1038/nphys1278`.

[12] D. E. Chang, A. S. Sørensen, E. A. Demler, and M. D. Lukin. "A single-photon transistor using nanoscale surface plasmons." In: *Nature physics* 3.11 (2007), pp. 807–812. DOI: `https://doi.org/10.1038/nphys708`.

[13] S. Slussarenko and G. J. Pryde. "Photonic quantum information processing: A concise review." In: *Applied Physics Reviews* 6.4 (2019). DOI: `https://doi.org/10.1063/1.5115814`.

[14] P. G. Kwiat, K. Mattle, H. Weinfurter, A. Zeilinger, A. V. Sergienko, and Y. Shih. "New High-Intensity Source of Polarization-Entangled Photon Pairs." In: *Phys. Rev. Lett.* 75 (1995), pp. 4337–4341. DOI: `10.1103/PhysRevLett.75.4337`.

[15] C.-Y. Lu, D. E. Browne, T. Yang, and J.-W. Pan. "Demonstration of a Compiled Version of Shor's Quantum Factoring Algorithm Using Photonic Qubits." In: *Phys. Rev. Lett.* 99 (2007), p. 250504. DOI: `10.1103/PhysRevLett.99.250504`.

[16] J.-H. Kim, S. Aghaeimeibodi, C. J. K. Richardson, R. P. Leavitt, D. Englund, and E. Waks. "Hybrid integration of solid-state quantum emitters on a silicon photonic chip." In: *Nano Letters* 17.12 (2017), pp. 7394–7400. DOI: `10.1021/acs.nanolett.7b03220`.

[17] P. Senellart, G. Solomon, and A. White. "High-performance semiconductor quantum-dot single-photon sources." In: *Nature Nanotechnology* 12 (2017), pp. 1026–1039. ISSN: 17483395. DOI: `10.1038/nnano.2017.218`.

[18] D. Huber, M. Reindl, Y. Huo, H. Huang, J. S. Wildmann, O. G. Schmidt, A. Rastelli, and R. Trotta. "Highly indistinguishable and strongly entangled photons from symmetric GaAs quantum dots." In: *Nature Communications* 8 (2017). DOI: `10.1038/ncomms15506`.

[19] L. Dusanowski, D. Köck, C. Schneider, and S. Höfling. "On-Chip Hong-Ou-Mandel Interference from Separate Quantum Dot Emitters in an Integrated Circuit." In: *ACS Photonics* 10 (2023), pp. 2941–2947. DOI: `10.1021/acsphotonics.3c00679`.

[20] S. Hepp, M. Jetter, S. L. Portalupi, and P. Michler. "Semiconductor Quantum Dots for Integrated Quantum Photonics." In: *Advanced Quantum Technologies* 2.9 (2019), p. 1900020. DOI: `https://doi.org/10.1002/qute.201900020`.

[21] G. Bracher, K. Schraml, M. Blauth, J. Wierzbowski, N. C. López, M. Bichler, K. Müller, J. J. Finley, and M. Kaniber. "Imaging surface plasmon polaritons using proximal self-assembled InGaAs quantum dots." In: *Journal of Applied Physics* 116 (2014). DOI: `10.1063/1.4889859`.

[22] X. Wu, P. Jiang, G. Razinskas, Y. Huo, H. Zhang, M. Kamp, A. Rastelli, O. G. Schmidt, B. Hecht, K. Lindfors, and M. Lippitz. "On-Chip Single-Plasmon Nanocircuit Driven by a Self-Assembled Quantum Dot." In: *Nano Letters* 17 (2017), pp. 4291–4296. DOI: `10.1021/acs.nanolett.7b01284`.

[23] P. Harrison. *Quantum wells, wires, and dots: theoretical and computational physics of semiconductor nanostructures*. John Wiley & Sons, 2005. DOI: `10.1002/0470010827`.

[24] J. S. Blakemore. "Semiconducting and other major properties of gallium arsenide." In: *Journal of Applied Physics* 53 (1982), R123–R181. DOI: `10.1063/1.331665`.

[25] A. K. Saxena. “The conduction band structure and deep levels in $\mathrm{Ga}_{1-x}\mathrm{Al}_x\mathrm{As}$ alloys from a high-pressure experiment.” In: *Journal of Physics C: Solid State Physics* 13.23 (1980), p. 4323. DOI: 10.1088/0022-3719/13/23/018.

[26] P. Yu and M. Cardona. *Fundamentals of Semiconductors: Physics and Materials Properties*. 4th ed. Springer Berlin, Heidelberg, 2010. DOI: https://doi.org/10.1007/978-3-642-00710-1.

[27] P. Michler. *Single Semiconductor Quantum Dots*. 1st ed. Springer Berlin, Heidelberg, 2009. DOI: https://doi.org/10.1007/978-3-540-87446-1.

[28] C. Weisbuch and B. Vinter. *Quantum Semiconductor Structures: Fundamentals and Applications*. San Diego: Academic Press, 1991. DOI: https://doi.org/10.1016/B978-0-08-051557-1.50005-6.

[29] D. Huber, M. Reindl, J. Aberl, A. Rastelli, and R. Trotta. “Semiconductor quantum dots as an ideal source of polarization-entangled photon pairs on-demand: A review.” In: *Journal of Optics* 20 (2018). DOI: 10.1088/2040-8986/aac4c4.

[30] S. F. Covre da Silva, G. Undeutsch, B. Lehner, S. Manna, T. M. Krieger, M. Reindl, C. Schimpf, R. Trotta, and A. Rastelli. “GaAs quantum dots grown by droplet etching epitaxy as quantum light sources.” In: *Applied Physics Letters* 119 (2021). DOI: 10.1063/5.0057070.

[31] M. Gurioli, Z. Wang, A. Rastelli, T. Kuroda, and S. Sanguinetti. “Droplet epitaxy of semiconductor nanostructures for quantum photonic devices.” In: *Nature Materials* 18 (2019), pp. 799–810. DOI: 10.1038/s41563-019-0355-y.

[32] Z. M. Wang, B. L. Liang, K. A. Sablon, and G. J. Salamo. “Nanoholes fabricated by self-assembled gallium nanodrill on GaAs (100).” In: *Applied Physics Letters* 90 (2007), p. 113120. DOI: 10.1063/1.2713745.

[33] Y. H. Huo, A. Rastelli, and O. G. Schmidt. “Ultra-small excitonic fine structure splitting in highly symmetric quantum dots on GaAs (001) substrate.” In: *Applied Physics Letters* 102 (2013), p. 152105. DOI: 10.1063/1.4802088.

[34] P. Atkinson, E. Zallo, and O. G. Schmidt. “Independent wavelength and density control of uniform GaAs/AlGaAs quantum dots grown by infilling self-assembled nanoholes.” In: *Journal of Applied Physics* 112.5 (2012), p. 054303. DOI: 10.1063/1.4748183.

[35] M. Reindl, J. H. Weber, D. Huber, C. Schimpf, S. F. Covre da Silva, S. L. Portalupi, R. Trotta, P. Michler, and A. Rastelli. “Highly indistinguishable single photons from incoherently excited quantum dots.” In: *Phys. Rev. B* 100 (2019), p. 155420. DOI: 10.1103/PhysRevB.100.155420.

[36] S. Stobbe, T. W. Schlereth, S. Höfling, A. Forchel, J. M. Hvam, and P. Lodahl. “Large quantum dots with small oscillator strength.” In: *Phys. Rev. B* 82 (2010), p. 233302. DOI: 10.1103/PhysRevB.82.233302.

[37] Takashi Kuroda et al. “Symmetric quantum dots as efficient sources of highly entangled photons: Violation of Bell’s inequality without spectral and temporal filtering.” In: *Phys. Rev. B* 88 (2013), p. 041306. DOI: 10.1103/PhysRevB.88.041306.

[38] A. N. Vamivakas, Y. Zhao, C. Y. Lu, and M. Atatüre. “Spin-resolved quantum-dot resonance fluorescence.” In: *Nature Physics* 5 (2009), pp. 198–202. DOI: 10.1038/nphys1182.

[39] S. Ates, S. M. Ulrich, S. Reitzenstein, A. Löffler, A. Forchel, and P. Michler. “Post-Selected Indistinguishable Photons from the Resonance Fluorescence of a Single Quantum Dot in a Microcavity.” In: *Physical Review Letters* 103 (2009). ISSN: 00319007. DOI: 10.1103/PhysRevLett.103.167402.

[40] D. Huber, B. U. Lehner, D. Csontosová, M. Reindl, S. Schuler, S. F. Covre da Silva, P. Klenovský, and A. Rastelli. “Single-particle-picture breakdown in laterally weakly confining GaAs quantum dots.” In: *Phys. Rev. B* 100 (2019), p. 235425. DOI: 10.1103/PhysRevB.100.235425.

[41] N. Akopian, R. Trotta, E. Zallo, S. Kumar, P. Atkinson, A. Rastelli, O. G. Schmidt, and V. Zwiller. *An artificial atom locked to natural atoms*. 2013. arXiv: 1302.2005.

[42] C. Heyn, M. Zocher, L. Pudewill, H. Runge, A. Küster, and W. Hansen. “Droplet etched GaAs quantum dots close to surfaces and metallic interfaces.” In: *Journal of Applied Physics* 121.4 (2017), p. 044306. DOI: https://doi.org/10.1063/1.4974965.

[43] H. Zhang, Y. Huo, K. Lindfors, Y. Chen, O. G. Schmidt, A. Rastelli, and M. Lippitz. “Narrow-line self-assembled GaAs quantum dots for plasmonics.” In: *Applied Physics Letters* 106 (2015). DOI: 10.1063/1.4914387.

[44] E. M. Purcell. “Spontaneous Emission Probabilities at Radio Frequencies.” In: *Phys. Rev.* 69 (1946), p. 674. URL: https://journals.aps.org/pr/pdf/10.1103/PhysRev.69.674.2.

[45] R. W. Heeres, L. P. Kouwenhoven, and V. Zwiller. “Quantum interference in plasmonic circuits.” In: *Nature Nanotechnology* 8 (2013), pp. 719–722. DOI: 10.1038/nnano.2013.150.

[46] S. G. Dlamini, J. T. Francis, X. Zhang, K. S. K. Özdemir, S. N. Chormaic, F. Petruccione, and M. S. Tame. “Probing Decoherence in Plasmonic Waveguides in the Quantum Regime.” In: *Physical Review Applied* 9 (2018). DOI: https://doi.org/10.1103/PhysRevApplied.9.024003.

[47] L. Novotny and B. Hecht. *Principles of Nano-Optics*. 2nd ed. Cambridge University Press, 2012. DOI: 10.1017/CBO9780511794193.

[48] P. B. Johnson and R. W. Christy. “Optical Constants of the Noble Metals.” In: *Phys. Rev. B* 6 (1972), pp. 4370–4379. DOI: 10.1103/PhysRevB.6.4370.

[49] D. E. Aspnes, S. M. Kelso, R. A. Logan, and R. Bhat. “Optical properties of $Al_xGa_{1-x}As$.” In: *Journal of Applied Physics* 60 (1986), pp. 754–767. DOI: 10.1063/1.337426.

[50] Y. Chen, T. R. Nielsen, N. Gregersen, P. Lodahl, and J. Mørk. "Finite-element modeling of spontaneous emission of a quantum emitter at nanoscale proximity to plasmonic waveguides." In: *Physical Review B - Condensed Matter and Materials Physics* 81 (2010). DOI: `10.1103/PhysRevB.81.125431`.

[51] Y. Chen, N. Gregersen, T. R. Nielsen, J. Mørk, and P. Lodahl. "Spontaneous decay of a single quantum dot coupled to a metallic slot waveguide in the presence of leaky plasmonic modes." In: *Optics Express* 18.12 (2010), pp. 12489–12498. DOI: `10.1364/OE.18.012489`.

[52] M. Song, A. Bouhelier, P. Bramant, J. Sharma, E. Dujardin, D. Zhang, and G. Colas-Des-Francs. "Imaging symmetry-selected corner plasmon modes in penta-twinned crystalline Ag nanowires." In: *ACS Nano* 5 (2011), pp. 5874–5880. DOI: `10.1021/nn201648d`.

[53] COMSOL Multiphysics Inc. *RF Module User's Guide, version 5.6*. URL: `https://doc.comsol.com/5.6/doc/com.comsol.help.rf/RFModuleUsersGuide.pdf`.

[54] J. Jung, T. Søndergaard, and S. I. Bozhevolnyi. "Theoretical analysis of square surface plasmon-polariton waveguides for long-range polarization-independent waveguiding." In: *Phys. Rev. B* 76 (2007), p. 035434. DOI: `10.1103/PhysRevB.76.035434`.

[55] S. Zhang and H. Xu. "Optimizing substrate-mediated plasmon coupling toward high-performance plasmonic nanowire waveguides." In: *ACS Nano* 6 (2012), pp. 8128–8135. DOI: `10.1021/nn302755a`.

[56] M. L. Andersen, S. Stobbe, A. S. Sørensen, and P. Lodahl. "Strongly modified plasmon-matter interaction with mesoscopic quantum emitters." In: *Nature Physics* 7 (2011), pp. 215–218. DOI: `10.1038/nphys1870`.

[57] C. Schörner, S. Adhikari, and M. Lippitz. "A Single-Crystalline Silver Plasmonic Circuit for Visible Quantum Emitters." In: *Nano Letters* 19 (2019), pp. 3238–3243. DOI: `10.1021/acs.nanolett.9b00773`.

[58] S. Rodt and S. Reitzenstein. "High-performance deterministic in situ electron-beam lithography enabled by cathodoluminescence spectroscopy." In: *Nano Express* 2.1 (2021), p. 014007. DOI: `10.1088/2632-959X/abed3c`.

[59] P. Michler. *Quantum dots for quantum information technologies*. 1st ed. Springer, 2017. DOI: `https://doi.org/10.1007/978-3-319-56378-7`.

[60] B. G. Yacobi and D. B. Holt. "Cathodoluminescence scanning electron microscopy of semiconductors." In: *Journal of Applied Physics* 59.4 (1986), R1–R24. DOI: `10.1063/1.336491`.

[61] S. M. Davidson and C. A. Dimitriadis. "Advances in the electrical assessment of semiconductors using the scanning electron microscope." In: *Journal of Microscopy* 118.3 (1980), pp. 275–290. DOI: `10.1111/j.1365-2818.1980.tb00274.x`.

[62] H. A. Zarem, P. C. Sercel, J. A. Lebens, L. E. Eng, A. Yariv, and K. J. Vahala. "Direct determination of the ambipolar diffusion length in GaAs/AlGaAs heterostructures by cathodoluminescence." In: *Applied Physics Letters* 55 (1989), pp. 1647–1649. DOI: 10.1063/1.102226.

[63] A. Rastelli, S. Stufler, A. Schliwa, R. Songmuang, C. Manzano, G. Costantini, K. Kern, A. Zrenner, D. Bimberg, and O. G. Schmidt. "Hierarchical self-assembly of GaAs/AlGaAs quantum dots." In: *Physical Review Letters* 92 (2004). DOI: 10.1103/PhysRevLett.92.166104.

[64] L. Wang, V. Krapek, F. Ding, F. Horton, A. Schliwa, D. Bimberg, A. Rastelli, and O. G. Schmidt. "Self-assembled quantum dots with tunable thickness of the wetting layer: Role of vertical confinement on interlevel spacing." In: *Phys. Rev. B* 80 (2009), p. 085309. DOI: 10.1103/PhysRevB.80.085309.

[65] M. Benyoucef, A. Rastelli, O. G. Schmidt, S. M. Ulrich, and P. Michler. "Temperature dependent optical properties of single, hierarchically self-assembled GaAs/AlGaAs quantum dots." In: *Nanoscale Research Letters* 1 (2006), pp. 172–176. DOI: 10.1007/s11671-006-9019-3.

[66] G. J. Schäfer. "Spektroskopie an einzelnen Halbleiter-Quantenpunkten: Aufbau zweier Tieftemperatur-Experimente." PhD thesis. Universität Bayreuth, 2021. URL: https://epub.uni-bayreuth.de/id/eprint/5629/.

[67] C. Wang, G. Thummes, and C. Heiden. *A two-stage pulse tube cooler operating below 4 K*. 1997, pp. 159–164. DOI: https://doi.org/10.1016/S0011-2275(96)00112-9.

[68] D. Durand, D. Adachi, D. Harvey, C. Jaco, M. Michaelian, T. Nguyen, M. Petach, and J. Raab. "Mid InfraRed Instrument (MIRI) cooler subsystem design." In: *Cryocoolers* 15 (2009), pp. 7–12. URL: https://api.semanticscholar.org/CorpusID:121196920.

[69] A. T. A. M. de Waele. "Basic operation of cryocoolers and related thermal machines." In: *Journal of Low Temperature Physics* 164 (2011), pp. 179–236. DOI: 10.1007/s10909-011-0373-x.

[70] C. Schimpf, S. Manna, S. F. Covre da Silva, M. Aigner, and A. Rastelli. "Entanglement-based quantum key distribution with a blinking-free quantum dot operated at a temperature up to 20 K." In: *Advanced Photonics* 3.6 (2021), p. 065001. DOI: 10.1117/1.AP.3.6.065001.

[71] P. Yeh and M. Hendry. *Optical waves in layered media*. 1st ed. John Wiley & Sons, 2005. ISBN: 978-0-471-73192-4.

[72] K. Papatryfonos, T. Angelova, A. Brimont, B. Reid, S. Guldin, P. R. Smith, M. Tang, K. Li, A. J. Seeds, H. Liu, and D. R. Selviah. "Refractive indices of MBE-grown $Al_xGa_{1-x}As$ ternary alloys in the transparent wavelength region." In: *AIP Advances* 11 (2021), p. 025327. DOI: 10.1063/5.0039631.

[73] A. D. Rakic and M. L. Majewski. "Modeling the optical dielectric function of GaAs and AlAs: Extension of Adachi's model." In: *Journal of Applied Physics* 80.10 (1996), pp. 5909–5914. DOI: 10.1063/1.363586.

[74] Dietrich Meyerhofer. “Characteristics of resist films produced by spinning.” In: *Journal of Applied Physics* 49.7 (1978), pp. 3993–3997. DOI: `10.1063/1.325357`.

[75] J. Alin. *Spin-on-Glas-Schichten zur Planarisierung nanoskaliger Strukturen*. Universtität Bayreuth, 2020. URL: `https://eref.uni-bayreuth.de/id/eprint/63045/`.

[76] S. I. Bozhevolnyi and J. B. Khurgin. “The case for quantum plasmonics.” In: *Nature Photonics* 11 (2017), pp. 398–400. DOI: `10.1038/nphoton.2017.103`.

[77] T. Heindel, J.-H. Kim, N. Gregersen, A. Rastelli, and S. Reitzenstein. “Quantum dots for photonic quantum information technology.” In: *Advances in Optics and Photonics* 15 (2023), p. 613. DOI: `10.1364/aop.490091`.

[78] G. V. Naik, V. M. Shalaev, and A. Boltasseva. “Alternative Plasmonic Materials: Beyond Gold and Silver.” In: *Advanced Materials* 25.24 (2013), pp. 3264–3294. DOI: `https://doi.org/10.1002/adma.201205076`.

[79] C. C. Neacsu, S. Berweger, R. L. Olmon, L. V. Saraf, C. Ropers, and M. B. Raschke. “Near-field localization in plasmonic superfocusing: A nanoemitter on a tip.” In: *Nano Letters* 10 (2010), pp. 592–596. DOI: `10.1021/nl903574a`.

[80] M. Pfeiffer, K. Lindfors, H. Zhang, B. Fenk, F. Phillipp, P. Atkinson, A. Rastelli, O. G. Schmidt, H. Giessen, and M. Lippitz. “Eleven nanometer alignment precision of a plasmonic nanoantenna with a self-assembled GaAs quantum dot.” In: *Nano Letters* 14 (2014), pp. 197–201. DOI: `10.1021/nl403730q`.

[81] D. Wolf, T. Schumacher, and M. Lippitz. “Shaping the nonlinear near field.” In: *Nature Communications* 7 (2016), p. 10361. DOI: `10.1038/ncomms10361`.

[82] S. Kumar and S. I. Bozhevolnyi. “Single Photon Emitters Coupled to Plasmonic Waveguides: A Review.” In: *Advanced Quantum Technologies* 4 (2021), p. 2100057. DOI: `https://doi.org/10.1002/qute.202100057`.

[83] S. Kumar, S. K. H. Andersen, and S. I. Bozhevolnyi. “Extremely Confined Gap-Plasmon Waveguide Modes Excited by Nitrogen-Vacancy Centers in Diamonds.” In: *ACS Photonics* 6 (2019), pp. 23–29. DOI: `10.1021/acsphotonics.8b01225`.

[84] C. Schörner and M. Lippitz. “Single Molecule Nonlinearity in a Plasmonic Waveguide.” In: *Nano Letters* 20 (2020), pp. 2152–2156. DOI: `10.1021/acs.nanolett.0c00196`.

[85] E. Bermúdez-Ureña, C. Gonzalez-Ballestero, M. Geiselmann, R. Marty, I. P. Radko, T. Holmgaard, Y. Alaverdyan, E. Moreno, F. J. García-Vidal, S. I. Bozhevolnyi, and R. Quidant. “Coupling of individual quantum emitters to channel plasmons.” In: *Nature Communications* 6 (2015). DOI: `10.1038/ncomms8883`.

[86] S. J. P. Kress, F. V. Antolinez, P. Richner, S. V. Jayanti, D. K. Kim, F. Prins, A. Riedinger, M. P. C. Fischer, S. Meyer, K. M. McPeak, D. Poulikakos, and D. J. Norris. “Wedge Waveguides and Resonators for Quantum Plasmonics.” In: *Nano Letters* 15 (2015), pp. 6267–6275. DOI: `10.1021/acs.nanolett.5b03051`.

[87] T. Mii and H. C. Casey. “Properties of Spin-on Glass as an Insulator Metal-Insulator-Semiconductor Structures for InP.” In: *Journal of Electronic Materials* 19 (1990). DOI: https://doi.org/10.1007/BF02673343.

[88] J. Wang, J. Jiu, T. Araki, M. Nogi, T. Sugahara, S. Nagao, H. Koga, P. He, and K. Suganuma. “Silver nanowire electrodes: Conductivity improvement without post-treatment and application in capacitive pressure sensors.” In: *Nano-Micro Letters* 7 (2015), pp. 51–58. DOI: 10.1007/s40820-014-0018-0.

[89] P. Johns, G. Beane, K. Yu, and G. V. Hartland. “Dynamics of Surface Plasmon Polaritons in Metal Nanowires.” In: *The Journal of Physical Chemistry C* 121.10 (2017), pp. 5445–5459. DOI: 10.1021/acs.jpcc.6b12748.

[90] X. Wu and Y. Wang. “A physics-based machine learning approach for modeling the complex reflection coefficients of metal nanowires.” In: *Nanotechnology* 33 (2022), p. 205701. DOI: 10.1088/1361-6528/ac512e.

[91] D. T. Schoen, A. C. Atre, A. García-Etxarri, J. A. Dionne, and M. L. Brongersma. “Probing complex reflection coefficients in one-dimensional surface plasmon polariton waveguides and cavities using STEM EELS.” In: *Nano Letters* 15 (2015), pp. 120–126. DOI: 10.1021/nl503179j.

[92] W. L. Barnes, G. Björk, J. M. Gérard, P. Jonsson, J. A. E. Wasey, P. T. Worthing, and V. Zwiller. “Solid-state single photon sources: Light collection strategies.” In: *European Physical Journal D* 18 (2002), pp. 197–210. DOI: 10.1140/epjd/e20020024.

[93] J. Yang, J. P. Hugonin, and P. Lalanne. “Near-to-Far Field Transformations for Radiative and Guided Waves.” In: *ACS Photonics* 3 (2016), pp. 395–402. DOI: 10.1021/acsphotonics.5b00559.

[94] P. Grimm, G. Razinskas, J. S. Huang, and B. Hecht. “Driving plasmonic nanoantennas at perfect impedance matching using generalized coherent perfect absorption.” In: *Nanophotonics* 10 (2021), pp. 1879–1887. DOI: 10.1515/nanoph-2021-0048.

[95] L. Zhai, M. C. Löbl, G. N. Nguyen, J. Ritzmann, A. Javadi, C. Spinnler, A. D. Wieck, A. Ludwig, and R. J. Warburton. “Low-noise GaAs quantum dots for quantum photonics.” In: *Nature Communications* 11 (2020), p. 4745. DOI: 10.1038/s41467-020-18625-z.

[96] P. Michler, A. Kiraz, C. Becher, W. V. Schoenfeld, P. M. Petroff, L. Zhang, E. Hu, and A. Imamoglu. “A Quantum Dot Single-Photon Turnstile Device.” In: *Science* 290.5500 (2000), pp. 2282–2285. DOI: 10.1126/science.290.5500.2282.

[97] L. Schweickert, K. D. Jöns, K. D. Zeuner, S. F. Covre Da Silva, H. Huang, T. Lettner, M. Reindl, J. Zichi, R. Trotta, A. Rastelli, and V. Zwiller. “On-demand generation of background-free single photons from a solid-state source.” In: *Applied Physics Letters* 112 (2018). DOI: 10.1063/1.5020038.

[98] S. Kumar and S. I. Bozhevolnyi. “Excitation of Hybrid Plasmonic Waveguide Modes by Colloidal Quantum Dots.” In: *ACS Photonics* 6 (2019), pp. 1587–1593. DOI: 10.1021/acsphotonics.9b00379.

[99] C. Gruber, A. Trügler, A. Hohenau, U. Hohenester, and J. R. Krenn. "Spectral modifications and polarization dependent coupling in tailored assemblies of quantum dots and plasmonic nanowires." In: *Nano Letters* 13.9 (2013), pp. 4257–4262. DOI: https://doi.org/10.1021/nl4019947.

[100] S. Kreinberg, W. W. Chow, J. Wolters, C. Schneider, C. Gies, F. Jahnke, S. Höfling, M. Kamp, and S. Reitzenstein. "Emission from quantum-dot high-ß microcavities: Transition from spontaneous emission to lasing and the effects of superradiant emitter coupling." In: *Light: Science and Applications* 6 (2017). DOI: 10.1038/lsa.2017.30.

[101] J. Alin. *Graustufen-Lithografie für plasmonische Wellenleiter*. Universität Bayreuth, 2023. URL: https://eref.uni-bayreuth.de/id/eprint/86138/.

[102] T. Pfadenhauer. *Numerical Optimization of the Coupling Between a Quantum Dot and a Plasmonic Waveguide on a Semiconductor Substrate*. Universität Bayreuth, 2022. URL: https://eref.uni-bayreuth.de/id/eprint/74076/.

[103] M. Gschrey et al. "Highly indistinguishable photons from deterministic quantum-dot microlenses utilizing three-dimensional in situ electron-beam lithography." In: *Nature Communications* 6 (2015). DOI: 10.1038/ncomms8662.

[104] M. Gschrey, F. Gericke, A. Schüßler, R. Schmidt, J. H. Schulze, T. Heindel, S. Rodt, A. Strittmatter, and S. Reitzenstein. "In situ electron-beam lithography of deterministic single-quantum-dot mesa-structures using low-temperature cathodoluminescence spectroscopy." In: *Applied Physics Letters* 102 (2013). DOI: 10.1063/1.4812343.

[105] P. Schnauber, J. Schall, S. Bounouar, T. Höhne, S. I. Park, G. H. Ryu, T. Heindel, S. Burger, J. D. Song, S. Rodt, and S. Reitzenstein. "Deterministic Integration of Quantum Dots into on-Chip Multimode Interference Beamsplitters Using in Situ Electron Beam Lithography." In: *Nano Letters* 18 (2018), pp. 2336–2342. DOI: 10.1021/acs.nanolett.7b05218.

[106] S. Manna, H. Huang, S. F. Covre da Silva, C. Schimpf, M. B. Rota, B. Lehner, M. Reindl, R. Trotta, and A. Rastelli. "Surface passivation and oxide encapsulation to improve optical properties of a single GaAs quantum dot close to the surface." In: *Applied Surface Science* 532 (2020), p. 147360. DOI: https://doi.org/10.1016/j.apsusc.2020.147360.

[107] L. B. Rothman. "Properties of Thin Polyimide Films." In: *Journal of The Electrochemical Society* 127.10 (1980), p. 2216. DOI: 10.1149/1.2129377.

[108] R. Yan, P. Pausauskie, J. Huang, and P. Yang. "Direct photonic–plasmonic coupling and routing in single nanowires." In: *Proceedings of the National Academy of Sciences* 106 (2009), pp. 21045–21050. DOI: 10.1073/pnas.0902064106.

[109] W. Wang, Q. Yang, F. Fan, H. Xu, and Z. L. Wang. "Light propagation in curved silver nanowire plasmonic waveguides." In: *Nano Letters* 11 (2011), pp. 1603–1608. DOI: 10.1021/nl104514m.

[110] D. Rossouw and G. A. Botton. "Plasmonic response of bent silver nanowires for nanophotonic subwavelength waveguiding." In: *Physical Review Letters* 110 (2013), p. 066801. DOI: 10.1103/PhysRevLett.110.066801.

[111] S. Li, Y. Yang, J. Schall, M. von Helversen, C. Palekar, H. Liu, L. Roche, S. Rodt, H. Ni, Y. Zhang, Z. Niu, and S. Reitzenstein. "Scalable Deterministic Integration of Two Quantum Dots into an On-Chip Quantum Circuit." In: *ACS Photonics* 10 (2023), pp. 2846–2853. DOI: `10.1021/acsphotonics.3c00547`.

[112] J. B. Khurgin. "How to deal with the loss in plasmonics and metamaterials." In: *Nature Nanotechnology* 10 (2015), pp. 2–6. DOI: `10.1038/nnano.2014.310`.

[113] A. V. Kuhlmann, J. H. Prechtel, J. Houel, A. Ludwig, D. Reuter, A. D. Wieck, and R. J. Warburton. "Transform-limited single photons from a single quantum dot." In: *Nature communications* 6.1 (2015), p. 8204. DOI: `https://doi.org/10.1038/ncomms9204`.

[114] N. Somaschi et al. "Near-optimal single-photon sources in the solid state." In: *Nature Photonics* 10 (2016), pp. 340–345. DOI: `https://doi.org/10.1038/nphoton.2016.23`.

[115] S. Kim and M. Qi. "Polarization rotation and coupling between silicon waveguide and hybrid plasmonic waveguide." In: *Optics Express* 23.8 (2015), pp. 9968–9978. DOI: `https://doi.org/10.1364/OE.23.009968`.

[116] O. Gazzano, S. M. de Vasconcellos, K. Gauthron, C. Symonds, J. Bloch, P. Voisin, J. Bellessa, A. Lemaître, and P. Senellart. "Evidence for confined Tamm plasmon modes under metallic microdisks and application to the control of spontaneous optical emission." In: *Physical Review Letters* 107 (2011). DOI: `10.1103/PhysRevLett.107.247402`.

[117] B. Demory, T. A. Hill, C.-H. Teng, L. Zhang, H. Deng, and P.-C. Ku. "Plasmonic Enhancement of Single Photon Emission from a Site-Controlled Quantum Dot." In: *ACS Photonics* 2.8 (2015), pp. 1065–1070. DOI: `10.1021/acsphotonics.5b00086`.

[118] F. B. Arango, A. Kwadrin, and A. F. Koenderink. "Plasmonic Antennas Hybridized with Dielectric Waveguides." In: *ACS Nano* 6.11 (2012), pp. 10156–10167. DOI: `10.1021/nn303907r`.

[119] L. Wang, A. Rastelli, S. Kiravittaya, M. Benyoucef, and O. G. Schmidt. "Self-assembled quantum dot molecules." In: *Advanced Materials* 21 (2009), pp. 2601–2618. DOI: `https://doi.org/10.1002/adma.200803109`.

EIDESSTATTLICHE ERKLÄRUNG

Hiermit versichere ich an Eides statt, dass ich die vorliegende Arbeit selbstständig verfasst und keine anderen als die von mir angegebenen Quellen und Hilfsmittel verwendet habe.

Weiterhin erkläre ich, dass ich die Hilfe von gewerblichen Promotionsberatern bzw. Promotionsvermittlern oder ähnlichen Dienstleistern weder bisher in Anspruch genommen habe, noch künftig in Anspruch nehmen werde.

Zusätzlich erkläre ich hiermit, dass ich keinerlei frühere Promotionsversuche unternommen habe.

Ort, Datum	Michael Seidel

DANKSAGUNG

Zunächst möchte ich mich bei Prof. Markus Lippitz bedanken, der jederzeit ein offenes Ohr für mich hatte und dessen Unterstützung ich mir immer sicher sein konnte. Besonders schätzte ich die Ermutigung zum selbständigen Arbeiten sowie die keineswegs selbstverständlichen Freiheiten bei der Gestaltung des Themas.

Weiterhin möchte ich mich bei dem Zweitgutachter Prof. Jürgen Köhler und der Prüfungskommission für das Interesse an meiner Arbeit danken. Insbesondere Prof. Georg Herink danke ich für die lehrreiche Zeit während meiner Masterarbeit.

Außerdem bedanke ich mich bei Prof. Stephan Reitzenstein und Yuhui Yang für die gute Zusammenarbeit bei den Kathodolumineszenzmessungen und die beiden Aufenthalte an der TU Berlin. Prof. Armando Rastelli und Dr. Saimon Covre da Silva von der JKU Linz danke ich für die hervorragenden Quantenpunkt-Proben.

Schließlich möchte ich meinen Kollegen und Freunden der Lehrstühle EP3 und EP8 meinen Dank aussprechen. Die fachlichen und außerfachlichen Diskussionen in den Kaffeepausen bleiben mir in bester Erinnerung. Besonderer Dank gilt Dr. Thorsten Schumacher, auf den ich mich sowohl wissenschaftlich als auch persönlich immer verlassen konnte.

Mein Dank gilt auch meinen Eltern, die mir stets das notwendige Maß an Vertrauen und Unterstützung gegeben haben, und meiner Sophie, die einige Höhen und Tiefen miterlebt hat und auch spätabendliche Kryostatenkontrollen toleriert hat.

COLOPHON

This document was typeset using the typographical look-and-feel `classicthesis` developed by André Miede and Ivo Pletikosić. The style was inspired by Robert Bringhurst's seminal book on typography *"The Elements of Typographic Style"*.